Measurements of Upsilon meson suppression in heavy ion collisions with the CMS experiment at the LHC

Nicolas Filipovic

NNT: 2015SACLS095

Thèse de doctorat de L'Université Paris-Saclay

préparée à

L'Université Paris Sud

École Doctorale n° 576

Particules, Hadrons, Énergie, Noyau, Instrumentation, Imagerie, Cosmos et Simulation (PHENIICS)

Spécialité Physique hadronique

Par

Nicolas Filipović

Measurements of Υ meson suppression in heavy ion collisions with the CMS experiment at the LHC

Thèse présentée et soutenue à Palaiseau, le 12 novembre 2015 :

Composition du Jury :

Marie-Hélène Schune	LAL, Orsay	Présidente
Jana Bielčiková	ASCR, Prague	Rapporteuse
Ginés Martinez	Subatech, Nantes	Rapporteur
Manuel Calderón de la Barca Sánchez	University of California, Davis	Examinateur
Yen-Jie Lee	MIT, Cambridge	Examinateur
Ágnes Mócsy	Pratt Institute, Brooklyn	Examinatrice
Raphaël Granier de Cassagnac	LLR, Palaiseau	Directeur de thèse

Contents

Résumé en français

Ce document, intitulé *Mesures de la suppression des mésons* Υ *en collisions d'ions lourds dans l'expérience CMS au LHC*, est une thèse rédigée en vue d'obtenir le grade de Docteur de l'Université Paris-Saclay, spécialité Physique Hadronique. Cette thèse est le résumé de trois années de recherche passées au sein du Laboratoire Leprince-Ringuet à l'École polytechnique à Palaiseau, sous la direction du directeur de recherche Raphaël Granier de Cassagnac. La présente thèse étant rédigée en anglais, elle nécessite l'addition d'un « résumé substantiel en français », selon la procédure de soutenance de doctorat rédigée par l'Université[1]. S'ensuit donc ce résumé dans le résumé.

La présente thèse relate de mesures de la suppression des mésons Υ en collisions d'ions plomb-plomb, relativement à leur production en collisions proton-proton, à l'énergie dans le centre de masse de $\sqrt{s} = 2.76$ TeV par paires de nucléons. Ces collisions furent délivrées par le Grand collisionneur de hadrons (LHC) au détecteur CMS en 2011 et 2013. Les mesures effectuées précédemment sur le même sujet [2, 3, 4] ont attesté de la quasi-complète suppression des états excités Υ(2S) et Υ(3S), ainsi que de la nette modification du taux de production de l'état fondamental Υ(1S), en fonction de la centralité de la collision plomb-plomb. Ces observations sont compatibles avec l'hypothèse de fonte séquentielle des quarkonia lors de la formation d'un plasma de quarks et de gluons (PQG).

Cette nouvelle analyse dispose d'un plus grand échantillon de données proton-proton, ainsi que d'une meilleure reconstruction des particules produites dans les collisions plomb-plomb. Avec ces deux améliorations, il est possible d'étudier plus en détail le mécanisme responsable de la suppression des quarkonia en présence du PQG. En particulier, l'étude présentée relate des taux de production en fonction de variables cinématiques telles que l'impulsion transverse et la rapidité, en plus d'une réitération de l'analyse en fonction de la centralité.

Dans le premier chapitre, certaines notions phénoménologiques nécessaires à la compréhension de la formation du PQG sont présentées. On fait d'abord un point historique sur l'avènement de la chromodynamique quantique, théorie quantique formalisant l'interaction forte entre quarks et gluons, dont le confinement et la liberté asymptotique sont deux propriétés bien connues. On se propose ensuite de monter en température, pour laisser apparaître le caractère déconfiné de la matière nucléaire portée à haute densité d'énergie. On énonce quelques conséquences de cette transition de phase qu'est le PQG sur les particules produites dans les collisions nucléaires ultrarelativistes. En particulier, la fonte séquentielle des quarkonia est, historiquement, une des preuves irréfutables de la formation du PQG. Le second chapitre se propose de décrire les quarkonia, autant du point de vue de la production en collisions proton-proton que dans le contexte de collisions nucléaires. Leurs mécanismes de production étant encore aujourd'hui disputés, il n'est pas possible de conclure sur ce sujet dans le contexte de

cette thèse. Cependant, une mesure de leur modification dans la matière nucléaire est possible dès lors qu'on dispose d'une référence, qui est mesuré expérimentalement en collisions proton-proton. La partie théorique de cette thèse se termine par un résumé de l'état de l'art de la recherche sur la suppression des quarkonia avant le début de cette thèse.

La deuxième partie du présent rapport est dédiée au contexte expérimental. Elle résume en deux chapitres les dispositifs expérimentaux nécessaires à la production des données ci-analysées, ainsi que les outils matériels et logiciels employés dans la présente analyse. Le troisième chapitre contient d'abord une description succinte du LHC et de sa capacité à produire des collisions ultrarelativistes de différent noyaux atomiques. Les détecteurs collectant des données auprès du LHC sont mentionnés, avant de présenter en détail le détecteur utilisé dans l'analyse. Le Solénoïde compact à muons (CMS) est une expérience polyvalente, capable de mesurer en détail des processus rares tel que le mécanisme de Higgs, ainsi que d'enregistrer l'ensemble des objets produits dans une collision d'ions lourds. Les moyens mis en place pour déclencher la prise de données doivent donc être flexibles et précis. Le quatrième chapitre présente les spécificités et les performances nécessaires au bon déroulement de l'analyse. Le système de déclenchement du détecteur est présenté, ainsi que ses performances lors des prises de données auxquelles j'ai assisté en 2013. Les différentes méthodes de reconstruction et de sélections des muons, ces leptons fugaces que le détecteur reconnaît si bien, sont également présentées dans le chapitre 4. Enfin, la catégorisation des collisions d'ions lourds en plusieurs classes de centralités est présentée. Cet aspect important des collisions d'ions lourds est indispensable pour bien identifier les collisions dans lesquelles le PQG est susceptible d'être créé.

La troisième partie, dédiée à l'analyse proprement dite, est séparée en trois chapitres. Le chapitre cinq représente probablement le cœur du travail effectué ces trois dernières années. Dans ce chapitre, on se propose de revisiter la sélection cinématique des muons découlant de la désintégration des Υ, afin d'améliorer le rapport signal sur bruit dans l'analyse. On découvre que les résonances étant produites dans un régime non relativiste, la désintégration en deux muons est nettement asymmétrique. Cette particularité permet de récupérer près de trente-cinq pourcent de données de bonne qualité, autrement perdues si une sélection plus standard eût été appliquée. Enfin, l'extraction du signal est détaillée, ainsi que les taux de signal résultant en fonction des variables cinématiques p_T, y, et de la centralité de la collisions plomb-plomb. Les variations nécessaires à l'établissement d'une erreur systématique sur l'extraction du signal sont présentées. Ces mesures permettront l'expression des résultats au chapitre sept, sous la forme de sections efficaces de production en collisions proton-proton, des taux corrigés en collisions plomb-plomb, ainsi que du facteur de modification nucléaire (R_{AA}) pour chaque méson, en fonction de l'observable considérée. Le sixième chapitre établit comment les taux bruts enregistrés au chapitre cinq sont corrigés de certains effets naturels de perte du signal. L'acceptance et l'efficacité de détection sont définies et calculées pour les trois états Υ(1S,2S,3S). Différentes sources d'erreur connues dans l'estimation de l'efficacité doivent être évaluées précisément, au regard de la méthode de déclenchement et de la méthode de sélection utilisées, afin de rendre à l'efficacité de

détection une valeur corrigée. Une méthode célèbre dans ce type d'analyse est présentée. Enfin, les erreurs systématiques relatives à chaque correction (acceptance, efficacité, correction de second ordre) sont estimées. Le chapitre sept présente les résultats obtenus grâce aux mesures et à leur corrections successives. Les sections efficaces de production en collisions proton-proton sont tout d'abord présentées pour les mésons Υ(1S), Υ(2S) et Υ(3S), en fonction de leur impulsion transverse et de leur rapidité. Des mesures équivalentes sont présentées ensuite dans le contexte des collisions plomb-plomb, afin d'extraire le facteur de modification nucléaire. On observe que les R_{AA} des Υ(1S,2S,3S) analysés ici sont compatibles et plus précis que les précédents résultats exprimés par CMS en 2012 à la même énergie dans le centre de masse [2, 3, 4]. Ces résultats montrent également que la suppression des Υ(1S) et Υ(2S) est indépendante de l'impulsion transverse à laquelle ces mésons sont produits. L'état excité Υ(3S) est encore insaisissable en collisions plomb-plomb, car fortement supprimé : on établit alors une limite supérieure à sa suppression, dans l'attente d'une mesure ultérieure, plus significative. Le R_{AA} mesuré pour le Υ(1S) en fonction de la rapidité est aussi compatible avec une mesure de l'expérience ALICE [5], et laisse à croire que la suppression de la suppression de ce dernier est essentiellement indépendante de la rapidité. Pour finir, les mesures de la présente analyse sont comparées à des modèles phénoménologiques de suppression des quarkonia dans le PQG. Dans la majeure partie de l'espace des paramètres considéré, les modèles reproduisent correctement les données.

Remerciements – Acknowledgments

Lord, have mercy on the hippies and faggots
And the dykes and the weird little children they grow
Help the black man
Help the poor man
Help the milk man
Help the door man
Help the lonely, neglected old farts that I know

Frank Zappa, in *Strictly Genteel (The Finale), 200 Motels*

Après avoir tant pris, il est temps de rendre !

Les trois années qui constituent cette thèse m'ont modelé, et c'est probablement incompréhensible pour qui n'est pas passé par là. Il est temps de remercier tous ces gens qui ont œuvré, de près comme de loin, à la bonne conduite de mes travaux. Et y'a pas à dire, il aura fallu beaucoup de gens pour faire de moi un docteur.

Raphaël, notre Général de Cavalerie, Boss. Qui de mieux placé pour figurer au sommet de cette liste ? Heureusement, il y a des gens comme toi pour avoir de l'indulgence et un peu d'espoir pour des trublions de mon espèce. Un merci ne suffit pas... alors merci et merci ! Merci d'avoir lutté avec moi pour quelques muons de plus. Merci de m'avoir défendu sans relâche. Café ?

To my thesis committee. Thank you very much for accepting to be part of this defence, and for accepting to review the document so fast. As I have said after the defence, you have supernatural powers and ought to be thanked for that. Thank you Marie-Hélène, Gines, Yen-Jie. Also, special thanks to Jana for a very careful account of the complete number of missing spaces in the document ;-). Thank you Manuel for all the enthusiasm and the brightness you've brought to this Υ analysis. Thank you Ágnes for not being angry at us when we broke the quarkonium thermometer (which I'm sure can be fixed). While lots of people use deception and the strength of arguments to ease their way through life, only a few dare to fight for a greater good with your integrity and courage. I have the utmost respect and gratitude for you, and we shall meet again.

Merci à toute l'équipe encadrante du LLR au sens large du terme, pour son soutien inconditionnel. Un grand merci en particulier à celles et ceux avec qui j'ai eu l'occasion d'intéragir, de boire du café, ou de rigoler simplement. J'ai une pensée spéciale pour Maïthé, Thu, Brigitte, Bambi, Hamid, avec qui j'ai eu des moments de complicités certains. Merci aux informaticiens et aux électroniciens et aux mécanos, et à l'équipe Omega, même si on se connaît pas trop. Vous avez l'air vachement sympas !

Les chercheurs de ce labo transportent avec eux ce qu'il y a de mieux dans ce métier. Je suis infiniment redevable à nombre d'entre eux pour m'avoir montré les ficelles. Je

peux affirmer que nulle part ailleurs que dans les bureaux, couloirs et salles de réunion du LLR je n'ai rencontré si souvent tant d'intelligence et de malice, dans ma petite vie. Heureusement que le nettoyage est régulier, il y a beaucoup de matière grise qui s'éparpille sur les sols, les murs et les écrans, chaque jour! Vous êtes tous un exemple pour chaque jeune qui passe par là. Merci à chacun d'entre vous. Un remerciement tout particulier aux anciens thésards David, Jonathan, Nadir, Benjamin, Ivo, Yacine, qui montrèrent fièrement l'exemple (ou pas !). Merci à Olivier Davignon pour sa complicité et sa fraicheur sans égal. Merci à Luca pour sa fraîcheur et sa complicité, sans égal. Merci à Thomas, Frédéric, Pascal, non seulement pour leur indulgence sur le cours de tennis, mais aussi pour le *bremsstrahlung* de science qui les suit partout. Merci également à Louis, Stéphanie, Christophe, Berrie, Olivier, Florian, Philippe. Et tant d'autres, qu'ils me pardonnent de ne pas les faire apparaître ici.

Un grand bon courage à tous ceux qui n'en ont pas encore terminé avec ce labo de fou(s) : Iurii, Stas, André, Thomas, Philipp, Simon, Floriana, Luca. Vous y êtes presque !

Merci aux membres de l'IPN Orsay, du SPhN et du CPhT Saclay pour avoir participé aux séminaires que j'ai co-organisé avec Igor et Katya. Merci à ces deux-là aussi ! Merci et bonne continuation à Antoine et Javier, les deux Nantais parachutés sur le plateau !

Je tiens aussi à remercier Ludwik et Philippe pour m'avoir accueilli dans leur bureau : malgré notre différence d'âge, je pense que nous avons formé une équipe de choc ! Enfin, un grand merci à Yves pour son dynamisme et son enthousiasme instoppables, vraiment exemplaires.

Le groupe CMS-Heavy Ions. Les gars, ne pas être avec vous pour faire de la physique, c'est dur. Ne plus être avec vous pour râler, dire du mal des autres, me goinfrer de cookies, de frites, de sauce poivre et de café, c'est pire. Je vous suis éternellement reconnaissant pour votre accueil et votre collaboration de tous les instants.

Matthew, tu m'as accompagné lors de ma première visite du groupe, et depuis tu n'as jamais cessé d'être de bon conseil sur toute la ligne : Merci.

Yetkin, you have shown calm and wisdom in many occasions. You will also be praised for your ability to absorb coffee at twice the rate of the average researcher. Thanks, and keep up the good fight.

Lamia, tu as quitté ce laboratoire il y a quelques années maintenant, mais tu as marqué mon esprit par ta bienveillance à mon égard, et ton éternelle bonne humeur bien de chez nous. Merci !

Alice, tu as enflammé les discussions de nos déjeuners et pauses café. Merci !

Torsten, you have given so much of your time in micro-managing my first steps in the dilepton world. Your help and your style really made a difference. Thank you.

Chad. Thanks for being such a good friend at all times. It is a pleasure to see someone going through similar things, and I know for a fact you are doing better than me. Great taste in beer, too.

Camelia, Master. Still waters run deep! There would be many things to say about our shared time in the yellow office and beyond, but I will follow your advice and *keep it short*. You have had an extraordinary influence on making my work a success, and I

am forever indebted to you. Thank you.

Émilien. Je ne mesure pas encore la chance que j'ai eu de collaborer avec toi. Ton talent et ton humilité dépassent le simple cadre du travail, tel que j'ai pu le constater en studio. Je te remercie pour tout.

Mihee. Thank you so much for your kindness and for always being so receptive to my silly jokes. 간지난다 !!

François. Mon cher compère, je ne sais pas ce que serait le freak office sans toi. Merci pour avoir répondu à toutes mes questions, merci pour ta patience, tu as vraiment été le premier rempart à tous mes accès de mauvaise humeur, et tu es resté positif. On a bien roulé notre bosse à travers le monde et je te suis tellement reconnaissant d'avoir été là dans tous ces moments ! Je te pardonne tes goûts musicaux déplorables et ta vénération d'un certain Roger. Puisses-tu continuer à trancher droit dans le lard des théoriciens qui n'ont pas encore accepté que tout est jet quenching. Un grand merci à Stéphane aussi, le père Confiance, pour nos multiples rencontres agréables.

Cette liste de remerciements ne serait complète sans l'apport extérieur de mes amis et de ma famille. Depuis mon arrivée à Paris, j'ai eu une chance inouïe, qui m'a amené à rencontrer quelques personnages clés. Pour rester dans le domaine de la physique des hautes énergies tout d'abord, je tiens à remercier Raphaël Chalmé-Calvet et Aurélie Mutschler pour tous les bons moments à NPAC et au-delà. Sylvestre Pires est très largement responsable pour ma réussite dans ce master. Peu de gens ont la témérité de ce charmant jeune homme. Merci d'être venu à ma soutenance et de ne pas m'avoir inclus dans tes remerciements, connard !

Sans Raphaël Riquier, je n'aurais simplement pas été le même. Merci pour les fous rires en TD et en amphi depuis la première année. Merci pour avoir trainé avec moi dans un maelstrom de *private jokes*, merci pour le stage de L3 où j'ai fait mon premier *fit*. Merci pour m'avoir initié à Civilization V et pour avoir créé un monstre. Merci pour les mafés, pour les parties de PS3. Merci pour avoir fourni une disquette et un ordinateur. Merci pour avoir prétendu m'écouter déblatérer si souvent. Merci pour la colocation !

Je connais une clique d'affreux jojos qu'on surnomme souvent les Michels. Peu de gens connaissent la composition exacte de cette confrérie. Dispersés comme la Communauté de l'Anneau, ils n'en reste pas moins uniques. J'aimerais que ceux-ci sachent que ça y est, ils peuvent enfin m'appeler docteur, mais que non, je ne suis pas chimiste. Que la physique, c'est différent (c'est mieux). Que j'ai été ravi d'être l'un de leur Mich-michs. J'aimerais tous les remercier. Parmi eux et autour d'eux, j'aimerais en particulier remercier Thomas, Léo et Camille Schweitzer, Alexandre et Solène Lopes, Loïc Orsini, Kévin Le Dû, Geoffroy Latour, Hugo Pacou, Boris Von Dahle, Rui Fernandes, Nicolas Turki, et Claire Saint-Sulpice, Charlotte Languiller, Claire Guillermic, Ariane Louis, Nina Duczmalewska, Margot Bertin, Piia Arvilommi, Amélie Guérin, et tant d'autres. Merci pour Jouy, pour les apéros, les bœufs.

Merci à Émilie Franco pour sa joie de vivre bien de chez nous. Puisses-tu devenir une grande actrice !

Merci à François Salmon, dont la prestigieuse institution m'a assuré un chez moi confortable le temps de deux très belles années à Belleville. Je t'envoie toute ma

gratitude, cher ami !

Guillaume Gosselin et Éléa Depoilly sont deux personnes sensationnelles. J'ai beaucoup rigolé avec vous et chaque passage chez vous a été un profond plaisir, indispensable pour s'éloigner de Palaiseau de temps en temps. Merci infiniment de m'avoir fait me sentir si bien !

Pierre-Jean Bonzom et Joséphine Rouaud. Je vous tire mon chapeau, vous m'avez bien surpris avec cette caméra ! J'espère que vous êtes fiers de vous, bande de cochons. Nous partagerons toujours le souvenir de l'agneau Pascal, et de toutes les grandes soirées qui s'ensuivirent. Merci à vous deux pour avoir pris tant de sens dans des instants si cruciaux pour chacun d'entre nous. L'histoire ne s'arrête pas ici. Je ne peux pas m'empêcher de penser au 7 Janvier 2015. Ce jour tragique nous a fortement rapprochés et je n'oublierai jamais nos débriefings et nos remises en question, tant elles furent fondamentales.

Je suis extrêmement reconnaissant envers ma mère et mon frère Julien pour avoir fait le chemin jusqu'à Paris la veille de ma soutenance. Les remerciements que je pense à vous faire n'ont peut-être pas leur place ici dans leur version complète. Je me limiterais à écrire que cette thèse, c'est vous. Merci d'exister, et revenez-moi vite ! Lou-Ann, sœurette, ne cesse jamais d'être folle, c'est bon pour toi. Merci d'exister. Merci à mon père pour m'avoir aidé à trouver qui je voulais être. *Srećan je onaj koji sjedi u svojoj kući.* Merci à Philippe pour avoir été. Merci Thierry pour ta spontanéité et ta générosité inaltérées. Je suis extrêmement fier de la partie croate de ma famille, que je remercie ici: *Dragi svi, hvala vam svima za sve!* Merci à mon grand-père Frédéric Noyen pour avoir éveillé une curiosité chez moi aussitôt qu'il a pu. Puisses-tu considérer cette thèse comme la conséquence directe de ton action.

Charlotte Béreaud. Par où commencer ? Il m'est impossible de résumer en quelques phrases l'ensemble de ta contribution à la réussite de cette thèse. Merci tout d'abord de m'avoir laissé tant de temps pour faire des trucs sur mon ordinateur. Ça a dû être dur pour toi plus que pour quiconque, de me voir trainer si tard. Merci pour avoir écouté ce que j'avais à dire quand j'étais en surchauffe. Merci pour m'avoir tiré vers le haut à chaque instant, particulièrement dans les moments les plus compliqués. Merci pour ton intégrité, pour ton obstination, pour ta détermination : je n'ai pas besoin de connaître plus de femmes pour savoir que toutes auraient échoué la où tu as réussi. Merci de dire de bonnes choses à l'Univers sur mon sujet de temps en temps, ça aide. Merci de m'avoir présenté toutes ces belles personnes qui composent ta famille et tes amis. Merci de venir avec moi, encore et encore. Merci d'exister. Voila, c'est tout ! Ah, et une dernière chose : Cornichon !

Part I

Phenomenology

Chapter 1

Aspects of quantum chromodynamics

Contents

Men of few words require but few laws.

King Χαρίλαος, in *Lycurgus*, Plutarch

A lot of work has been carried out over the last century to explain and understand what are the building blocks of the universe and how they interact. One of the current undertakings is carried by CERN, the European Organisation for Nuclear Research, involving theoretical and experimental physicists, engineers and technical operators altogether.

Among the recent milestones reached in fundamental science, the discovery of the Higgs boson at the Large Hadron Collider (LHC) is of outstanding importance. It validates the Standard Model of particle physics as the common framework for elementary fermions and bosons, and for three of the four fundamental interactions. The

new particle indeed appears to be consistent with massive excitations of the field of the Brout-Englert-Higgs mechanism, describing the spontaneous breaking of electroweak symmetry $SU(2) \times U(1)$ [6]. This symmetry breaking occurs at an energy scale within the reach of the proton-proton collisions performed at the LHC, and the coming years will allow to verify that the new particle corresponds to the Higgs mechanism, in particular that all its couplings to known elementary fermions and bosons are as predicted.

But let us keep the electroweak theory on the side for now and take a step back. In the past century, our understanding of the interactions between "light and matter" – now called fermions and bosons – went from classical electrodynamics, where it was already known that any internal symmetry in a closed system translates into a conservation law, to the Standard Model of particle physics, benefiting of the advent of quantum field theories (QFT). It has been understood that, for a *fundamental* physical theory to live in the subnuclear world, it ought to be:

- *quantised*, i.e. it should be possible to recast the classical fields in quantum mechanical terms, with field operators acting on quantum states. Commutation relations between fields and/or operators should appear as a result;
- *locally gauge-invariant*, requiring the physical content of the theory to be unchanged by space-time transformations;
- as a consequence of gauge invariance, the theory should be *symmetric under transformations of the gauge group*, and a set of generators define the Lie algebra;
- *renormalisable*, i.e. the physical modes of the newly-formulated quantum theory do not give rise to uncancellable divergences when looking at various energy scales;
- In addition, the theory could be relatively *weakly coupled*; this is a loose requirement as we shall see, but a small coupling constant allows to compute developments in terms of a perturbation theory.

For electrodynamics and the theory of weak interactions, this has been achieved with the formulation of the electroweak theory. The degrees of freedom of this theory are the spin-1/2 particles called fermions (leptons and quarks), and spin-1 particles called the electroweak bosons $W^{\pm}$, γ, Z^0. The electroweak theory has the gauge group $SU(2)_{\mathrm{L}} \times U(1)_{\mathrm{hypercharge}}$. It is a renormalisable Yang-Mills theory, as demonstrated in 1972 by the 1999 Nobel-prize winners 't Hooft and Veltman [7].

Unfortunately, this theory does not explain by itself the stability of nuclei as we know them. Nowadays it is understood that the cohesion of the nucleus is due to some residual Van-der-Waals type of force [8], as an extension of the pion exchange first postulated by Yukawa [9]. But neither does it explain how the inner degrees of freedom are trapped together in a proton, and why free bare quarks are never directly observed.

The coming section is devoted to present several aspects folding together into quantum chromodynamics, QCD, the gauge theory of the strong interaction between quarks and gluons.

1.1 Building a theory of strong interactions

Since the first formulation of neutrons and protons as components of a nuclear isospin doublet in 1932 by Heisenberg [10], experiments at particle accelerators have rapidly discovered an increasing number of new particles, eventually forming a "particle zoo". For about three decades, the dynamics behind this new wealth of unstable particles remained a puzzle, as every new experiment was discovering a particle, and additional schematic rules were proposed. Here follows a short chronological review of what led to formulate $SU(3)_C$ as the group theoretical structure of strong interactions.

1.1.1 Nuclear isospin

The proton and neutron have almost equal mass ($\mathrm{m}_n = 939.56$ MeV/c^2, $\mathrm{m}_p = 938.27$ MeV/c^2). The proton carries one positive unit of electric charge, while the neutron is electrically neutral. At low scattering energies, the experimental data suggested that the nuclear interaction V_{ij} is charge independent:

$$V_{pp} \approx V_{pn} \approx V_{nn} \tag{1.1}$$

and the small difference in mass suggested that these two belong to a single entity, a nuclear isospin $I = \frac{1}{2}$ doublet. Nuclear isospin is a quantity algebraically equivalent to angular momentum, but conserved in strong interactions. In this sense, the new isospin symmetry would be spontaneously broken (because of the mass degeneracy between the two components of the $SU(2)$ doublet). This formulation proved practical to establish a list of isospin multiplets, corresponding to the first discovered hadrons. Indeed, from an isospin mutliplet $|I, I_3\rangle$ one can construct $2I{+}1$ states, including for example the pions and Δ resonances:

$$\eta = |0,0\rangle$$

$$p = |\tfrac{1}{2}, \tfrac{1}{2}\rangle \qquad n = |\tfrac{1}{2}, -\tfrac{1}{2}\rangle$$

$$\pi^+ = |1,1\rangle \qquad \pi^0 = |1,0\rangle \qquad \pi^- = |1,-1\rangle$$

$$\Delta^{++} = |\tfrac{3}{2}, \tfrac{3}{2}\rangle \qquad \Delta^{+} = |\tfrac{3}{2}, \tfrac{1}{2}\rangle \qquad \Delta^{0} = |\tfrac{3}{2}, -\tfrac{1}{2}\rangle \qquad \Delta^{-} = |\tfrac{3}{2}, -\tfrac{3}{2}\rangle$$

The study of the Δ resonances, located at masses around 1232 MeV/c^2, helped validating such a model for some time.

1.1.2 The Eightfold way, strangeness, and SU(3) flavour symmetry

In the fifties, the kaon family ($K^{\pm}, K^0$) and the Lambda baryon discovery in cosmic rays led to an addition to the isospin model. These particles were found to be long-lived, produced in pairs with strict rules: for instance a Λ can be produced with a K^+, but never with a K^-. So it was advocated that a new quantum number was

needed, *strangeness* S, that would be conserved in production occurring from the strong interaction. This way, the $K^+(S = +1)$ produced in addition with $\Lambda(S = -1)$ was indeed favoured.

A generalised theory of nuclear isospin was underway. As mentioned above, the isospin multiplets of π, nucleons and Δ would conform to a theoretical group classification with three generators $I_\pm, I_3$, making $SU(2)$ a proper group for the isospin symmetry. With the advent of strangeness, Gell-Mann and Ne'eman independently put forth a $SU(3)$ model with three flavours (u,d,s) [11, 12]. Gell-Mann suggested that the current meson ($q\bar{q}$) and baryon (qqq) spectroscopies could be understood in terms of irreducible representations of the new $SU(3)_F$ flavour group. For objects with integer electric charge, the first representations contained one, eight, ten members. For fractional electric charge objects, a triplet and a sextet were envisioned, but no particles with fractional charge were found. People at that time did not take the existence of fractional electric charges seriously, and the fractional charge triplet (later known as the u, d and s *quarks*) was regarded as a mathematical artifact, since the electric charge and the baryon number must be conserved.

Adding strangeness to the number of flavours led to the Gell-Mann–Nishijima empirical relation between electric charge Q, baryon number B, strangeness S and isospin I_3:

$$Q = I_3 + \frac{1}{2}(B + S) \tag{1.2}$$

where:

$$I_3 = \frac{1}{2}[(n_{\mathrm{u}} - n_{\bar{\mathrm{u}}}) - (n_{\mathrm{d}} - n_{\bar{\mathrm{d}}})], \tag{1.3}$$

$$S = -(n_{\mathrm{s}} - n_{\bar{\mathrm{s}}}), \tag{1.4}$$

and the baryon number[1] B of a hadron is here defined as the sum of the contained net quarks:

$$B = \frac{1}{3}[(n_{\mathrm{u}} - n_{\bar{\mathrm{u}}}) + (n_{\mathrm{d}} - n_{\bar{\mathrm{d}}}) + (n_{\mathrm{s}} - n_{\bar{\mathrm{s}}})]. \tag{1.5}$$

The electric charge Q would then equal to the following, exhibiting somewhat unforeseen fractional electric charges for each (not-yet-quark) flavour:

$$Q = \frac{2}{3}(n_{\mathrm{u}} - n_{\bar{\mathrm{u}}}) - \frac{1}{3}[(n_{\mathrm{d}} - n_{\bar{\mathrm{d}}}) + (n_{\mathrm{s}} - n_{\bar{\mathrm{s}}})] \tag{1.6}$$

Both mesons and baryons would turn out to fit in the octet description mentioned above, leading Gell-Mann to coin this model the *eightfold way* [11], in a reference to the Eightfold Path of Buddhism[2]. A pictorial representation of the meson octets is presented in Figure 1.1. In each representation, the meson family members share the same spin-parity: On the left, the ($J^P = 0^-$) pseudo-scalar meson family is outlayed, and the vector mesons ($J^P = 1^-$) are shown on the right.

[1] This definition is nowadays extended to include all six quark flavours.

[2] Noble Eightfold Path, Wikipedia: https://en.wikipedia.org/wiki/Noble_Eightfold_Path

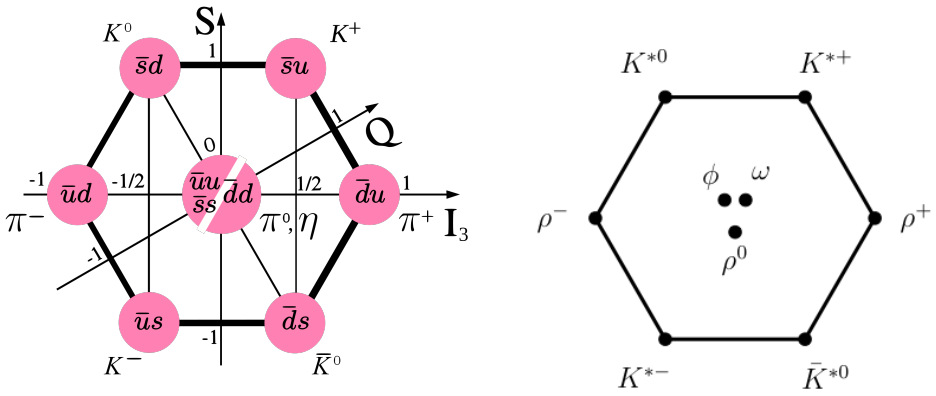

Figure 1.1: Left: the pseudo-scalar meson octet. Right: the vector meson octet.

As a consequence of the octet structure, Gell-Mann went on to predict in the same paper the existence of an electrically neutral meson completing the pseudo-scalar meson octet. The η meson was discovered in 1961 by Pevsner and others [13].

Gell-Mann also pointed out in a 1962 conference that nine known excited baryons of spin-parity $J^P = 3/2^+$ would fit nicely into a decuplet representation of $SU(3)$ if a tenth baryon carrying strangeness $S = -3$ were to be found [14]. The discovery of the Ω^- baryon in 1964 at Brookhaven [15] at precisely the mass given by the theory estimation [16, 17] sealed the success of the $SU(3)_F$ flavour symmetry. The complete baryon $J^P = 1/2^+$ octet and $J^P = 3/2^+$ decuplet are presented in Figure 1.2.

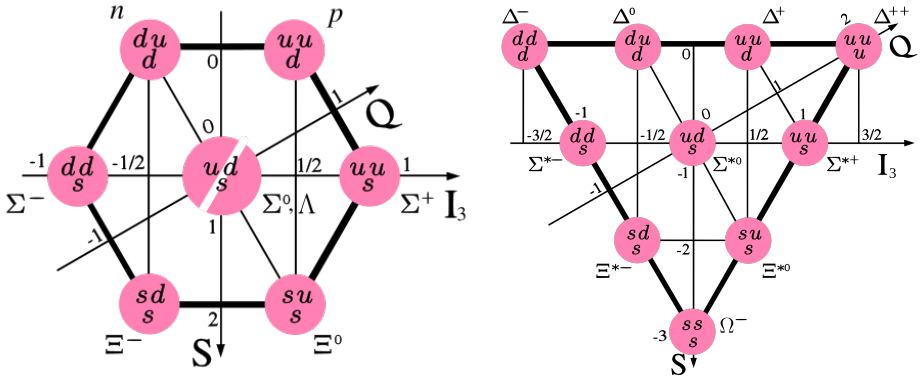

Figure 1.2: Left: the $J^P = 1/2^+$ baryon octet. Right: the $J^P = 3/2^+$ baryon decuplet, showing the $S = -3$ baryon Ω^- at the bottom of the decuplet.

1.1.3 The need for colour

By 1964, the static picture of hadrons had emerged. There was an understanding in the community that a theory of strong interactions of non-abelian nature is underlying, but

its dynamics was yet unknown. What is the force carrier behind the strong interaction? Where is the triplet of particles of the fundamental representation of $SU(3)$? These questions would be answered in the coming ten years with the formulation of the quark model, the parton picture and eventually that of QCD.

What I have described here is already a quark model[3], with three flavours. Because the masses are not all equal between the three quark flavours, we can only consider the flavour symmetry as approximate.

Furthermore, hadron spectroscopy seems to be driven by the wrong statistics. Indeed, according to spin-parity of the baryon decuplet, $J^P = \frac{3}{2}^+$, the baryon wave functions should be fully antisymmetric. Let us consider the states Ω^-, Δ^{++} and Δ^- at the corners of the decuplet diagram (cf. Figure 1.2 right):

$$
\begin{aligned}
|\Delta^{++}(S_z = 3/2)\rangle &\sim |u^\uparrow u^\uparrow u^\uparrow\rangle, \\
|\Delta^{-}(S_z = 3/2)\rangle &\sim |d^\uparrow d^\uparrow d^\uparrow\rangle, \\
|\Omega^{-}(S_z = 3/2)\rangle &\sim |s^\uparrow s^\uparrow s^\uparrow\rangle
\end{aligned}
$$

We see that each state has three identical spin-aligned quarks. Furthermore, the decuplet states are at the fundamental level ($L = 0$), and all relative angular momenta between quarks equal to zero. This leads to a fully symmetric wave function and therefore the three states obey the wrong statistics. In other words, Pauli's exclusion principle should preclude these particle from existing.

To anti-symmetrise the baryon states, one can introduce an additional quantum number, *colour*, such that in this picture, a sum of permutations of the colour states are contributing to the observed baryon. In the case of Δ^{++}, one has:

$$
|\Delta^{++}\rangle \sim \frac{1}{\sqrt{6}} \varepsilon^{\alpha\beta\gamma} |u^\uparrow_\alpha u^\uparrow_\beta u^\uparrow_\gamma\rangle, \tag{1.7}
$$

Where the sum is implicit (using Einstein's convention) over colours, and $\varepsilon^{\alpha\beta\gamma}$ is the fully anti-symmetric Levi-Civita tensor. One sees that at least three colours are needed to have an antisymmetric state. In this description one can construct 9 different colour combinations for the $q\bar{q}$ meson wave functions, out of which only 3 seem to exist. Also, the fact that only $q\bar{q}$ and qqq states are observed is a puzzle.

These two problems are solved by the ad-hoc colour *confinement hypothesis* that should have a dynamical nature: since quarks carry colour and hadrons are colour-singlet states, there must be a mechanism responsible for equilibrating the colour content in the final state. Nowadays the colours used for quarks are **red**, **green** and **blue**, while anti-**red**, anti-**green** and anti-**blue** are antiquark colours. The choice is of course arbitrary, but inspired by the analogy of colour-singlet states appearing white.

1.1.4 Evidence for quarks

The quark picture put forth in the early sixties did not get firm approval in the community immediately. Quarks were lacking an experimental evidence, and it was by no

[3] Sometimes, the (u,d,s) model is referred to as the 'naive' quark model.

means clear that experiments would ever be able to produce fractional electric charge particles. The evidence came from a series of deeply inelastic electron-nucleon scattering experiments performed by the SLAC-MIT collaboration (for which Friedman, Kendall and Taylor were awarded the Nobel Prize in Physics in 1990).

The impact of deep inelastic scattering experiments on the inception of chromodynamics is considerable, and the basics are presented here. Let us consider the typical reaction $e^- + p \rightarrow e^- + X$ where X is any number of hadronic remnants in the final state. The diagram in Figure 1.3 lays out the kinematics of the reaction.

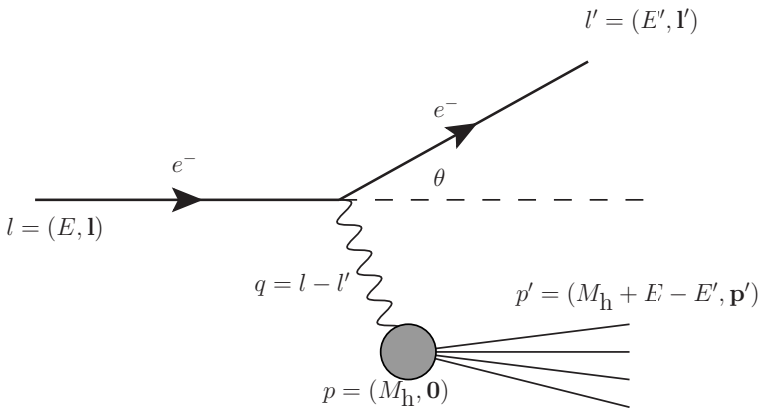

Figure 1.3: Deep inelastic $e^- p$ scattering. A photon is exchanged and a hadronic final state X is formed.

The initial high-energy electron scatters off a proton of mass M and four momentum p, via the exchange of a space-like virtual photon. In the final state, θ is the electron scattering angle, the electron has a four-momentum l' and the hadronic system has invariant mass W. The energy transfer between the electron and the hadronic system is ν:

$$\nu = E - E' = \frac{q \cdot p}{M} \tag{1.8}$$

and the virtuality of the photon, i.e. its squared momentum transfer Q^2 is defined as:

$$Q^2 = -(l - l')^2 = 2M\nu + M^2 - W^2 \leq 2M\nu. \tag{1.9}$$

In the elastic scattering, where X is made of the initial scattered proton, the rightmost terms of Equation 1.9 would turn into an equality. We can now introduce the so called Bjorken-x, x_B, that would represent how much the process deviates from the elastic scattering

$$x_B = \frac{Q^2}{2M\nu}, \qquad 0 \leq x_B \leq 1. \tag{1.10}$$

In this sense, when the momentum exchange is negligible, the final-state invariant mass W tends to M, and $x_B = 1$ (elastic scattering). In turn, small values of x_B

correspond to high momentum exchange, $Q^2 \gg M\nu$. To test if a target proton contains inner degrees of freedom, one can consider the cross-section for scattering of a lepton off a spin-1/2 fermion of mass M, charge e_q and specific to the case of non pointlike particles[4]. A double-differential cross section can be derived as a function of two *structure functions* W_1 and W_2 [18]:

$$\frac{d^2\sigma}{dQ^2 d\nu} = \frac{4\pi\alpha_{QED}^2}{Q^4}\frac{E'}{E}\left(W_2(Q^2,\nu)\cos^2\frac{\theta}{2} + 2W_1(Q^2,\nu)\sin^2\frac{\theta}{2}\right) \tag{1.11}$$

In Equation 1.11, the scattering process occurs via the exchange of a photon, hence the QED coupling constant α_{QED}. Equation 1.11 assumes the hypothesis that a nucleon is an extended particle, composed of several pointlike particles with electric charge e_i. One then defines *parton distribution functions* (PDF) $f_i(x_i)$, representing the probability that the struck *parton* carries a momentum fraction x_i of the nucleon. Thus, the structure constants built with the parton distribution functions are:

$$W_1(Q^2,\nu) = \sum_i e_i^2 f_i(x_B)\frac{1}{2M} \tag{1.12}$$

and

$$W_2(Q^2,\nu) = \sum_i e_i^2 f_i(x_B)\frac{x_B}{\nu}. \tag{1.13}$$

One can absorb M and ν into these definitions to parameterize the lepton-nucleon cross section in deep inelastic scattering (DIS) with two functions that depend only on how the momentum is shared between the nucleon constituents:

$$F_1 \equiv M_h W_1 = \frac{1}{2}\sum_i e_i^2 f_i(x), \qquad F_2 \equiv \nu W_2 = \sum_i e_i^2 x f_i(x). \tag{1.14}$$

The fact that DIS processes depend only on x, a dimensionless parameter, translates into the independence of the structure function F_2 with the Q^2 of the reaction. This is called *Bjorken scaling*, and is the main feature of the parton model [19]. This scaling behaviour was first measured by the MIT-SLAC collaboration in 1970. Figure 1.4 shows the F_2 structure function, as a function of x, for various DIS energies on a proton target. The scaling here manifests itself in the form of this universal curve holding for very different values of Q^2. This is a definite proof of the existence of pointlike consituents at these energy scales, as the presence of non-pointlike particles would make structure functions depend on Q/Q_0, with $1/Q_0$ the typical size of the non-pointlike object.

1.1.5 On the verge of a revolution

I have presented the inherent colour in the quark model, and how quarks have been discovered in early DIS experiments. There are many aspects of the puzzle of this pre-QCD era which have not been dealt with. For example, I did not mention that

[4] A textbook example of this calculation is available for example in Appendix F of [18].

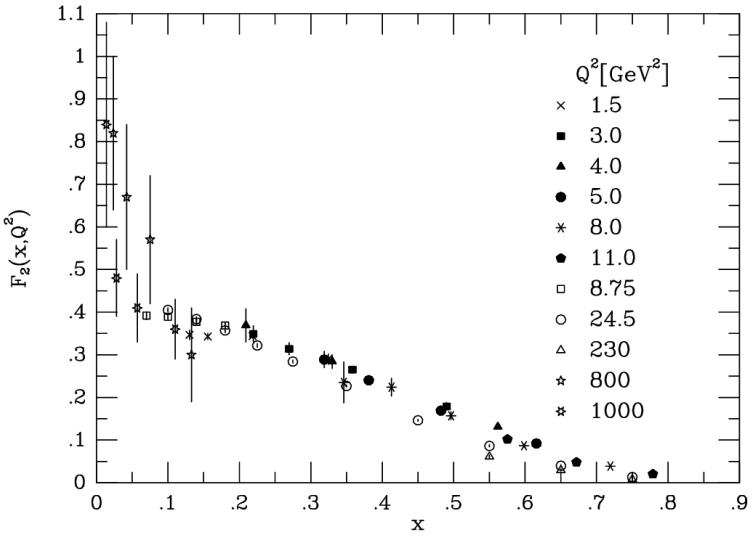

Figure 1.4: Structure function F_2 as a function of x. Emergence of scaling at various Q^2 energies in proton DIS. Compilation of PETRA data taken from [19].

structure functions can be expressed in terms of the quark – and anti-quark – densities inside the target hadron. For example for u and d quarks one has:

$$u = u_{\rm p}(x) \quad d = d_{\rm p}(x) \quad \bar{u} = \bar{u}_{\rm p}(x) \quad \bar{d} = \bar{d}_{\rm p}(x) \tag{1.15}$$

In this sense, doing a DIS experiment allows one to measure the PDFs of each quark flavour. In the case of electron-deuterium scattering for example, one can write the two $F_2(x)$ of electron-proton and electron-neutron processes:

$$F_2^{ep}(x) = x\left[\frac{4}{9}(u+\bar{u}) + \frac{1}{9}(d+\bar{d})\right] \tag{1.16}$$

$$F_2^{en}(x) = x\left[\frac{1}{9}(u+\bar{u}) + \frac{4}{9}(d+\bar{d})\right]. \tag{1.17}$$

These two can be averaged[5] to compute the F_2^{eN} of the deuteron:

$$F_2^{eN}(x) = \frac{5}{18}x\left(u+\bar{u}+d+\bar{d}\right). \tag{1.18}$$

Implicitly, each parton distribution contains a contribution from the three *valence* quarks of a nucleon, as well as *sea* quarks and anti-quarks coming from vacuum excitations. It follows that integrating over x should give the total fraction of momentum carried by quark degrees of freedom. One finds experimentally:

$$\int_0^1 dx\, F_2^{eN}(x) = \int_0^1 dx\, \frac{5}{18}x\left(u+\bar{u}+d+\bar{d}\right) \simeq 0.5 \tag{1.19}$$

[5]The average in any nucleus is $F_2^{eA}(x) = ZF_2^{ep}(x) + (A-Z)F_2^{en}(x)$.

This puzzling result indicates that charged partons in the deuterium nucleus (valence quarks + sea quarks and anti-quarks) carry nearly half of the total momentum. The rest has to be carried by other particles trapped in the nucleon, which do not carry electric charge since their momentum is not probed with electromagnetic processes such as DIS. These are in fact the *gluons*, which will be discovered later.

A second puzzle is related to the Bjorken scaling presented in the parton model, in Section 1.1.4. Assuming that one increases the energy indefinitely, a DIS experiment would eventually reach the scale of vacuum fluctuations. In other terms, more partons compose the nucleon at very high Q^2 values, and hence more partons share the momentum of the nucleon, leading to softer structure functions at high-Q^2. This is a *violation* of the Bjorken scaling at high energy. Anticipating that the decrease in structure functions is proportional to the coupling between partons [18], one has:

$$\frac{dF}{F} \sim \alpha \frac{dQ^2}{Q^2} \qquad \Longrightarrow \qquad \frac{d\ln F}{d\ln Q^2} \sim \alpha \tag{1.20}$$

If this interaction between partons were to be electromagnetic, the obtained α would be quite small (reminder: $\alpha_{QED} \approx 1/137$). Although Figure 1.4 largely exhibits the scaling of structure functions (all lining up on top of each other in a large x range and for various Q^2 values), let us look at some of the high-Q^2 points (provided the error bars are small enough), to see what the Equation 1.20 yields. Using the values at $x_B = 0.55$ of Figure 1.4, $F_2(x = 0.55, Q^2 = 230\ \text{GeV}^2) \approx 0.063$, and $F_2(x = 0.55, Q^2 = 24.5\ \text{GeV}^2) \approx 0.086$, we get the large value of[6]:

$$\left| \frac{\Delta \ln F}{\Delta \ln Q^2} \right| \sim 0.14 \tag{1.21}$$

We have witnessed the existence of a strong interaction between partons. The quark model gave us a group structure, $SU(3)$, and a quantum number, colour. Now that the symmetry of the group seems to be due to three colours (and not flavours), that leaves no clear limit on the number of quarks. The next section will indeed introduce extra flavours. We will start by presenting the main theoretical concepts of QCD, and some experimental confirmations that this is the quantum theory of strong nuclear interactions.

1.2 QCD: Theoretical grounds, experimental milestones

1.2.1 The QCD Lagrangian

Equation 1.22 introduces the Lagrangian of QCD:

$$\mathcal{L}_{\text{QCD}} = -\frac{1}{4} F^A_{\alpha\beta} F_A^{\alpha\beta} + \sum_{\text{flavours}} \bar{q}_a (i \not{D} - m)_{ab} q_b + \mathcal{L}_{\text{gauge-fixing}} \tag{1.22}$$

$$F^A_{\alpha\beta} = \partial_\alpha \mathcal{A}^A_\beta - \partial_\beta \mathcal{A}^A_\alpha - g f^{ABC} \mathcal{A}^B_\alpha \mathcal{A}^C_\beta \tag{1.23}$$

[6] I have used http://rhig.physics.yale.edu/~ullrich/software/xyscan/.

The QCD Lagrangian has some similarities with the one of QED, except that:

- The stress tensors' product $-\frac{1}{4}F^A_{\alpha\beta}F^{\alpha\beta}_A$ runs over 8 gluon fields, labeled by their colour indices (A),
- There is a non-abelian quadratic term in the stress tensor $F^A_{\alpha\beta}$,
- There are N_f quark fields q_a in the triplet colour representation,
- Coupling between fermions and bosons occurs at strength $\alpha_S \equiv g^2/4\pi$, through the following $\bar{q}_a \not{D}_{ab} q_b$ term.

$\not{D}$ is the Dirac notation for $\gamma^\alpha D_\alpha$, the contraction of Dirac γ^α matrices and the covariant derivative D_α, defined as:

$$(D_\alpha)_{ab} = \partial_\alpha \delta_{ab} + ig\left(t^C \mathcal{A}^C_\alpha\right)_{ab} \tag{1.24}$$

$$(D_\alpha)_{AB} = \partial_\alpha \delta_{AB} + ig\left(T^C \mathcal{A}^C_\alpha\right)_{AB} \tag{1.25}$$

f^{ABC} are numbers called the *structure constants* of $SU(3)$ (the terminology has nothing in common with structure functions seen in Section 1.1) and connects with t and T colour matrices in either the fundamental or the adjoint representation, respectively:

$$\left[t^A, t^B\right] = i f^{ABC}\, t^C, \qquad \left[T^A, T^B\right] = i f^{ABC}\, T^C \tag{1.26}$$

In group theory such commutation relations ensure completeness (as is needed in quantum mechanics), and the normalisation of t matrices follows:

$$\mathsf{Tr}\, t^A t^B = T_R\, \delta^{AB}, \quad T_R = \frac{1}{2}. \tag{1.27}$$

From colour matrices one also gets the *colour factors*, generalised to $SU(N)$:

$$\sum_A t^A_{ab} t^A_{bc} = C_F\, \delta_{ac}, \quad C_F = \frac{N^2-1}{2N} \tag{1.28}$$

$$\mathsf{Tr}\, T^C T^D = C_A\, \delta_{CD}, \quad C_A = N \tag{1.29}$$

which, in the case of $SU(3)$, are $C_F = 4/3$ and $C_A = 3$.

1.2.2 The running of the coupling constant α_S

One of the ways often used to bring up the notion of the running of α_S (for instance in [20]) is to consider a dimensionless physical observable R which depends on an energy scale Q that is much larger than the masses m in consideration. We shall see such a quantity at the end of this section.

Dimensional analysis suggests that R should be independent of Q, when much larger than m. This does not hold in quantum field theory, because the perturbative

development in α_S requires *renormalization*. This procedure introduces a new scale μ, where the subtraction removing divergences is performed.

Dimensional analysis suggests again that R depends on Q^2/μ^2 and on α_S, which itself depends on μ. Since μ is arbitrary, R cannot depend on μ, and it follows that:

$$\mu^2 \frac{d}{d\mu^2} R\left(\frac{Q^2}{\mu^2}, \alpha_S\right) \equiv \left(\mu^2 \frac{\partial}{\partial \mu^2} + \mu^2 \frac{\partial \alpha_s}{\partial \mu^2} \frac{\partial}{\partial \alpha_S}\right) R = 0. \tag{1.30}$$

This partial differential equation can be simplified introducing the following:

$$\tau = \ln\left(\frac{Q^2}{\mu^2}\right), \qquad \beta(\alpha_S) = \mu^2 \frac{\partial \alpha_S}{\partial \mu^2} \tag{1.31}$$

We now have a *renormalisation group equation* for R:

$$\left(-\frac{\partial}{\partial \tau} + \beta(\alpha_S) \frac{\partial}{\partial \alpha_S}\right) R \; = \; 0. \tag{1.32}$$

This can be solved by defining a coupling varying with the scale, the *running coupling*:

$$\tau = \int_{\alpha_S(\mu)}^{\alpha_S(Q)} \frac{dx}{\beta(x)}, \tag{1.33}$$

and the way α_S varies is determined by the β function. Anticipating that a determination of α_S with the β function is based on an infinite series of ever more complicated diagrams revolving around gluon self interactions and quark loops, let us just jump to the result and say that β at first order in α_S (*leading order*, or LO) is given by:

$$\beta(\alpha_S) \;=\; -b\alpha_S^2(1 + \mathcal{O}(\alpha_S)) \tag{1.34}$$

$$b \;=\; \frac{11C_A - 2N_f}{12\pi} > 0 \tag{1.35}$$

where $C_A = 3$ and N_f the number of active flavours. The β function values decrease as α_S increases, and the first order $-b$ parameter is *negative*[7], contrary to the two electroweak constants. For QED, $\beta(\alpha_{QED}) = \alpha_{QED}^2/3\pi$. It is positive, such that the coupling increases when one resolves the charged particle with higher and higher energies. Inversely, for quantum chromodynamics, the coupling decreases as energy increases: this is known as *asymptotic freedom*.

Modern measurements of $\alpha_S(Q)$ will be shown in Section 1.2.5.3 and we will see how well they match with the theoretical prediction of running α_S. I have decided to limit myself to the running of the coupling and the basic structure of the Lagrangian, for the following reasons:

- These two points are fundamental for the building of QCD, and make it a unique theory,
- the non-abelian term in the Lagrangian is crucial for the appearance of this asymptotic freedom property,

[7] That is, as long as the number of active quark flavours is $N_f < 16$.

- the dynamical evolution of the coupling sets the basis to turn to *deconfinement*.

The rest of this section will be devoted to present experimental successes, or milestones, of QCD.

Let us look first at a concrete quantity, that is the ratio R of cross sections for hadron production and dimuon production in e^+e^- annihilation:

$$R \stackrel{\text{def}}{=} \frac{\sigma(e^+e^- \to \text{hadrons})}{\sigma(e^+e^- \to \mu^+\mu^-)}. \tag{1.36}$$

This quantity, as plotted in Figure 1.5, varies mildly and continuously as a function of $\sqrt{s}$ above 5 GeV, in a way that is well reproduced by the running coupling constant (see [21], Section 9.2.1). It also reveals striking features: resonances, and steps that are thresholds for the production of new quarks, that I shall discuss in the next section.

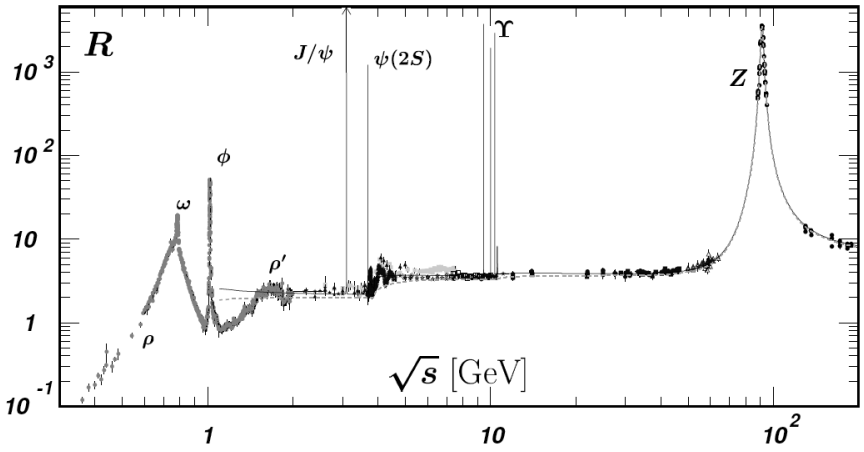

Figure 1.5: R ratio of electron positron cross section to hadrons and leptons, as a function of centre-of-mass energy.

1.2.3 The November Revolution

In Section 1.1.5, I have argued that even though the group theory grounds were there for QCD to be built already in the sixties, there was a lot of skepticism regarding the existence of quarks, as well as the number of quark flavours. At the same time, a large portion of the theoretical physics community was working on the weak interaction unification with QED and the renormalisability of quantum gauge field theories. On the experimental side, strange mesons and baryons were discovered, and their spectroscopy was well studied. The s quark mass being presumably heavier than the other two known quarks, it was clear that hadrons carrying one or more units of strangeness would be rather unstable. Indeed, the Ξ baryons and Ω^- were discovered through decay processes. But some transitions, namely the ones with $\Delta S = 2$ remained elusive. Using the framework of current algebra, Glashow and Bjorken put out the idea of a

fourth quark, the charmed quark, already in 1964. The idea was to enforce an analogy between the weak leptonic current and weak hadronic current: if two weak lepton doublets exist, (e,ν_e) and (μ,ν_μ), there had two be two weak doublets for quarks as well [22].

One of the doubts on the existence of quarks, before DIS experiments came to light, was the fact that the $SU(3)_F$ flavour symmetry of the quark model was a *global symmetry* [23]. In this sense, the free fermion fields for $SU(3)_F$ quarks $q_i(x)$ are such that:

$$\chi(x) = \begin{pmatrix} q_u(x) \\ q_d(x) \\ q_s(x) \end{pmatrix} \qquad \bar{\chi}(x) = \begin{pmatrix} \bar{q}_u(x) & \bar{q}_d(x) & \bar{q}_s(x) \end{pmatrix} \tag{1.37}$$

and the Lagrangian for the three free fields is

$$\mathcal{L} = \sum_{i=u,d,s} \bar{q}_i(x)\,(i\gamma^\mu\partial_\mu - m)\,q_i(x), \tag{1.38}$$

$$= \bar{\chi}(x)\,(i\gamma^\mu\partial_\mu - m)\,\chi(x). \tag{1.39}$$

Let us express the effect of V, a $U(3)$ transformation:

$$\begin{aligned} \chi(x) &\rightarrow V\chi(x), \\ \bar{\chi}(x) &\rightarrow \bar{\chi}(x)V^\dagger, \\ \mathcal{L} &\rightarrow \bar{\chi}V^\dagger\,(i\gamma^\mu\partial_\mu - m)\,V\chi(x) = \mathcal{L}. \end{aligned}$$

Given that $U(3) = SU(3)\times U(1)$, such transformations are unitary 3×3 matrices, with unit determinant. This is the $SU(3)$ generalised isotopic spin symmetry of Gell-Mann's Eightfold Way [11], only if the quark masses were equal! Entering quark masses would strongly hurt the symmetry to the point where it is explicitly broken, and as Gell-Mann puts it in [11],

> In the limit of unitary symmetry and with the mass of these vector mesons "turned off", we have a completely gauge-invariant and minimal theory, just like electromagnetism. When the mass is turned on, the gauge invariance is reduced (the gauge function may no longer be space-time-dependent) but the conservation of unitary spin remains exact. [...] there are also the many symmetry rules associated with the unitary spin. All of these are broken, though, by whatever destroys the unitary symmetry, and it is a delicate matter to find ways in which these effects of a broken symmetry can be explored experimentally.

From there, we can easily imagine what harm it would do to include a fourth, heavier quark in any such model. In a quite different attempt to understand flavour-changing currents, Glashow, Iliopoulos and Maiani [24], suggested in 1970 a mechanism which explains how the flavour changing process $K^0 \rightarrow \mu\mu$ is naturally rare. A simple picture of the GIM mechanism is presented in the Figure 1.6. They postulate the existence of a fourth quark, c, that would have the charge $+2/3$ as the u quark.

For the next four years the charm quark existence was largely overlooked. During the summer of 1974, Ting and his research team started accumulating proton-proton

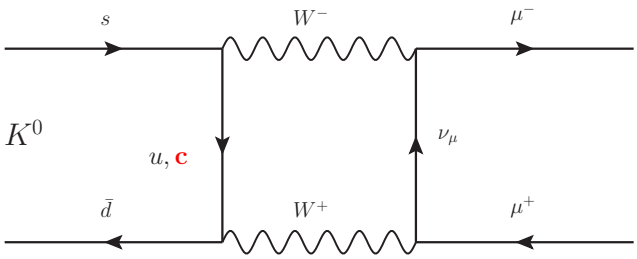

Figure 1.6: The GIM mechanism in $K^0 \to \mu\mu$ decay. Note the appearance of a charm quark contribution inside the box diagram.

data from the AGS at Brookhaven, hinting at the production of a new, very narrow resonance of mass ~ 3.1 GeV/c^2. Because of the very narrow aspect the resonance had, it did not go into immediate publication. On November 10, 1974, the team led by Richter who was operating the SPEAR electron-positron collider at SLAC discovered that at beam energies around $E_b \sim 1.55$ GeV, the counters went berserk. On November 11, 1974, both collaborations at Stanford and Brookhaven announced their discoveries of the J/ψ particle, which was quickly interpreted as a resonant $c\bar{c}$ state, that is, a bound state of a charm quark and an anti-charm quark.

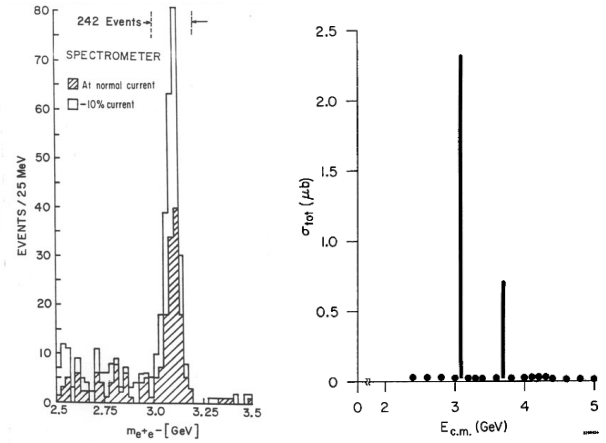

Figure 1.7: First charmonium data. Left: statistics accumulated at BNL [25]. Right: e^+e^- events from SPEAR, showing a second resonance, the ψ' [26].

Two weeks later, in an energy scan for new particles in the charmonium spectrum, excitement struck again as the team at SPEAR discovers a second narrow resonance, as can be seen in Figure 1.7. One can see on the plot to the right, events stacking at 3.1 GeV/c^2 and at 3.7 GeV/c^2, indicating the presence of the ψ'. Only two years later, both Richter (SLAC) and Ting (MIT) received the Nobel Prize in Physics "for their pioneering work in the discovery of a heavy elementary particle of a new kind".

Shortly thereafter, the τ lepton was discovered at the SPEAR facility [21]. This new

lepton, discovered indirectly through its weak decay in $e^+e^- \to \tau^+\tau^- \to \mu^\pm e^\mp + 2\nu$ came first as an anomaly, before DESY confirmed the signal. After establishing the quantum numbers of the newly-discovered particle, it became clear that a new family of leptons was released. With this discovery, the community soon concluded that two additional quarks, b and t for bottom and top (or beauty and truth) were to be expected. And indeed, in 1977, after seeing a hint of a bump at $m \sim 9.6$ GeV/c^2 prior to a significant upgrade, the E288 collaboration (Lederman et al.) published their observation of a new resonant structure in the di-lepton decay channel [27], which turned out to be the Υ family, of particular interest for this thesis.

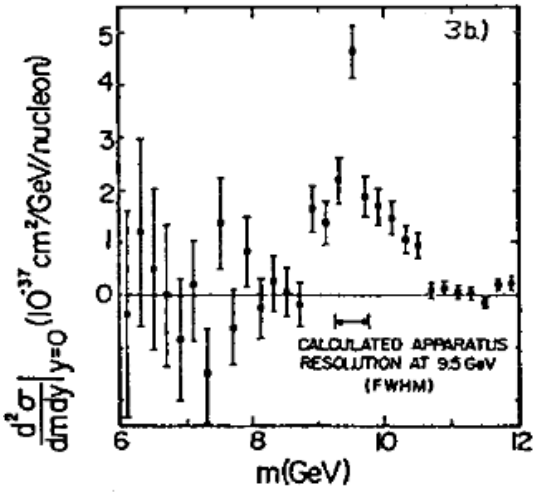

Figure 1.8: First bottomonium data, 1977. Dimuon events from proton-nucleus collisions at $E_p = 400$ GeV with the E288 experiment at Fermilab [27].

1.2.4 The discovery of the gluon

It is now clear that quarks exist confined in the nucleons, and are probed only when increasing the scattering energy enough so that the Compton wavelength of the exchanged photon (in the case of DIS) is much smaller than the size of the nucleon wavefunction. And doing so, we have seen in Equation 1.19 that the momentum fraction carried by the quarks was only approximately half of the total available nucleon momentum. So it seems clear that the colour field holding quarks in place is naturally giving rise to other objects contributing to the nucleon integrity.

A recent account by Ellis [28] makes a very interesting report of the events that led to think of strong interactions in term a non-abelian $SU(3)$ theory. The first experimental signature involving gluons in the final state was to be formulated in a 1976 paper by Gaillard, Ellis and Ross, where they compute the gluon bremsstrahlung[8] process in QCD [29] at e^+e^- facilities, stating that it should give rise to $q\bar{q}g$ final states. This

[8] From the German word for "deceleration radiation".

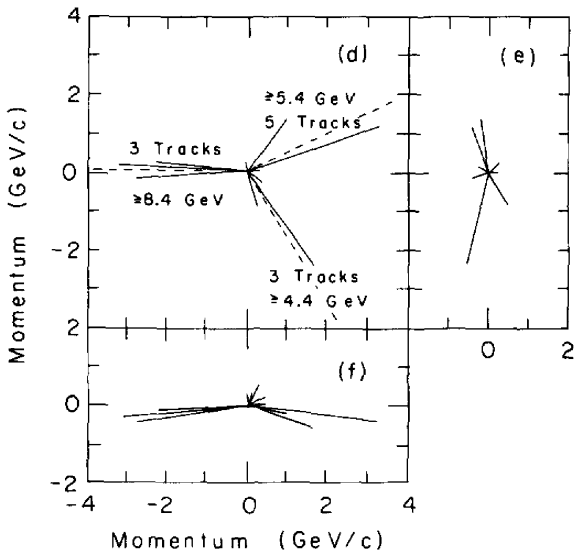

Figure 1.9: A three-jet $q\bar{q}g$ event, from the TASSO collaboration [30].

final state is observed experimentally in the form of three distinct clusters of particles, further called *jets*.

Circumstantial evidence that gluons did exist was already available. For example, charmonium and bottomonium decays to three gluons, were computed to be the dominant decay mode for these new objects. The discovery of the gluon radiation in 3-jet events, and hence of its survival to the long-distance process of hadronisation was announced jointly by all four PETRA experiments at a Fermilab Lepton-Photon Symposium in August 1979 [31]. Figure 1.9 shows one of the first such $q\bar{q}g$ events recorded by the TASSO collaboration, where the three jets are easily seen in the transverse plane (main panel).

This evidence for gluon bremsstrahlung is actually the basis for the crucial QCD test described hereafter.

1.2.5 Testing QCD at e^+e^-, DIS and hadron colliders

I will go briefly through several selected results from QCD analyses of collider data from the eighties and nineties, which confirmed with great accuracy many features of *perturbative* QCD dynamics, as imposed by Equation 1.22.

1.2.5.1 The non-Abelian nature of QCD

The QCD Lagrangian discussed in Section 1.2.1, contains Feynman diagrams with three-gluon and four-gluons vertices. This is a specificity of the non-Abelian nature of $SU(3)$, which has many consequences for the amplitude of various processes. One example: 4-jet events in e^+e^- collisions are produced with tree-level QCD diagrams of

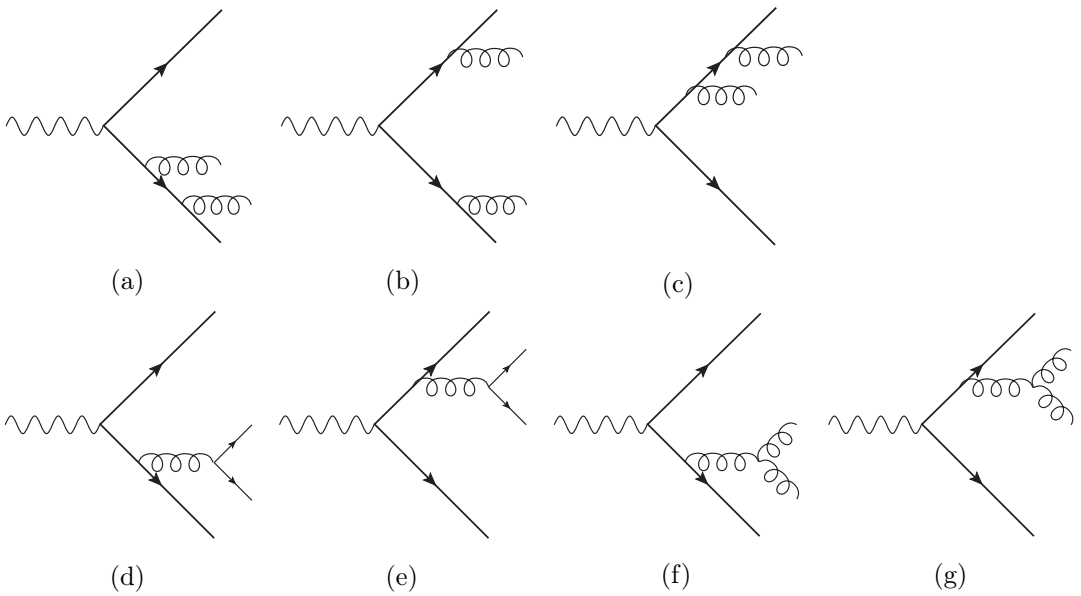

Figure 1.10: Tree-level Feynman diagrams for four jet events in electron positron collisions.

Figure 1.10. Such events will produce four clustered energy deposits (known as *jets*) in the final state, from which one can for example make an event shape analysis.

Take the four jet momenta (p_1, p_2, p_3, p_4) such that they are energy ordered, $E_1 > E_2 > E_3 > E_4$. Most likely the first two most energetic jets will come from the quark lines, and one can define a plane $\mathcal{P}_{1,2}$. The question is to know the angle between the plane $\mathcal{P}_{1,2}$ and the plane delimited by the two sub-leading jets p_3 and p_4, $\mathcal{P}_{3,4}$. First let me point out that double-bremsstrahlung diagrams (a), (b) and (c) do not contribute very much to the correlation angle between $\mathcal{P}_{1,2}$ and $\mathcal{P}_{3,4}$.

Next, if gluon radiation was like photon radiation in electromagnetism, i.e. Abelian, then there would be no $g \to gg$ terms. There would then only be the four-quark diagrams (d), (e). These would contribute as a strong anticorrelation: Indeed, one can conclude from the gluon polarisation that radiated gluons tend to be polarised in the plane of the primary jets, and will split in two quarks of perpendicular direction with respect to the g polarisation. So diagrams (d), (e) would give a wide angle between $\mathcal{P}_{1,2}$ and $\mathcal{P}_{3,4}$.

Finally, because of the non-Abelian nature of QCD, one has to consider diagrams (f) and (g). It turns out that $g \to gg$ is dominant in QCD, by virtue of the colour factor $N_c = 3$, as well as the soft gluon enhancement. Still using the polarisation properties of gluon emission, the first gluon is radiated along the plane $\mathcal{P}_{1,2}$, splitting in two gluons this time mostly parallel to the polarisation. This correlation is weak but the process is very abundant, resulting in a clear flattening of the angular distribution in Figure 1.11.

The angle χ_{BZ} used herein is called the Bengtsson-Zerwas angle [33], defined by the plane between the two leading jets and the two subleading jets. The data from

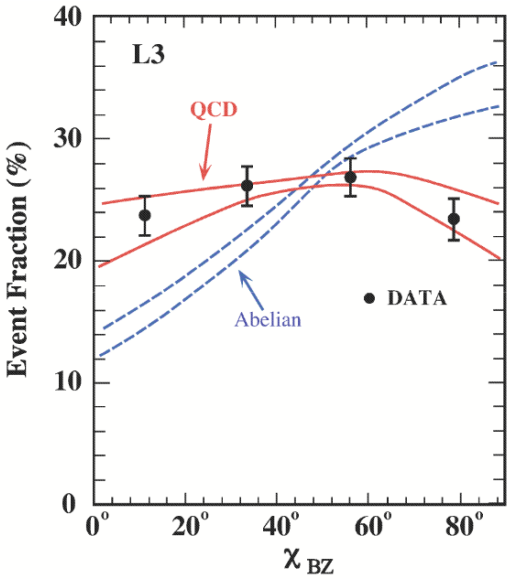

Figure 1.11: The Bengtsson-Zerwas angle χ_{BZ} in four-jet events recorded by the L3 collaboration [32].

L3 collaboration is compared to a full-fledged QCD simulation as well as to a straw-person model where only Abelian terms are allowed. The Abelian theory curve is indeed peaking at $\chi_{BZ} \sim \pi/2$, and does not match with the experimental data, indicating that the data does conform to a non-Abelian theory.

Such four-jet analyses can be combined with other event shape analysis and 3-jet events to yield a precise evaluation of QCD colour factors. Figure 1.12 presents a famous combination of results from LEP experiments (OPAL, ALEPH, DELPHI) that shed light on the true value of QCD colour factors, further confirming the $SU(3)$ group as its underlying theoretical structure.

1.2.5.2 Precision measurements of QCD effects

Since the first attempt at measuring precisely α_S at the time of PETRA and PEP colliders, many different processes from e^+e^- annihilation as well as lepton-hadron scattering gave estimates of α_S with increasing precision. The total hadronic cross section ratio R, the three-jet rate, event shape observables, all yield experimental results on α_S. It may be worth noting that the JADE collaboration did find out a clear experimental confirmation of the running of α_S in the rate of three-jet events, already before the coupling constant value was precise; back then, the data was compared to analytic QCD computations at next-to-leading order in perturbation theory, including various hadronisation models which performed relatively well, giving α_S a mere 10% precision [35].

The QCD programme at LEP, among other key results proving the non-Abelian

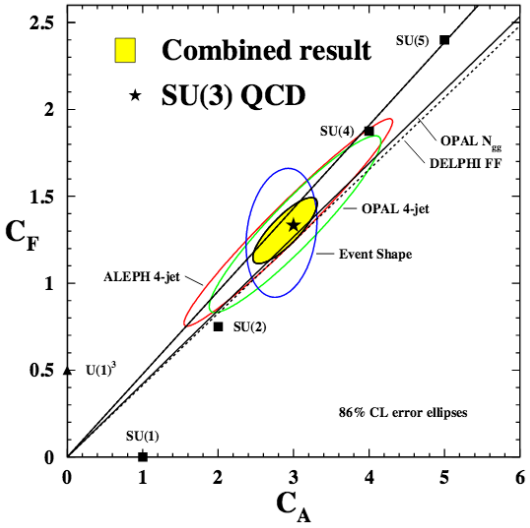

Figure 1.12: The LEP-combined plot of C_A and C_F. The yellow ellipsoid area is the combined uncertainty of the various jet and event shape measurements. Taken from [34].

nature of QCD (cf. previous subsection) reduced considerably these uncertainties, with $\mathcal{O}(\alpha_S^3)$ precision observables: at the end of the LEP2 operation phase, the world average was $\alpha_S(M_Z) = 0.1184 \pm 0.0031$ (NNLO) [36].

Along came HERA (*Hadron Elektron Ring Anlage*), at DESY in Hamburg, with its two operation eras fully dedicated to lepton-hadron scattering. Operating at $E_e = 27.5$ GeV, and $E_p = (820, 920)$ GeV, the HERA experiments (H1, ZEUS, HERMES) have accumulated, up to 2007, DIS data in an impressive phase space interval:

$$\begin{aligned} 0.045\,\text{GeV}^2 < \quad & Q^2 \quad < 5.10^5\,\text{GeV}^2, \\ 6.10^{-7} < \quad & x_B \quad < 0.65 \end{aligned}$$

Capabilities of HERA experiments are very large: thanks to the precise data accumulated in charged-current and neutral-current modes, the QCD contributions to all processes, and the various parton PDFs can be computed simultaneously. For example, inclusive jet cross section is measured to the level of precision that one can see from ZEUS data in Figure 1.13 and compared to NLO QCD perturbation theory predictions. From that one can extract for example α_S, or measure the charm or bottom quark mass with precision [37]. Figure 1.13 (right) shows a comparison of α_S from inclusive jets to NLO QCD calculations, where the main sources of theory uncertainty come from the various assumptions on either the perturbative part (DGLAP evolution equations [38]) or the PDF.

This is only one small account of the various successes of QCD. In 2015, HERA experiments released a seminal paper updating their long-collected parton PDF data [40]. One of the most striking figures is reproduced as Figure 1.14, where the quark and

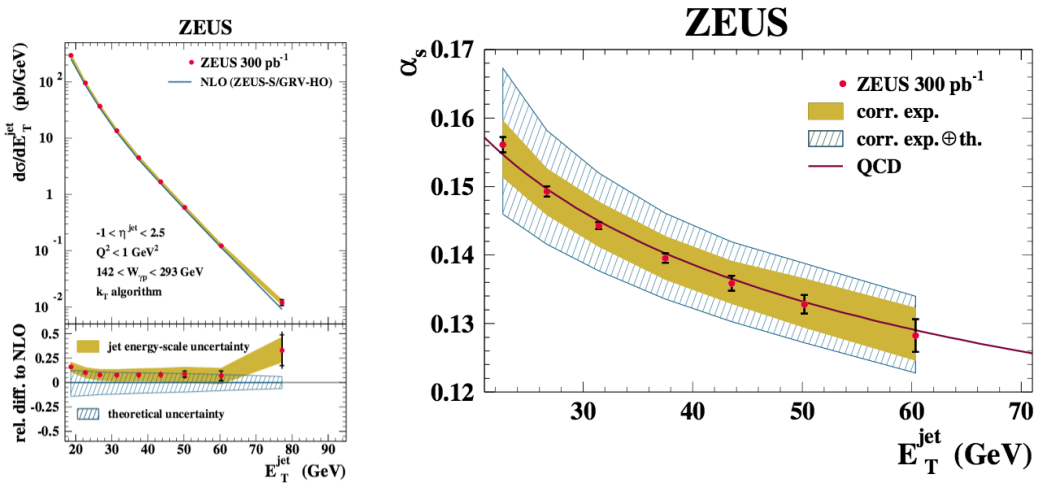

Figure 1.13: Inclusive jet productions from the ZEUS collaboration. Left: the p_T differential cross section. Right: α_S. In both plots comparisons to dedicated NLO QCD calculations are shown. Taken from [39].

gluon PDFs are reproduced at NNLO at a very close level of precision with fits to data. This genuine piece of information will provide important tuning to the study of hadron-hadron processes at LHC experiments. Indeed, almost all processes (especially the most challenging ones, e.g. searches for Higgs couplings to quarks) rely heavily on parametrising the momentum fraction carried by gluons and quarks in the proton. For heavy quarkonia this also plays a role, as gluon fusion is the dominant process at LHC energies.

1.2.5.3 Modern running coupling constant measurements

Finally, the best illustration of QCD success is the comparison of its predicted running of α_S with experimental measurements related to this quantity, at various orders of perturbation theory. This is presented in Figure 1.15, from [21]. Nowadays, the running of α_S is well understood, and is of prime importance for a large majority of Standard Model physics analyses. Indeed, almost every rare physics process studied at the LHC is usually extracted from the sum of several templates of signals whose cross section is known to several orders of the strong coupling constant. The precise knowledge of QCD is crucial also in the modelling of *hadronisation*, which is the process by which final state particles radiate softer particles and form detectable jets.

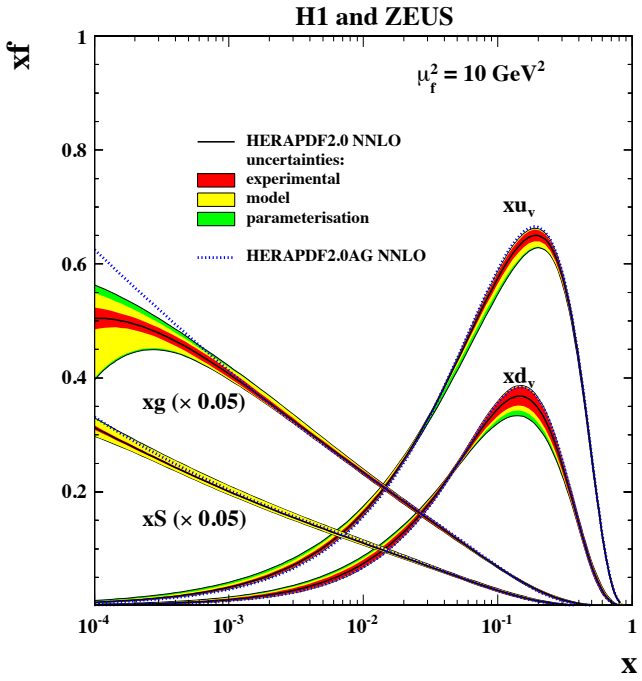

Figure 1.14: Parton distribution functions xu_v, xd_v, $xS = 2x(\bar{U} + \bar{D})$ and xg of HERAPDF2.0 NNLO at $\mu_f = 10$ GeV^2 [40]. Gluon and sea distributions are scaled down by a factor of 20.

In this section I have presented how the quantum theory for quarks and gluons came to be constructed, and to show some of its basic properties.
One of the key open questions of QCD is colour confinement. What actually drives the colour charges to equilibrate together and cancel themselves in the final state? What are the thermodynamical properties of a many-body system of colour degrees of freedom ? ? What experimental possibilities are available today to assess these questions? That is what the next section is about.

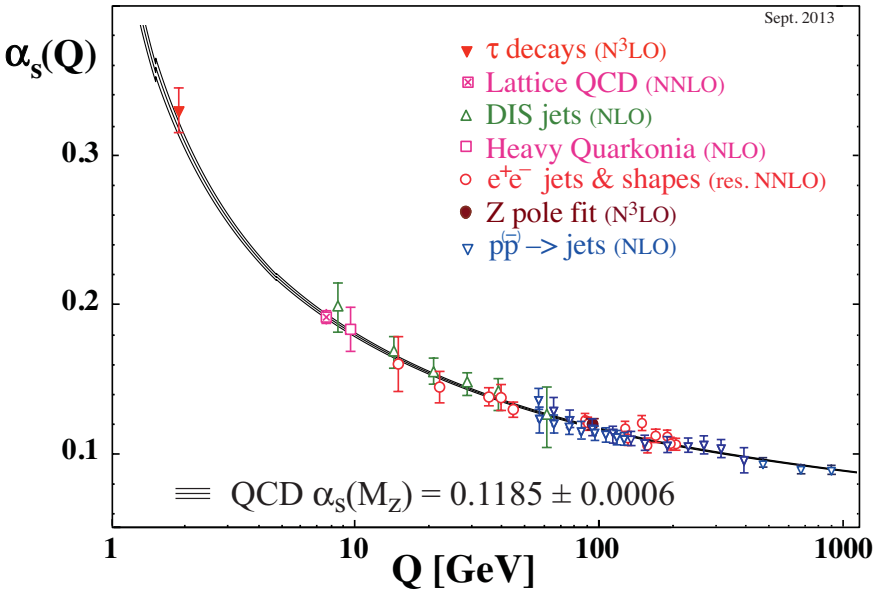

Figure 1.15: The running of the coupling constant of QCD [21].

1.3 From confinement to deconfinement

1.3.1 Phase transition at finite temperature

Contemporary to the quark model is the discovery of microwave background. The idea had peered through that the universe *cooled down* to the T$\sim 3K$ measured in 1965, providing evidence for a hot primordial universe. At the same time, people studying nuclear interaction in high-energy collisions were trying to predict the particle yields in a self-consistent way. Hagedorn's hypothesis [41] is worth mentioning at this point, since it connects directly with the deconfinement sought in current day high-energy nuclear interactions. His statistical bootstrap model suggests that the density of hadronic states as a function of their mass, $\rho(m)$, must be asymptotically equivalent to the particle yields, $\sigma(E)$:

$$log(\rho(m)) = log(\sigma(E)) \tag{1.40}$$

Indeed, Hagedorn went on to conjecture a set of equations for $\rho(m)$ and $\sigma(E)$ that would satisfy this criterion. In the asymptotic limit, it translates into a density of available states which increases exponentially with the mass:

$$\rho(m) \approx e^{\frac{m}{T_H}} \tag{1.41}$$

and T_H is called the Hagedorn temperature, of a value around 170 MeV. At this temperature, the partition function becomes singular. It was deduced that in a hot Big Bang model, the universe did produce a wealth of unstable particles which eventually cooled down, but with Hagedorn's temperature one could foresee that about 10 microseconds after the Big Bang, the temperature of the universe was around 170 MeV.

In 1975, Cabibbo and Parisi [42] suggested that the exponential decrease in spectrum ($\sigma(E)$) is in fact connected to the existence of a deconfined phase for quarks, transition that was thought to occur at $T_H \sim 170$ MeV.

So the immediate question comes along: Can we recreate this in laboratory conditions, using ultrarelativistic nuclear beams? It should be possible to ramp up the energy of the beams and collide enough hadronic matter in a small volume as to increase the density and eventually probe the existence (or absence) of this deconfinement transition.

Figure 1.16 shows how the temperature and the baryon chemical potential μ_B are related in the current picture of the phase diagram.

The study of the QCD phase transition with calculations on the lattice helped drawing the thermal properties of a strongly interacting set of objects (fermions and/or bosons) enduring increasing temperature and pressure. For pure gluonic matter for example, the equation of state from [43] shows a rapid approach toward an ideal gas behaviour. Increasing computational power helped increasing the complexity of lattice simulations. Eventually, the energy-density/temperature profile of models including two or three degenerate flavours of quarks was computed and compared to what experiments were able to perform. Figure 1.17 from [44] shows such a comparison, where we see that the transition temperature is at $T_c = (173 \pm 15)$ MeV for two quark flavours,

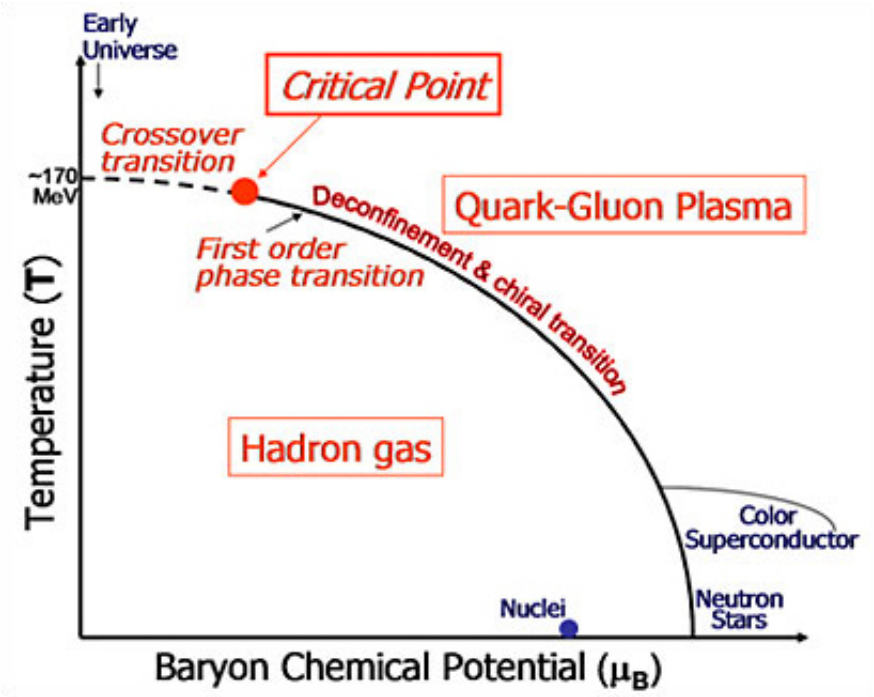

Figure 1.16: A schematic approach to the QCD phase transition.

and is accessible at the Super Proton Synchroton (SPS) at CERN as well as at the Relativistic Heavy Ion Collider (RHIC) at Brookhaven National Laboratory (BNL).

There are currently two laboratories able to put the conditions together to study the phase transition. At BNL, RHIC collides protons, deuterons, gold nuclei, and more. For gold-gold collisions, the energy in the centre of mass reaches $\sqrt{s_{NN}} = 200$ GeV. At CERN, fixed target experiments near the SPS reached a $\sqrt{s_{NN}} \approx 17$ GeV, while the LHC can provide lead beams to CMS, ALICE, ATLAS, and LHCb detectors, reaching a $\sqrt{s_{NN}} = 5.1$ TeV in PbPb collisions[9].

If the thermal behaviour of nuclear matter under extreme pressure and density can be studied, one can wonder what is the time evolution of the hot medium produced. Indeed, the deconfined phase sets in progressively[10]. In Figure 1.18 the timescales of the various processes thought to occur in ultrarelativistic heavy ion collisions are layed out.

I have asserted that colliders such as LHC and RHIC should be able to produce a deconfined phase of QCD, known as the Quark-Gluon Plasma (QGP). Now we should try to find out what are the properties of the 'little bang' produced in laboratory, and how can we build strategies to probe this little bang efficiently? Finally, how can experimental observation be related to the predicted transition?

[9] As I write this, these collisions have not yet started but correspond to the 13 TeV pp collisions that are currently ongoing.

[10] This is a *crossover* instead of a phase transition.

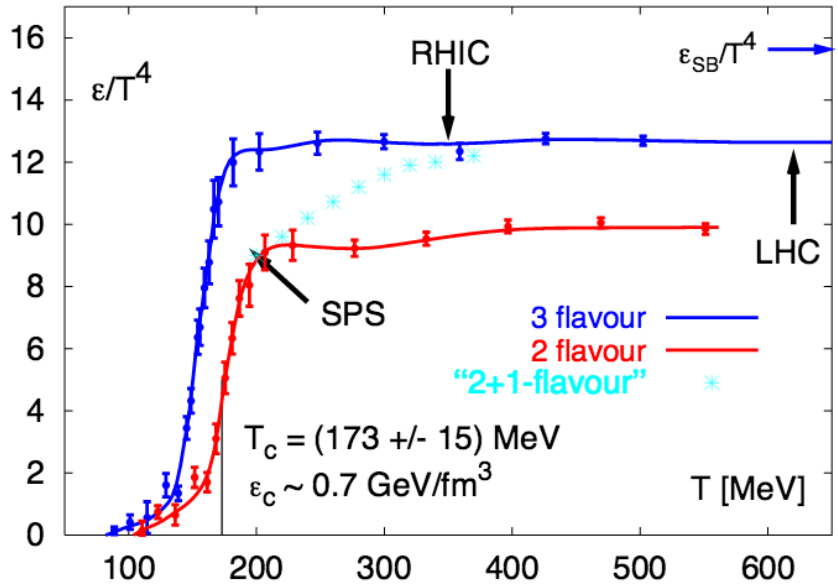

Figure 1.17: Lattice calculations of the energy density as a function of lattice temperature, from [44].

1.3.2 Measuring the properties of the quark-gluon plasma

In DIS experiments, physicists have been able to identify and probe the distribution of point-like objects and the force binding them together inside the nucleons. In a way, experimental heavy ion collisions can follow the same strategy. If we were able to use as a probe, one object not interacting strongly with nuclear matter, then it should be possible to use the alteration of the probe passing through to extract physics on the created medium. I am intentionally using loose terms. For now, let us set some rules:

1 I do not know beforehand what to expect from colliding nuclei, from textbook, that are mostly dealing with zero temperature particle physics;

2 I anticipate that some probes may be very altered, some less. We would be interested in the spectrum of each type of probe, passing through whatever was created, as much as in their normalisation: their total yield can carry information about the phase they traversed;

3 I can however anticipate that if my experimental settings reach the deconfinement transition, effects on some probes would be very clear: I need a baseline for whatever would happen before the transition. This is crucial if my transition is continuous, from vacuum QCD to above the critical density.

4 Finally, I need to get an experimental handle on an effective 'temperature', a measure of the violence of the collision.

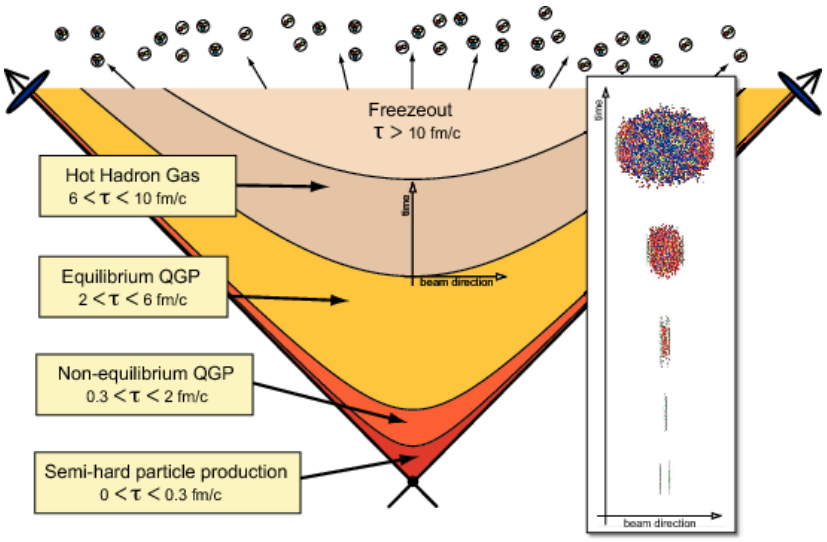

Figure 1.18: A time frame cartoon for the thermodynamics of the QGP in heavy ion collisions. Both diagonals represent the light-cone projection of incident beams. The overlay on the right shows the evolution in the laboratory frame. From [45].

When colliding nuclei at very-high velocities, the relativistic contraction of length scales plays a role: the crossing time Δt for nuclei can be estimated as:

$$t \sim \frac{d}{c} \Longrightarrow \Delta t \approx \frac{2R_o/\gamma}{c}. \tag{1.42}$$

Taking 10 fm as an order of magnitude for the nucleus radius R_o, and using the energies at which the LHC operated for the lead-lead scheme, $E_{Pb} = 1.38\ A$ TeV, we have the Lorentz factor $\gamma = 1380$ and the crossing time for lead nuclei at LHC energies is $\Delta t \approx 10^{-2}$ fm/c. This can be compared to the timescale of strong interactions,

$$t_{QCD} \sim \frac{1}{\Lambda_{QCD}} \approx 1\text{fm}/c \Longrightarrow \Delta t \ll t_{QCD} \tag{1.43}$$

As a consequence, any effects related to particle production via strong interactions will occur well after the nuclei have crossed.

There comes a big difference with DIS experiments: one has to produce the probe just before the QGP is formed because it does not last for long. The cartoon in Figure 1.18 informed on the lifetime of the QGP: the kinetic freeze-out occurs around 10 fm/c. It would be hopeless to try to shoot something at a QGP that lasts for less than 10 fm/c.

What objects can be produced in the high-energy nuclear collision early enough to see the rise and fall of the deconfined phase? Hard (high-Q^2) particle production, including photons and weak bosons that should not be sensitive to the strongly interacting medium. In this sense, the large energy carried by jets would be good a candidate, as they should see a lot of the QGP on their way out towards the detector.

Heavy quarks would also be good candidates, provided that the initial process was hard enough (say, above 1 GeV).

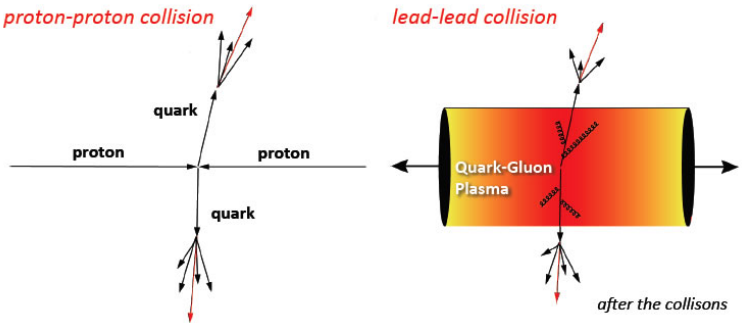

Figure 1.19: A schematic approach to a hard partonic interaction in (left) a proton-proton interaction and (right) a coloured medium.

Figure 1.19 is here to give a schematic idea of what happens in the case of the production of two quark jets. Both quarks are emitted back to back in the initial parton reference frame. If they are produced close to the QGP boundary, it is likely that one will escape, while the second one will scatter and interact strongly with most of the medium, changing significantly the topology: the away side is completely absorbed, as measured by the STAR collaboration in gold-gold (AuAu) collisions [46], and presented in Figure 1.20.

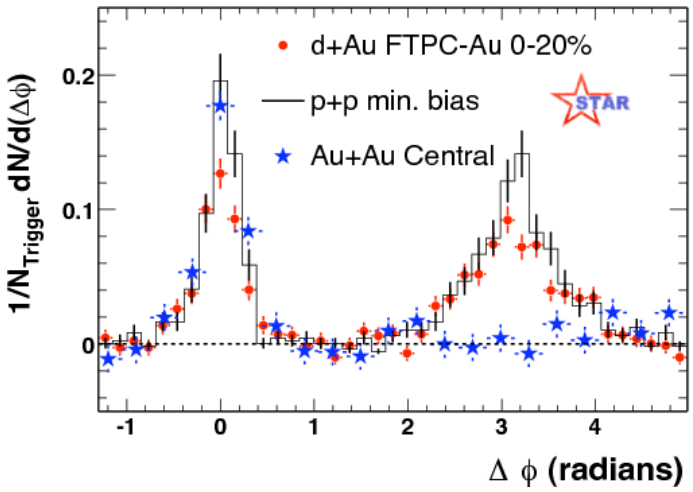

Figure 1.20: Azimuthal di-hadron correlations in pp (black histogram), dAu (red circles) and AuAu (blue stars) collisions from the STAR collaboration.

On the figure one can see that away-side jets are also slightly modified in deuteron-gold (dAu) collisions [46], indicating some interaction with non-QGP nuclear matter.

Indeed, one does not expect to match the conditions for a hot medium formation when a very light nucleus (such as a deuteron) hits a much heavier one. This constitutes a measurement of nuclear matter effects.

This immediately raises the question of the 'violence' of the QGP phenomenon. The impact parameter not being measurable, one has to rely on a model to estimate the *centrality* of the collision. In various Since the early heavy ion experiments of the seventies and eighties, the charged hadron multiplicity has been measured to increase as a function of log $\sqrt{\sqrt{s_{NN}}}$, as is shown on Figure 1.21.

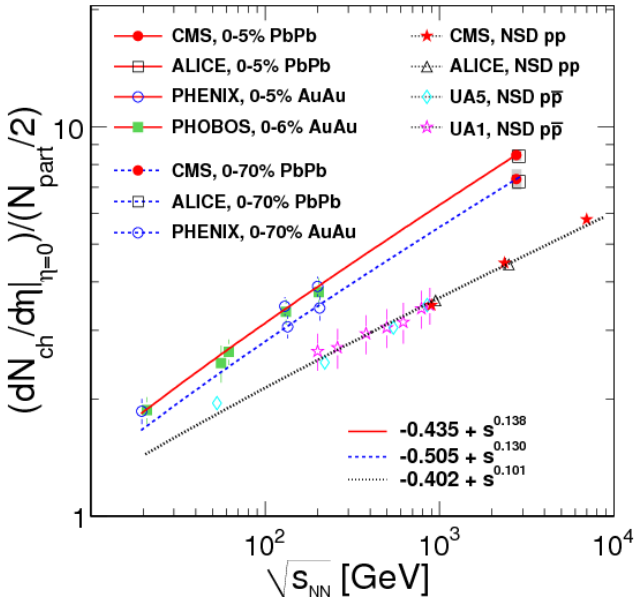

Figure 1.21: Charged hadron multiplicity in proton-proton and heavy ion collisions [47].

One can see that this log $\sqrt{\sqrt{s_{NN}}}$ dependence also applies to central heavy ion collisions. The plot shows that for the most central values, the charged particle yield changes, as well as the slope, indicating a classification of events as a function of global event variables works well. Nowadays the events are cut in percentiles of increasing centrality, that are directly correlated to the charged hadron multiplicity in the event or the sum of energy deposits in the forward directions of the detector.

This short review of possibilities led me to present the centrality of the collisions, as well as the (p-A or d-A) baseline for cold nuclear matter effects. This anticipated a discussion of global event variables which are relevant for any heavy ion measurement. In Section 4.3.3 I shall present in more detail how these experimental handles correlate with the assumed number of nucleons participating in the collisions, as well as with the number of hard scatterings, both derived from a Glauber model calculation [48].

Finally, bound states of heavy quarks should play a central role in measuring the thermal properties as they also come from a hard process. Furthermore, the spectroscopy of quarkonia is such that one family (charmonium or bottomonium) has

members with increasing sizes or binding energy, with different radial and/or orbital quantum numbers. It turns out that in the most simple considerations, the energy levels computed are of the order of the deconfinement temperature, or of small integer multiples of T_c. This means that J/ψ, $\psi(2S)$, Υ(1S,2S,3S) may react differently to the quark-gluon heat. This is covered in the next section, in a larger detail.

1.3.3 Sequential melting

As seen in Section 1.2.3, the quarkonium states of the charmonium family and of the bottomonium family are heavy quark resonances, i.e. a bound state of heavy quark (c or b) and a heavy anti-quark of the same flavour ($\bar{c}$ or $\bar{b}$, respectively).

Each family has its own spectroscopy, meaning that one can observe several energy levels of this resonant structure. For example, in the case of charmonium, the J/ψ represents the fundamental level of $c\bar{c}$ states with a spin-parity combination $J^P = 1^-$. The $\psi(2S)$ state often called "psi-prime", is the first radial excitation of this level. There are other states in the charmonium family as we shall see in Chapter 2.

When studying the effects of the QGP on heavy quark resonances, Matsui and Satz have found in 1986 [49] that considering a non-relativistic interaction potential for two heavy quarks Q and $\bar{Q}$,

$$V(r) = \sigma r - \frac{\alpha_{\text{Coul.}}}{r}, \tag{1.44}$$

the string tension σ depends on the temperature T. For an isolated system (meaning $T = 0$) of charm quarks (let us take for instance the J/ψ), we can take $\sigma \approx 1$ GeV/fm, and $\alpha_{\text{Coul.}} \approx 0.5$ for the effective Coulomb interaction coupling. Solving the radial energy equation they get a J/ψ radius at zero temperature of

$$E_{J/\psi} = 3.1 \text{ GeV}, m_c = 1.56 \text{ GeV} \Longrightarrow r_{J/\psi} \approx 0.25 \text{ fm}. \tag{1.45}$$

The colour screening evolution towards and above QGP transition temperatures had been studied previously in [50]. For a quark/anti-quark pair, the relevant quantity accounting for a 'size' is the correlation function $\Gamma_{q\bar{q}}(r, T)$, with r being the static system's radius, and T the temperature of the gluonic bath[11]. From lattice simulations one can observe the correlation length decreasing steadily when the temperature passes $T \sim 200$ MeV. Matsui and Satz identify this with the binding string tension decreasing with T, arguing that at the deconfinement temperature, $\sigma(T_c) = 0$. Above deconfinement a colour-screened version of the Coulombic potential persists, from which one can expect dissociation of the quarkonium states at definite temperature values. In this picture, the resulting physical outcome is a sequential reduction of the overall charmonium yield with increasing of the energy density created in the collision.

[11] At that time, full SU(3) gluons + quarks lattice simulation were not available yet.

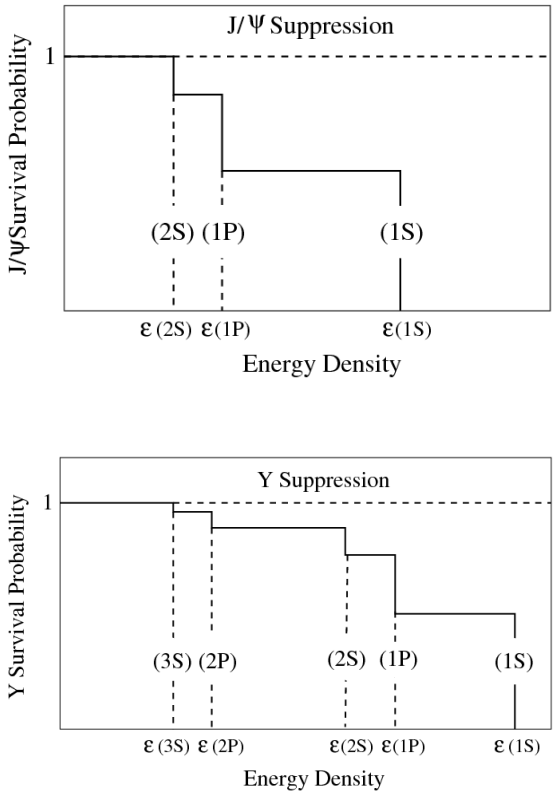

Figure 1.22: A schematic approach to sequential melting of quarkonium ground states as a function of energy density. Top: the J/ψ suppression sequence. Bottom: the Υ(1S) suppression sequence.

This is often called a *sequential melting* scenario, which resembles the rough sketch depicted in Figure 1.22. One can see that the bottomonium family is slightly more complicated than the charmonium family. I will elaborate more on the spectroscopies of each family in the next Chapter. Finally, the height of each step in Figure 1.22 is driven by the spectroscopy of each quarkonium family, where de-excitations from excited levels populate the lower-lying states.

This marks the end of Chapter 1. I have presented how QCD came together and imposed itself as the theory for strong interactions between quarks and gluons. I have briefly presented some aspects of what makes QCD special, and some connections with ultrarelativistic nuclear collisons in experiments. I have also presented how some observables are relevant to estimate the effect of the QGP, either in an alteration of their spectrum, or of their production rate. In the next Chapter I will concentrate on the case of quarkonia: How do we understand the production in vacuum of such extended objects, and how we explain their observed modification in nuclear matter.

Chapter 2

Aspects of quarkonium physics

Contents

At least we can all agree on one thing: The people who see the dress as white are utterly, completely wrong.

Adam Rogers, in *The Science of Why No One Agrees on the Color of This Dress*, www.wired.com

2.1 Quarkonium production in vacuum

Quarkonia were first studied extensively at e^+e^- colliders. For example, the BABAR detector at Stanford (USA) and BELLE at Tsukuba (Japan) have analysed hundreds of inverse femtobarns of e^+e^- events at the centre-of-mass energy of a $\Upsilon(4S)$ at rest (and above), to study B meson production and other heavy flavour related processes. Among these, the spectroscopy of heavy flavour and quarkonia has been studied with great precision [51]. The quarkonium production mechanisms are however, still debated. I will start with a discussion of the allowed decay processes for quarkonia, by virtue of the Okubo-Zweig-Iizuka (OZI) rule [52, 53, 54]; this will help me to give a naive view of the possible production modes, by simply turning around the decay process. Then, I will discuss what the binding of two quarks means in terms of spectroscopy and

decay, before moving to an experimental review of some interesting results, and finish with an increase in temperature to see to what risks a quarkonium exposes itself when wandering in nuclear matter. Beginning with an experimental review, I will make a detour in charmonium physics, before moving to a discussion of available results in the bottomonium sector.

2.1.1 Introductory remarks: the OZI rule

In Chapter 1, I have mentioned the existence of new resonances in the 1970's dilepton spectrum of e^+e^- colliders. One of the particularities of these new J/ψ and Υ peaks is their very narrow signal shape, compared to what was usually known in the lower part of the mass spectrum (except for the ϕ meson, which is $s\bar{s}$).
This is a consequence of the OZI rule. For heavy quark-antiquark states ψ of the same flavour $s\bar{s}$, $c\bar{c}$, $b\bar{b}$, the possible decay processes are: electromagnetic annihilation or hadronic decays. The rate of the electromagnetic annihilation quarkonium is of a typical order α^2_{QED} [55]. On the other hand, the hadronic decay is mediated by the strong interaction. So at first, one can say that quarkonia will either decay strongly via the hadronic channel, or via QED-mediated processes, seemingly with a smaller rate (as $\alpha_{QED} < \alpha_S$). For a chosen ψ state having spin 1, and odd parity, and the hadrons being colour singlets, there are several constraints to the QCD mediated decay:

- the final state being composed of colour singlets (e.g. pions), the decay cannot be mediated by one gluon (which is a colour octet[1]);

- the two-gluon decay is also prohibited, since a vector meson can not decay into two massless vector gluons, by virtue of the charge conjugation (C) quantum number conservation;

- but, the decay to three gluons would be allowed, as well as decays into more gluons.

With these considerations, the quarkonium hadronic decay is driven by α^3_S and higher orders. For the ϕ meson, the decay into two kaons is favoured by the conservation of the strangeness content. The OZI rule then states that decays where quark lines do not connect the initial and the final state are suppressed. One such example of OZI-suppressed diagrams is presented in Figure 2.1.

What we have seen applies to ϕ mesons, as well as to heavy quarkonium states, our main interest. The J/ψ for instance, has a mass of $m_{J/\psi} = 3.096$ GeV/c^2, which is smaller than the twice the D^0 mass. This means that decays of the kind $J/\psi \to D^0\bar{D}^0$ are kinematically ruled out, leaving only QED annihilation and OZI-forbidden hadronic decays. This results in an experimental width of the order of 10 keV, which was smaller than the experimental resolution at that time! It is the combination

[1] I did not mention it when discussing group theory, but the existence of a ninth, colour-singlet gluon would make QCD = U(3), and the interaction length would be infinite: no confinement.

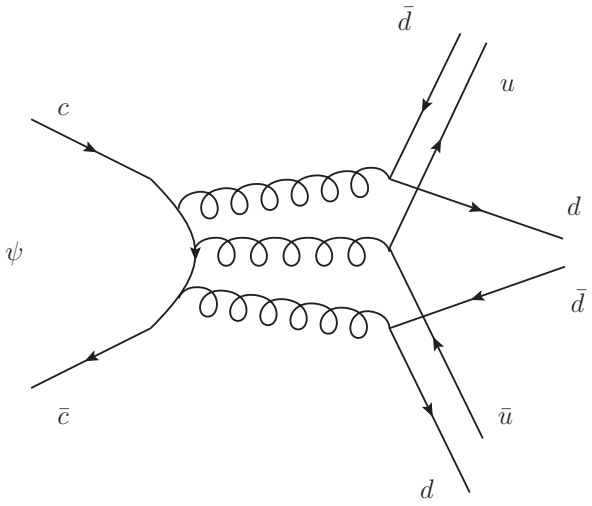

Figure 2.1: A J/ψ decay to three gluons, suppressed by the OZI rule.

of the D meson observation above the J/ψ mass and the narrow width of ψ states which definitely identified the new resonances and hadrons as from a new quark flavour.

2.1.2 Production mechanisms: the hard part

One of the important questions of this Chapter (the question is likely to remain unanswered), is whether we know what is (are) the production mechanism(s) of quarkonia. I will restrict myself to the case of hadron-hadron collisions, but there is also quarkonium production in electron-positron annihilation, photoproduction, DIS. These channels have been very fertile and would require a whole separate review, which I will not engage in.
The hadron-hadron interaction can produce at tree level in QCD a pair of quark and antiquark:

- via QCD-annihilation $q\bar{q} \to Q\bar{Q}$,
- via gluon fusion and splitting, $gg \to Q\bar{Q}$.

At the LHC, the large distribution of gluons inside each proton makes the gluon fusion the *dominant* channel for large Q^2 and small-x processes, which leads us to consider gluon fusion as the dominant initial state for quarkonium production in our review. Then comes the issue of the quantum numbers in the final state.
We have $J^{PC} = 1^{--}$ for J/ψ and Υ. From the OZI rule we have seen that the decay of J/ψ into one gluon is impossible kinematically; Additionally, the two-gluon decay would violate the charge conjugation parity, as the left part is C-odd, and the right part is C-even.
Strictly speaking, it is possible to turn the OZI rule around and realise that the only

way to produce a quarkonium with the correct quantum numbers is by the interaction of at least three gluons. A process with three gluons in the initial state has a too small rate, that could not account for the measured J/ψ rate.

So at LHC energies, gluon fusion is dominant *and* the pre-quarkonium state formed has to emit gluons to equilibrate its degrees of freedom of angular momentum and/or colour. This in some sense resembles hadronisation, although we do not know what is the colour of the initial state; Rather, nothing prevents the gluon fusion to produce a white or a coloured $Q\bar{Q}$ pair at the partonic level a priori. It is only afterwards when the pair hadronises that the colour is equilibrated.

There are various ways to recover the proper quantum numbers for each quarkonium wave function: in fact, when expanding to ever higher orders of the perturbative α_S expansion, one finds an infinity of terms contributing to quarkonium production. Some models have been proposed to describe the production processes:

- The Colour Singlet Model (CSM) [56] assumes that quarkonia are directly produced with the 'good' quantum numbers, i.e. the one they have when they decay: this poses strong constraints on either the kinematics or the total rate for producing a given state, as can be seen in Figure 2.2;

- The Colour Octet Model (COM) [57] suggests that quarkonium production via a pre-resonant colour octet intermediate state would in fact matter, to the point where these extra terms may become dominant. In this point of view the CSM alone can not account for the spectrum of a given quarkonium and its integrated cross section at the same time;

- Non-Relativistic QCD (NRQCD) [58] tries to unify CSM and COM: Stating that a hard process can be factorised from the long distance hadronisation part, it details the amplitudes of quarkonium production as an expansion of terms involving a short distance (hard part) resembling the CSM, and a long distance matrix element (LDME) containing the color octet contributions. Given the fact that both quarks are heavy, they can be treated non-relativistically in the quarkonium rest frame;

- Finally, the Colour Evaporation Model (CEM) [59] suggests a quarkonium production following dynamics comparable to that of heavy flavour hadron pairs ($D\bar{D}$ in the case of charmonium, *etc.*). In this case, the colour equilibration is treated as a nonperturbative process, related to the hadronisation phase.

The p_T (J/ψ) spectrum measured at CDF in $p\bar{p}$ collisions does not match the colour singlet (LO), neither qualitatively nor quantitatively [60]. At tree level (LO), the expected p_T-spectrum behaves according to the CSM as p_T^{-8}, which disagrees strongly with the experimental measurement of CDF, as one can see on both panels of Figure 2.2.

The left hand side specifically treats the case of J/ψ, and the $\psi(2S)$ case is presented on the right hand side of Figure 2.2. In the colour singlet hypothesis, the quarkonium ψ is produced from a gluon fusion process $gg \rightarrow ? \rightarrow \psi + X$ with a colour singlet wavefunction ψ and its allowed quantum numbers are that of η ($^1S_0$) or $chi_{0,2}$

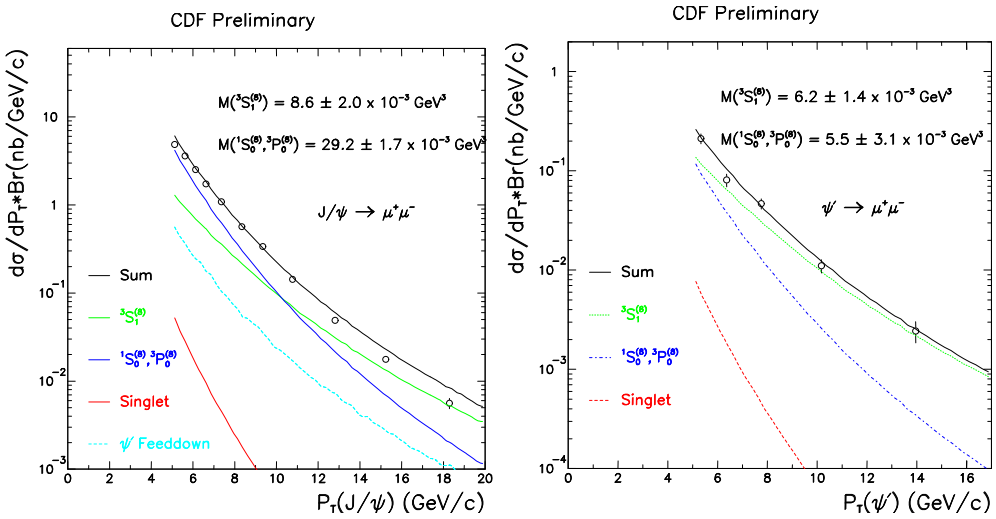

Figure 2.2: Charmonium momentum distributions from CDF [60]. Left, the J/ψ spectrum compared to LO CSM and additional colour octet terms. Right: same computation for $\psi(2S)$.

($^3P_{0,2}$). This would mean that all J/ψ come from radiative decays $\chi_c \to J/\psi\gamma$, and all $\psi(2S)$ come from b decays. A measurement of the prompt $\psi(2S)$ rate compared to the non-prompt $b \to \psi(2S)$ rate, by the CDF collaboration in 1994, has shown that the theoretical prediciton were in an order of magnitude of disagreement with the experimental data [61].

2.1.3 Quarkonium spectroscopy

Associating a quark and an antiquark of the same flavour (often called hidden heavy flavour) in a bound state will result in a constrained spectroscopy. One can find common examples of simple semi-classical systems (treated quantum mechanically, but where the dynamics are non-relativistic) such as the positronium system or the hydrogen atom, or the H_2 molecule, that would produce comparable classifications of energy levels. Of course the quantum formalism would be that of QED, and since we are interested in QCD in this case, the analogy has some limitations. Nonetheless, one can model an effective quarkonium potential of the form that was used in Equation 1.44 and solve the Schrödinger equation, to extract a spectroscopy, i.e. energy levels that can be compared to experimental data by simply measuring the mass of each resonance discovered.

For both charm and beauty, the spectroscopy begins with a ground state with quantum numbers $n = 0$, $L = 0$, $S = 0$, $J = 0$, which is usually identified as an η_c or an η_b meson. One finds higher energy bound states of various quantum numbers up to the $D^0\bar{D}^0$ threshold or the $B^0\bar{B}^0$ threshold, for charm and beauty respectively. Above the threshold, the inital $Q\bar{Q}$ system contains enough rest energy to decay dominantly in D

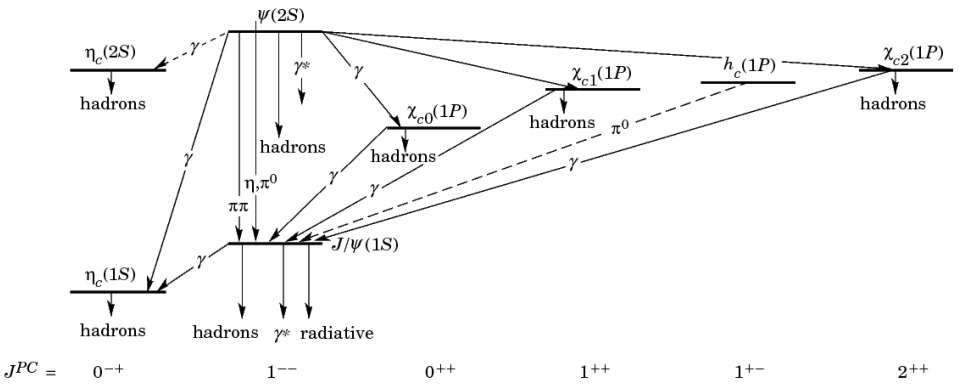

Figure 2.3: Charmonium spectroscopy. The abscissae are J^{PC} indices (spin, parity, charge conjugation). From [62].

or B mesons. Resonances existing above this threshold are far wider, as for example $\Upsilon(4S), \Upsilon(5S), \Upsilon(6S)$. For these, all OZI-favored hadronic transitions are measurable, hence their very large width (for example $\Gamma(\Upsilon(4S))/\Gamma(\Upsilon(nS)) \approx 500$ for n < 4).

The charmonium spectroscopy is depicted in Figure 2.3. All states appearing are below the $D\bar{D}$ threshold. Other states have been discovered, for which a very consequent review is done by the Quarkonium Working Group [51]. The simplest possible transitions are drawn with arrows, and correspond to radiative deexcitations (dipolar electric E1 transitions) or emission of one or several light hadrons.

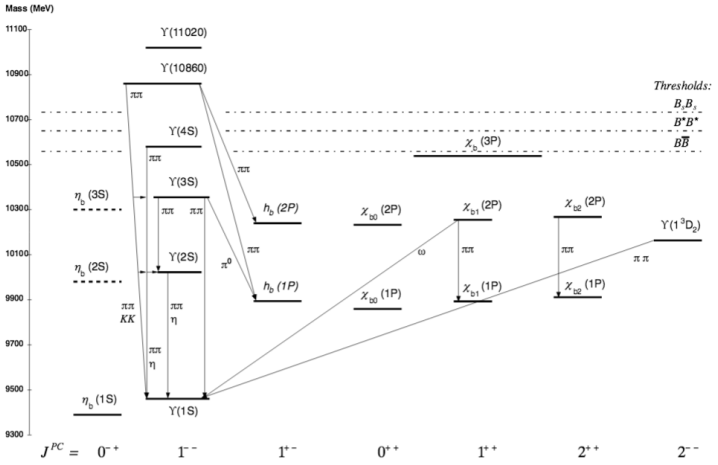

Figure 2.4: Bottomonium spectroscopy. The abscissae are J^{PC} indices (spin, parity, charge conjugation). The vertical axis, not displayed, would represent increasing theoretical rest masses. From [62].

For bottomonia, the picture is somewhat more complicated by the larger gap be-

tween the ground state mass and the $B\bar{B}$ threshold. As one can see on Figure 2.4, the spectroscopy resembles that of charmonium, as expected. The recently discovered $\chi_b(3P)$ state [63, 64] does not appear in this picture and would stand between $\chi_b(2P)$ and the $B\bar{B}$ threshold.

The transitions from excited states to lower levels of the bottomonium family, called feed-down fractions, are summed up in Figure 2.5. These fractions represent the ratio of cross sections for bottomonium states decaying into another, as a function of the product Υ p_T. Here are of interest the radiative E1 transitions $\chi(mP) \to \Upsilon(nS)$, with $n \leq m-1$ and the hadronic transitions $\Upsilon(nS) \to \Upsilon(n'S)$, with $n' \leq n-1$. As we can anticipate, the kinematics of the decay constrain the total Υ decay rate, and this has in the past led to misconceptions regarding feed-down fractions of Υ(1S) from higher states. These feed-down fractions may be crucial to interpret the suppression pattern of quarkonium modification or suppression in heavy ion collisions.

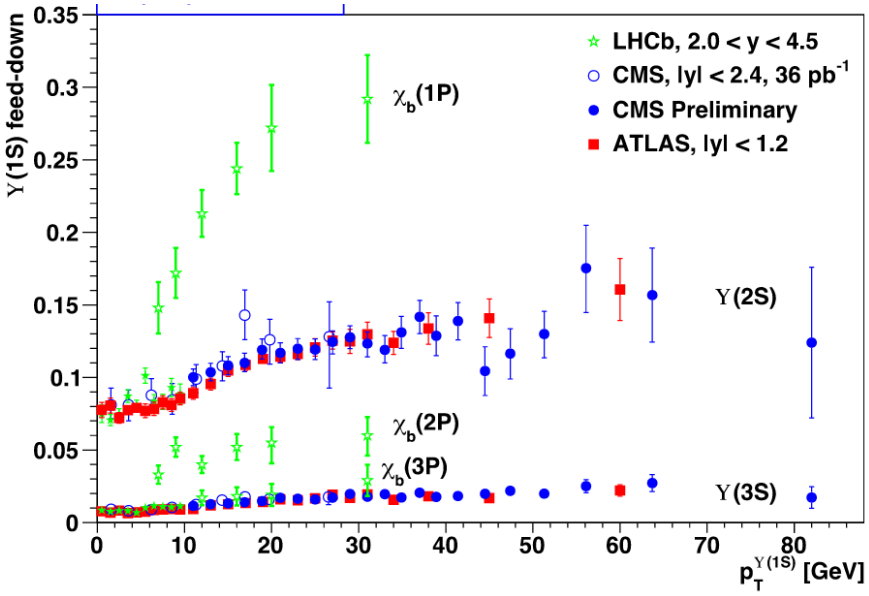

Figure 2.5: Feed-down fractions of excited bottomonia to Υ(1S), as a function of the transverse momentum of the Υ(1S) meson. From [65]

In this section the basis of our understanding of quarkonium production in vacuum was presented. The experimental data from Tevatron provided a long standing puzzle to a theoretical formulation that would reproduce the data. However, with newer high-luminosity experiments such as the LHC or future experiments, a larger understanding of quarkonium production in pp can be possible.

2.2 Charmonia in nuclear matter

2.2.1 At the SPS

The CERN SPS fixed target experiments NA38, NA50 and NA60 investigated the charmonium sector in various heavy ion systems (pp, p-A, A-B, A-A, with various ions A and B), to look for the onset of suppression [66, 67, 68, 69, 70, 71]. In all cases, the experiment could use multiple targets, allowing for a precise scan of the energy density dependence of the collision.

Each experiment reconstructed dimuon invariant mass pairs in the charmonium region and around, to measure the signal and background constributions. The J/ψ and $\psi(2S)$ cross sections were extracted from other same-charge background dimuon sources In order to measure the centrality, one could record the energy deposited in zero degree calorimeters (ZDC) or using the multiplicity in a nearby silicon tracking device, and later use a Glauber model calculation to extract an effective length L of nuclear material seen by the probe. The Drell-Yan cross section $\sigma(A + B \to \mu^+\mu^-)$, measured around the J/ψ peak ($2.9 < m_{\mu\mu} < 4.5$ GeV/c^2) [70], is used as a reference in all collision setups to compare with the J/ψ cross section, as is shown on Figure 2.6.

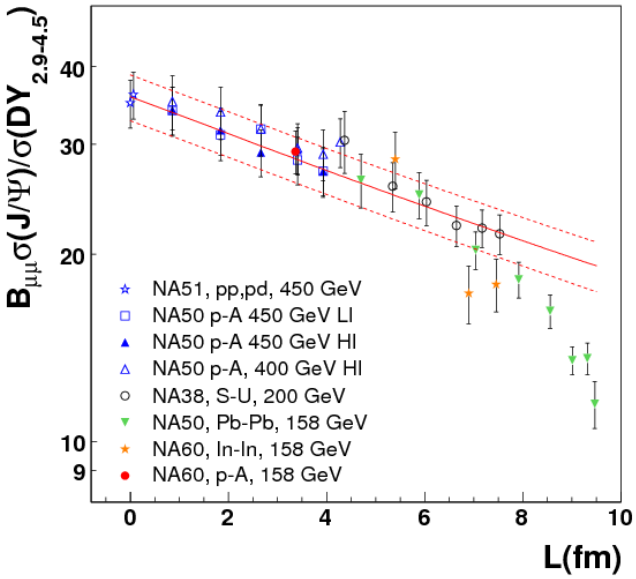

Figure 2.6: J/ψ suppression from SPS experiments as a function of nuclear length L. From [72].

The green points represent what was called an 'anomalous' suppression, in the sense that above $L = 7$ fm the observed data does not conform to pure nuclear absorption. The nuclear absorption is estimated using a Woods-Saxon nuclear distribution fitted to data, exhibiting an absorption cross section of $\sigma_{\text{abs}} = 4.18 \pm 0.35$ mb.

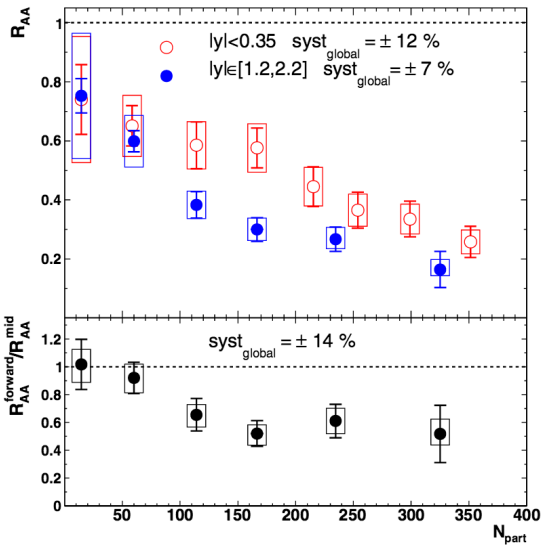

Figure 2.7: J/ψ suppression in AuAu collisions at $\sqrt{s_{NN}} = 200$ GeV from PHENIX at RHIC, as a function of centrality. Two rapidity regions are shown: central (open symbols), forward (closed symbols). From [74].

2.2.2 At RHIC

Studies to find the effects of deconfinement progressed at Brookhaven with the start of RHIC (Relativisitc Heavy Ion Collider) operation in 2000. The charmonium system was measured there in pp collisions at $\sqrt{s} = 500$ GeV, in deuteron-gold (dAu) and gold-gold (AuAu) collisions at $\sqrt{s_{NN}} = 200$ GeV.

The dependence of charmonium suppression was investigated there as a function of transverse momentum, rapidity and centrality percentiles, the latter instead of nuclear matter length. The centrality is again obtained via a Glauber model calculation, which in the case of the PHENIX experiment, is correlated to the collected charge in the Beam Beam Counters (BBC). A complete review of centrality measurements for AuAu and dAu collisions with the PHENIX detector from RHIC is available in [73]. Figure 2.7 shows the centrality dependence of J/ψ suppression at $\sqrt{s_{NN}} = 200$ GeV from PHENIX. The J/ψ yields are measured in the central region (open symbols) and in the forward direction (blue). This seems to show that the J/ψ is more suppressed at RHIC in the forward direction, which is counterintuitive: indeed the energy density is expected to be higher in the central rapidity region, which would lead to more suppression in the central arm.

The J/ψ suppression from fixed target experiments at SPS energies was probing regions of the Bjorken-$x \approx 0.1$, a region where the gluon density is relatively unmodified in nuclei, compared to the x regime of PHENIX measurements (smaller x values, typically $10^{-3} < x < 10^{-2}$). In this small-x region, the gluon density can suffer a depletion (*shadowing*) effect in nuclei, resulting in a J/ψ yield slightly affected downwards. The nuclear modification factor in dAu from PHENIX [75], R_{dAu} is presented in Figure 2.8

(left) and presents indeed some suppression in the p-going direction, which is in this case positive rapidities.

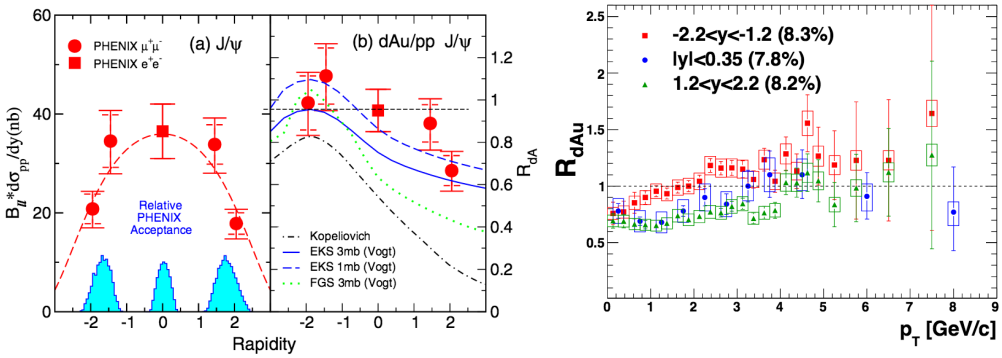

Figure 2.8: J/ψ suppression in dAu collisions at $\sqrt{s_{NN}} = 200$ GeV measured by the PHENIX experiment at RHIC, as a function of J/ψ rapidity (left) and transverse momentum (right). From [76, 77].

One can also notice on Figure 2.8 (right) the p_T dependence of the J/ψ dAu suppression. The J/ψ seems to be slightly suppressed in low transverse momenta. This p_T-dependent measurement of the suppression in dAu need to be completed with a measurement involving two ions, to see if any additional suppression is thus also reflected in the AA p_T spectrum.

Thanks to RHIC data, the suppreesion of J/ψ in AuAu and dAu has been clearly measured, to finally reach a lowest suppression point of approximately $R_{\rm AA} \approx 0.2$ in low-p_T central AuAu collisions. In Figure 2.9 the p_T-dependence of J/ψ in AuAu collisions is presented with various centrality classes. The suppression seems to be stronger in high centrality, low-p_T events. However, a mild difference between forward and central rapidities is observed, and could be explained by more nuclear absorption setting in at forward rapidities, or a possible gluon shadowing effect.

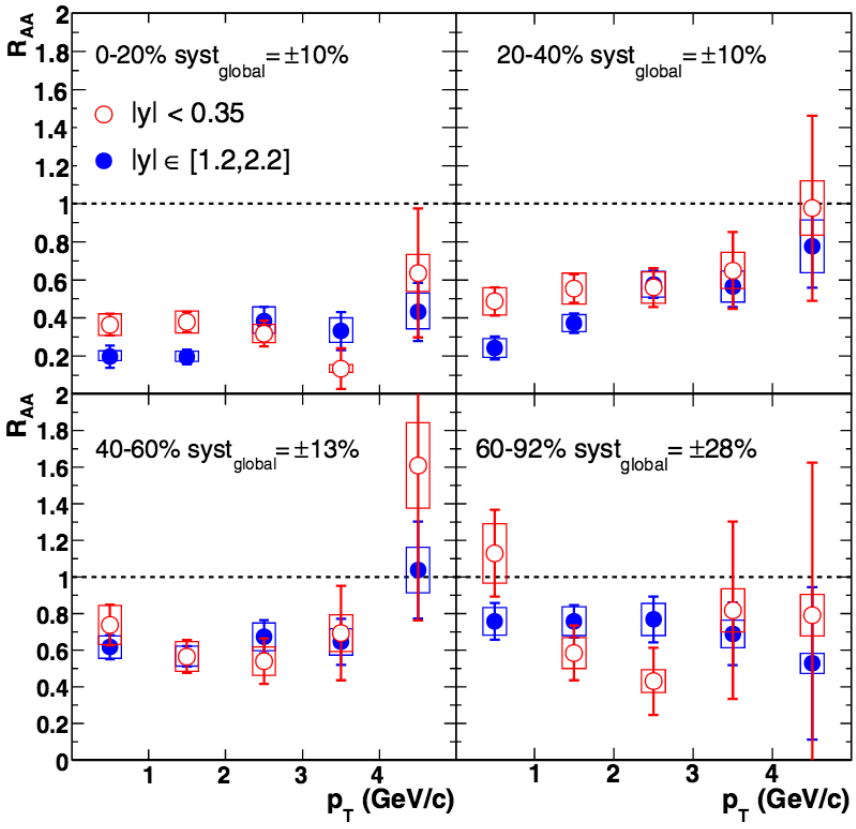

Figure 2.9: J/ψ suppression in AuAu collisions at $\sqrt{s_{NN}} = 200$ GeV measured with the PHENIX experiment at RHIC, as a function of J/ψ transverse momentum. The four panels from top left to bottom right correspond to decreasing centrality classes. Open symbols: central rapidity, closed symbols: forward rapidity. From [74].

2.2.3 At the LHC

At the LHC, the energy in the centre-of-mass for PbPb collisions is $\sqrt{s_{NN}} = 2.76$ TeV for the first operation period (Run1, up to 2013). The center of mass energy in pPb is $\sqrt{s_{NN}} = 5.02$ TeV, while pp data was taken at $\sqrt{s} = 2.76$, 7, 8 TeV. The ALICE and CMS experiments have measured J/ψ yields with high precision in pp, pPb and PbPb, yielding several suprises. First of all, the suppression measured at ALICE is much less pronounced at low transverse momentum than in the RHIC data, as is shown on Figure 2.10 (left). This plot also has J/ψ data from the CMS collaboration (prompt J/ψ, $p_T > 6.5$ GeV/c) in the central rapidity region. The right hand side of Figure 2.10 has the rapidity dependence of inclusive J/ψ suppression in PbPb, exhibiting less suppression at midrapidity than at RHIC (cf. Figure 2.9), and a stronger suppression when going to higher rapidity ranges.

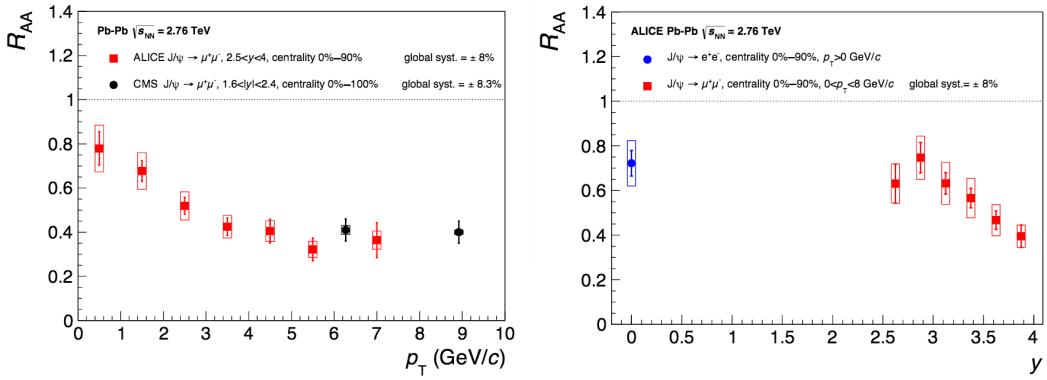

Figure 2.10: J/ψ suppression in PbPb collisions at LHC energies, as a function of the J/ψ p_T in ALICE forward data and CMS data (left), and as a function of J/ψ rapidity with ALICE (right). Red squares: forward rapidity, blue circles: central rapidity. Black squares: CMS high p_T data. From [78].

On Figure 2.11, the centrality dependence is presented, and appears saturating at $R_{\rm AA} \sim 0.65$ from $N_{\rm part} = 100$. When comparing with RHIC results, this looks like a strong enhancement, or a much weaker suppression. Models accounting for statistical recombination of decorrelated charm quarks [79, 80] into J/ψ suggest that at LHC energies, the energy density is such that about 100 $c\bar{c}$ pairs are produced in central PbPb events, leading to a large probability for these quarks to combine in the hadronic freeze out phase in a J/ψ (or $\psi(2S)$) state, hence populating the spectrum and reducing the observed suppression in this phase space region.

The CMS collaboration has published a p_T, rapidity and centrality dependent J/ψ result [2] for high p_T J/ψ (prompt and non-prompt, i.e. coming from secondary displaced vertices). The $R_{\rm AA}$was further recently updated with higher statistics in pp data in [81] and is presented in Figure 2.12.

There may be nuclear modification process(es) affecting the J/ψ production (pPb data from CMS [82] and ALICE [83] that I have not covered here, and that seem to go

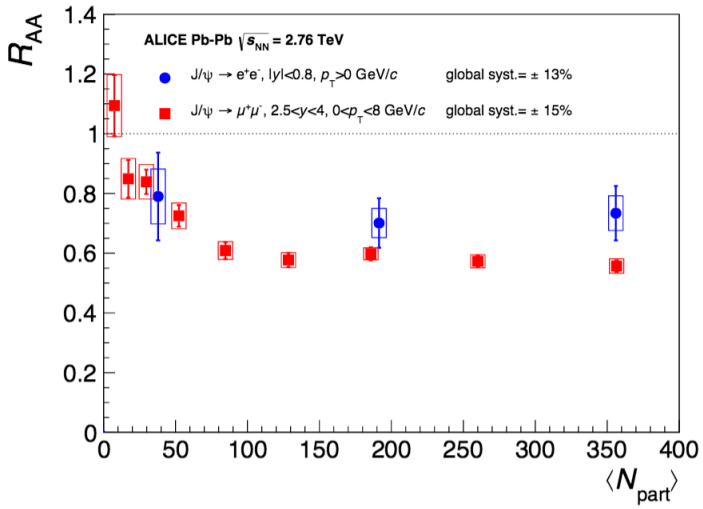

Figure 2.11: J/ψ suppression in PbPb collisions from ALICE, as a function of the centrality of the collision. Red squares: forward rapidity, blue circles: central rapidity. From [78].

in the direction of a reduction of the J/ψ yield in cold nuclear matter). Finally, there is a lot of interest regarding the $\psi(2S)$ suppression in PbPb collisions. First, this is a very challenging measurement given the naturally small $\psi(2S)$ yield when comparing with J/ψ. Second, a measurement from CMS [84] seems to show less suppression for $\psi(2S)$ than for J/ψ in an intermediate p_T region, where some recombination effects could still be at play. This would only be settled with a careful look at a more abundant PbPb dataset in the coming years. In 2015, the LHC will operate Pb ion beams reaching an energy in the center of mass of about 5 TeV, which will allow one to reach even higher energy densities than previously, and will enhance slightly the cross section for hard processes such as the J/ψ and $\psi(2S)$.

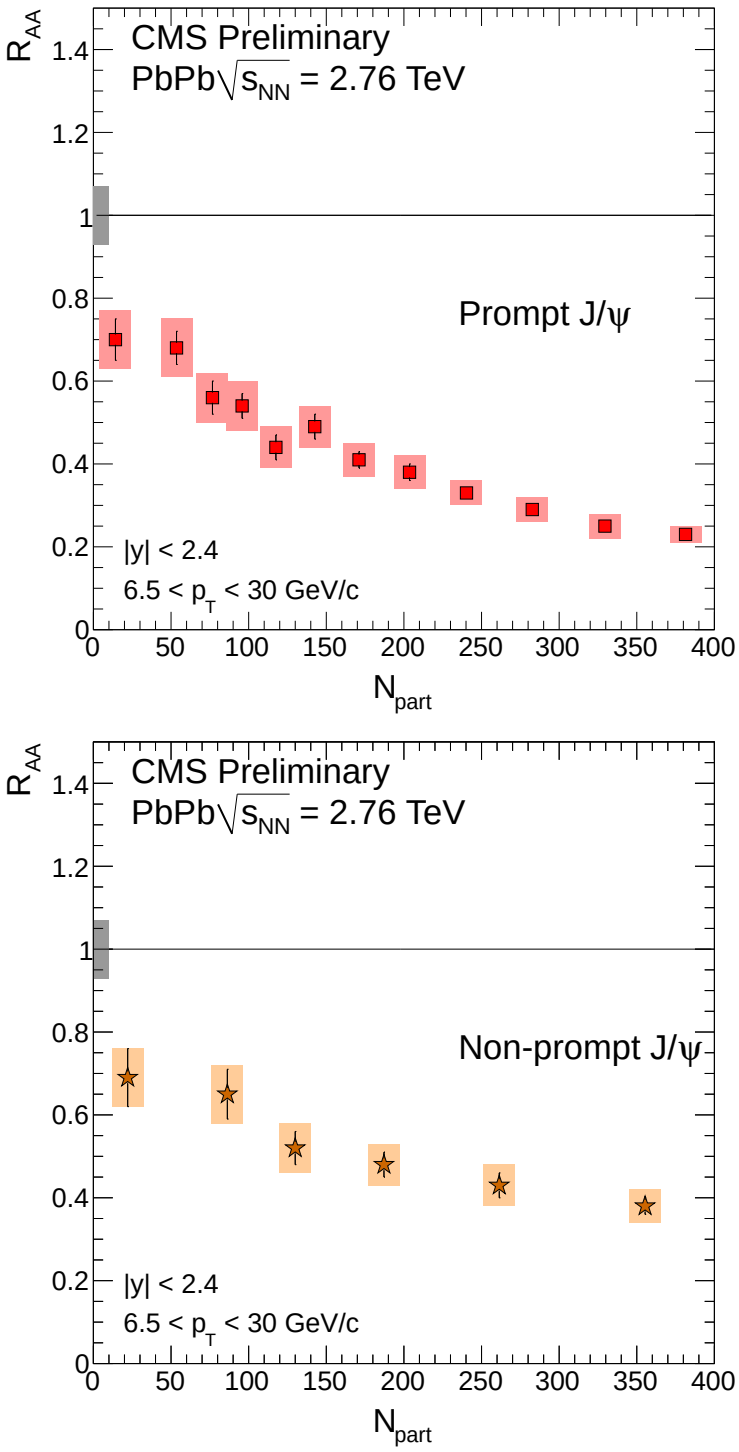

Figure 2.12: high p_T J/ψ suppression in PbPb collisions from CMS, as a function of the centrality of the collision. Top: prompt J/ψ, Bottom: non-prompt J/ψ. From [81].

2.3 The bottomonium case

Since the b quark mass is higher than the c quark, it is likely that perturbative calculations find a better agreement on Υ data than what was observed in J/ψ data. Also, one can make a more stringent test of the non-relativistic hypothesis given the higher quark mass. Although the feed-down fractions were known from $p_T = 8$ GeV/c and above with Tevatron data, the LHC measurements provide with more information on the transition from higher energy levels to the ground state, which is an important constraint for our understanding of Υ suppression in heavy ion collisions. The feed-down fractions from Υ(nS), χ_b(mP), to Υ(1S) were previously shown on Figure 2.4.
Next I will move to the case of bottomonia in heavy ions. The melting temperature is expected to be different for states with different binding, hence it is interesting to look for the yields of all three Υ states in heavy ion collisions. These provide interesting constraints on the temperature of the medium produced in heavy ion collisions at the energies of the LHC (as well as RHIC energies as we shall see). In the case of Υ states, the mass being larger than for charmonia, it is possible that binding energies from potential models are more stable. When it comes to the nuclear absorption effects and shadowing, these should also be smaller than for charmonia, given the fact that the initial parton is slightly harder. Finally I will present some results regarding Υ measurements as a function of the event centrality in PbPb collisions that exhibited a strong suppression of the excited states for the first time, shortly before the beginning of my thesis.

2.3.1 Υ production in pp collisions

The LHC data collected during Run 1 provides several useful constraints on quarkonium production, and that is seen for J/ψ as well as for Υ. We now turn to the case of Υ production in pp collisions.

The ATLAS experiment measures Υ states decaying in two muons in the pseudorapidity range $|\eta^\mu| < 2.25$. This measurement in 7 TeV pp data [85] scans the p_T spectrum up to 70 GeV/c with an integrated luminosity of $\mathcal{L} = 1.8$ fb^{-1}. The invariant mass plot for the central rapidities $|y| < 1.2$ appears in Figure 2.13 (top, left).

CMS has measured Υ states in the dimuon channel with pp data at 7 TeV as well, dedicating two papers (post-ICHEP 2010 which consisted of about 3 pb^{-1} of 2010 data). The first publication [86] presented Υ spectra up to $p_T = 50$ GeV/c, with approximately 36 pb^{-1} of pp data, using the full coverage of muon detectors and of the inner tracking system, $|\eta| < 2.4$. Next, a further measurement [87] using $\mathcal{L} = 4.9$ fb^{-1} of pp data focuses on events with $p_T > 10$ GeV/c with a rapidity cut at $|y^{\mu\mu}| < 1.2$, where the dimuon resolution is as good as to separate clearly the three upsilon states, as shown in Figure 2.13 (top, right).

The LHCb collaboration has also measured Υ states in $\mathcal{L} = 36$ pb^{-1} of pp collisions at $\sqrt{s} = 7$ TeV, in a publication extending to events with $p_T < 15$GeV/c, in the dimuon rapidity coverage of LHCb ($2.5 < y < 4$) [88]. The dimuon invariant mass plot in the Υ mass range is presented in Figure 2.13 (bottom, left).

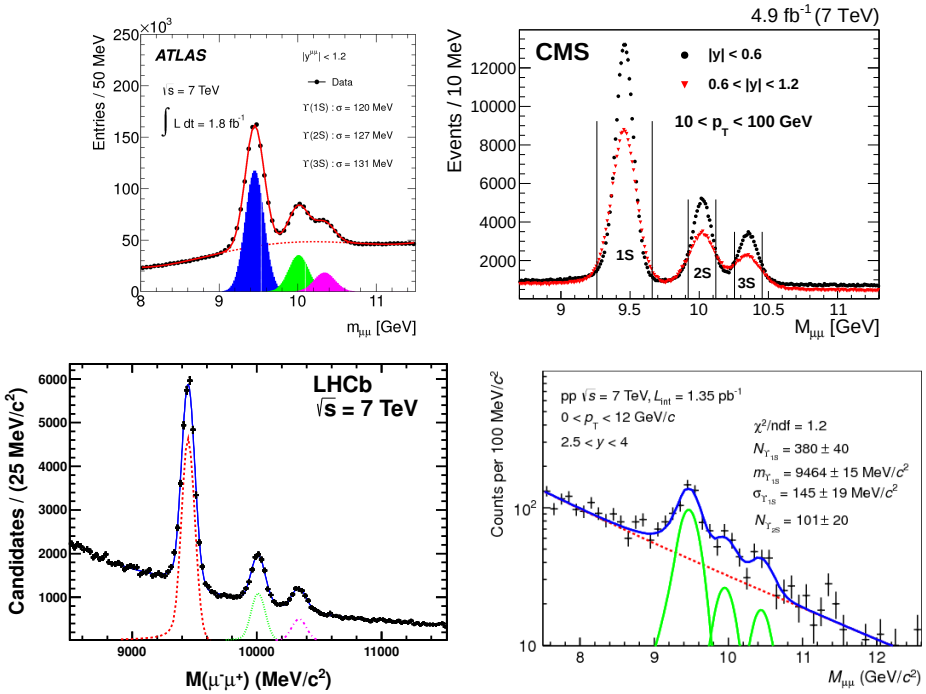

Figure 2.13: The dimuon invariant mass distribution in the vicinity of the Υ resonances for ATLAS data (top, left), CMS data (top, right), LHCb data (bottom left) and ALICE data (bottom right). The solid lines in ATLAS, LHCb and ALICE plots represent fits to the invariant mass distributions, as described in respective publications [85, 88, 89].

The ALICE collaboration has measured quarkonium states in 7 TeV collisions as well, with $\mathcal{L} = 1.35\text{pb}^{-1}$ of pp data, recorded in the rapidity range $2.5 < y < 4$. The measurement [89] extends to $p_T = 12$ GeV/c, and the invariant mass plot is presented in Figure 2.13 (bottom, right).

The various mass plots of Figure 2.13 are all different in that they do not all span the same phase space window, and the detector settings vary from one experiment to the other. The unexhaustive details given here are based on the four plots of Figure 2.13:

1. CMS and ATLAS invariant mass figures (upper panels of Figure 2.13) cover the mid-rapidity region, $|y| < 1.2$. The analyses performed in the two experiments are comparable, in terms of reconstruction and trigger strategies. As a consequence, the only difference comes from the mass resolution of the peaks: in ATLAS, the reported $\Upsilon(1S)$ width is 120 MeV, while in CMS it is roughly two times less (the actual number for the presented plot was not made public). The broader peak seen in ATLAS is explained by the smaller magnetic field intensity, rendering a poorer momentum resolution on individual muons. The momentum resolution in both experiments is of the order of 1 to 5 % for J/ψ muons, as reported in [90, 91].

2. ALICE and LHCb have similar rapidity coverage, $2.5 < y < 4$, a region where

the dimuon mass spectrum can be populated with combinatorial background exponentially decreasing with increasing dimuon mass, as is seen in both figures (lower panels of Figure 2.13).

The p_T spectra are measured in all four experiments, and presented in Figure 2.14. The differential cross sections are computed after extracting the yield from invariant mass plots similar to what is shown on Figure 2.13, with a differential binning in the observable under consideration, p_T or y. The extraction is performed using empirical functions to describe the signal and background, which are fitted to data. For each peak, as is shown in Figure 2.13 (top, left and bottom, right) there is a different fit curve, and each curve is integrated to get a raw yield for the considered Υ state. The yield is further corrected for effects relative to the detectors inefficiencies or inadequate modeling. Applying the proper luminosity normalisations and efficiency corrections, one can derive a differential cross section times branching fraction for the signal observed in the dimuon channel (as it would be the case in our analysis).

After having applied all corrections that give a proper image of the physical rate of Υ production in the experiment, one can compare to theoretical models, such as the ones presented in Section 2.1.2. With their larger mass, the perturbative calculations in QCD are expected to yield more accurate results on bottomonia than what we have seen previously for J/ψ.

Figure 2.15 shows a theory comparison of ATLAS Υ(1S) cross section results to the CSM expectation, scaled to a normalisation factor, and the CSM calculation is taken up to some terms of the $\mathcal{O}(\alpha_S^5)$ expansion, that is, at partial next-to-next-to-leading order (NNLO*) [94]. The star symbol is here to indicate that the only NNLO terms considered in this calculation are those considered by the author of [94] to give a dominant contribution in the α_S^5. As is shown in the first bottom panel of the figure, the NNLO* prediction drops faster than the data at high p_T. Another comparison visible in the lowest panel of Figure 2.15 is the CEM expectation, and this one shows another disagreement, again with large uncertainties. The blue band associated with data points results from a variation of polarisation hypotheses. Spin alignment measurements have been since performed, for example with CMS Υ data, for which the result will be presented below.

The ALICE Υ(1S) p_T spectrum in Figure 2.14 shows a comparison with NRQCD (that is, including colour singlet and colour octet contributions) at NLO, which seems to find quantitative agreement at high p_T. As mentioned in Section 2.1.2, one should note that NRQCD developments predict a large transverse polarisation for J/ψ or Υ resonances, saturating to an almost full transverse polarisation at high p_T. One should then compare NRQCD expectations to the polarisation of measured quarkonia in hadron-hadron collisions to look for a possible agreement.

CMS has published a measurement of the polarisation of all three Υ(1S,2S,3S) states in pp collisions in [95]. The results for Υ(1S) and Υ(3S) are displayed in Figure 2.16. It shows a helicity component λ_ϑ compatible with zero for both Υ(1S) and Υ(3S), and

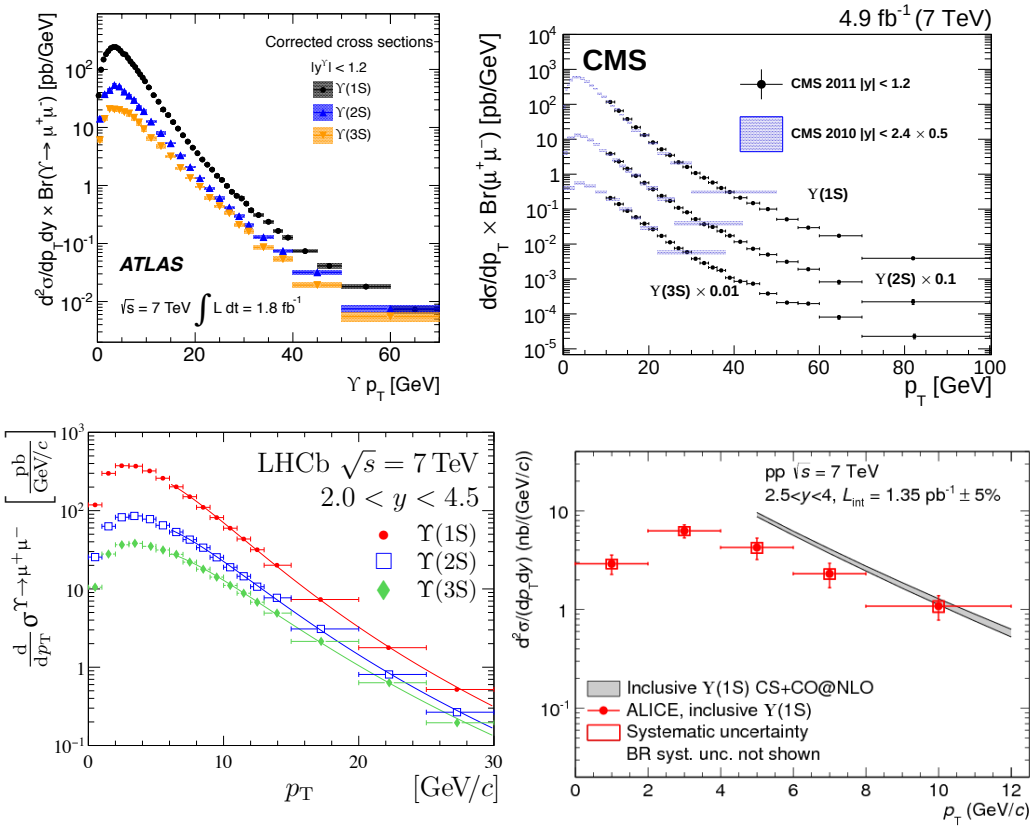

Figure 2.14: Transverse momentum dependence of Υ states' production in pp data at 7 TeV. Data from ATLAS (top, left) [85], CMS (top, right) [86], [87], LHCb (bottom left) [92], and ALICE (bottom right) [89]. The CMS data displayed also contains low-p_T results from a 2010 analysis [86], scaled to account for the rapidity range difference with [87]. The LHCb data is fitted with a Tsallis distribution function as described in [92]. The ALICE data is compared to a NLO prediction of quarkonium production in the NRQCD approach [93].

is overlayed with a theory comparison in the case of Υ(3S). As one can see, in the NRQCD formalism and contrary to the CSM, colour octet and higher order contributions should exhibit a transverse polarisation for S-wave quarkonia. Unfortunately, the agreement seen in p_T spectra (relatively good, given uncertainty bands) should be taken with caution because of this. To elaborate more on comparisons with NRQCD without going into polarisation details (which may be poorly constrained when the prediction is restricted to a phase space region), I would like to end with a comparison of LHCb cross section data from [92] for Υ(1S,2S,3S) versus p_T and rapidity. Figure 2.17 shows the ratio of such cross sections at the two $\sqrt{s} = 7$ and 8 TeV energies, $\mathcal{R}_{8,7} = \sigma(\Upsilon(nS))_{\sqrt{s}=8\text{TeV}}/\sigma(\Upsilon(nS))_{\sqrt{s}=7\text{TeV}}$. NRQCD predicts a large contribution of the CO terms in the cross section ratio, the colour singlet contributions mostly canceling as is emphasised in [92]. The prediction for the cross section ratio in NRQCD does in

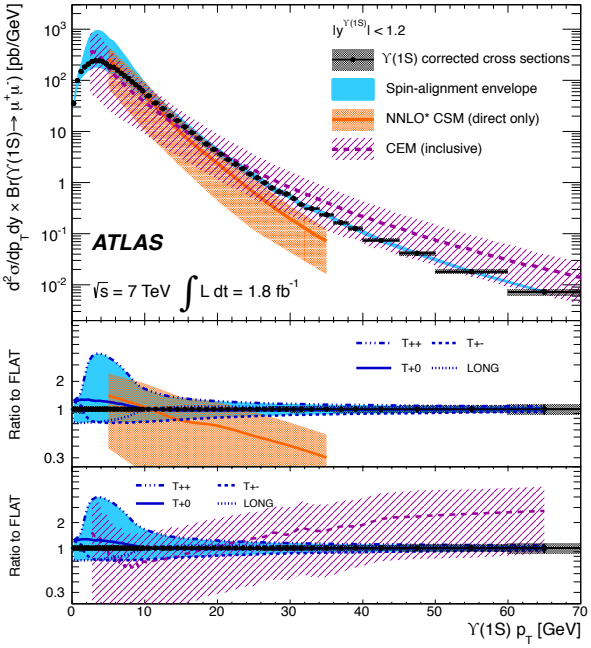

Figure 2.15: Υ(1S) differential cross section as a function of p_T, from ATLAS 7 TeV pp data [85]. Model comparisons include a truncated $\mathcal{O}(\alpha_S^5)$ calculation (NNLO*) from the colour singlet model (CSM), in an orange uncertainty band, compared to data in the intermediate panel. The bottom panel has a colour evaporation model (CEM) prediction compared to data. On all panels, the blue band corresponds to a variation of the acceptance corrections with maximal longitudinal and transverse polarisations.

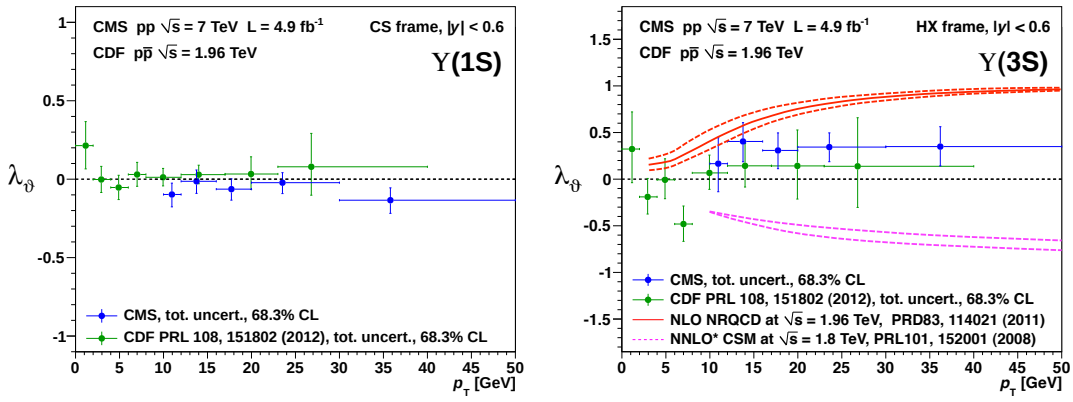

Figure 2.16: Υ(1S) and Υ(3S) polarisations measured by CMS in pp and compared to CDF (Tevatron) in $p\bar{p}$ collisions as a function of p_T. The vertical axis corresponds to the polarisation component in the helicity frame (HX). Taken from [95].

fact depend sharply on rapidity and is plotted in straight lines in Figure 2.17 (black on the left for the p_T-dependence, coloured on the right for the rapidity dependence). This disagreement in the comparison of the $\sqrt{s}$ evolution of NRQCD predictions to data is a striking feature of our lack of theoretical modeling of quarkonia in hadroproduction.

In order to complete our picture of the bottomonium family, we must take some time to analyse the other states with some detail: the χ_b mesons and their decay are important to understand the production rates for bottomonia in general, as these states are usually quite difficult to detect as we shall see. The χ_b mesons are pseudovectors (even parity) and correspond to the following spectroscopy levels [21] [64]:

$$
\begin{aligned}
\chi_{bJ}(mP) \Longrightarrow m = \text{energy level},\ j &= \text{value of angular momentum J as in } J^{PC};\\
m(\chi_{b0}(1P)) &= 9859.44 \pm 0.42 \pm 0.31 \text{ MeV}\\
m(\chi_{b1}(1P)) &= 9892.78 \pm 0.26 \pm 0.31 \text{ MeV}\\
m(\chi_{b2}(1P)) &= 9912.21 \pm 0.26 \pm 0.31 \text{ MeV}\\
&--\\
m(\chi_{b0}(2P)) &= 10\,232 \pm 0.40 \pm 0.50 \text{ MeV}\\
m(\chi_{b1}(2P)) &= 10\,255 \pm 0.22 \pm 0.50 \text{ MeV}\\
m(\chi_{b2}(2P)) &= 10\,268 \pm 0.22 \pm 0.50 \text{ MeV}\\
&--\\
m(\chi_{b0}(3P)) &= ?? \text{ MeV}\\
m(\chi_{b1}(3P)) &= 10\,511 \pm 1.7 \pm 2.5 \text{ MeV}\\
m(\chi_{b2}(3P)) &= 10\,551 \pm 14 \pm 17 \text{ MeV}
\end{aligned}
$$

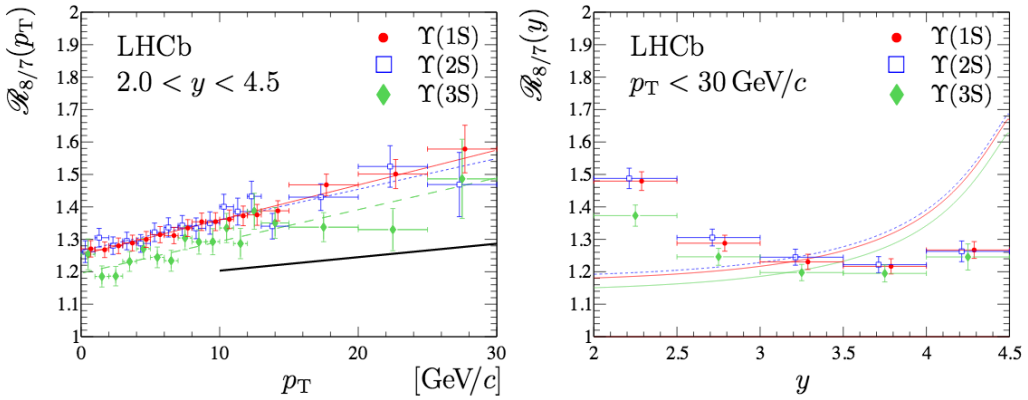

Figure 2.17: Ratio of Υ cross sections as a function of rapidity for two different centre-of-mass energies, $\sqrt{s} = 7$, 8 TeV, from LHCb. On the left, the black line represents the p_T-dependent expectation from NRQCD. To the right, the prediction is dependent on the level of the state, and each line corresponds to the NRQCD prediction for its state (red: Υ(1S), blue: Υ(2S), green: Υ(3S)). Taken from [92].

These states are all important in the bottomonium spectroscopy as some account for up to 30 % of one of the (S-wave) Υ yields. They are especially hard to detect in hadron-hadron collisions, because their favorite decay (apart from the many-gluon channel, which is intangible) is $\chi_b \to \Upsilon + \gamma$, and the photon often carries a quite small momentum (of the order of 500 MeV), making it difficult to detect. The photons can be reconstructed by their e^+e^- conversion in the tracker or the electromagnetic calorimeter of most LHC experiments, but because of the small photon momentum, the probability for reconstructing this decay is *very* small (of the order of less than a percent, at low-p_T, in CMS).
Fortunately, the fractions of χ_b mesons decaying to Υ states, either via emission of a ρ meson or two pions, or a photon, can be well reconstructed at moderate-p_T, especially by LHCb, which performed a first-time measurement of the $\chi_{b1}(3P)$ mass and feed-down fraction towards Υ(1S), Υ(2S) and Υ(3S) [64].

These feed-down fractions are especially important in the understanding of two (quite orthogonal) points in bottomonium physics: first of all, the polarization and production rates of most lower-lying states in theoretical models, such as Υ(3S), which rely a lot on the (expectedly small) fraction coming from $\chi_{bJ}(3P)$. Second, the intepretations of Υ(1S) suppression in heavy ions (pA or AA) are strongly dependent on what is expected for the $\chi_{bJ}(1P)$ states, which are quite well measured in pp and e^+e^- collisions, but are still elusive in heavy ion experiments. The feed-down fractions go as high as 30% at high p_T, with a clear p_T dependence as is shown in Figure 2.18 [64] in the case of $\chi_b(mP) \to \Upsilon$(1S) decays through a dipolar E1 transition.

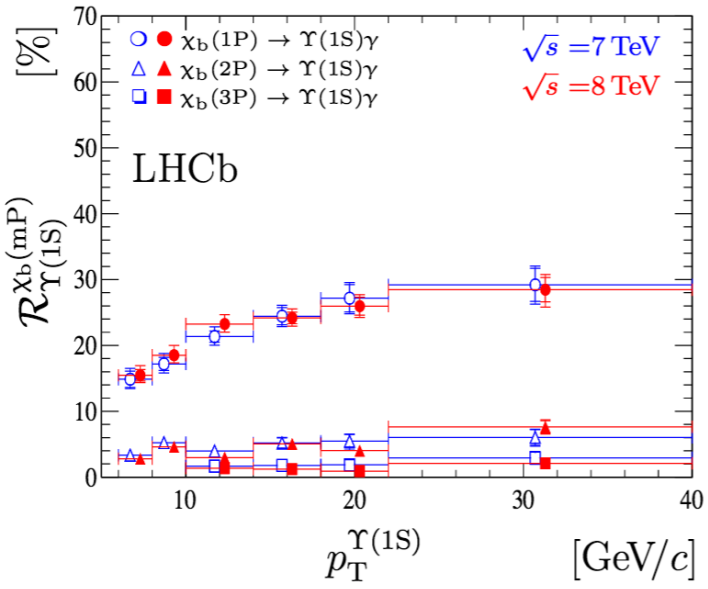

Figure 2.18: Measurements of the feed-down fractions of $\chi_{bJ}(mP)$ states to Υ(1S) at LHCb. From [64].

2.3.2 Υ suppression in heavy-ion collisions

After the review on Υ production, which was aiming at a proper 'calibration' of the *pp* reference measurement, I now turn to the measurements of Υ mesons in heavy ion collisions.

First of all, it may be worth noting that bottomonia in general, when compared to charmonia, represent cleaner probes of the QGP. In the case of charmonium states, newer measurements have often (if not always) led to more complicated interpretations related to the relatively small mass of the quark-antiquark pair. Even if the mass of charm quark is quite large ($m_c \sim 1.5$ GeV/c^2) compared to light quark masses m_d, m_u, m_s and to Λ_{QCD}, the measurements at the SPS followed by RHIC and the LHC could not bring a unifying physical interpretation of the nuclear matter effects on charmonia.

Fortunately, the Υ mesons benefit from a larger mass, and one could hope for many effects to either turn off or being still very small in the presently analysed data. In the case of recombination for example, it can be argued that not more than 2$\sim$5 $b\bar{b}$ pairs can be formed in a central heavy ion collision [96]: as a result, the recombination effect should be negligible, until a sufficient energy density is reached.

Recent results from the CMS collaboration [2, 3, 4] have reported a strong suppression in the Υ decay to two muons, with a relatively small *pp* reference, giving quite large normalisation uncertainties. A measurement of Υ dimuon mass distributions in *pp* and PbPb is presented in Figure 2.19, where the invariant mass plots for *pp* and PbPb data are displayed in a simultaneous fit exhibiting the observed PbPb suppression. On Figure 2.20 the centrality dependence of the suppression is presented for Υ(1S) and

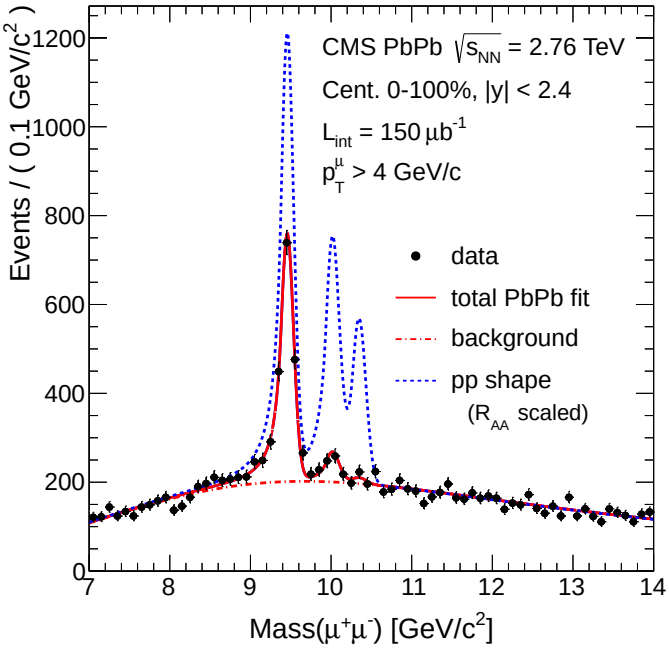

Figure 2.19: The simultaneous fit of *pp* and PbPb data recorded by CMS in the Υ mass range, exhibiting a clear suppression of the excited states. From [4].

Υ(2S), hinting at an ordered pattern, while the Υ(3S) remains unobserved in PbPb. Since then, a larger *pp* reference dataset has been recorded by CMS, allowing for a more precise measurement in centrality, and opening for the possibility of a kinematic measurement of the suppression. This is the topic covered in the present document. The following Chapters will present the experimental setup and techniques put in place to measure the Υ suppression in PbPb with a new level of precision.

In this Chapter, I have presented the basics of quarkonium measurements at hadron colliders. I have laid out the main results of the search for deconfinement in the quarkonium sector, and presented the state of the art of quarkonium measurements in *pp* and PbPb data at the time of the beginning of this thesis. In 2013, a large *pp* reference dataset has been recorded by CMS, allowing for a more precise measurement in centrality, and opening for the possibility of a kinematic measurement of the suppression.

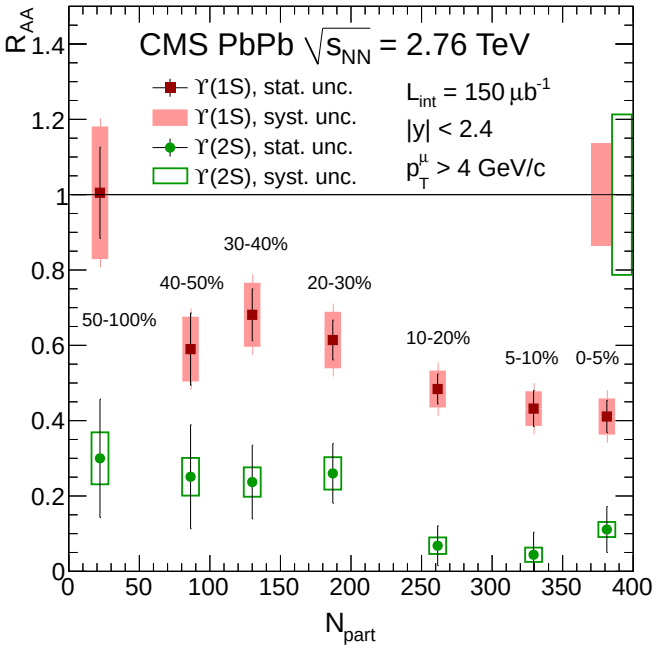

Figure 2.20: CMS measurement of the centrality dependence of Υ(1S) and Υ(2S) suppression in PbPb collisions at $\sqrt{s_{NN}} = 2.76$ TeV. From [4].

Part II

Experimental apparatus

Chapter 3

The CMS experiment at the LHC

Contents

[...]: l'esprit d'une nation réside toujours dans le petit nombre, qui fait travailler le grand, est nourri par lui, et le gouverne.

Voltaire, in *Essai sur les mœurs et l'esprit des nations*

In this Chapter, I present the experimental setups deployed at CERN to produce and record ultrarelativistic nuclear collision data. The Chapter begins with a description of the accelerator chain behind the Large Hadron Collider, before detailing the LHC itself, emphasising on the various collision setups and energies achieved so far. The discussion then moves to the experiments placed at the four interaction points, with a natural focus on the one that produced the data used in this Thesis, the Compact Muon Solenoid. The CMS detector geometry and components are defined, with a focus on the parts which are the most exploited here.

3.1 The Large Hadron Collider

The Large Hadron Collider [97] is the machine based at CERN to study elementary particle physics of the Standard Model and beyond, by the means of accelerating and colliding beams of atomic nuclei to the highest energies ever made by men. The beams are injected into the LHC after having followed several refinement steps in other particle

accelerators presented below. After injection into the LHC, the beam energies are ramped up to the desired collision energy, in a process detailed in Section 3.1.2. The experiments are provided with parts of the available beams that are squeezed in the interaction points to provoke collisions. Detectors are placed at interaction points 1, 2, 5 and 8, and these would be presented in Section 3.1.3.

3.1.1 Acceleration devices

The LHC is an accelerator and a collider maintained at CERN near Geneva (Switzerland), inside the 27 kilometer tunnel previously hosting the LEP machine. The tunnel has eight straight sections, eight arcs, and eight underground access shafts. The LHC tunnel is connected to the rest of the CERN accelerator complex by two transfer tunnels (named TI2 and TI8, see Figure 3.1) of $\sim$ 2.5 kilometer length.

A simplified picture of the LHC and its injector chain is presented in Figure 3.1. The linear accelerators (LINAC) are present at the beginning of the injection chain: LINAC2 is used as a proton accelerator, and LINAC3 serves as ion accelerator.

The LINAC2 provides low energy proton beams to the Proton Synchrotron Booster (PSB). The protons arrive from LINAC2 at 50 MeV into the PSB, which further accelerates them to 1.4 GeV and aggregates the beam in a bunch before delivering it to the Proton Synchrotron (PS). The PS has various bunch filling schemes possible for protons (8, 16 or 64 bunches per injection). Protons are taken to an energy of 25 GeV prior to the ejection towards the Super Proton Synchrotron (SPS), in bunches of 10^{11} protons each. The SPS further accelerates the proton beam to 450 GeV and can store up to 240 bunches per fill [98].

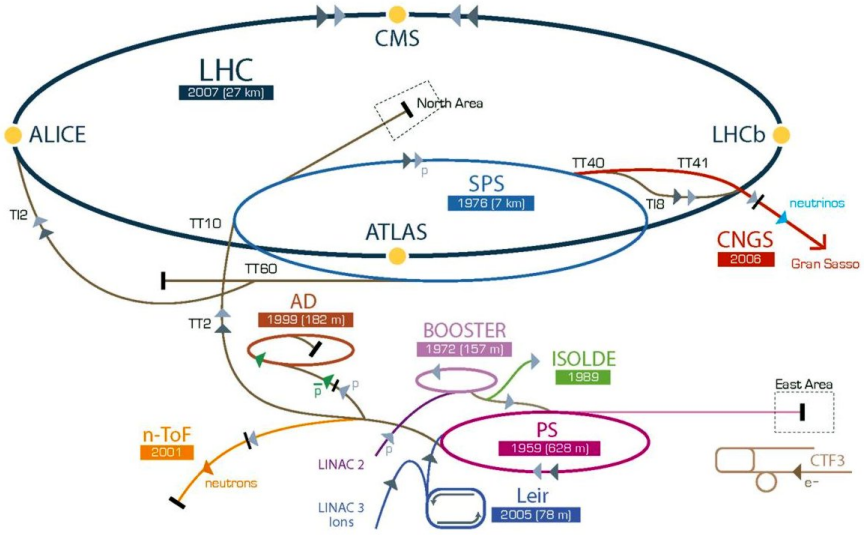

Figure 3.1: The CERN injection and acceleration chain for LHC experiments. Relative positions and sizes are not to scale.

Lead ions do not follow the same route as protons. Ions are generated in LINAC3,

which communicates its pulses to the Low Energy Ion Ring (LEIR). The LEIR accumulates up to 4 bunches of Pb^{54+} beams at 0.0148 GeV per unit charge (GeV/u), which are then sent to the PS. During the PS acceleration up to the SPS injection, the remaining charges are stripped from the ion beams, and the required LHC bunch spacing (125 ns) is attained. The energy per unit charge is also increased from 4.26 GeV/u to 177 GeV/u, and the number of bunches in the SPS train increases from 4 to 52 [98].

The proton or ion beams are carried into the LHC tunnel from two injection tunnels going in opposite directions. The injected beams are then cycling in the tunnel until the energy and current requirements are met.

Acceleration of the LHC beams is performed with superconducting radiofrequency cavities, that are set to work in the proton acceleration case at a 400 MHz frequency (i.e. 25 ns spacing between p bunches) and operating at 4.5 K [99].

In the case of Pb ions, the settings are slightly different: inevitable limitations to the beam stability arise when accelerating Pb nuclei, such as intra beam interactions (e.g. electron capture by pair production) [100]. All known limitations to the brightness of ion beams were studied from previous experience at other facilities such as PETRA or HERA, and led to reduction of the luminosity of beams injected in the LHC to prevent heat-induced magnet quenches [101].

Bending of the LHC beams is achieved by the magnet system. The arc sections of the LHC comprise 7000 multipole magnets, the most important of them being the 1232 dipoles, weighing about 35 tons. Quadrupoles and higher order multipole magnets are also used to maintain the transverse shape of the beam.

The dipole magnets are made of niobium-titanium (Nb-Ti) superconductive coils powered at up to 12 kA and maintained in their superconductive state by a single 1.9 K helium fueled cryostat. In achieving a 7 TeV beam energy (i.e. in pp collisions at $\sqrt{s}$ =14 TeV), the magnets would produce a 8.33 Tesla field strength.

3.1.2 LHC setups and energies

From the Run1 startup in 2008 to the beginning of the Run2 proton-proton data taking in 2015, the LHC has delivered experiments with an ever increasing energy and luminosity, in p or Pb beams. Table 3.1 sums up the energy and luminosity delivered to the CMS experiment from the 2010 start[1] to October 2015.

3.1.3 The LHC experiments

As we can see in Figure 3.1, there are four main experiments on the LHC path. These are situated at Interaction Points (IP) where beam crossing occurs. Each experiment has its own collaboration of institutes, researchers, and distinct physics programme:

[1] On September 19, 2008, an electrical fault occurred in a ramp up test in Sector 3-4. The fault affected several dipoles and quadrupoles, releasing a two-ton helium leak in the tunnel and delaying the LHC commissioning phase for approximately a year and a half.

	2010	2011	2012	2013	2015
pp	$\sqrt{s} = 2.76$ TeV $\mathcal{L} = 235$ nb^{-1}			$\sqrt{s} = 2.76$ TeV $\mathcal{L} = 5.6$ pb^{-1}	
	$\sqrt{s} = 7$ TeV $\mathcal{L} = 45$ pb^{-1}	$\mathcal{L} = 6.1$ fb^{-1}	$\sqrt{s} = 8$ TeV $\mathcal{L} = 23.3$ fb^{-1}		$\sqrt{s}$ =13 TeV $\mathcal{L} = 2.8$ fb^{-1}
pPb				$\sqrt{s_{NN}} = 5$ TeV $\mathcal{L} = 36$ nb^{-1}	
PbPb	$\sqrt{s_{NN}} = 2.76$ TeV $\mathcal{L}$ =9.3 µb^{-1}	$\mathcal{L}$ =184 µb^{-1}			

Table 3.1: LHC collision setup and energies from startup to October 2015. Integrated luminosities correspond to what was **delivered** to CMS until Oct. 25$^{\text{th}}$, 2015 [102].

IP1 is where the **ATLAS** detector is placed. The ATLAS acronym stands for A Toroidal LHC Apparatus [103]. As its name suggests, the detector holds a toroidal magnet, supplementing a 2 T solenoid surrounding the tracker. The main goal of ATLAS is to study the Higgs mechanism and to search for physics beyond the Standard Model, although the collaboration also works on heavy ion physics [104].

The **ALICE** (A Large Ion Collider Experiment) detector is located at IP2 [105]. It is a general purpose detector aiming at a precise study of QCD in extreme conditions, especially via its extended heavy ion physics programme. Its excellent particle identification capabilities permit a fine measurement of multiplicity, energy flow and heavy flavour measurements in ultrarelativistic heavy ion collisions [106].

The Compact Muon Solenoid **CMS** is located at IP5. CMS is a multipurpose detector, aiming first at the precise measurement of Higgs boson properties and couplings with other particles, as well as a search for physics beyond the Standard Model [107]. The central feature of the CMS detector is a solenoid magnet of 3.8 T surrounding the trackers and calorimeters. Its muon chambers are especially precise at measuring muon hits up to the TeV scale with a momentum resolution below 1%. The CMS experiment also has a heavy ion programme (this Thesis is a part of it!), mostly steered towards a detailed study of parton energy loss and heavy flavour physics, but also capable of global heavy ion event measurements [108]. The CMS detector is discussed in more detail in the next Section.

At IP8, the LHC-beauty experiment (**LHCb**) is mostly dedicated to measuring rare physics processes involving b quarks, CP violation and the search for beyond-Standard-Model physics in the flavour sector [109]. There are two specifities in the LHCb detector: First, the detector is fully instrumented in only one side of the interaction point with a dipole magnet around the outgoing (forward) beam

direction. Second, the luminosity leveling ensuring a low (practically *constant*) instantaneous luminosity from beginning to end of a data taking period. This is achieved by the LHC accelerator operators applying a slight transverse offset between the two beams. It also reduces the number of primary *pp* vertices (also known as pile-up), facilitating the tracking of particles, especially important in measuring the flight distances of heavy hadrons. Recently, the LHCb collaboration got more involved with a promising heavy ion physics programme [110].

3.2 CMS

The CMS detector will now be described. Although mainly conceived to detect particles coming from *pp* collisions, it can also perform well in heavy ion collisions, as well as detecting cosmic ray muons. The central feature is a superconducting solenoid magnet operating at 3.8 T, coupled with an iron yoke for magnetic flux return.

3.2.1 General concepts

The CMS detector is placed in IP5 of LHC, in a cavern down an approximately hundred meter deep shaft in Cessy, France. The detector weighs approximately 12.5 tons, is 15 meters in diameter and 21 meters long. Its precise geographical location with respect to the rest of CERN sites can be seen at the top of Figure 3.2.

A schematic view of the CMS detector is shown in Figure 3.3.

The coordinate system used in CMS takes its origin in the nominal collision point at the centre of the experiment, with the y-axis pointing vertically upward, the x-axis pointing towards the center of the LHC 'circle', and the z-axis then pointing along one of the beam directions, namely towards the Jura mountains (or in the counterclockwise direction, when looking from above). The azimuthal angle ϕ is measured in the $x-y$ plane with respect to the x axis. The radial coordinate r is taken in the $x-y$ plane, and the polar angle coordinate θ is measured from the z-axis [107].

Pseudorapidity, the preferred experimental measure for angular position of detected particles, is defined in Equation 3.1.

$$\eta = -\ln \tan\frac{\theta}{2} \tag{3.1}$$

Transverse quantities such as p_T, E_T, and E_T^{miss} are computed in the $x-y$ plane.

The logic behind the detector design is governed by the necessity of measuring large momentum muons with great accuracy. A large bending power is thus necessary, hence the large magnetic field. The magnet is thirteen meters long, its inner diameter is six meters and surrounded by a complex return yoke of more than 1.5 meter thickness of iron in total, with muon stations hitherto embedded.

From the interaction point out, the subdetectors are:

- The tracker system, composed of 3 layers of silicon pixel detectors and 10 layers of silicon microstrips;

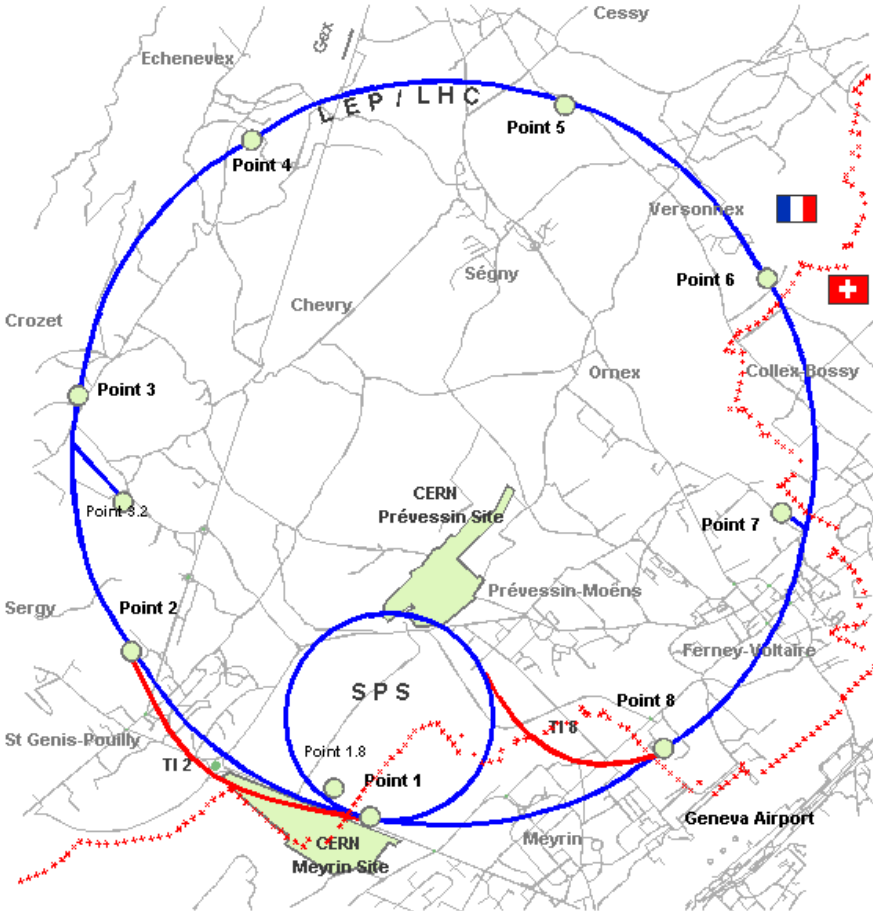

Figure 3.2: Top view of the SPS and LHC, including main CERN sites. CMS is located at Point 5.

- The elctromagnetic calorimeter (ECal), composed of transparent, radiation hard lead tungstate ($PbWO_4$) crystals;

- The hadron calorimeters (HCal), covering the barrel, endcaps and forward regions, and made of a brass/scintillator array of steel and light collection devices;

- Finally, the muon detector is a combination of drift tubes (DT) in the barrel and cathode strip chambers (CSC) in the endcaps, complemented by resistive plate chambers (RPC) in both regions.

3.2.2 Trackers

To achieve most of its physics programme, CMS needs fast and efficient track and vertex reconstruction. The tracking system evolves in high multiplicity environments, either due to the multiple *pp* interactions piling up in a single bunch crossing or due to a single heavy ion collision. The trackers are contained in a cylindrical volume of 5.8

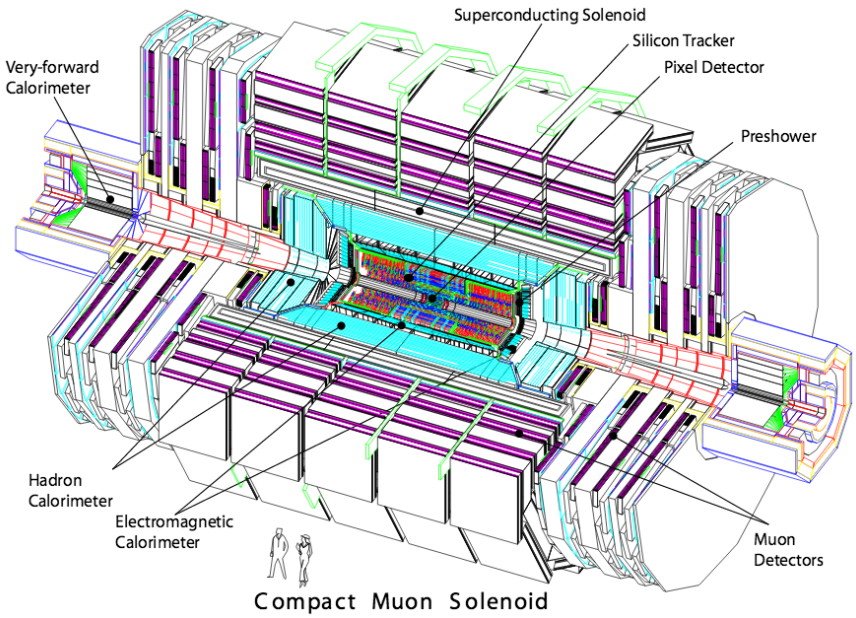

Figure 3.3: Cut-away view of the CMS detector [107].

meters in length and 2.5 meters in diameter.

To cope with the track multiplicity, the number of primary and secondary vertices, a high granularity and quickly responsive system is needed. Although this is achievable by repeating the layers of sensitive material, there is a compromise to be found with the amount of material, to minimise multiple scattering, and the cooling of electronics when the tracker operates, as the whole tracker is plunged in the solenoid magnetic field.

The CMS tracking system is split in two main parts: the silicon pixel detectors and the silicon strip tracker. The closest subdetector to the interaction point is the pixel detector, as can be seen to the center of Figure 3.4.

The Pixel detector comes in 3 layers in the barrel and 2 disks at each endcap. The barrel layers are concentric, within 4.4 to 10.2 centimeters of radius.

The strip tracker has 10 detection layers in the barrel extending outwards, up to 1.1 meter of radius (forming the TIB and TOB subdetectors). Each endcap contains 9 disks of silicon strips (forming the TEC subdetector), and the full system covers the pseudorapidity range $|\eta| < 2.5$.

The Pixel detector is made of 1440 pixel modules, and the strips contain 15148 modules. In total, there is about 200 square meters of sensitive silicon area in the tracker.

Using pixelated cells at radii below 10 cm is necessary for the occupancy of the full system to be kept as low as possible, typically of the order of 1%. The pixel cells are 100×150 square micrometers wide, and the multiplication of layers allows a three dimensional vertex reconstruction in space. In total, the barrel (BPix) and endcaps

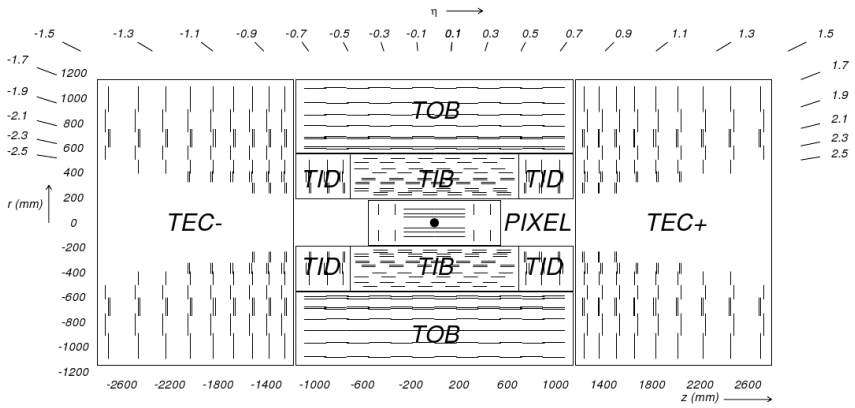

Figure 3.4: Schematic view of the sensitive areas in the CMS tracker system.

(FPix) contain 48 million and 18 million pixels, respectively. The 3.8 T field acts strongly on the Lorentz drift ($\mathbf{E}\times\mathbf{B}$) of electron-hole pairs, resulting in charge sharing between adjacent cells. Adjacent FPix modules are tilted of 20 degrees in a turbine geometry to achieve a spatial resolution of 15 to 20 micrometers [107].

When moving away from the interaction point, the particle flux reduces, allowing the use of micro-strips of variable sizes and pitches, depending on the position (inner or outer, barrel or endcap). The four Tracker Inner Barrel (TIB) and the three Disk (TID) layers (cf. Figure 3.4) are conceived in 320 micrometer thick silicon microstrip sensors of variable pitch, achieving up to 4 $r-\phi$ measurements on a trajectory with a single point resolution of about 30 micrometers. The outer barrel (TOB) and endcap (TEC) layers provide another 6 and 9 $r-\phi$ measurements, respectively, with respective single point resolutions of 35 to 50 micrometers. Figure 3.5 shows some of the performance of the tracker system on muons in a pp collision environment. On the left panel, the resolution of transverse momentum for muons of 1, 10 and 100 GeV/c is displayed *vs.* pseudorapidity. On the right hand side, the track reconstruction efficiency for muons, of 99% percent in most regions, is displayed for the three p_T regimes.

3.2.3 Electromagnetic calorimetry

The electromagnetic calorimeter (ECal) is made of 61200 lead tungstate ($PbWO_4$) crystals mounted side by side in the barrel, plus 7324 adjacent crystals in each endcap, forming a hermetic and homogeneous detector. One of the prime goals of this detector is the precise detection of Higgs bosons decaying to two photons, maintaining a high energy resolution and fine granularity.

The ECal is placed between the trackers and hadron calorimeters of CMS. On Figure 3.6 is shown an ECal crystal and the way they are arranged. The granularity is 360-fold in the ϕ coordinate and 170-fold in $|\eta|$, amounting to a total of 61200 crystals. The light collection occurs at the far end of each crystal, using avalanche photodiodes (APD) in the barrel and vacuum phototriodes (VPT) in the endcaps. One

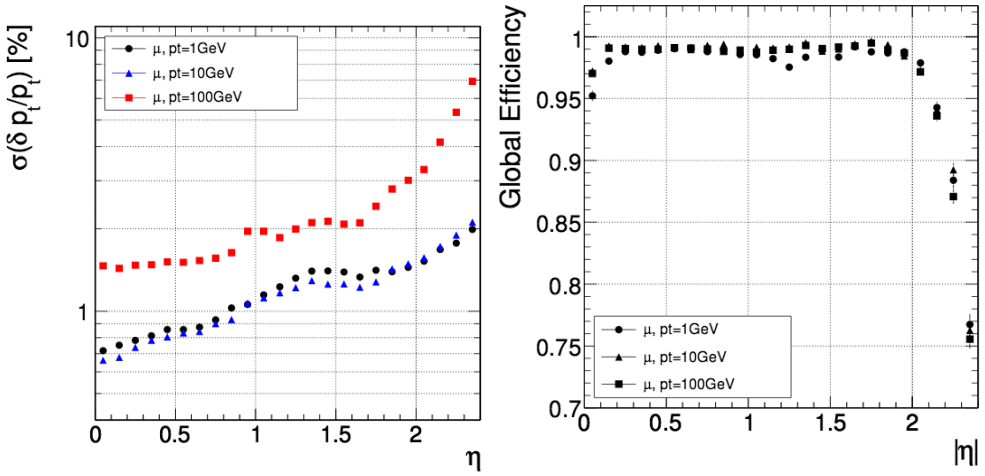

Figure 3.5: p_T resolution (left) and efficiency (right) for single muons reconstructed with the tracker system of CMS [107].

endcap crystal apppended with its VPT is displayed on the left of 3.6. The scintillation properties of the crystal are expected to decrease with radiation damage over the years of CMS operation, and a dedicated laser injection system was put in place to track and correct the crystals ageing.

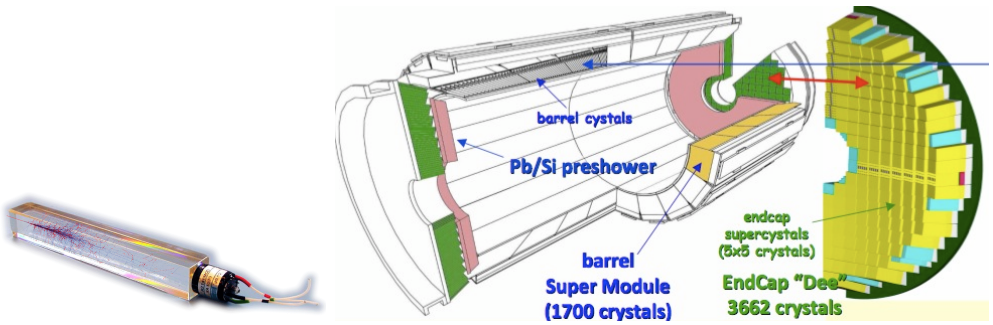

Figure 3.6: Features of the electromagnetic calorimeter of CMS. Left: artistic view of a particle shower in a forward ECal crystal, with VPT collector downstream. Right: cut-away overview of the full ECal.

The $PbWO_4$ crystals have a density of 8.28 g/cm^3, a high refractive index of $n = 2.29$ at peak wavelength and emit blue-green scintillation light (420-430 nanometers). At room temperature, the light output is low: 4.5 photoelectrons per MeV, uniformly over the 23 centimeter length of the crystal.

The ECal energy resolution is computed as a function of electron energy as the sum of a stochastic term (S), a noise term (N) and a constant term (C), as defined in

Equation 3.2. The resulting energy resolution is shown in Figure 3.7.

$$\left(\frac{\sigma(E)}{E}\right)^2 = \left(\frac{S}{\sqrt{E}}\right)^2 + \left(\frac{N}{E}\right)^2 + C^2 \tag{3.2}$$

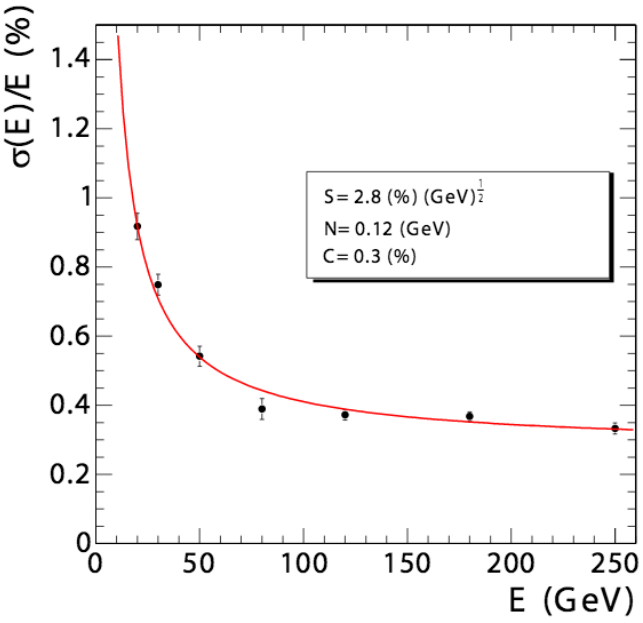

Figure 3.7: ECal energy resolution as a function of electron energy [107].

3.2.4 Hadronic calorimetry

Hadron calorimetry plays an important role in the measurement of jets, total energy deposits, or in the detection of specific topologies as two forward energy jets with a large empty region between the two (known as a *rapidity gap*). The HCal of CMS is contained between the ECal and the magnet coil, as is shown in Figure 3.8.

The barrel section of the HCal (HB) is covering the pseudorapidity range $|\eta| < 1.3$. It consists of 36 azimuthal wedges of absorber forming two half barrels (HB+ and HB-) inserted from each side of the magnet, combined with a plastic scintillator divided in 16 η regions. Each wedge is composed of an innermost stainless steel plate, a sampling of scintillating plastic tiles and flat absorber plates made of brass (70% Cu, 30% Zn), a steel back-plate and a wavelength shifting fibre exiting the wedge downstream of particle propagation.

Outside the vacuum tank of the solenoid stands the outer HCal (HO) 'tail-catcher', adding further sampling depth to the HB and identifying late starting hadron showers.

The endcap HCal (HE) covers the range $1.3 < |\eta| < 3$, a large region containing 13.2% of the solid angle. The total 300 tons of brass were produced from the decommissioning of over a million World War II shell cases from the Russian navy, as is shown in Figure 3.9, completed with 1 million dollars worth of American copper [111].

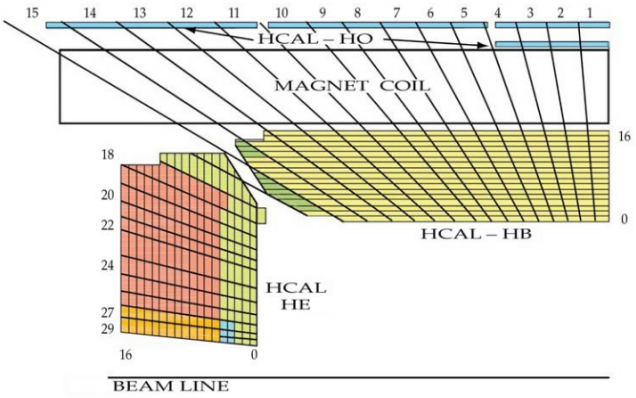

Figure 3.8: Hadron Calorimeter of CMS (HCal).

Figure 3.9: Russian navy shells re-used in the CMS Hadron Calorimeter.

The forward section of the HCal (HF) spans over 40% of the available phase space in CMS, in $3 < |\eta| < 5$. It was designed to sustain unprecedented particle rate (10^{11}) and energy deposit (over 700 GeV in pp collisions, and over 4 TeV in central PbPb collisions [47]). A schematic view of the HF is presented on Figure 3.10. The steel absorber is sampled with quartz fibres that are insensitive to neutrons and produce Cherenkov light guided towards the photomultipliers (PMTs), shielded behind 40 centimeters of steel, concrete and polyehtylene.

The HF can help tag forward jets, as well as measure a global event activity, particularly useful in heavy ion collisions. The HF can be used to infer the mean number of interactions per bunch crossing, the luminosity in real time, and the centrality of a PbPb collision, as we shall see in the next Chapter, Section 4.3.3.

Continuing to more forward directions, at $|\eta| < 8.3$ there are the Zero Degree Calorimeters (ZDC). Located at 140 meters on every side of the CMS detector, these calorimeters are made of tungsten sampled with quartz fibres, having the ability to measure neutral and charged particles scattered at very small angles in diffractive pp

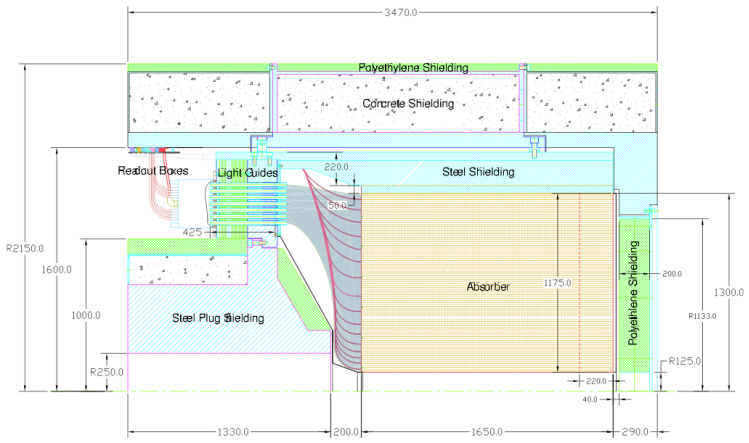

Figure 3.10: Cross section view of the HF calorimeter. The absorber is encased in steel and polyethylene shielding, and each tower is connected to light guides and PMTs situated 13 meters away from the beamspot (to the right) [107].

processes, as well as to reconstruct the energy carried by spectator neutrons with a resolution of 10%.

3.2.5 Muon chambers

The muon system in CMS is a crucial part of many measurements. Particles are detected via a preferred signature often including at least a muon, as in the case of quarkonium or heavy flavour decays. In another energy range, the SM Higgs decaying to two Z bosons would produce a 4 lepton decay, and the 4-μ channel was effectively detected with the CMS muon detectors. Even higher in energy, the search for new heavy dimuon resonances may unveil particles at the TeV scale, requiring an efficient and high-resolution measurement at such muon momenta.

As can be seen in Figure 3.11, the magnetic field geometry is particularly complicated, with large **B** gradients inside and around the return yoke (left part of the image: field intensity), causing the field lines to curve back in the region where muon stations are located. This delicate geometry over a wide volume calls for a very high quality measurement of the position and orientation of outgoing muons, as well as a highly reliable alignment of all subdetectors.

CMS uses three types of gaseous detectors to ensure muon triggering, identification and reconstruction. With 25 000 square meters of sensitive material, the muon chambers cover the barrel and endcap region with up to 4 layers of muon stations embedded in the magnet's iron return yoke. The muon stations are arranged in wheels around the solenoid and HCal endcap regions, in the pseudorapidity range $|\eta| < 2.4$.

In the barrel region, the muon stations (in blue on Figure 3.12, left) combine Drift Tubes (DT) stacked with Resistive Plate Chambers (RPC). In the endcaps, the RPC are combined with Cathode Strip Chambers (CSC) (in pink on Figure 3.12, right).

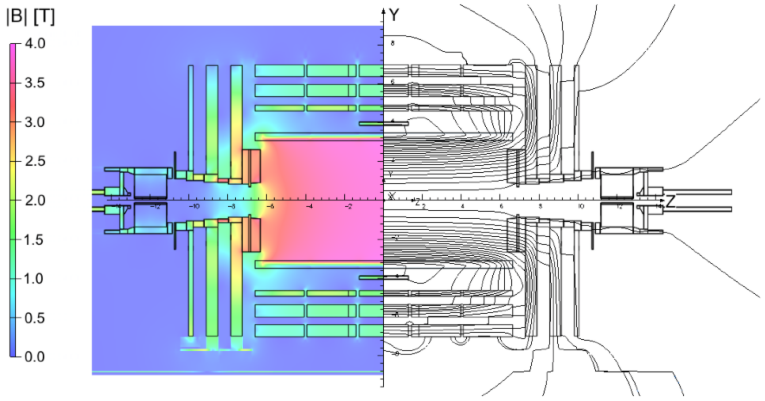

Figure 3.11: Magnetic field intensity and field lines in CMS. Only insensitive material is displayed [112].

The DTs cover the pseudorapidity range $|\eta| < 1.2$ in 4 cylindrical stations, embedded in wheels of the flux return plates. The three innermost DT stations have 60 drift chambers and the outer has 70. There are about 172 thousand sensitive wires of 2.4 meters each, over the full drift chambers. These are used as tracking detectors for the barrel muon system.

The interplay between RPC/DT, and CSC/DT subsystems can be clearly seen in Figure 3.13.

A DT chamber comprises two or three independent blocks, called SuperLayers (SL), of 4 layers of rectangular drift cells, separated by a honeycomb plate. The whole SL+honeycomb+SL system is inbetween RPC plates. The full DT-RPC set are encased together in the iron yoke, but act independently. The inner SL measures the ϕ position where a muon entered the chamber. The muon then passes through the honeycomb, reaches a second SL measuring z (always present in the 3 innermost stations, never in the fourth station). The third SL is parallel to the first SL (and perpendicular to the second, if there is one) and measures the ϕ position again.

In each SL, 4 layers of drift cells help having enough redundancy in the muon tracking. Each layer has a slight horizontal offset with the next, to ensure a high coverage over the full SL surface. Every DT cell represents a 1.5 mm material wall for the muon to pass through, which is enough to decouple the measurement of the muon energy deposit in each layer. The honeycomb (which is just a lightweight object used for spacing between the SLs), yields an improved angular resolution. In total, there are up to 8 ϕ points and up to 4 z points, giving the muon track a 95% efficiency in all of the barrel region, and a 100 micrometer position resolution with only one chamber, up to $p_T = 200$ GeV/c. The DT chamber (with RPC system not detailed) design is shown in Figure 3.14, left. The information from SL is combined in the first level of the trigger system, with RPC timing information, to get a precise beam-crossing time coincidence, position and momentum resolution, as we shall see in Section 4.1.

The gas mixture inside a drift cell is 85% argon, 15% carbon dioxide. The drift cell

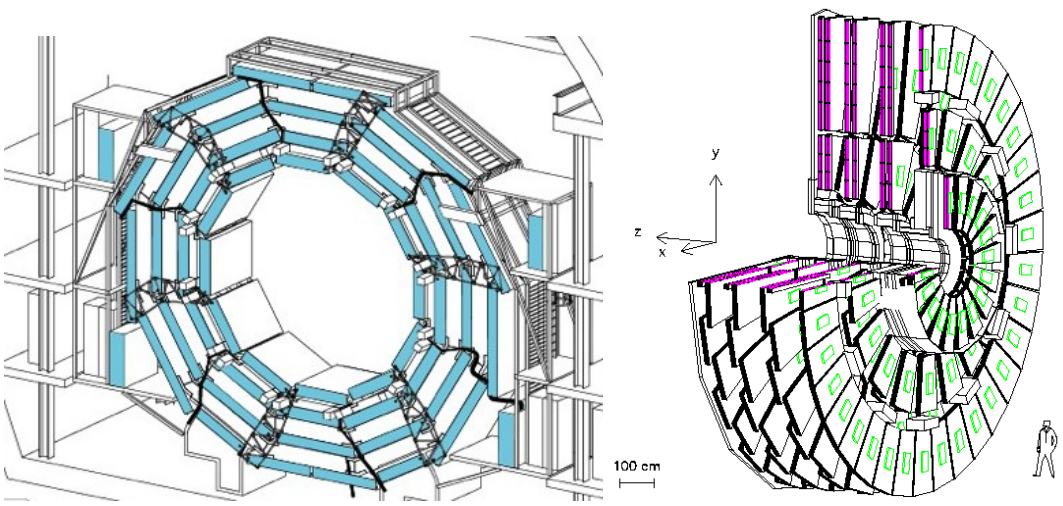

Figure 3.12: Barrel and endcap muon station wheels. Active material is displayed in colours. The reference axes belong to the right hand side figure [112].

contains a 50-μm-diameter gold plated anode wire, two 50-μm-thick aluminium tape acting as electrode on top and bottom, 23 mm of insulating mylar tape, and a cathode made of 50-μm-thick aluminium foil, insulated from the next cell with a 100-μm-thick mylar tape layer. The full drift cell design is laid out in Figure 3.14, right.

In the endcap regions of CMS, the muon rates and background levels are higher; There, CSC provide a radiation resistant solution, with fine segmentation and fast response time. The CSCs cover the range $0.9 < |\eta| < 2.4$. The endcap wheels being perpendicular to the beam line, the CSC strips are in the radial plane and provide a precise measurement in the $r - \phi$ plane. The anode wires are perpendicular to the strips, and their readout provides a pseudorapidity measurement and the coincidence of the muon passing through with its beam-crossing time. All six CSC layers informations are used in pattern recognition for non-muon rejection and provide a helpful anchor point for matching between stations and tracker hits.

The CSCs are multiwire proportional chambers (MWPC), containing 6 anode wire planes interleaved with 7 cathode panels. The schematic CSC design is shown in Figure 3.15 (left). The wires are aligned in azimuth and used to get the radial coordinate. Strips are carved into cathode panels aligned at constant $\Delta\phi$ width. The muon ϕ coordinate is then obtained by collection of ionisation charge on the cathode strips close to where the muon passed. The repeated measurement of charges collected over the six planes of strips can be correlated to measure unambiguously the trajectory of the muon, as is shown in Figure 3.15 (right).

Over the two endcaps, 540 CSC chambers are deployed in 2 times 4 disks (or stations), covering an active area of 6 000 square meters, and overlapping in ϕ and η to reduce dead regions. The CSCs count 2.5 million wires total. Although the CSC system is very precise, it is also relatively slow: full charge recollection can take up to

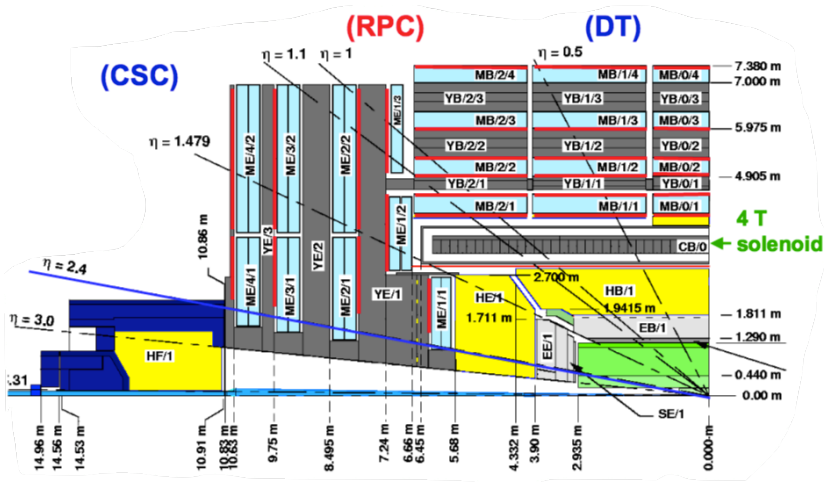

Figure 3.13: Cross section view of the CMS detector, highlighting the muon detectors: RPCs are red, DT are in blue in the barrel wheels and CSC are blue in endcap wheels.

300 nanoseconds. The data acqusition chain is detailed in [107].

In the initial design of the LHC and CMS, the actual nominal luminosity and muon rates were not well known. To overcome the possibility of saturated muon chambers, a third system was added. The RPCs provide a fast and independent measurement of the muons, with a sharp momentum threshold, very useful in triggering on the proper muon-beam-crossing combinations. RPCs are double gap chambers surrounding the DT or CSC modules, also helpful to resolve ambiguities when multiple track-hit combinations are formed at the track reconstruction step.

A RPC is capable of tagging the muon ionisation time faster than 25 ns, making it an efficient first level muon trigger.

At present, there are two layers of (double gap) RPC chambers in the two inner stations, and one RPC chamber per outer muon station. In the barrel region, the RPCs thus form 6 coaxial cylinders around the beam axis. Chambers are approximately 2 meters long and their widths vary from 1.5 to 2.5 meters. As seen in Figure 3.14, the innermost barrel RPCs surround the DT chambers, while for the two outer stations they are placed before DT chambers.

The double gap structure is detailed here: two strips of bakelite (in red in Figure 3.16 left), a highly resistive plastic material, are placed 2 millimeters away from each other and operated at high voltage (9 kV). Between the bakelite layers a gas mixture of tetrafluoroethane, tetraprotonated ethane ($C_2H_2F_4$ and C_2H_{10}) and water vapour is inserted. The full system operates in avalanche mode (quick appearance of current flow after a muon passes through). When the muon passes inside the RPC gaps, copper strips (on top of Figure 3.16 left) collect charges within 1 nanosecond. The system described here represents a single gap: the double gap is obtained by duplicating the system, improving dramatically the charge collection for minimally ionising particles

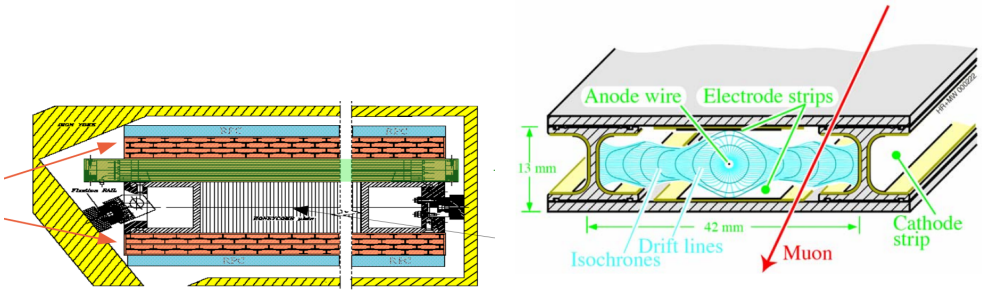

Figure 3.14: Drift Tube chamber and cell design. Left: full DT chamber design, including iron yoke (yellow), and RPCs (blue), $r-\phi$ Super Layers (in red and pointed by red arrows), fixation rail and honeycomb (black), $r-z$ Super Layer (green). Each SL contains 4 layers of DT cells. Right: design of a single DT cell. High voltage of -1.2, +1.8, +3.6 kV is applied to cathode, strips and wires, respectively.

such as muons.

To minimise further the time taken to readout information from RPCs, the double gaps are lined up two by two in a RPC plane, with a front-end readout board running in the middle, along the closest side of the RPC to the interaction point and perpendicular to the beam line. For example, the z axis displayed in the schematic design of Figure 3.16 (right) shows the beam line direction, and points toward the beamspot.

Endcap RPC chambers do not differ a lot from the structure outlined here: placed around or upstream of CSCs, the chambers are also consisting of double-gap bakelite-and-strip gas chambers. There size is trapezoidal to fit in the endcap wheel, and the strip run radially.

In this Chapter, details of the LHC machine were presented. This particle collider of an unprecedented scale is equipped with four large experiments. The Thesis presented here relies on data from the CMS experiment, whose prime asset is the fast and efficient muon subdetector equipment. The CMS experiment was originally designed to detect rare events in pp collisions, but proved efficient in heavy ion environments as well. This ability will be covered in Chapter 4.

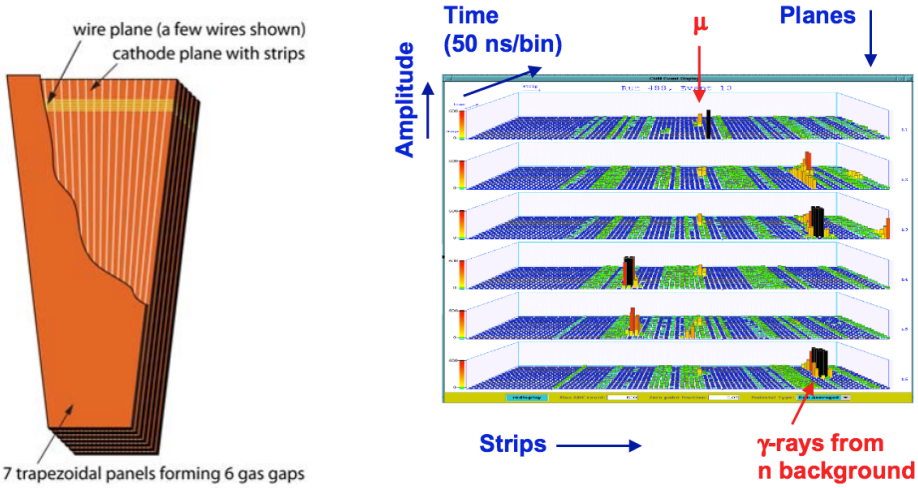

Figure 3.15: CSC schematic design, and effect of background and muon signals on charge collection. The muon track path can be seen passing in the middle of all 6 planes, with surrounding spurious spikes identified as background.

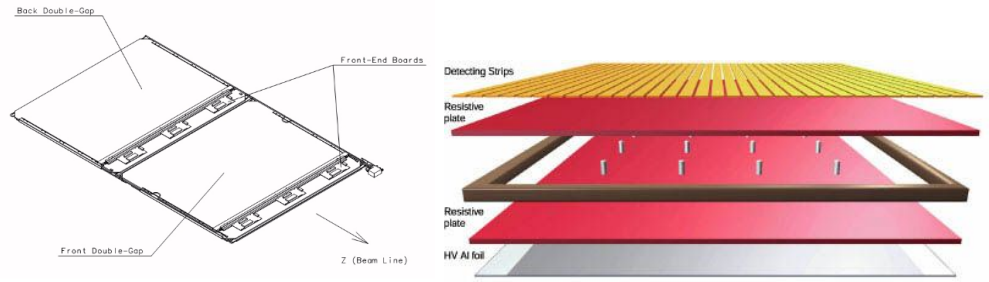

Figure 3.16: RPC system outline. Left: schematics of a barrel RPC chamber, as described in text. Right: exploded view of subparts of a RPC, gas is trapped between the two bakelite (red) layers [113].

Chapter 4

Muon triggering and reconstruction

Contents

On est à une époque où toutes les connaissances sont accessibles si l'on s'en donne la peine : la difficulté est de trier, sélectionner, savoir où aller.

Cédric Villani, in *Les scientifiques doivent reprendre la main sur le partage des connaissances*, interview for Sciencespourtous.univ-lyon1.fr

In this section we will see how CMS selects and processes collision events delivered by the LHC.

The multipurpose experiments CMS and ATLAS have primarily been built to explore physics up to the TeV scale, the Higgs boson discovery being one example [114]. Other high precision measurements are at stake in the electroweak sector, on the t and b quarks, as well as on QCD in extreme regimes. Some processes are extremely rare

or not discovered, yet every analysis needs a dedicated selection, from raw data to the latest stages of the analysis. One example from heavy ion physics: the Υ(3S), although well measured in e^+e^-, pp, $p\bar{p}$ and pA collisions, is so suppressed that it is not observed at this point in heavy ion collisions, and its nuclear modification is only expressed in the form of an upper limit on the total PbPb sample (all centralities involved) [4].

The Υ(3S) decaying to two muons may be a simple signature, it is nonetheless a detection challenge in a heavy ion environment. To get an idea of what is the heavy ion multiplicity, we can for example consider that in the 5% most central PbPb events at $\sqrt{s_{NN}} = 2.76$ TeV, CMS measured in 2010 a charged hadron density per unit pseudorapidity of $dN_{\mathrm{ch}}/d\eta|_{\eta=0} = 1612 \pm 55$ (*syst.*) [47]. The centrality in heavy ion collisions will be covered later (Section 4.3.3), however, this simple measurement informs us on the main difficulty encountered when measuring harder and rarer probes: they are produced on top of an overwhelming background of tracks that can cause the performance of the detector to degrade.For this reason, a dedicated triggering strategy is indispensable to maintain good event quality throughout analysis.

The architecture and strategy of dimuon triggers for Υ used in this Thesis are detailed in Section 4.1. The muons are reconstructed and further filtered offline, based on quality requirements that are presented in Section 4.2. In parallel of most physics analyses, a more general event selection is needed, to get an estimate of the luminosity of the pp and PbPb samples. Section 4.3 will present how the number of hadronic events are counted in CMS, and how the global selection is engineered to extract an information on the centrality of the PbPb collision.

4.1 Triggers

From its startup in 2009, the LHC has gradually increased its instantaneous luminosity with time, almost reaching the nominal value of 10^{34} cm^{-2} s^{-1}, or 100 nb^{-1} s^{-1}. At the design luminosity of the LHC, the beam crossing frequency in each experiment is 25 ns. Under these conditions, each experiment is delivered up to 10^8 individual collisions. The input rate of computing farms reconstructing data must be reduced down to the order of less than 1 kHz, and several trigger levels are deployed in CMS to achieve this task.

4.1.1 The Level 1 Trigger

The first trigger level of CMS, called L1 [115], is a trigger system relying on hardware, meaning that it takes decisions upon looking at raw data from the custom front end readout electronics.

Its main challenge is to reduce the flow of events CMS processes from the level of the collision rate (CR) down to a rate sustainable by the HLT online processing computer farm.

In the nominal settings of the LHC, the collision rate is 40 MHz; in 2012 when the instantaneous luminosity was 2×10^{33} cm^{-2} s^{-1} (2 nb^{-1} s^{-1}), the collision rate was 13 MHz.

The decision to retain or reject an event has to be taken at every bunch crossing, i.e. every 25 ns, under nominal conditions. The L1 trigger rate being limited by detector electronics, the trigger electronics are pipelined and deadtimeless. This is important to treat in a fast manner the Megabyte-sized raw events collected at every beam crossing. Since new collision data arrive every 25 ns, the processing of individual data cannot take more than 25 ns, prohibiting the use of complicated algorithms. The pipelined architecture also requires that decisions about one piece of an event are not based on data located somewhere else in the event, not allowing for example a dimuon invariant mass to be computed. The trigger based operations are simple arithmetic ones, using lookup tables addressing segments of the subdetectors in broad $\eta - \phi$ regions.

The size of the detector cavern and the distance to the trigger electronics places a time limit of 3.2 μs on L1 trigger processing for a single event. Under nominal design, this corresponds to 128 beam crossings. The longest data processing time comes from Muon Barrel drift chambers, whose drift time takes 400 ns before full signal collection. The 3.2 μs time restriction also means that the trigger cannot include ECal preshower or Tracker data in the decision.

The remaining subdetectors (ECal and HCal Barrel plus Endcaps, HF, Muon RPC, CSC and DT) read out event data separately. The architecture of the L1 trigger, described here, is summed up in Figure 4.1. The readout data sent to the Data Acquisition system (DAQ) is bundled in trigger *primitives*.

The Electronic Calorimeter (ECal), the Hadronic Calorimeter (HCal) and Hadron Forward calorimeters (HF) record energy that is summed in 'trigger towers' directly from calorimeter cell energies. The Regional Calorimeter Trigger (RCT) identifies electron, photon, tau, jet candidates and E_T sums, forwards it to the Global Calorimeter Trigger (GCT) which is in charge of sorting the top 4 candidates of each type and calculate total E_T and missing E_T. The information is then sent to the Global Trigger.

Since muons are minimally ionising the calorimeters, the quiet $\eta - \phi$ calorimeter regions can be mapped by the RCT, to be transmitted to the Global Muon Trigger (GMT) for muon isolation cuts.
Each muon subdetector has its own trigger logic.

Resisitve Plate Chambers (RPC) use a projective pattern comparator to form trigger segments from lighting RPC strips. These segments can be connected together to find tracks and calculate their p_T. Since RPC overlap with Cathode Strip Chambers (CSC), the RPC logic is allowed to communicate with the CSC trigger system, which improves the resolve of ambiguities when two muons hit the same CSC.

The CSC form Local Charged Tracks (LCT). The LCTs are assigned a p_T and a quality bit, which are sent to the CSC Track Finder (CSCTF) to sort the best 3 LCTs sector by sector[1]. The CSCTF further combines the LCTs into full muon tracks, and in the region where the CSC overlap with the Drift Tubes (DT), both CSCTF and Drift Tube track finders (DTTF) exchange segment information to improve themselves.

In the barrel, the DT uses a track identifier to match aligned hits in each DT layer into segments matched to a single superlayer (SL). The track segments' positions and

[1] A sector is composed of nine CSC chambers.

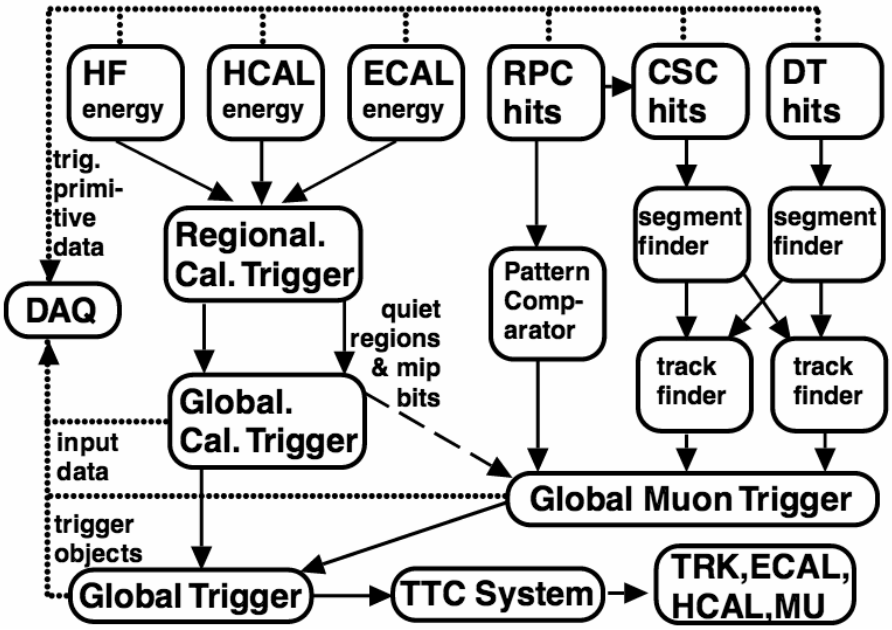

Figure 4.1: Overview of the L1 Trigger architecture [115].

angles are correlated when their ϕ coordinate coincide, and the best two combinations are sent to the DTTF, merging them into full muon tracks assigned with a p_T.

The GMT later receives the best muon tracks from RPC, CSC and DT track finders, sorts them by quality, and the best four muon candidates are sent to the Global Trigger (GT).

Based on GCT and GMT signals, the GT accepts muon and calorimeter candidates, sending L1 Trigger decisions to the Timing Trigger and Control module (TTC) which then communicates back with subdetectors to initiate the readout. The L1 decisions are logical *trigger paths* defined by user and requesting for example:

- The presence of up to four muon candidates, eventually close or far from each other in $\eta - \phi$, above a p_T threshold, in $|\eta| < 2.4$;

- The firing of up to four calorimeter towers above e.g. 30 GeV by electron/photon candidates, in $|\eta| < 2.5$;

The full list of L1 triggering possibilities is detailed in Sections 2.2 and 2.3 of [115]. The above two examples can be used to identify Standard Model physics processes, such as $\Upsilon \to \mu\mu$, $Z^0 \to \mu\mu$, or $H \to \gamma\gamma$, $H \to 4l$, etc. In the same time, some of the 128 L1 trigger bits available can be used to implement global event measurements (geared towards a luminosity estimation), or efficiency measurements (RPC efficiency while triggering on CSC-DT and vice versa).

The LHC will operate at least up to 2035 [116]. In this time, additional computing nodes can be added to the trigger system, as well as network technologies and electronics

can evolve. For these reasons, although the event builder and event filter can perform at 100 kHz (design capabilities [115]), the L1 trigger output rate capability was in 2012 bridled at 50 kHz.

The LHC filling scheme for heavy ions is different to that of *pp* collisions and as a result, the beam crossing time changes to 200 ns. The collision rate is smaller, which is good for the triggers since high multiplicity events are large (the raw event data can exceed 5 Mb). Separately of L1 decisions, the Pixel detector, which is closest to the beam pipe, is under high illumination at every moment. To stay in the bandwidth of the pixel readout system, the L1 output rate is generally limited to 5∼10 kHz.

The output L1 and readout data are sent to the High Level Trigger for refined filtering.

4.1.2 The High Level Trigger

The second and third levels of the CMS trigger system are called the High Level Trigger (HLT). The HLT relies on software algorithms running on an online computing farm of 13,000 commercial CPU cores [117]. The raw output data accepted at L1 is streamed to a subset of the computer farm (L2) which is then sent to the other subset (L3) for further filtering. The data reduction rate, from the L1 output to the HLT output, is of the order of 10^3, i.e., the HLT output rate is of the order of 100 Hz to 1 kHz. The size and processing time of events is again an important limiting factor, especially in the case of heavy ion data, where the multiplicity of tracks is huge. In order to maintain a smooth transfer to the Tier0 storage system, both the L1 and HLT rates have to be kept within the bandwidth (of the order of 1 Gb/s).

The HLT relies on more refined algorithms than L1 to decide if the event should be kept. The $\sim$ 200 paths of a total typical HLT menu are run in parallel in the computing farm, using data from all subdetectors to proceed to a first reconstruction of the physical objects (muons, electrons, taus, missing energy). This online reconstruction is a streamlined copy of the offline reconstruction, and kept only to regions of the event where the physical object of interest is defined, to save computing time.

The various HLT paths can be seen as non exclusive streams, meaning that all data accepted under a certain condition at L1 *seeds* one or many HLT paths. Several HLT paths can originate from the same L1 seed.

In the following, I will focus on muon trigger sequences: other reasonings apply to e/γ triggers, as their L1 seeds originate from other parts of CMS.

The HLT path used in the case of Υ decaying to two muons is a dimuon HLT path, seeded by a dimuon L1 seed. A HLT path is a sequence of reconstruction and filtering modules, developed by the user or the analysis group, for the needs of a physics analysis or an efficiency estimation. The HLT path sequence begins with the L2 reconstruction sequence, using the L1 seed and digitised readout from the CSC, RPC and DT to construct a *standalone* (STA) muon, based solely on muon detector informations. The STA muon is of usually poor resolution. The L2 reconstructed object is optionally filtered for some quality requirements (on the muon chamber hits) or kinematics (η, p_T cuts). If the event does not pass the filtering step, it is discarded and will not be sent

to L3.

The L3 step uses the L2 output STA muon as seed to an outside-in reconstruction, involving the digitised data read out of the pixel detector and silicon trackers. The reconstruction sequence can either stop here and proceed to final filtering, or extend to include an inside-out refitting of the muon track and STA global object. Filtering cuts on the L3 level resemble that of L2, to the exception that the resolution is improved with the input of the tracker information, and cuts can also apply to the tracker part. Additional cuts on the four-momentum of a dimuon system can be computed, for example on impact parameter, mass or transverse momentum.

In the preparation of a physics analysis, one should always develop at least one control trigger, dedicated to efficiency studies of the various trigger steps involved the 'physics' trigger(s). In the case of dimuon triggers, one way to assess the various levels of reconstruction is to prepare single muons triggers essentially following the same selection at L2 and L3 as the dimuon trigger. One can also develop a L2 single muon trigger and a L3 single muon trigger to understand the efficiency of the matching of L2 and L3 objects.

In cases when the rate expected for a certain trigger (for physics or efficiency) gets too high, either because of the collision rate or because of the loose requirement of the trigger, one can apply a prescale factor k, such that at HLT processing, only one event out of k events firing the L1 seed will be processed.

In the following, we will see in what conditions the detector was operated for the 2011 PbPb collision run.

4.1.3 Settings for the 2011 PbPb run

To measure hard probes such as quarkonia in PbPb collisions, the requirement that a hadronic event occurred is important to remove ultra-peripheral events, beam-gas interactions and other beam remnants. This is implemented at level-1, with the requirements that enough energy deposits in both sides of the HF are coincident with the hard event of interest. This global event selection will be further detailed in Section 4.3, and the rest of the subsection is dedicated to beam and detector settings for the 2011 PbPb data taking, with a focus on the dimuons of interest in this Υ analysis.

In a typical heavy ion LHC fill of 2011, for example fill 2328, the filling scheme was:

`200ns_358b_356_336_0`

This means that the bunch spacing was 200 ns, 358 bunches were injected, 356 were distributed to IP1/5 (i.e. ATLAS and CMS), 336 were distributed to IP2 (ALICE), and none to LHCb. At 200 ns bunch spacing, the L1 and the detector electronics face a collision rate of 5 MHz, which is well below the limits of what the hardware trigger can handle.

Under these conditions, the L1 trigger is set to handle an instantaneous luminosity scenario of 10^{28} cm^{-2} s^{-1} (10 mb^{-1} s^{-1}) maximum.

Again using the example case of LHC fill 2328 (CMS run number 182572), which is comparable to other runs of the 2011 data taking, the luminosity at starting time

of the run was 470×10^{27} cm^{-2} s^{-1} (4.7 mb^{-1} s^{-1}). The L1 output rate was 1483 Hz, indicating that only a small amount of filtering would be needed at further levels. The run lasted for approximately seven hours, with an instantaneous luminosity of 153×10^{27} cm^{-2} s^{-1} (1.53 mb^{-1} s^{-1}) at the time of the beam dump. The integrated luminosity delivered to CMS for this run was 5.76 µb^{-1}, representing about 3% of the total luminosity delivered to CMS in the PbPb run of 2011. The integrated luminosity recorded by CMS was 5.64 µb^{-1}, which represents a 98% data taking efficiency.

The L1 seeds for our dimuon triggers are 'open', in the sense that they do not cut on the p_T of the muons or that of the dimuon, and retain every event identified as a dimuon candidate by the GMT and GT. In our case, calorimeter based isolation is not used. The L1 seed is called `L1_DoubleMuOpen_BptxAND`. The BPTX suffix is here to denote that the dimuon L1 signal is coincident with the signal rise time of beam position monitors (Beam Position and Timing for LHC eXperiments, BPTX [118]) . This *gating* was implemented during the run to remove the cosmic ray contribution to the L1 dimuon rate.

In the same run as considered previously (number 182572), the L1 rate for the path `L1_DoubleMuOpen_BptxAND` started at about 95 Hz, down to 35 Hz at dump time. The rate *vs.* time can be seen in Figure 4.2 (left).

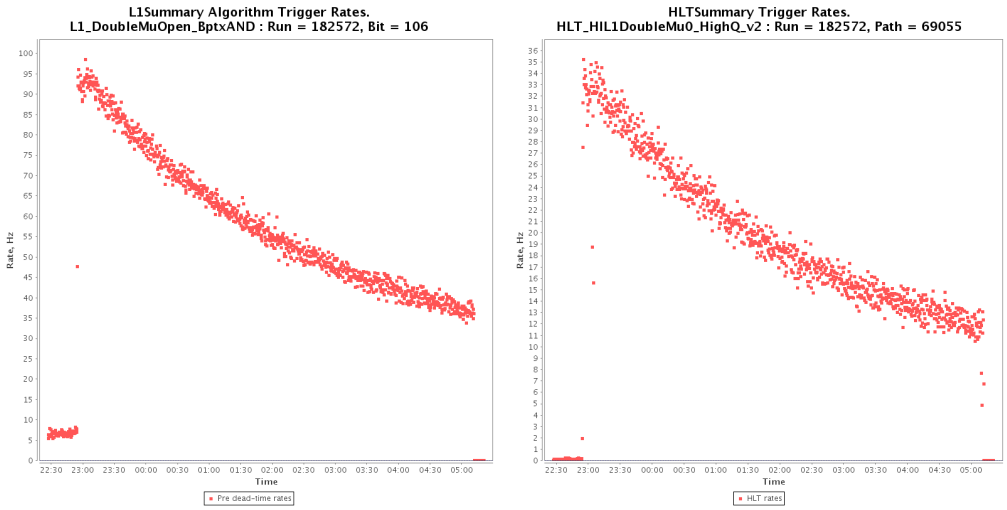

Figure 4.2: Rates of the open dimuon trigger in the 2011 PbPb run. Left: rate of L1_DoubleMuOpen_BptxAND; Right: rate of HLT_HIL1_DoubleMu0_HighQ.

Thanks to the low rate at L1, a reasonable HLT rate could be maintained in the muon 'menu' at HLT. Four dimuon HLT paths based on `L1_DoubleMuOpen_BptxAND` were configured, all of them unprescaled (i.e. no L1 event is skipped, $k = 1$). Their

names are:

`HLT_HIL1_DoubleMu0_HighQ`

`HLT_HIL3_DoubleMuOpen`

`HLT_HIL2_DoubleMu3`

`HLT_HIL3_DoubleMuOpen_Mgt2_OS_NoCowboy`

The four HLT paths have different levels of filtering, as well as rate, and efficiency. The HighQ suffix in the first path is a Level-1 quality bit cut. The L1 muons are assigned a quality bit depending on their status in muon subdetectors; in this case, the quality bits of L1 muons are the following:

bit 0 **(rejected)** - Empty muon candidate;

bit 1 **(rejected)** - Halo muon for alignment;

bit 2 **(rejected)** - Very Low Quality Type 1, skipped in single and di-muon triggers;

bit 3 **(rejected)** - Very Low Quality Type 2, skipped in single muon triggers;

bit 4 **(rejected)** - Very Low Quality Type 3, skipped in di-muon triggers;

bit 5 **(kept)** - Candidate muon detected in DT and/or CSC, but not confirmed in RPC;

bit 6 **(kept)** - Candidate muon detected in RPC, but not confirmed in DT and/or CSC;

bit 7 **(kept)** - Candidate muon detected in RPC and DT, or in RPC and CSC.

The 'HighQ' decisions are highlighted in bold, to exclude halo muons used for alignment and calibration, as well as very low quality or empty muon candidates.

`HLT_HIL3_DoubleMuOpen` has basically no filtering specific to L2 and L3; however the online reconstruction chain is done up to L3. Such a trigger can be useful in express streams (i.e. immediate reconstruction to check the quality of recorded data), or for timing of the full reconstruction chain.

The L2 trigger `HLT_HIL2_DoubleMu3` has a cut on each L2 muons of p_T =3 GeV/c. This trigger is not used in quarkonia, as it would discard a lot of events in the forward region (where the p_T reach of J/ψ can be extended to zero, interesting if one wants to measure charmonium regeneration in heavy ions). It is however a useful trigger for the Z boson, since the rate is reduced compared to the open trigger.

The L3 trigger `HLT_HIL3_DoubleMuOpen_Mgt2_OS_NoCowboy` attempts to remove events where muons bend towards each other, in the x-y plane. Such dimuon events are called 'cowboys', and can have a lower efficiency, since they would often cross each other in the first muon station at low p_T, lowering the track matching efficiency. This trigger also cuts on opposite sign muon pairs, with an invariant mass above 2 GeV/c^2.

Typical HLT rates of the 2011 PbPb runs are taken from run 182572 and presented in Table 4.1. The table reports the maximal rate (at the beginning of the physics run),

the average rate, and the fraction of the total HLT output (computed by dividing the average rate and the average HLT total rate of 239 Hz).

HLT path	Max (Hz)	Avg. (Hz)	% of total HLT
HLT_HIL1DoubleMu0_HighQ	35	18	7.5%
HLT_HIL3_DoubleMuOpen	23	12	5%
HLT_HIL2_DoubleMu3	11	5	2%
HLT_HIL3_DoubleMuOpen_Mgt2_OS_NoCowboy	7	3	1.25%

Table 4.1: HLT rates for dimuon triggers in the PbPb data taking of 2011. Columns report the total rate, average rate, in Hz, and the fraction of total HLT rate.

These triggers are meant for physics and need to be backed up with efficiency triggers. The list of active single muon triggers for efficiency studies is reported here:

HLT_HIL3_Mu3

HLT_HIL2_Mu3_NHitQ

HLT_HIL2_Mu7

HLT_HIL2_Mu15

Each single muon trigger starts with a L1 seed called L1_SingleMu3_BptxAND. This seed requires that each L1 candidate has a p_T of more than 3 GeV/c.
The L3 path HLT_HIL3_Mu3 is constructed along requiring at every level that the L2 or L3 object has a p_T above 3 GeV/c.

The L2 path HLT_HIL2_Mu3_NHitQ applies a prefilter on the L1 object prior to reconstruction, requesting the L1 to contain at least one muon chamber hit. The L2 reconstruction sequence further requires that the L2 muon track is reconstructed from at least 2 hits.

The L2 path HLT_HIL2_Mu7 does not apply strict requirements on the number of hits further than what the L2 reconstruction sequence asks for, but the p_T of the L2 muon has to exceed 7 GeV/c to pass, which is useful in Z boson efficiency studies.

The L3 path HLT_HIL2_Mu15 has the strongest p_T requirement, of 15 GeV/c. This requirement is useful to record muons coming from Z bosons, as well as W bosons.

The rates of single muon paths are reported in Table 4.2. The table reports the max rate (at the beginning of the physics run), the average rate, and the fraction of the total HLT output (computed by dividing the average rate and the average HLT total rate of 239 Hz).

4.1.4 Monitoring of the 2013 *pp* run

I have participated to the *pp* and *p*Pb data taking run of 2013 and have done some service work on the monitoring of the muon triggers. Some of these triggers are used

HLT path	Maximum rate (Hz)	Average rate (Hz)	% of total HLT
HLT_HIL3_Mu3	99	51	21%
HLT_HIL2_Mu3_NHitQ	97	50	21%
HLT_HIL2_Mu7	26	13	5.5%
HLT_HIL2_Mu15	9.5	4	1.8%

Table 4.2: HLT rates for single muon triggers in the PbPb data taking of 2011. Columns report the total rate, average rate, in Hz, and the fraction of total HLT rate.

to record the *pp* data used in this thesis.

The proton-proton run of 2013, at the centre-of-mass energy of $\sqrt{s} = 2.76$ TeV, was recorded from LHC fill 3555 to 3564, between February, 11^{th}, 2013, and February, 14^{th}, 2013.

In the following Table 4.3, the run conditions of the *pp* data taking are presented: LHC Fill, CMS run number, initial instantaneous luminosity, L1 average accept rate, HLT average accept rate. The collision rate varied from 100 kHz to 5 MHz, because of the increase bunch filled in the LHC for each fill.

LHC Fill	CMS run	Max $\mathcal{L}$ ($\times 10^{30}$ cm^{-2} s^{-1})	L1 rate (kHz)	HLT rate (kHz)
3555	211739, 211740	4	14	0.72
3556	211752	55	28.5	1.09
3557	211760	123	44	0.96
3558	211765	141	73	1.60
3559	211765	135	41	1.55
3560	211797	143	54	1.75
3564	211831	117	53	1.84

Table 4.3: Run conditions for the *pp* data taking in 2013, at $\sqrt{s} = 2.76$ TeV.

The total HLT rate is composed at $\approx 30\%$ of data reserved for alignment and calibration purposes. The actual rate of physics triggers did not exceed 1 kHz.

The muon triggers deployed during the 2013 runs contain equivalents to the 2011 paths, as well as new additions, overlapping with the 'jet physics' menu. The list of L1 muon and dimuon paths active for quarkonia and electroweak probes[2] during the run is detailed below:

L1_SingleMu3

L1_SingleMu7

L1_SingleMu12

L1_DoubleMuOpen_BptxAND

[2]Paths related to B mesons, jets and ultraperipheral quarkonia are not included in the list.

The HLT paths seeded by these L1 paths are reported next:

HLT_PAMu3
HLT_PAMu7
HLT_PAMu12
HLT_PAL1DoubleMuOpen
HLT_PAL1DoubleMu0_HighQ
HLT_PAL2DoubleMu3

The single muon paths were seeded with the L1 path of same p_T threshold, and the double muon paths all originate from the only double muon L1 seed.

Typical HLT rates of the *pp* runs are taken from run 211797 and presented in Table 4.4. The table reports the max rate (at the beginning of the physics run), the average rate, and the fraction of the total HLT output (computed by dividing the average rate and the average HLT total rate of 1.751 kHz) of muon and dimuon paths.

HLT path	Maximum rate (Hz)	Average rate (Hz)	% of total HLT
HLT_PAMu3	763	498	29 %
HLT_PAMu7	69	40	2.2 %
HLT_PAMu12	7	3.6	0.2 %
HLT_PAL1DoubleMuOpen	100	58	3.3 %
HLT_PAL1DoubleMu0_HighQ	49	29	1.7 %
HLT_PAL2DoubleMu3	16	9	0.5 %

Table 4.4: HLT rates for dimuon triggers in the PbPb data taking of 2011. Columns report the total rate, average rate, in Hz, and the fraction of total HLT rate.

We can see in Table 4.4 that the total muon rate accounts for about 36 % of the total recorded data. While the average HLT output rate is high, let us recall that about 30 % of the HLT rate does not go to the physics-oriented reconstruction, and is used for alignment and calibration of subdetectors. Additionally, the CPU load was kept reasonable throughout the processing, at an average of 27 % of the total available bandwidth, benefitting from the small number of HLT paths processed and the small size per event.

In the muon dataset, at an average total rate of 600 Hz, the average file size is 100 kilobytes per event. This information can be retrieved from web based monitoring servers recording statistics on data quality and processing rate.

At the beginning of a *pp* run, the total muon rate (dominated by the single muon triggers) could go up around 800 Hz alone. This is high, however, looking at the file size per event, we can compute the bandwidth occupied by raw muon data in the HLT stream, which is 80 Mb per second. This is well below the limits of the HLT stream

to storage centers (on the order of 1 Gb/s) and gave us confidence in maintaining high rates.

In the muon trigger HLT menu, the fact that various HLT paths come from a common L1 seed will induce correlations between the firing of HLT paths. For example, a muon of $p_T = 9$ GeV/c will fire the L1 seed `L1_SingleMu3`, which would then fire the HLT paths `HLT_PAMu3` and `HLT_PAMu7`, but not the path `HLT_PAMu12`.

It is important to know the correlations in our triggers, since one of the triggers, `HLT_PAMu3` dominates the total muon HLT rate; if the rate gets high at the beginning of a new run, we want to be able to act fast and decide what prescale to apply to this trigger. In doing so we can also know what the effect of the prescale would have on the rates of the rest of the triggers (`HLT_PAMu7`, `HLT_PAMu12`, but also dimuon triggers and jet+muon triggers).

To investigate the effect of the correlation, one can construct a correlation matrix between all muon paths including the ones using jets, which would help to map out all the overlaps between triggers firing on muons. Figure 4.3 shows such a matrix.

The correlation matrix shown was computed for the run 211752, in which the `HLT_PAMu3` path produces 69.2 % the total rate. If we look back at Table 4.3, we can see that run 211752 came in one of the first fill, when the luminosity of the proton beams was being ramped up progressively by the accelerator teams. To anticipate the rate of muon triggers at full luminosity (e.g. in runs posterior to 211752, cf. Table 4.3), I have produced this correlation matrix.

To get a good idea of how triggers overlap, one can look at the second column of Figure 4.3 to read what fraction of `HLT_PAMu3` firings (which dominate, as said above) is shared with other triggers. This is relevant since `HLT_PAMu3` dominates the total muon rate, all other correlations having smaller effects. The largest overlap of `HLT_PAMu3` is with the jet + muon path `HLT_PAMu3_PFJet20`, and is of 8.3 %. For a predictive total muon rate of 800 Hz, the `HLT_PAMu3` rate would be 550 Hz. With an overlap of 8.3 % of `HLT_PAMu3` with `HLT_PAMu3_PFJet20`, we obtain that the dominant `HLT_PAMu3` rate would be responsible for 45.7 Hz out of the `HLT_PAMu3_PFJet20` rate. This turned out to be close to the rate of `HLT_PAMu3_PFJet20` in consecutive runs at nominal luminosity (for example, `HLT_PAMu3_PFJet20`(run 211797) = 49.5 Hz), confirming that our predictions were accurate.

In this section we have seen how collision data gets stripped down to only the subset of events of interest for further analysis, thanks to the L1 and HLT trigger levels of CMS. The data has to be passing trigger filtering requirements that can be organised in three levels, along the various reconstruction sequences. In 2013, high muon rates above the 100 Hz level were affordable for analysis and were dominated by efficiency-oriented trigger paths. This ensures a large pp sample for physics and for efficiency studies, important to know the suppression in PbPb with good precision. The HLT procedes to a muon object online reconstruction that is close to the offline one, which will be detailed in the next Section.

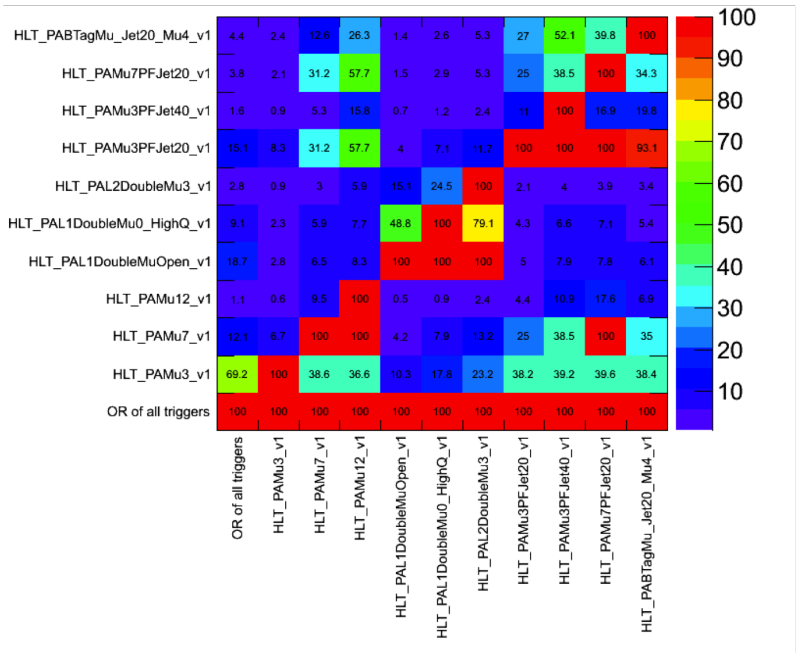

Figure 4.3: Correlation matrix of HLT muon rates, used to compute the overlap between paths sharing common L1 seeds. The dominant rate of HLT_PAMu3 is prescaled by a factor three.

4.2 Muons

The present section details how a muon object is formed in CMS, using information from separate subdetectors. The muons formed for use in this analysis are called global muons and correspond to the matching of a standalone (STA) chamber muon track with a tracker (TRK) identified muon. The formed *global muon* has a good reconstruction efficiency and resolution, comparable between *pp* and PbPb setups.

4.2.1 Muon reconstruction

The muons detection in CMS makes use of tracking facilities of the pixel detector, the strip trackers, and the muon stations (CSC+RPC, CSC+DT). The ECal can also be used in cases where isolation is needed in quiet regions where a muon could have gone through (the muon interacts minimally with ECal crystals). The rest of this discussion will not focus on calorimeters, although the muon energy deposits in ECal, HCal and HO can be used for identification purposes.

To properly measure the momentum of the muon, the most important aspect is probably the magnetic field. CMS was built with the goal of maintaining a high momentum resolution, of $\sigma(p_T)/p_T \sim 1\%$ at $p_T = 100$ GeV/c and of $\sim$10% at 1 TeV/c [119]. For these reasons, a particularly large magnetic field was needed.

Reconstruction begins with identifying the hits left by a muon in the multiple detection layers of a muon chamber. This first step is independent of the tracker system and relies only on local information from CSC, RPC and DT. This step is the standalone/Level-2 muon reconstruction sequence[120], and is presented in Section 4.2.2.

The muon trajectories can be extended to include hits in the silicon tracker (strip and pixel detectors). This procedure, usually used for the accurate measurement of TeV-scale muons, is also used (and tuned) in heavy ions for low-momentum muons, to ensure a high efficiency and momentum resolution even in the largest multiplicities recorded. This step is the global/Level-3 muon reconstruction sequence [120], and is presented in Section 4.2.3.

The common reconstruction sequence for low-momentum muons in *pp* data is tracker based, with a late extrapolation to the first muon chamber, to improve overall momentum performance. This is a particularly powerful procedure since the tracker information is very reliable, and timed with muon trigger signals originating from the muon chambers. These *tracker* based muons present the best position and momentum resolution below ≈ 200 GeV/c, and usually require the smallest amount of corrections overall. Tracker muons are presented in Section 4.2.4.

In heavy ions however, the track multiplicity is too high to afford a tracker-only muon reconstruction. Track reconstruction in heavy ions will be briefly outlined in Section 4.2.5.

4.2.2 Standalone muons

The RPC gives a very accurate timing resolution (below 2 ns) for the muon flying through [112]. Unlike CSC and DT subsystems, RPC does not form trigger primitives, but is used for synchronisation of trigger with the readout data. The RPC hits are hence used for muon trigger candidate recognition.

The DT and CSC subsystems perform straight line fits to the positions of hits they have recorded in each of the 8-12 DT layers or 6 CSC layers. These fits form track segments from three dimensional state vectors (the three dimensions are position, direction and p_T estimate), used as seeds in the combination with RPC recorded hits. Track fits in the full barrel muon system are based on a Kalman-filter technique [121], fitting from the inside out the DT segments together. In the endcap CSC chambers however, because of the inhomogeneities in the magnetic field, the three dimensional vector states are used directly. Reconstructed hits from the RPC are also included. χ^2 cuts are applied to remove bad hits from the refitting, and the track building proceeds towards outer stations. While doing so, the forming muon track parameters and errors are updated. This procedure is iterated until the outermost muon stations are reached. An outside-in Kalman filter is applied, to extrapolate the track parameters back to the innermost muon station. Last, an extrapolation to the beam crossing region is performed, and an offline-based vertex constraint is applied, to further improve the track's space and momentum parameters.

An example of STA muon can be found in Figure 4.4, where an event display of a cosmic muon passing through CMS is shown. This event, compared to collision events, has the particularity of having no backgrounds, and a trajectory very displaced from the beamspot.

4.2.3 Global muons

The Global muon object (GLB) extends the muon trajectories to include silicon tracker hits. From the standalone muon previously obtained, the trajectory is extrapolated to the outer tracker layers. The outcome of this extrapolation is the definition of a region of interest in the trackers' sensitive areas where the track reconstruction is performed. Within the region of interest, initial track candidates for the matching with the extrapolated STA are built from pairs of reconstructed tracker hits originating from two different tracking layers. All combinations of pixel layers and double sided silicon strips are used in the pairing. The track reconstruction algorithm, based on the Kalman-filter technique,

- builds tracks in the region of interest from pixel-seeded pattern recognition,
- cleans the built tracks by resolving position and momentum ambiguities,
- refits the obtained trajectory.

Starting from the innermost layer, the trajectory is propagated to the above layers, and the measurement improves at each iteration. The best χ^2 for the track fit is

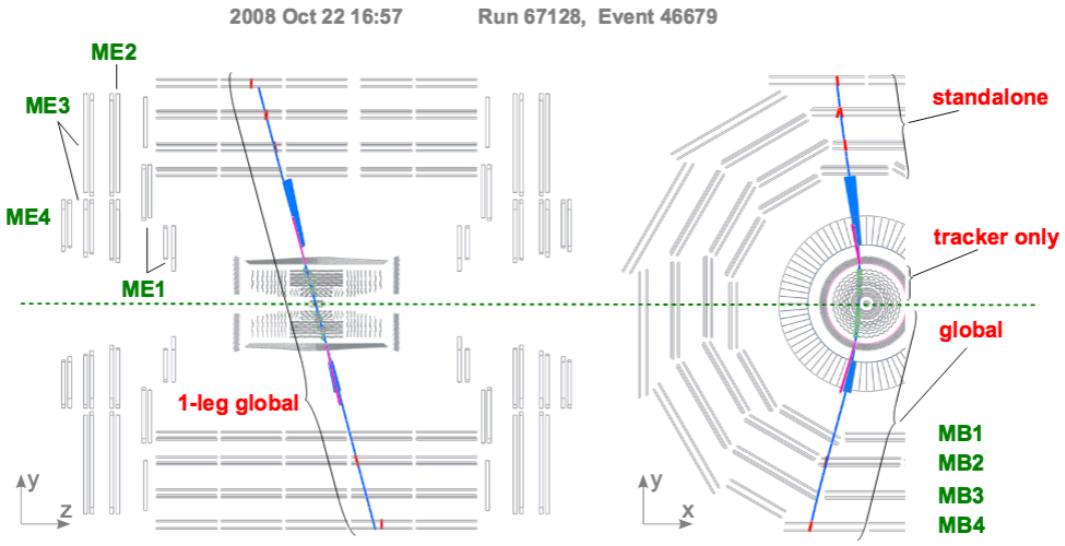

Figure 4.4: Event display of a cosmic muon passing through the CMS detector. Standalone and global trajectories are outlined. From [122].

retained if multiple tracks are compatible. Finally, all reconstructed tracks are fitted again without any beamspot constraint, and using STA muon hits. The GLB muon candidates are further cleaned by a χ^2 cut on this global fit. The candidates with high global χ^2 are discarded. The remaining trajectories undergo an additional fit, excluding muon chamber hits and segments with high χ^2 values, and using only silicon tracker fits plus the innermost muon station measurements. The χ^2 probability of the new fit is compared with the tracker only trajectory, which helps detecting energy loss before the muon reached the first muon station. This procedure ensures a good momentum reconstruction up to $p_T \sim 1$ TeV/c.

An example of GLB muon can be found in Figure 4.4, where an event display of a cosmic muon passing through CMS is shown. This event, compared to collision events, has the particularity of having no backgrounds, and a trajectory very displaced from the beamspot.

4.2.4 Tracker muons

An approach complementary to the GLB muon reconstruction consists in considering all tracker tracks to be potential muon candidates and in checking this hypothesis by looking for compatible signatures in the calorimeters and in the first layer of muon systems. The reconstructed tracks with p_T above 2.5 GeV/c compatible with at least one hit in one of the inner muon stations, are kept for further refitting following the procedure described above. This approach is famous for low p_T muons in pp data, but would be unaffordable given the CPU time it would require to run over all tracker

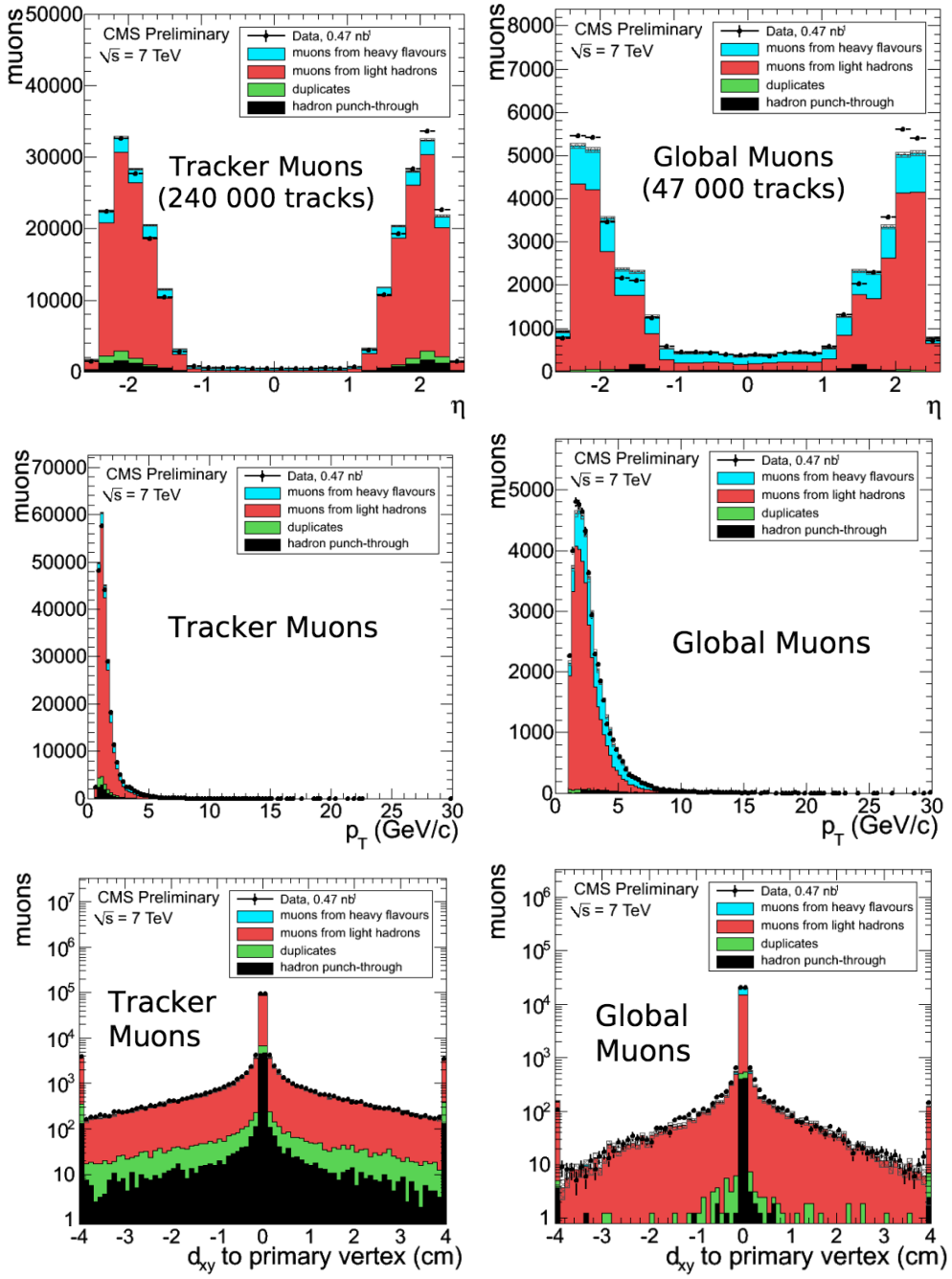

Figure 4.5: Kinematic distributions for tracker muons (left) and global muons (right), in early 7 TeV pp data. Top: pseudorapidity distributions. Middle: p_T distributions. Bottom: distance to the primary vertex in the $x - y$ plane [123].

tracks in heavy ion collisions.

A comparison between global and tracker muons is possible, and was done with early

2010 pp data at $\sqrt{s} = 2.76$ TeV [123]. The Muon Physics Object Group of CMS (Muon POG) [124] is responsible of maintaining the reconstruction codes and provides useful guidelines on how to reconstruct muons in CMS. The Muon POG is also responsible of preparing performance studies on muon identification and reconstruction for every data taking period (Run1, Run2, etc.) [112] [125]. In Figure 4.5, some basic kinematic distributions comparing 7 TeV tracker and global muons are compared. We can see that in the three distributions (η, p_T, d_{xy}), the tracker muon data is consistently more populated by light flavour (simulated) muon decays, duplicates, and hadron punch through. The global muons, although comparable, seem to perform better when one wants to discriminate easily the light flavour muons from heavy flavour muons. These plots were made with no specific quality requirement; we can understand that tracker muons will perform well as long as some additional offline cuts on the track quality are met.

4.2.5 Tracking in heavy ion collisions

Specific reconstruction and tracking algorithms are required to build muon trajectories in heavy ion collisions. Furthermore, the kinematic region of interest for muons in heavy ion physics is mostly located at low p_T, where charmonia, bottomonia and open heavy flavour are abundantly produced. However, the relatively low luminosity at which the LHC delivers PbPb collisions to the detectors (cf. Section 4.1.3) makes it possible to reconstruct a large fraction of the heavy ion event, without burning the pixel detector and without losing performance dramatically in all of the subdetectors.

The track reconstruction sequence is modified in heavy ion collisions from what was presented in Section 4.2.3, in the following way [96]:

- Instead of building a pixel hit start pair and extrapolate along a rectangular region of interest using pattern recognition, the builder extrapolates the trajectory helix to the transverse plane region where the next layer is, forming a smaller circular area to pick tracker hits into. This is the *modified hit triplet finding*;

- *triplet cleaning*: if one of the hits in the triplet is not compatible with the incidence angle of the track, the triplet is discarded;

The muon and track reconstruction strategies in heavy ion collisions have improved in 2012, leading to a re-reconstruction of the PbPb 2011 run.

The 2011 track reconstruction consisted of three iterations of the process mentioned in Section 4.2.3. The first two iterations began with triplet seeds, while the third formed tracks using a very limited subset of doublet seeds.

In the current muon reconstruction, the tracking algorithm is called Regional Iterative Tracking (RegIT). RegIt doubled the number of iterations, restricted in a cone around the STA muon extrapolation to beamspot, to minimise the computing time.

To further optimise the tracker reconstruction in PbPb, e.g. in the case of displaced muons (non-prompt J/ψ), two additional steps were added to further improve the reconstruction efficiency: first, a displaced triplet step was added by removing the

beamspot constraint. Second, the triplet seed for tracking, usually based on pixel hits, was allowed to pick starting hits in the silicon tracker, making the seed a *mixed triplet seed* (Pixel+strip triplet).

These two improvements have an effect of approximately 15% on each muon in a dimuon pair, when integrating over position variables (r, ϕ). A similar strategy is applied in high pile-up *pp* data, and the efficiency improvement is clear in tracks highly distant from the beamspot, starting from the fourth tracking iteration and above [126].

4.2.6 Muon selection

In the previous subsection we have seen what muon types are available. Especially, it was argued in Figure 4.5 that the tracker muons, for example, can be overwhelmed by light flavour muons, or duplicates. To the contrary, global muons, whose reconstruction sequence initiates in the muon chamber and propagates to the inner tracker, with a refitting including the primary vertex, can gain better discriminative power for heavy flavour and relatively high-p_T muons (i.e. below the TeV scale, roughly).

Since the analysis envisioned in this Thesis aims at performing the same signal extraction, $\Upsilon \to \mu\mu$ in two samples with very different tracker occupancy, a safe strategy must be adopted, to ensure high reconstruction efficiency and reasonable processing time (of the order of 5 seconds for central PbPb events). Global muons were used, since tracker based muons are not affordable starting from mid-central PbPb events.

While doing the GLB muon reconstruction, the code stores the information relative to the number of hits in the muon chambers, the number of pixel hits and tracker layers in the tracker systems, as well as the info from the global track refitting (total number of hits, reduced χ^2 of global fit). These could be further used to discard low-purity tracks. Additionally, the fitted tracker track distance from the primary interaction vertex is computed and can be used to remove muons originating from long lived particle decays $(\pi, K, ...)$ as well as cosmic rays.

The list of available *identification* variables is detailed below, along with the cut applied in our *pp* and PbPb analyses, placed in parenthesis and in bold. This set of cuts is recommended for most analyses using low p_T muons in CMS using the software developed at the time of PbPb data[3] re-reconstruction (2012):

1 Tracker based quantities:

- Number of valid pixel hits ($\geq$ **1**): final number of pixel hits from the total tracker track fit (some can be discarded, from the second iteration of the Kalman-filter method). A cut on this variable would remove muons from decays in flight;
- Number of silicon tracker layers with measurement ($\geq$ **10**). To guarantee a good p_T measurement, for which some minimal number of measurement points in the tracker is needed. Also suppresses muons from decays in flight;

[3] CMSSW_4_4_X

- d_{xy} ($<$ **3 cm**): tracker track transverse impact parameter, i.e. closest distance in the $x-y$ plane to the primary vertex. To suppress cosmic muons and further suppress muons from decays in flight;
- d_z ($<$ **15 cm**): longitudinal distance of the tracker track with respect to the primary vertex. To further suppress cosmic muons, muons from decays in flight and tracks from pile-up;
- reduced χ^2 of the muon track ($<$ **4**): to cut the badly reconstructed tracks (duplicates, punchtrough, long-lived);
- tracker arbitration (**true**): if there exist an ambiguity in the track-muon segment matching. The one arbitrated track has the closest geometric coordinates to the muon track (i.e. within three centimeters) when extrapolated to the muon station;
- `TMOneStationTight` (**not used**): Tracker track matched with at least one muon segment in any station in three standard deviations of the size of the STA muon track, in the $x-y$ plane. To resolve ambiguities when first muon station is shared by several tracks.

2 Global muon quantities:

- `isGlobal()` (**true**): requires the existence of a global muon. To remove empty muon station events;
- number of valid muon chamber hits (**not used**): removes a good part of the hadronic punchthrough;
- reduced χ^2 of the global muon trajectory ($<$ **10**): To suppress hadronic punch-through and muons from decays in flight.

In this section, the procedures to reconstruct muons passing the trigger requirements were outlined. We have seen that the pp and PbPb reconstruction algotrithms involve information from muon subdetectors to first reconstruct a *standalone* muon track, then propagated inwards to try to match it with a tracker track. The muon identification is meant to remove at the analysis step (offline) muons being poorly reconstructed, and enrich our sample in muons of good resolution. The muon selection used in further Chapters for yield extraction and efficiency corrections retains *global* muons. The reconstruction efficiency of these muons will be covered in Chapter 6.

4.3 Event selection and centrality

In this section we will see how the global event selection is applied to our muon sample. This will help extract the correct normalisations in order to compute an Υ production rate compatible with a cross section times branching ratio.

4.3.1 *pp* luminosity

The instantaneous luminosity $\mathcal{L}_{\text{inst.}}$, encountered previously when discussing trigger rates, is defined in Equation 4.1:

$$R = \mathcal{L}_{\text{inst.}}\sigma, \tag{4.1}$$

where R is the rate of a physical process, corresponding to a production cross section σ. The integrated luminosity is the integral of $\mathcal{L}_{\text{inst.}}$ over the whole data taking time.

Since the LHC settings are not optimal to measure the total *pp* cross section with precision [120], one cannot rely on the above formula to compute the luminosity recorded over a full physics run, without making an assumption on the total *pp* interaction cross section, which is dependent on the centre-of-mass energy.

However, the *minimum bias* requirement to select events originating from a hard diffusion, i.e. removing photo production and double pomeron physics, as well as other elastic processes, is nowadays done in CMS by requesting a minimal number of energy deposits in the Hadron Forward (HF) detectors. Our requirement is to record at least one tower with energy above 3 GeV on each side of the HF, when performing *pp* collisions. The counted number of events can be used to extract a luminosity.

The validation procedure of this number requires to define a set of good running times (i.e. when the high voltage is on and all subdetectors are running well). In this way the HF detector also fulfills a role of luminometer. It can also be cross checked by the LHC accelerator team by performing Van der Meer scans upstream of the machine. The Van der Meer procedure is to scan the transverse profile of proton beams; by doing so, and knowing the LHC filling scheme and the number of circulating protons, allows to determine an absolute luminosity scale, which can in turn be used to calibrate the HF luminometer.

In 2013, the certified *pp* integrated luminosity recorded during the CMS run at $\sqrt{s}$ = 2.76 TeV is:

$$\mathcal{L}_{pp} = (5.4 \pm 0.2)\ \text{pb}^{-1}. \tag{4.2}$$

4.3.2 Minimum bias event selection in PbPb collisions

If one wants to compute a cross section in PbPb collisions, one would need an equivalent measurement as the *pp* luminosity measurement of Equation 4.2. The *pp* luminosity is dependent on the total cross section for proton-proton interaction at the centre-of-mass energy of $\sqrt{s}$ = 2.76 TeV.

Unfortunately, the total PbPb cross section (inelastic plus elastic scattering cross section) is not known, and one would need a workaround, namely, an estimate of the total number of recorded hadronic interaction events. This number has to be counted with the total PbPb run data: it is not the number of events producing dimuons.

Additional care has to be taken in the event selection of the PbPb sample: since the Pb ions carry 82 positive electric charges each, it is much more probable that long range electromagnetic interactions occur between the Pb ions. Furthermore, any beam-gas interaction should be removed, both from the event counting and the dimuon sample. For this reason, the following event *minimum bias* selection cuts are applied to the overall PbPb dataset:

- Beam-halo muons (accelerator-induced particles that travel along the beam line and can be detected at any height r in both endcaps [127]) are removed by requesting that dimuon triggers are in time with beam-scintillator counters used for beam crossing precise timing, placed at the ends of both HF sides;

- Ultraperipheral collisions (induced by the electric charges in presence, for example γ Pb $\rightarrow \mu^+\mu^-$ Pb) and beam-gas events are vetoed by an offline filter requesting the firing of three HF towers on each side of the interaction point, with a total deposited energy of more than 3 GeV, in coincidence with the trigger dimuon event;

- A reconstructed vertex of at least two tracks of p_T above 75 MeV/c should be found, consistent with the transverse beam spot position and the expected collisions region along the z-axis;

- Further rejection of beam-gas and beam scraping events is done by requesting the longitudinal length of pixel clusters to be compatible with particles originating from the primary vertex. This selection proved efficient since the first publication on pseudorapidity and p_T distributions of charged particles in 7 TeV pp collisions [128]. This cut is placed along the red line visible on Figure 4.6 (left);

This selection ensures a tight correlation between the sum energy recorded by the two HF calorimeters and the number of pixel hits. The correlation can be seen on Figure 4.6 (right). It furthermore indicates that the HF energy sum can be later used as a classification variable for the 'centrality' of the collision, defined below.

With this selection, the total number of events recorded in 2011 passing the cuts is N_{MBraw}, the raw *number of minimum bias events*, which is equal to:

$$N_{\mathrm{MB\,raw}} = 1\,126\,653\,312 \tag{4.3}$$

The minimum bias selection efficiency, i.e. the fraction of the total inelastic PbPb cross section covered by this selection, was estimated in [129] to 97 $\pm$ 3 %.

The corrected number of minimum bias events, $N_{\mathrm{MB}} = 1\,161\,498\,260$, is used in the normalisation of the PbPb sample, to get a number close to the actual Υ cross section. In the following subsection we will see how the dimensionality of a cross section is recovered, and how the PbPb events are split in centrality classes.

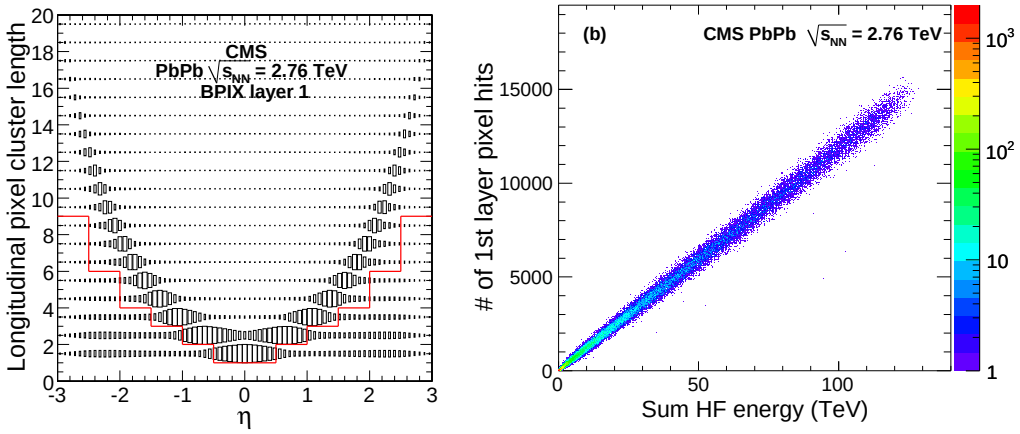

Figure 4.6: Global PbPb event selection performance-oriented plots. Left: Pixel-cluster length along the beam direction in units of pixel cells for hits from the first layer of the pixel detector, as a function pseudorapidity, after the rest of the event selection. The solid red line shows the selection on the minimum cluster length used [47] Right: Correlation between the number of pixel hits and HF total energy for a single run containing 60 000 minimum bias events after the selections described in Section 4.3.2 [129].

4.3.3 Centrality

The centrality of a nucleus-nucleus collision accounts for the overlap of the two nuclei at the moment of their collision. If the overlap is maximal, the maximum number of nucleons will participate in the collision: in the case of Pb ions, it is $208\times2 = 416$. The most central events are the ones close to this number of participating (or *wounded*) nucleons.

In a collider experiment, we cannot have a direct access to the exact number of nucleons colliding in any Pb-Pb interaction. One experimental handle would be the total event multiplicity for example, as the collision events with large impact parameter (i.e., the most *peripheral* events) produce very few particles, while the central ones with small impact parameter can produce many more particles.

We also know from *pp* interactions at recent and past collider energies that the multiplicity of particles produced in a head on *pp* scattering can be larger than the number of particles in the initial state (that is 2), and can vary event by event. Counting the number of final state particles would then be helpless, especially in the very high density regime reached in PbPb collisions as $\sqrt{s_{NN}} = 2.76$ TeV.

However, we have seen in Section 4.3.2 that after the minimum bias selection, the multiplicity of pixel hits in the first layer, seen in Figure 4.6, correlates very well with the sum of energy accumulated in the forward hadron calorimeters, with only few events deviating significantly[4].

[4]To verify this, the electronic version of Figure 4.6 (right) may work best, as the binning of the 2D plot may be too small to notice deviations in the printed version.

The distribution of this total forward energy was then used to divide the event sample into forty centrality classes, each representing 2.5% of the total nucleus nucleus interaction cross section. The sorting of the $\sum E_T^{HF}$ distribution in centrality classes is shown in Figure 4.7.

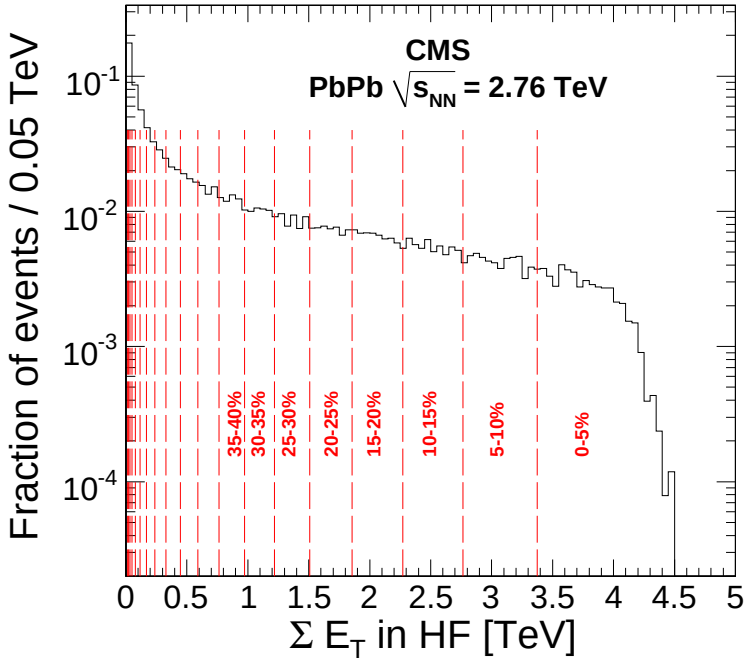

Figure 4.7: Centrality sampling on the total HF energy recorded in PbPb collisions at $\sqrt{s_{NN}}$ = 2.76 TeV, from [47].

Simulations can be used to correlate the defined centrality to the impact parameter b between the two nuclei, and to other properties of the collisions. The main quantities of interest are:

- N_{part}, the total number of nucleons that have experienced at least one inelastic scattering in the AA collision. This number cannot exceed 2×A, with A = 208 for Pb nuclei;

- N_{coll}, the total number of nucleon-nucleon scatterings in the nucleus-nucleus collision. This number can very well exceed N_{part} or 2 × A, depending on the impact parameter: for example, in the 10% most central events, we have b = [3.4 ± 0.1 (RMS = 1.2)] fm, $\langle N_{\text{part}} \rangle$ = 355 ± 3 (RMS = 33), and $\langle N_{\text{coll}} \rangle$ = 1484 ± 120 (RMS = 241);

- T_{AA}, the nuclear overlap function, which has units of a cross section. T_{AA} is equal to N_{coll} divided by the elementary nucleon-nucleon cross section and can be interpreted as the equivalent integrated luminosity per heavy ion collision, in

a given centrality range. For Pb ions at 2.76 TeV, the centrality averaged value is $T_{\mathrm{AA}} = [5.66 \pm 0.35\ (\mathrm{RMS} = 7.54)]\ \mathrm{mb}^{-1}$;

The average values and variances for b, N_{part}, N_{coll} and T_{AA} are obtained in a calculation based on a Glauber model, in which it is assumed that nucleons follow straight line trajectories in the PbPb collision [130]. The distribution of nucleons inside each nucleus is assumed to follow a Woods-Saxon distribution [131]. The resulting number of nucleon-nucleon interactions depends on how close the nucleons need to be in the transverse plane of the PbPb collision for a nucleon-nucleon scattering to occur; Based on fits to the available total and elastic cross sections in proton-proton and proton-antiproton collisions [21], the elementary nucleon-nucleon cross section is taken to be $\sigma_{\mathrm{inel}}(\mathrm{NN}) = 64 \pm 5$ mb.

The values for b, N_{part} and N_{coll}, in fine 2.5% bins are reported in Appendix B. The N_{part} and T_{AA} values used in this analysis are however presented in larger bins in Table 4.5, corresponding to the centrality bins used in Chapter 5.

Dimuon triggered events such as J/ψ or Υ decays are not distributed evenly among centrality classes. In fact, dimuon events originate from hard parton-parton scatterings, that do not conform to the centrality distribution of soft events. The soft particle rate (of π, K for example) is proportional to N_{part}, the number of participating nucleons in the collision, while harder probes (such as open heavy flavour, jets, quarkonia and electroweak bosons) are produced proportional to N_{coll}, which increases faster than N_{part} with increasing centrality. This can be seen in Figure 4.8, where the centrality distribution of minimum bias triggered events is compared to dimuon triggered events.

Centrality (%)	N_{part}	T_{AA} (mb^{-1})
0–5	381	25.9 ± 1.1
5–10	329	20.5 ± 0.9
10–20	261	14.5 ± 0.76
20–30	187	8.78 ± 0.58
30–40	130	5.09 ± 0.43
40–50	86.3	2.75 ± 0.30
50–70	42.0	0.985 ± 0.145
70–100	8.75	0.130 ± 0.020
50–100	22.1	0.486 ± 0.073
0–100	113	5.66 ± 0.35

Table 4.5: Average values of the number of participating nucleons (N_{part}) and of the nuclear overlap function (T_{AA}) in PbPb collisions, with the centrality bins used in this analysis [129].

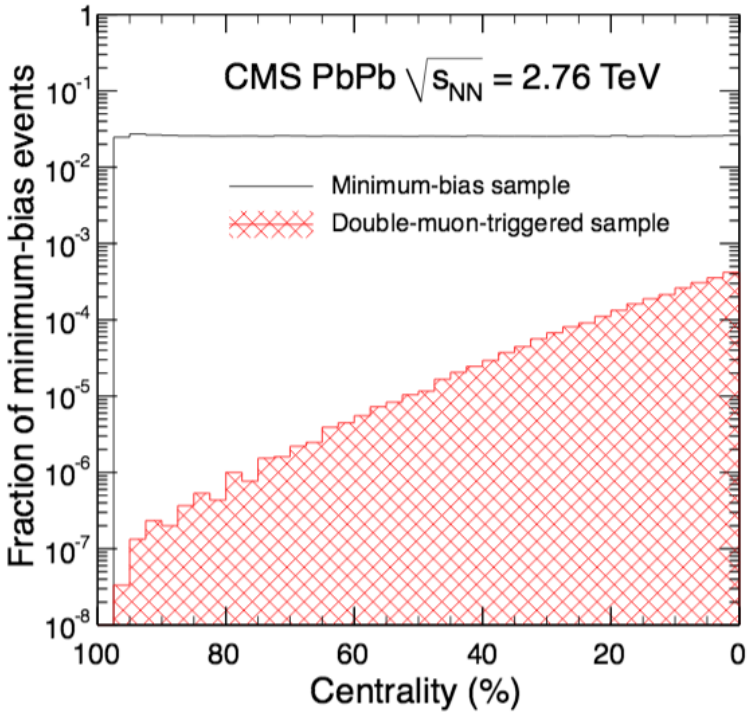

Figure 4.8: Centrality distribution of events passing minimum bias triggers compared to dimuon triggered events, in bins of 2.5% [2].

In this section we have seen how hadronic events are selected in pp and PbPb collisions, which led us to introduce the integrated luminosity used in the pp sample. One measure of the total number of hadronic (*minimum bias*) events in PbPb collisions is presented. The centrality of the collision has been defined, and is indispensable to estimate the amount suppression seen by quarkonia at increasing energy densities in nuclear matter. This closes the chapter of event selection and muon selection, providing us with all the tools needed for the study of Υ yields in data in the next part.

Part III

Analysis

Chapter 5

Signal optimisation and extraction

Contents

What I would recommend to them is, if they have some idea – however crazy it is – they should check up on it. Once in a hundred times it will turn out to be a good idea.

Simon van der Meer

5.1 Preamble

5.1.1 Analysis strategy

Our goal is to understand Υ modification and suppression in heavy ion collisions, to the largest possible extent. We have seen in the introductory chapters that the most prominent signature of deconfinement is quarkonium melting; Moreover, this melting is thought to be sequential, with the looser bound states diluting into the plasma before the tighter ones, as the energy density increases.

The simplest way to investigate the sequential melting of quarkonium states is to look at the individual yields recorded in centrality classes. A first measurement of the

centrality dependence of Υ suppression has been presented in Figure 2.20, page 58. This measurement made use of the nuclear modification factor:

$$R_{\mathrm{AA}} = \frac{N^{\mathrm{PbPb}}}{T_{\mathrm{AA}}\,\sigma_{pp}}, \tag{5.1}$$

where N^{PbPb} is the measured rate of the process of interest in PbPb collisions, and T_{AA} is the average nuclear overlap for a given impact parameter (or centrality) range. This gives a normalised yield directly comparable to the pp cross section, σ_{pp}, for the particle of interest.

When R_{AA} is equal to unity, it means that the rate observed for a particle produced in PbPb is strictly equal to that of a superposition of incoherent pp collisions, indicating that the particle rate does not suffer from nuclear or plasma effects. This is for example the case with electroweak probes $W^{\pm}$ and Z^0, and high-p_T photons. One should be very careful however as in many cases the R_{AA} can suffer from several effects that add up or compensate themselves. One infamous example being the interplay between J/ψ suppression and regeneration, that compensate to produce a flat R_{AA} over a wide centrality range [78].

5.1.2 First observations motivating newer measurements

For Figure 2.20, the R_{AA} was computed for Υ(1S) and Υ(2S) in seven bins of increasing centrality, using PbPb data of 2011 ($\mathcal{L} = 150\ \mu\mathrm{b}^{-1}$) and $\mathcal{L}_{pp} = 230\ \mathrm{nb}^{-1}$ of pp data at the same center of mass energy, $\sqrt{s} = \sqrt{s_{NN}} = 2.76$ TeV. We have seen that Υ(2S) is consistently more suppressed than Υ(1S): this is one reason to believe that suppression is sequential. However, in the simple hypothesis of sequential melting occurring to the full, one would expect the onsets of the Υ(2S) and Υ(1S) suppressions to coincide, which was apparently not the case in this data.

Another popular belief is that either one of the quarkonium states – dissociating or not – may escape the PbPb interaction without suffering from colour screening (cause for melting) if they have sufficient momentum. In this frame of ideas, high-p_T quarkonia may survive, and the R_{AA} should depend on p_T. This could also explain the Υ(2S) being non-zero in central events. The following Figures 5.1 left and right present the first attempt to measure the kinematical dependences of the Υ(1S) [2], motivating further the analysis presented here.

In Figure 5.1 (left), the Υ(1S) is obviously suppressed at low-p_T, with increasing R_{AA} (i.e. less suppression) when the transverse momentum of the Υ(1S) increase. At higher momenta the large statistical uncertainties prevent to reach any strong conclusion on the p_T dependence of the suppression. In the rapidity compilation on Figure 5.1 (right), the CMS data at mid-rapidity appears at tension (though again with large uncertainties) with the higher rapidity points of ALICE [5], themselves exhibiting a relatively stronger suppression than CMS data overall. This would tend to indicate that the Υ suppression is located at low-p_T.

However, considering the dissociation temperature of Υ(1S) being at least two times larger than the deconfinement temperature, it is often thought that Υ(1S) are not

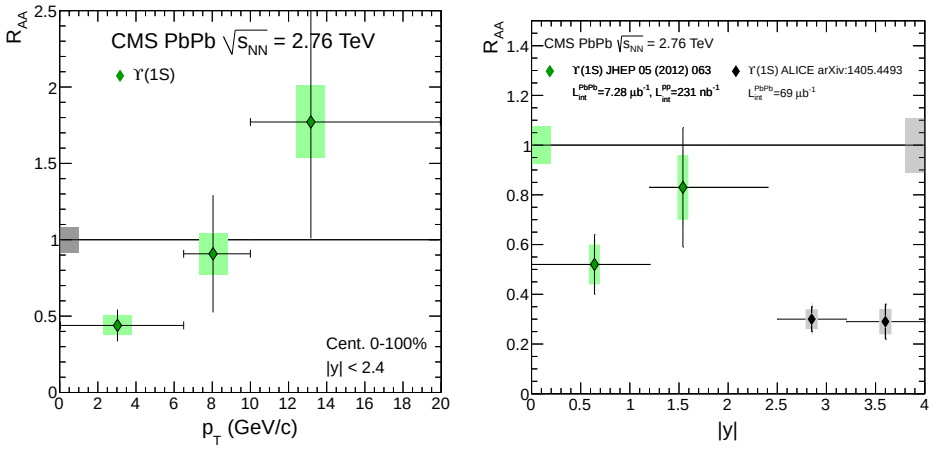

Figure 5.1: Nuclear modification factor R_{AA} of Υ(1S) in PbPb, measured with 2010 CMS data ($\mathcal{L}_{\mathrm{PbPb}} = 7.28\ \mu\mathrm{b}^{-1}$, $\mathcal{L}_{pp} = 230\ \mathrm{nb}^{-1}$). Left: transverse mometum dependence. The high-p_T points, albeit of poor significance, seem to exhibit less suppression than low-p_T ones. From [2]. Right: Rapidity dependence, compiling also ALICE data from [5].

'melting' in the QGP. The apparent Υ(1S) suppression would thus be the result of the excited state suppression, and the feed-down contributions from excited states being lost would bring the R_{AA} of Υ(1S) down to lower values.

Unfortunately, the *pp* and PbPb data recorded in 2010 that was used in [2] to produce the R_{AA} of Figure 5.1 (left and right) did not allow a precise kinematic mapping of all three Υ states. It has also been revealed in [3] that the Υ(3S) is likely to be fully dissociated, its yield being still not measured in the larger PbPb dataset of 2011 ($\mathcal{L}_{\mathrm{PbPb}} = 150\ \mu\mathrm{b}^{-1}$).

5.1.3 First look at PbPb data

In the heavy ion run of 2011 total number of minimum bias events $N_{\mathrm{MB}} \sim 1.13{\times}10^9$ was recorded. This corresponds to an integrated luminosity of $\mathcal{L} = 166\ \mu\mathrm{b}^{-1}$, hence 20 times more than before [2]. Out of these events, this analysis focuses on the subsample passing ultraperipheral and beam halo vetos, as well as an open dimuon trigger and offline muon quality cuts (often abbreviated to 'ID' cuts). The effect of subsequent cuts (trigger, ID, kinematics) in the dimuon invariant mass region of the Υ ($m_{\mu\mu} \in [7, 14]\ \mathrm{GeV}/c^2$) is presented in Figure 5.2. The total number of events in this range has been tabulated in Table 5.1 for all four cases.

When removing low quality muons from the dataset, the dimuon background is halved, and the Υ(1S) peak also appears clearer, its height apparently unaltered. In turn, cutting on the kinematics of the recorded muons (gold and black histograms) plays a role in removing most of the background in the mass plot and maintain most of the Υ(1S) peak. Because of the large y-axis scale of the left hand side plot in Figure 5.2

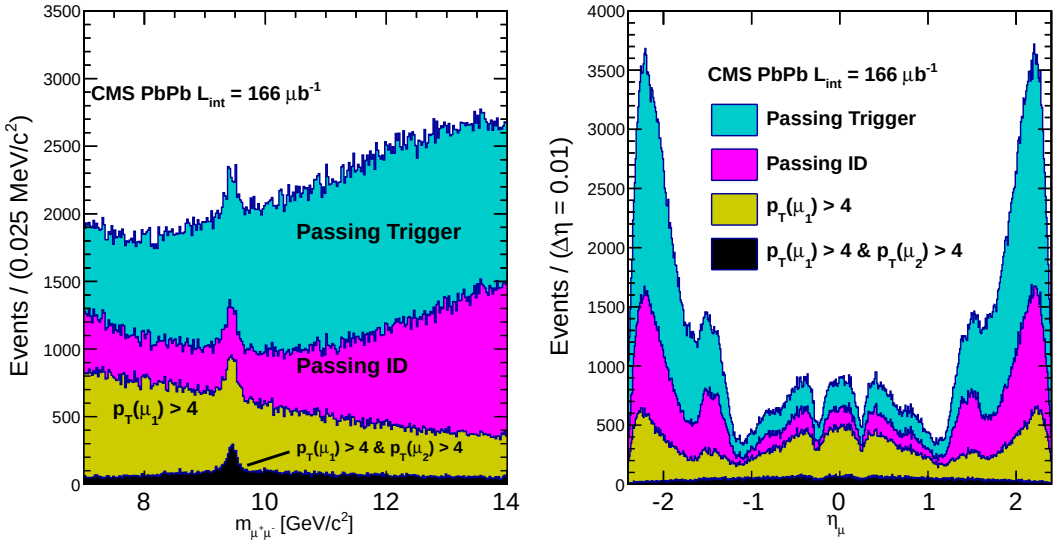

Figure 5.2: PbPb data in the Υ mass range, following three successive cuts. Samples in decreasing size are (cyan) the events firing the analysis trigger, (magenta) subsequent events passing the analysis ID cuts, (gold) subsequent events with one muon of p_T above 4 GeV/c, (black) events with both muons above 4 GeV/c. Left: dimuon invariant mass, right: muon pseudorapidity. Integrals of events are tabulated in Table 5.1.

it is hard to tell whether excited Υ(2S) can be seen at all, however a closer look in the following Sections will provide more information on this subject.

On the right hand side of Figure 5.2, several observations can be made. First, at $\eta \sim \pm 0.3$, dead areas between Wheel 0 and Wheel 1 of the steel yoke are responsible for the loss of events in that region. A similar feature appears with $\eta \sim \pm 1.1$, along with the change of material distribution from barrel to endcap. In the forward region, muons need a smaller p_T to reach the muon stations: this results in a very large background of soft muon events, which has been reduced by more than half when applying the muon ID cuts. This could be the sign of pion and kaon decays, as seen in Section 4.2.6, the muons with a large distance to the primary vertex being cleaned away in our analysis.

In previous analyses of Υ in CMS, an offline $p_T > 4$ GeV/c cut was applied to both muons. After applying this cut in the present data, the remaining events are presumably originating from a hard process, such as quarkonium production, heavy flavour decays and Drell-Yan. We see from the comparison between gold and black histograms of Figure 5.2 that some of the Υ signal is lost in the $p_T > 4$ GeV/c cut, while a lot of the background has been cut away.

Pushing further the comparison between the gold histogram ($p_T(\mu_1) > 4$ GeV/c) and the black histogram ($p_T(\mu_{1,2}) > 4$ GeV/c) of Figure 5.2, I have tried several sets of p_T cuts to get a clear insight of what was the kinematics of the events in the PbPb sample. The goal was to get the best signal at the edge the rapidity distribution, as well as at low p_T. Figure 5.3 shows what can be done when tuning the p_T cuts of the two

Type of cut	Number of events, $m_{\mu\mu} \in [7,14]$ GeV/c^2
Passing `HLT_HIL1DoubleMu0_HighQ`	620640
Passing muon ID cuts	320393
$p_T(\mu_1) > 4$ GeV/c	161510
$p_T(\mu_1)$ and $p_T(\mu_2) > 4$ GeV/c	21692

Table 5.1: Total number of dimuon events in the Υ mass range [7,14] GeV/c^2, after applying subsequent cuts (trigger, ID, kinematics).

muons, either in conjunction or separately: When the p_T threshold is the only difference between two cuts (as in grey *vs.* black histograms) the number of events passing cuts decreases quite constantly with pseudorapidity. The amount of decrease depends on the p_T difference between the two cuts. Tightening the cut further would only reduce the yield. Next, by releasing the cut applied to only one of the muons (as is black *vs.* pink histograms), the number of events increases more at large pseudorapitities than in the barrel region. This is a *flattening* of the accepted number of events as a function of pseudorapidity.

Up to now, we have seen that the excited states are suppressed in heavy ions, and a mapping of the kinematics of the suppression in the whole Υ sector is crucial. The questions to be answered in this analysis are:

- Does the suppression of individual Υ states appear to depend on the kinematics of the resonance?
- Is there Υ(1S) suppression in heavy ion collisions, or is it only excited state feeddowns suppression that we see?
- Is the Υ(3S) measurable at all?

In order to get the most information out of the available PbPb data, I have studied how the signal and background behave under certain kinematic restrictions on the single muons. The following Section details more about the optimisation of the kinematic cuts, looking at signal simulation, as well as pp and PbPb data.

5.2 Statistical optimisation

Previous analyses on Υ in heavy ions [3, 4] performed in the CMS experiment relied on a $p_T > 4$GeV/c cut on each muon, to discard much of the large dimuon continuum (called background hereafter). We have seen in Figures 5.2 and 5.3 that signal and background seem to react differently to muon p_T cuts, and I have tried to benefit from this to optimise the significance of the Υ(1S) (defined as yield over statistical uncertainty) to secure a satisfactory signal in all bins. This investigation has started during the first days of 2013, at the time of the p-Pb data taking, when the event

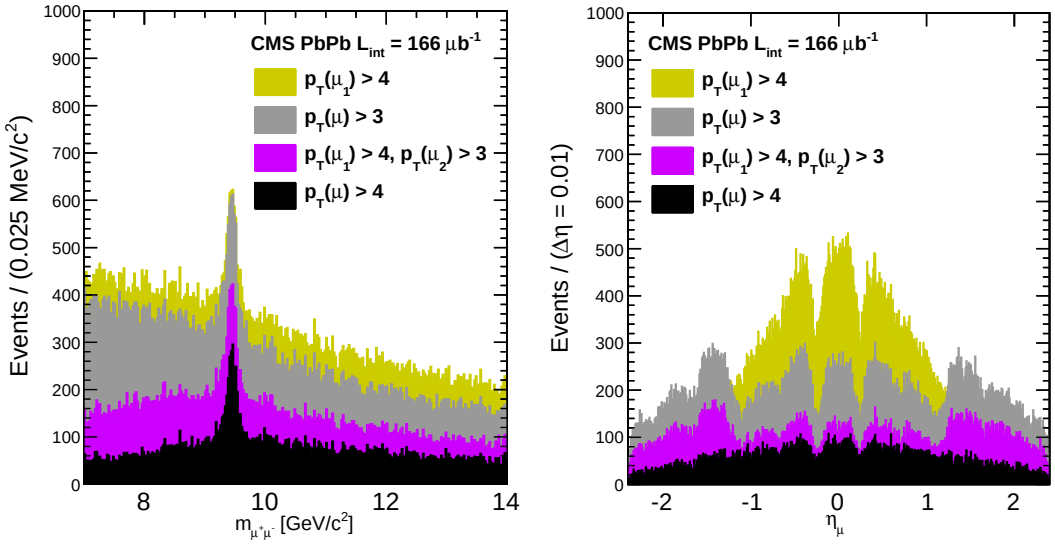

Figure 5.3: PbPb data in the Υ mass range, for various cuts on the single muon transverse momentum. Gold and black histograms are equivalent to Figure 5.2. Gray corresponds to a $p_T > 3$ cut looser than gold, however applied on both muons. Violet corresponds to an asymmetric cut where one muon has a $p_T > 3$ cut, while the second has a $p_T > 4$ cut (independently of the charge).

display on Figure 5.4 was produced from the first 'physics run'. One can see that for an Υ candidate with relatively low p_T, the decay appears rather *asymmetric*: one of the muons takes away a good fraction of the available momentum and propagates close to the direction of the parent Υ, while the other one recoils with a smaller momentum. In the usual $p_T >$ 4GeV/c selection, this event would not have been kept.

Another account of asymmetric event selection can be found in the 2013 STAR collaboration paper of Υ production in dAu collisions [132].

5.2.1 Simulation based studies

In the following, the effect of various p_T cuts is reported for simulated signal. One should not forget the high background seen in PbPb: this would be investigated further.

In Figure 5.5 left and right, the dimuon mass and muon η distributions are presented for various complementary p_T intervals. The histograms have been stacked as to represent the contribution of each p_T interval separately. We can see that about 80% of Υ have at least one muon below 5 GeV/c, and almost 45% have at least one muon below 4 GeV/c. From the dimuon mass plot (Figure 5.5 left), the resolution of the peak do not seem do depend strongly on the muon momentum. It can also be seen that the high momentum muons tend to be rare in the forward region and mostly located in the barrel, while the lower p_T intervals are more evenly distributed in pseudorapidity. These observations should be correlated with the individual muon

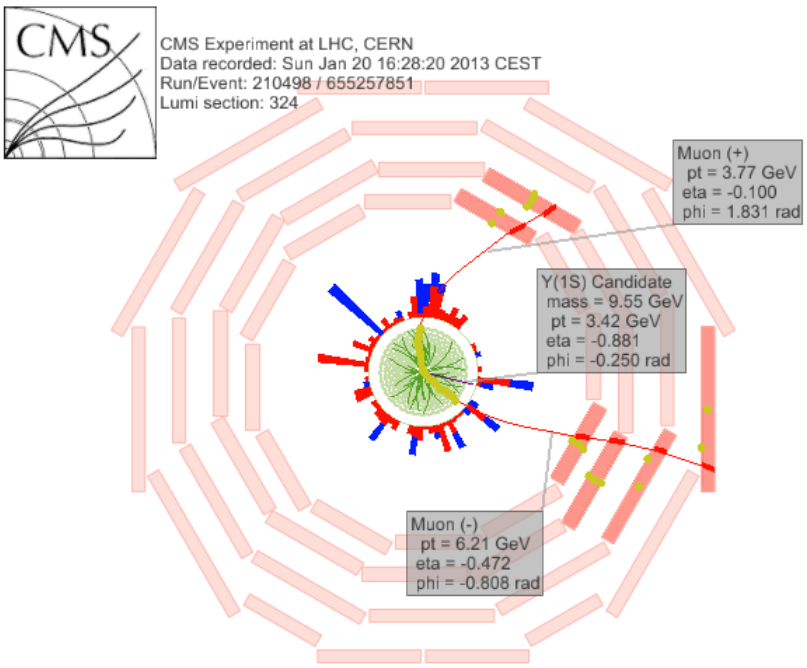

Figure 5.4: Event display of an Υ candidate decaying to two muons. View in the transverse plane of the detector (also called $r-\phi$ plane). Also shown in green are tracks coming from the rest of the proton-lead collision event, and ECAL energy deposits in red and blue.

reconstruction efficiency, presented for low-p_T muons in the two-dimensional histogram of Figure 5.6.

The muons have been generated flat in p_T over the whole pseudorapidity coverage of CMS muon stations. The effect of the magnetic field is clearly visible; below a certain threshold defining going as high as $p_T \simeq 3.2$ GeV/c, muons are not reconstructed. This *edge of the acceptance* is our limit for the muon p_T cuts applied in the analysis, and reduces at higher pseudo-rapidity because a more significant fraction of the momentum is longitudinal.

The edge of the acceptance has been previously defined in [2] as the region where the single muon reconstruction efficiency is higher than 10%:

$$\begin{aligned} |\eta^\mu| < 1.0 \quad &\rightarrow \quad p_T^\mu > 3.4 \text{ GeV}/c, \\ 1.0 \leq |\eta^\mu| < 1.6 \quad &\rightarrow \quad p_T^\mu > 5.8 - 2.4 \times |\eta^\mu| \text{ GeV}/c, \\ 1.6 \leq |\eta^\mu| < 2.4 \quad &\rightarrow \quad p_T^\mu > 3.4 - 0.78 \times |\eta^\mu| \text{ GeV}/c. \end{aligned} \tag{5.2}$$

Considering Figures 5.5 and 5.6, it looks like the single muons kinematic cuts could

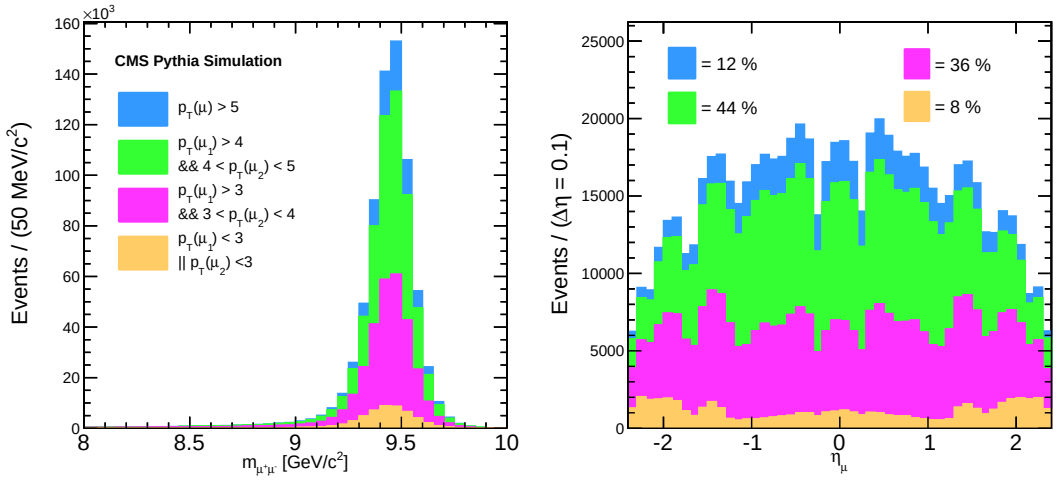

Figure 5.5: Υ(1S) simulated events reconstructed in CMS, for various cuts on the single muon transverse momentum. The dimuon mass spectrum is presented on the left, and the pseudorapidity distribution of decay muons is displayed on the right. Histograms are stacked because of their complementarity. Colours correspond to complementary single muon p_T ranges.

be extended below $p_T = 4$ GeV/c. This has to be tempered by the fact that in data, releasing such a cut would also enhance the background level.

The effect of releasing such cuts on muons in the PbPb sample can be seen on invariant dimuon mass plots in Figure 5.7. These histograms are binned in 3 dimuon rapidity intervals.

To understand the interplay between the background shape increase and the signal increase, several cuts were tried.
Here follows a list of the cuts applied in Figure 5.7 and observations related to them:

- *Red histogram:* $p_T(\mu) > 4$ GeV/c is applied to both muons. The background seems well behaving and relatively flat, but peaking under the Υ(1S) mass peak.

- *Yellow histogram:* $p_T(\mu) > 3.5$ GeV/c is applied to both muons. The background has largely increased compared to the previous case, and its shape clearly changes when moving to forward rapidities. The signal peak of Υ(1S) has also increased.

- *Blue histogram:* $p_T(\mu_1) > 3.5$ GeV/c and $p_T(\mu_2) > 4$GeV/c is applied. This asymmetric cut seems to reduce background of a certain amount, while leaving the signal untouched, compared to the blue histogram case.

To better illustrate the motivations for an asymmetric muon p_T cut to isolate signal from background, let us look at the 2D distribution of Figure 5.8, where the p_T of each muon is reported on x- and y- axes, for PbPb simulation and data. The signal Υ produces two muons with anti-correlated p_T, which is understandable by kinematics of the decay. When the resonance is produced with a given p_T, the decay in the rest

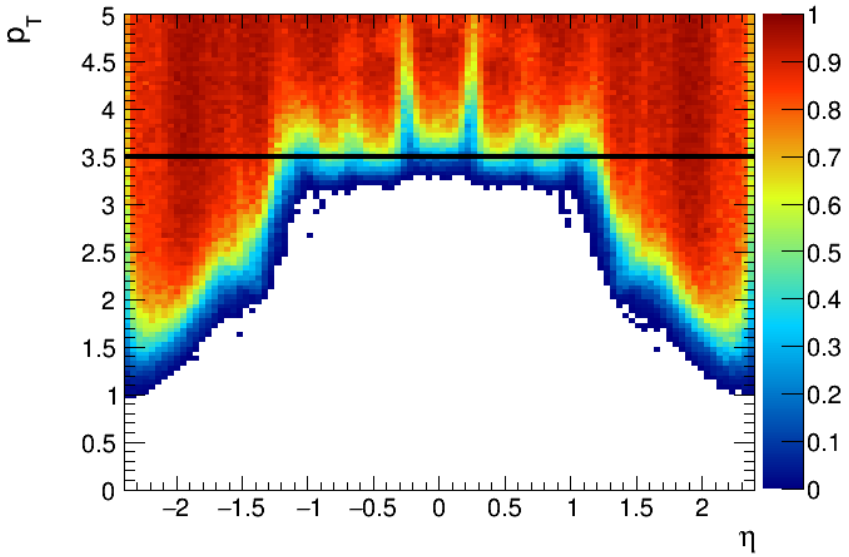

Figure 5.6: 2D distribution (p_T, η) of the muon reconstruction efficiency (defined in Section 6), based on a simulated sample of low-momentum muons with the PbPb muon reconstruction chain.

frame of the experiment is asymmetric, one muon taking away more momentum than the second. On the right hand side of Figure 5.8, one can see the bulk of the muon multiplicity produced in PbPb collisions is located at low p_T values, necessarily in the forward region since such low momentum values can only be reached in the endcaps.

From Figure 5.8 and the red histograms of Figure 5.7, one can conclude that cutting on the muons with a p_T above 4 GeV/c is limiting the available statistics, although cutting away a large fraction of the background yield. Additionally, cutting too low in p_T adds a lot of background in the mass plot. Finally, we turn to asymmetric cuts and observe that the signal amount appears conserved, while some of the background is rejected. This cut is going to be investigated in more detail.

5.2.2 Asymmetric single-muon transverse momentum cuts

The goal of the analysis being to evaluate the suppression of Υ mesons in various kinematic regimes (low-p_T, high-p_T, increasing rapidity) by the means of a nuclear modification factor, the important figure in our evaluation is the precision with which this suppression is extracted. The relative uncertainty on the suppression, that is to mean the statistical uncertainty obtained from optimizing with the cuts in pp and PbPb data at the same time, is the factor to be minimised.

In Figure 5.7, we followed the logic of comparing blue and yellow histograms to the red one, where both muons suffer a p_T cut of 4 GeV/c. The next step is to estimate the statistical increase in signal and background regions, as is done in Table 5.2. The

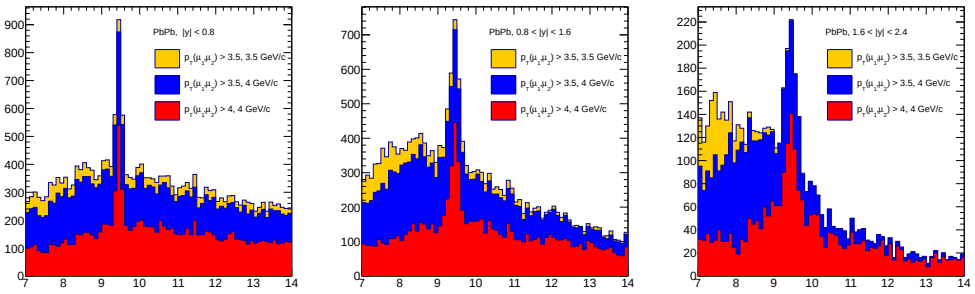

Figure 5.7: Dimuon invariant mass histogram for three different sets of cuts, in three rapidity regions: barrel |y|<0.8 (left), intermediate 0.8<|y|<1.6 (center), end-cap 1.6<|y|<2.4 (right).

increases are formulated in terms of gains (in percent) with respect to the red histogram. One can note that both cuts being looser, the gains in blue and yellow histograms with respect to the red one *are* positive.

The three regions studied are: $m_{\mu\mu} \in [9.2, 9.7]$ GeV/c^2 for the signal region, $m_{\mu\mu} \in$ [7,9.2] and $m_{\mu\mu} \in$ [9.7,14] GeV/c^2 for the background regions, respectively called 'SB_L' and 'SB_R' for left and right *sidebands*. In the signal region, the gains are computed with simulated yields. This procedure allows to avoid any bias in the signal region.

The cut tested in the upper part of Table 5.2 corresponds to the yellow histogram of Figure 5.7, while the lower part of the table compares the gains of the blue histogram of Figure 5.7.

When studying the sidebands (first and third columns of Table 5.2), one can see that both histograms present an increase of more than 70 % in every region. The symmetric cut tested in the upper part of the table (yellow histograms) shows an increase of more than 100 % on the left sideband, in all three rapidity bins, and in two of the three rapidity bins of the right sideband. This indicates that, when reducing of only 500 MeV/c the p_T threshold for both muons, the background level is approximately doubled.

For the lower part of the table (blue histogram) where an asymmetric cut is tested, a smaller increase of 70∼90 % is seen in both sidebands. This is understood since the p_T threshold was reduced on only one muon. In the same time, the signal region sees an increase of approximately 20 percent, consistent between the two cuts tested. This last observation leads us to conclude that while the background yield varies with the two cuts tested, the signal is already well maximised. The asymmetric cuts thus has the advantage of reducing the extra background yield while maintaining an improved signal yield.

The figure of merit used in the following is referred to as *fit significance*, and is defined as the ratio of fitted yield over fitted error:

$$\Sigma_{\text{fit}} = \frac{\mathcal{N}_{\text{Fit}}}{\sigma(\mathcal{N}_{\text{Fit}})}, \tag{5.3}$$

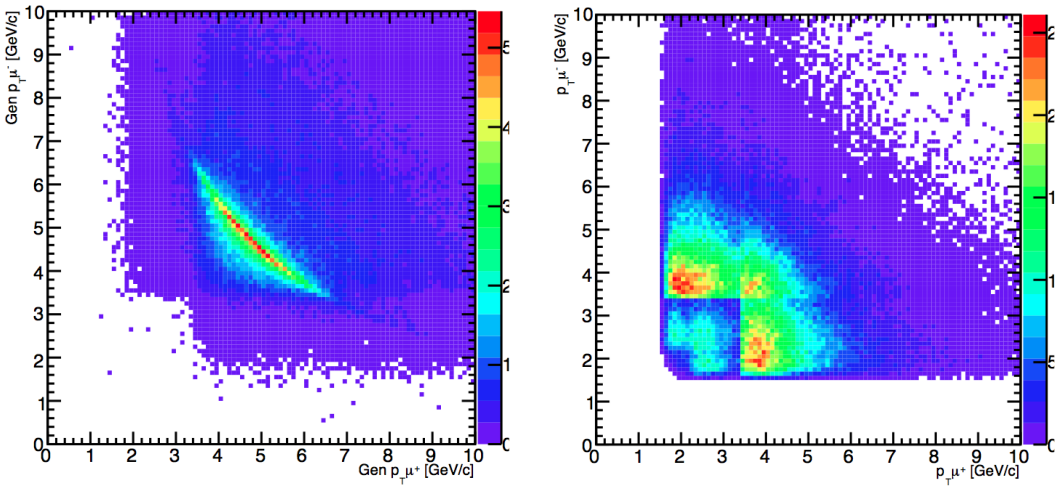

Figure 5.8: 2D-distribution of muon p_T for generator-level Υ (left) and PbPb data in the Υ mass range (right).

where $\mathcal{N}_{\rm Fit}$ stands for the extracted number of events from the Υ(1S) resonance when performing a maximum likelihood estimation on data, and where $\sigma(\mathcal{N}_{\rm Fit})$ comes from the 1-σ error on $\mathcal{N}_{\rm Fit}$ estimation.The method used in fitting corresponds to that of Section 5.3.

The significance is computed in all three cuts for every bin of the analysis *vs.* $N_{\rm part}$, p_T, y. The p_T and y bins are investigated twice: once when looking into pp data, and looking into PbPb data. The output of all the significances extracted is reported in Figure 5.9.

From the significances, a first important observation is the clear gain in precision when releasing the muon p_T cuts from 4 GeV/c to 3.5 GeV/c for one muon. It was decided to do the study with settings as close as possible to what the final analysis is, to get a clear handle of the gain in precision in outcome of this study. Second, although the gains in PbPb data are of the order of 4 σ in the low-p_T bins, the relative precision obtained in the nuclear modification factor will be largely increased thanks to the gain in pp statistics, where the background is smaller and therefore easier to control. In the two lowest-p_T bins, the pp statistics is increased of 10 to 12 σ from the grey symbols in Figure 5.9, which is very encouraging.

In summary, the symmetric 3.5 GeV/c cut does not seem to increase the significance; however, we have seen in previous mass plots that this cut enhances the low mass part of the background. In the same time, the asymmetric cut does a better job in the sideband regions, while the signal is improved. As a conclusion, it was decided to use the asymmetric cut $p_{T1} > 3.5$ GeV/c and $p_{T2} > 3.5$ GeV/c as the kinematic cut for the Υ(1S) signal extraction. In the case of the Υ(2S) and Υ(3S) it can be shown that both signals are consistently low, the Υ(3S) remaining unobserved in heavy ion collisions, and the Υ(2S) peaking at a 3 σ significance level. In these conditions, it was decided to keep a symmetric cut of $p_T > 4$ GeV/c for the Υ(2S), Υ(3S) analyses.

$p_T >$ (3.5, 3.5) GeV/c	Gains in SB_L	Gain in MC Signal	Gain in SB_R
Rapidity interval	$m_{\mu\mu} \in$ [7,9.2] GeV/c^2	$m_{\mu\mu} \in$ [9.2,9.7] GeV/c^2	$m_{\mu\mu} \in$ [9.7,14] GeV/c^2
$\lvert y\rvert < 0.8$	101%	18.3%	101 %
$0.8 < \lvert y\rvert < 1.6$	126%	22 %	79.2%
$1.6 < \lvert y\rvert < 2.4$	101%	18.3%	101 %
$p_T >$ (3.5, 4) GeV/c	Gains in SB_L	Gain in MC Signal	Gain in SB_R
Rapidity interval	$m_{\mu\mu} \in$ [7,9.2] GeV/c^2	$m_{\mu\mu} \in$ [9.2,9.7] GeV/c^2	$m_{\mu\mu} \in$ [9.7,14] GeV/c^2
$\lvert y\rvert < 0.8$	79.9%	17.9%	81.3%
$0.8 < \lvert y\rvert < 1.6$	96.1%	21.5%	68.1%
$1.6 < \lvert y\rvert < 2.4$	79.9%	17.9%	81.3%

Table 5.2: Added values from releasing the muon p_T cuts, in symmetric and asymmetric cuts, in PbPb data and MC. Added values are computed as relative to the standard tight cut ($p_T >$ (4 GeV/c, 4 GeV/c)). The signal region is computed using MC simulations.

In this Section, I have shown some aspects of my study of the low-momentum muons in CMS. We have seen the following points:

- A large fraction of Υ events have at least one muon below the previously used cut $p_T > 4$ GeV/c,
- While the magnetic field in the barrel naturally places a lower p_T limit at $p_T(\lvert\eta\rvert < 1.2) \approx 3.4$ GeV/c, going lower in p_T in the endcaps does not enhance the Υ data signal, and includes unwanted background events,
- Various p_T constraints were tested on each muons and led us to consider asymmetric muon p_T cuts as the best choice to optimise the $\Upsilon(1S)$ signal,
- This strategy however is not sustainable in the case of $\Upsilon(2S)$, which suffers more suppression.

With these points covered, the sets of kinematic cuts for each $\Upsilon(nS)$ are:

$\Upsilon(1S)$	"loose cut"	$p_T^{\mu_1} > 3.5$ GeV/c	$p_T^{\mu_2} > 4$ GeV/c
$\Upsilon(2S)$, $\Upsilon(3S)$	"tight cut"	$p_T^{\mu_1} > 4$ GeV/c	$p_T^{\mu_2} > 4$ GeV/c

In the following section, the fitting strategy is presented. After a short review of the lineshape study motivated by the signal peak resolution varying with rapidity, we then turn to the resulting Υ yields. A large $\Upsilon(1S)$ significance in every bin comes to confirm the validity of the chosen cuts, before the systematic uncertainties are studied.

5.3 Signal extraction

5.3.1 Fits to the invariant mass spectrum

The raw yields were extracted by fitting the dimuon invariant mass spectrum in the range

$$7.5 \leq m_{\mu\mu}\ [\mathrm{GeV}/c^2] < 14\ .$$

Yield extraction makes use of an unbinned maximum likelihood technique. Using standard minimisation tools of RooFit [133], the data is fitted with a user defined probability density function (PDF) in an attempt at minimising the negative log-likelihood $-\ln\mathcal{L}$ of the distribution.

The Υ resonances are commonly modeled experimentally by a Crystal Ball (CB) function. The Crystal Ball function consists of a Gaussian distribution and of a power law on the low-mass tail accounting for muon final state radiation. It is given by

$$\mathrm{CB}(x;\bar{x},n,\alpha,\sigma) = N\cdot\begin{cases}\exp(-\frac{(x-\bar{x})^2}{2\sigma^2}) & \text{for } \frac{x-\bar{x}}{\sigma} > -\alpha \\ A\cdot(B-\frac{x-\bar{x}}{\sigma})^{-n} & \text{for } \frac{x-\bar{x}}{\sigma} \leq -\alpha\,,\end{cases} \tag{5.4}$$

where

$$\begin{aligned} A &= \left(\frac{n}{|\alpha|}\right)^n \cdot \exp\left(-\frac{|\alpha|^2}{2}\right)\,, \\ B &= \frac{n}{|\alpha|} - |\alpha|\ . \end{aligned}$$

Since this analysis spans various p_T and rapidity regions, the resolution of the peaks may change from a bin to another one. This could already be sensed in the three panels of Figure 5.7. The previous analyses of Υ in heavy ion collisions [2, 3, 4] used a Crystal Ball function for each Υ state, fixing its width and final state radiation tail to values obtained from MC simulations. In the next Section 5.3.2 I present an equivalent study. The main difference with previous works comes from the fact that our fine binning in rapidity and p_T motivates to tune the signal shape parameters independently for each bin, instead of fixing them to a 'minimum bias' value.

For the sake of presenting the full fitting strategy before looking at the results of the lineshape study in detail, I want to anticipate and present the total signal and background PDF used in fitting data. A sum of two Crystal Ball functions was preferred over a single Crystal Ball because of the varying mass resolution with increasing dimuon rapidity. The resulting signal PDF used for the Υ(1S) resonance is defined as

$$\Sigma_{1S}\left(m_{\mu\mu};m_0,n,\alpha,\sigma_0,f,x\right) = f\cdot\mathrm{CB}_1\left(m_{\mu\mu};m_0,n,\alpha,\sigma_0\right)+(1-f)\cdot\mathrm{CB}_2\left(m_{\mu\mu};m_0,n,\alpha,x\cdot\sigma_0\right)\ . \tag{5.5}$$

In order to reduce the number of free independent parameters in the fit, we assume the values of m_0 and final state parameters n, and α to be shared by both Crystal Ball functions. The six fitting parameters (omitting the peak normalisation, see further) for Σ_{1S} are therefore the Gaussian peak mean and width m_0 and σ_0, Crystal Ball

parameters n and α for final state radiation, the ratio of the two Crystal Ball widths x, and the ratio of the two Crystal Ball normalisations, f.

The fitting was hence performed first on MC reconstructed peaks, that yielded separate results from PYTHIA (for pp) and the samples embedded in HYDJET (for PbPb). As a result, pp and PbPb peaks have separate constraints.

Regarding the PDF of the Υ(2S) and Υ(3S) excited states, the parameters n, α, f and x are set to be identical to those of the Υ(1S) PDF, Eq. (5.5). In order to account for the mass-dependent detector resolution, we shall assume that both the width σ_{nS} and the mass m_{nS} scale like

$$\begin{aligned} m_{nS} &= m_0 \cdot \frac{m_{PDG}^{nS}}{m_{PDG}^{1S}} \\ \sigma_{nS} &= \sigma_0 \cdot \frac{m_{PDG}^{nS}}{m_{PDG}^{1S}} \ . \end{aligned} \tag{5.6}$$

With this prescription, the Υ(nS) PDFs read

$$\Sigma_{nS}\left(m_{\mu\mu}; m_0, n, \alpha, \sigma_0, f, x\right) = \Sigma_{1S}\left(m_{\mu\mu}; m_0 \cdot \frac{m_{PDG}^{nS}}{m_{PDG}^{1S}}, n, \alpha, \sigma_0 \cdot \frac{m_{PDG}^{nS}}{m_{PDG}^{1S}}, f, x\right) \ . \tag{5.7}$$

The 5 parameters n, α, f, σ_0, x are determined from pure signal Monte Carlo simulations in Section 5.3.2, with distinct constraints for pp and PbPb signals. The mean parameter m_0 is kept free in the fit to the data to account for varying muon momentum scale inaccuracies over various areas of the detector. Once these are fixed, the signal $\mathcal{S}$ is defined as a weighted sum of the Υ(1S), Υ(2S), and Υ(3S) PDF,[1]

$$\mathcal{S}(m_{\mu\mu}; \mathcal{N}_{1S}, \mathcal{N}_{2S}, \mathcal{N}_{3S}, m_0 \big|\, n, \alpha, \sigma_0, f, x) = \mathcal{N}_{1S} \cdot \Sigma_{1S}\left(m_{\mu\mu}\right) + \mathcal{N}_{2S} \cdot \Sigma_{2S}\left(m_{\mu\mu}\right) + \mathcal{N}_{3S} \cdot \Sigma_{3S}\left(m_{\mu\mu}\right) \ . \tag{5.8}$$

where the raw yields $\mathcal{N}_{1S}$, $\mathcal{N}_{2S}$, $\mathcal{N}_{3S}$ and m_0 are left as free parameters in the fit to the data sample.The fits are performed on opposite-charge di-muon pairs. The signal in data lies on top of a continuum of events identified as background showing a smooth kinematic increase saturating slightly below the Υ mass.

The typical exponentially falling mass spectrum is multiplied by an error function rendering the kinematic turn-on arising from the single muon p_T selection.

The background model is formed of a real-valued Error function multiplied by an exponential, and used for the PDF of the background shape, $\mathcal{B}$,

$$\mathcal{B}\left(m_{\mu\mu}; \mu, \sigma, \lambda\right) = \exp\left(-\frac{m_{\mu\mu}}{\lambda}\right) \cdot \left(1 + \mathrm{Erf}\left(\frac{m_{\mu\mu} - \mu}{\sigma}\right)\right) \ . \tag{5.9}$$

It depends on three parameters left free in the fitting with this nominal procedure:

- The kinematic turn-on parameter μ, at which the error function starts increasing,

[1] In the following, we shall use for clarity the shorthand notation $\mathcal{S}(m_{\mu\mu}; \mathcal{N}_{1S}, \mathcal{N}_{2S}, \mathcal{N}_{3S}, m_0) \equiv \mathcal{S}(m_{\mu\mu}; \mathcal{N}_{1S}, \mathcal{N}_{2S}, \mathcal{N}_{3S}, m_0 \,\big|\, n, \alpha, \sigma_0, f, x)$.

- The width σ of the normal distribution from which the error function is derived,
- The decay constant λ of the exponential function.

The normalization $\mathcal{N}_{\rm bkgd}$ comes as an extra fitting parameter. As a result, the fit function $\mathcal{F}$ can be summarized as the sum of signal events and background events:

$$\mathcal{F}(m_{\mu\mu};\mathcal{N}_{\rm 1S},\mathcal{N}_{\rm 2S},\mathcal{N}_{\rm 3S},\mathcal{N}_{\rm bkgd},m_0,\mu,\sigma,\lambda) = \tag{5.10}$$
$$\mathcal{S}(m_{\mu\mu};\mathcal{N}_{\rm 1S},\mathcal{N}_{\rm 2S},\mathcal{N}_{\rm 3S},m_0)+\mathcal{N}_{\rm bkgd}\cdot\mathcal{B}(m_{\mu\mu};\mu,\sigma,\lambda) \tag{5.11}$$

Variations on signal and background shapes were also performed and are used to estimate the systematic error on the yields, as discussed in Section 5.3.4.

5.3.2 Signal lineshape study

The Monte Carlo samples used in the following paragraph are a set of PYTHIA samples for Υ(1S) decaying to muons. One of them is a pure signal sample, while the other one is embedded in a generated sample of events mimicking the heavy-ion environment, simulated with HYDJET.

The radiative decay $\mu \to \gamma\mu$ further denoted as *final state radiation* is carried by PHOTOS, and corresponds to muon bremsstrahlung. Effects of the muon energy loss on the Υ mass lineshape have already been studied in [134], in the context of the 7 TeV Υ cross section measurement in pp performed by CMS. There, a study of the reconstructed mass and error from track error matrices was performed, in the rapidity range $|y_{\mu\mu}| < 0.6$. The photon radiation was also refined with the computation of probability for photon radiation at a given E_γ in QED. Given the statistical and kinematical reaches of the data samples used in this analysis though, a similar study is out of scope.

In the context of the present analysis, the events are split in classes of dimuon rapidity extending to the limits of the muon spectrometer's reach. Hence, the observed peak resolution is reflecting detector effects coming from parts of the detector which can be different in terms of efficiency and material budget, making the resolution varying with rapidity. Furthermore, the resolution of the dimuon mass peak integrated over all rapidities is a convolution of resolutions belonging to separate parts of the detector. We then studied the resolution and final state radiation with a large simulation sample used to further constrain the fitting technique, as mentioned in 5.3.1. The binning applied hereafter follows the one used in the analysis of Υ(1S) as well as that of excited states, to get reasonable estimations of the mass lineshape in both cases. This binning is reported on page 123 of Section 5.3.3.1. As said above, this is motivated by the mass resolution varying with rapidity seen in fits, and the poor stability of mass fits when releasing constraints on some of the signal shape parameters.

The outcomes of this study are:

- Crystal Ball tail parameters α_{CB}, n_{CB} varying with increasing rapidity,

- necessity for adding a signal p.d.f. for varying resolution in bins which are inclusive over rapidity (i.e. p_T bins),

- correlations in some fit parameters that were taken care of when replacing the second width σ_2 with a scaled parameter to σ_1, $x_{\text{scale}} = \sigma_2/\sigma_1$.

The functions tried for fitting are: Gaussian, double Gaussian (with varying widths), Crystal Ball, double Crystal Ball, Crystal Ball plus Gaussian (varying widths). The double Crystal Ball signal function was defined in Equation 5.5. The choice retained for FSR studies is the double Crystal Ball, as can be seen in figures below. The Crystal Ball + Gaussian seemed like a sufficient choice at first, eventually discarded because of a poor description at high-mass and pole mass.

The minimum-bias fit is reported in the following Figure 5.10 and the fits to all analysis bins are reported in Figures A.31 to A.33. A line is added to the fit, to account for spurious and misreconstructed muons. Although the event selection is supposed to remove most of them, the embedding procedure can alter the reconstruction of muon tracks overall. This additive component in the simulation signal is shown not to exceed 2 percent of the total simulated statistics available.

Sanity checks on fits were performed with the help of likelihood scans (cf. Figure 5.11 for the Minimum Bias example, and Figure A.35 for the $2.0 < |y| < 2.4$), i.e. projection of the obtained (negative) log-likelihood on the axis of a given parameter. This allows to see how the fits are performing with respect to individual fit parameters, but also gives information on the non-linearities brought into the model. The scans yielded very satisfactory results for the most cases, except for high-rapidity bins where the power-law tail exponent is poorly constrained. The plots for likelihood scans are built so that one can read on the x-axis the value obtained for each parameter at the step where the negative-log-likelihood (often referred to as NLL) is minimized. Looking at the trend of the likelihood scan informs on potential non-linearities or local minima if any, and looking at the abscissae where NLL crosses horizontal y=0.5 or y=2 lines (not drawn) gives respectively the P=68.3% and P=95.5% for finding the minimized value. Also, the x-axis was plotted as to be centered on the minimized value, and varied two times the error on the value (which is symmetric, before MINOS [135]).

The Table A.1 in Appendix A provides the central values obtained for each parameter in the signal shape. These parameters are further used for signal fitting and systematics.

5.3.3 Extraction of raw Υ yields

Figures 5.12 and 5.13 show the fit to the full datasets extracted in both (pp and PbPb) data sets, with the signal-plus-background function $\mathcal{F}$. Figure 5.12 presents results of the Υ(1S) analysis selection (with loose muon p_T cuts), while Figure 5.13 presents results for the excited states (tight muon p_T cuts). Results are also reported in Table 5.3.

Loose cuts	$\mathcal{N}_{1S}$	$\mathcal{N}_{2S}$	$\mathcal{N}_{3S}$
PbPb	2534±76	158±52	-32±48
pp	5014 ± 87	1580±59	770±49
Tight cuts	$\mathcal{N}_{1S}$	$\mathcal{N}_{2S}$	$\mathcal{N}_{3S}$
PbPb	1793±61	173± 41	7±9
pp	3511 ± 71	1208±49	619±41

Table 5.3: Table for fit results of the three Υ states, when measured on the full *pp* and PbPb samples.

5.3.3.1 Transverse momentum bins

For both the pp and PbPb analyses, the p_T binning used is

$$\Upsilon(1S): \quad p_T \ [\mathrm{GeV}/c] \in [0-2.5], [2.5-5], [5-8], [8-12], [12-20] \ ,$$
$$\Upsilon(2S): \quad p_T \ [\mathrm{GeV}/c] \in [0-5], [5-12] \ ,$$

for $\Upsilon(1S)$ and $\Upsilon(2S)$, respectively. This binning has been chosen specifically to obtain about the same number of candidates in most of the bins.

The fits to data for $\Upsilon(1S)$ (loose muon cuts) and $\Upsilon(2S)$ (tight muon cuts) are reported from in Appendix A.1.1, Figures A.1 to A.7.

5.3.3.2 Rapidity binning

For both the pp and PbPb analyses, the y binning used is

$$\Upsilon(1S): \quad y \in [0-0.4], [0.4-0.8], [0.8-1.2], [1.2-1.6], [1.6-2], [2-2.4] \ ,$$
$$\Upsilon(2S): \quad y \in [0-1.2], [1.2-2.4] \ ,$$

for $\Upsilon(1S)$ and $\Upsilon(2S)$.

The fits to data for $\Upsilon(1S)$ and $\Upsilon(2S)$ analyses are reported in Appendix A.1.2, from Figures A.10 to A.17, respectively.

5.3.3.3 Centrality dependence

The study of the centrality dependence is performed separately for Υ(1S) and Υ(2S) states.The centrality binning used in PbPb is:

$$\begin{aligned}
&\Upsilon(1S) \quad \text{Cent.} \in [0-5], [5-10], [10-20], [20-30], [30-40], [40-50], [50-70], [70-100]\% \\
&\Upsilon(2S) \quad \text{Cent.} \in [0-10], [10-30], [30-50], [50-100]\%,
\end{aligned}$$

The fits to data for the Υ(1S) analysis are reported in Appendix A.1.4, Figures A.24 and A.25. For the Υ(2S), the PbPb yields were too low to bin in centrality with a binning as fine as Υ(1S). The 2011 analysis [4] reported Υ(2S) yields in small bins equivalent to those of the Υ(1S) analysis, however most of them yielded results compatible with zero. In order to avoid poorly significant results where one cannot tell if the observed measurement are due to statistical fluctuations, the centrality bins have been reduced to four in the present analysis. Yields for the Υ(2S) analysis are extracted from the fits reported in Figure A.26.

5.3.4 Systematic uncertainties from signal extraction

As mentioned in Section 5.3.1, variations are performed upon the nominal fit function in order to compute the systematic uncertainty from the fitting method. The uncertainty from fitting is computed as the quadratic sum of two sources: varying the signal lineshape by releasing constraints on the signal parameters, and varying the PDF used for the background continuum. The variations on the signal $\mathcal{S}$ and background $\mathcal{B}$ are described below and were performed independently for each analysis bin and muon p_T cut:

Signal shape variation

- To test the hypothesis that fit parameters could be poorly reproduced by the MC simulations, all the 5 parameters $(n, \alpha, \sigma_0, f, x)$ released one by one in the fit to the data (the other 4 being fixed to their constrained MC value), leading to 5 fits per bin. For the signal, the systematic uncertainty is taken to be the RMS of the five variations to the nominal fit in a given bin.

Background shape variation

- To estimate the signal systematic uncertainty coming from our description of the background continuum below the peak, variations on the background PDF are performed. The default background shape $\mathcal{B}$ receives an additional (unconstrained) first order Chebychev polynomial

- Same operation, with a second order Chebychev polynomial. The uncertainty from background is computed as the maximum of the two deviations to the nominal fit.

In Appendix A.1.5, Figure A.27, the fit variations of the *pp* all-integrated sample are reported, and continued onto Figure A.28.

In Appendix A.1.5, Figure A.29, the fit variations of the PbPb all-integrated sample are reported, and continued onto Figure A.30.

In the following Tables 5.4, 5.5, 5.6, the systematic uncertainties computed for each bin are reported for Υ(1S) (pp and PbPb), Υ(2S) and Υ(3S) pp, and Υ(2S) PbPb analyses respectively. Namely, the relative deviations are shown for each fit in every bin. The total systematic uncertainty per bin is derived in the last column (quadratic sum of total signal and total background uncertainties).

5.3.5 Tabulated results

This Section sums up the fit results of each analysis. The paragraph is organised as follows: Table 5.7 reports the results on raw yields for the extraction of Υ(1S) cross-section and $R_{\rm AA}$ differential in rapidity or transverse momentum. As a reminder, let me mention here the Υ(1S) analysis is performed with what was earlier called 'loose' single muon p_T cuts. For completeness, the yields of excited states from these Υ(1S) fits are also reported, but do not enter in the computation of excited states cross sections or $R_{\rm AA}$.

Table 5.8 reports the results on raw yields for the extraction of yields with the 'tight' single muon p_T cut. This cut is applied to the Υ(2S,3S) pp cross section and $R_{\rm AA}$. Since the available statistics is large in pp, the results for pp cross sections are taken from small bins (lower panel). The PbPb yields are tabulated for both binning formats, and the $R_{\rm AA}$results are taken from large bins (upper panel).

Table 5.9 reports the results on raw yields in bins of centrality. The upper panel consists of yields used in the Υ(1S) $R_{\rm AA}$ analysis, extracted with loose muon p_T cuts, while the lower panel consists of yields extracted with $\mathrm{p}_T^{\mu} > 4$ GeV/c, for the Υ(2S) $R_{\rm AA}$. The Υ(1S) yields from the lower panel can be used to compare with 2011 results, and feature an overall 35 percent signal increase attributed to the improved reconstruction (RegIT).

In this Section I have presented the core of the Υ analysis: the extraction of raw yields in pp and PbPb, for all three Υ states. After seeing in the previous section that a customised cut could be envisioned to minimise the statistical uncertainty of Υ(1S) $R_{\rm AA}$, I have presented the fitting method, how it is improved by MC tuning of the fit parameters, and how the systematic uncertainties are computed.

In 2011 PbPb and 2013, the total number of detected Υ candidates passing the trigger and quality selection are:

Loose p_T cuts	$\mathcal{N}_{\rm 1S}$	$\mathcal{N}_{\rm 2S}$	$\mathcal{N}_{\rm 3S}$
PbPb	2534 ± 76	158 ± 52	-32 ± 48
pp	5014 ± 87	1580 ± 59	770 ± 49
Tight p_T cuts	$\mathcal{N}_{\rm 1S}$	$\mathcal{N}_{\rm 2S}$	$\mathcal{N}_{\rm 3S}$
PbPb	1793 ± 61	173 ± 41	7 ± 9
pp	3511 ± 71	1208 ± 49	619 ± 41

In the following, I will present how the raw yields are converted into actual cross sections that will ultimately lead us to the nuclear modification factor comuptation.

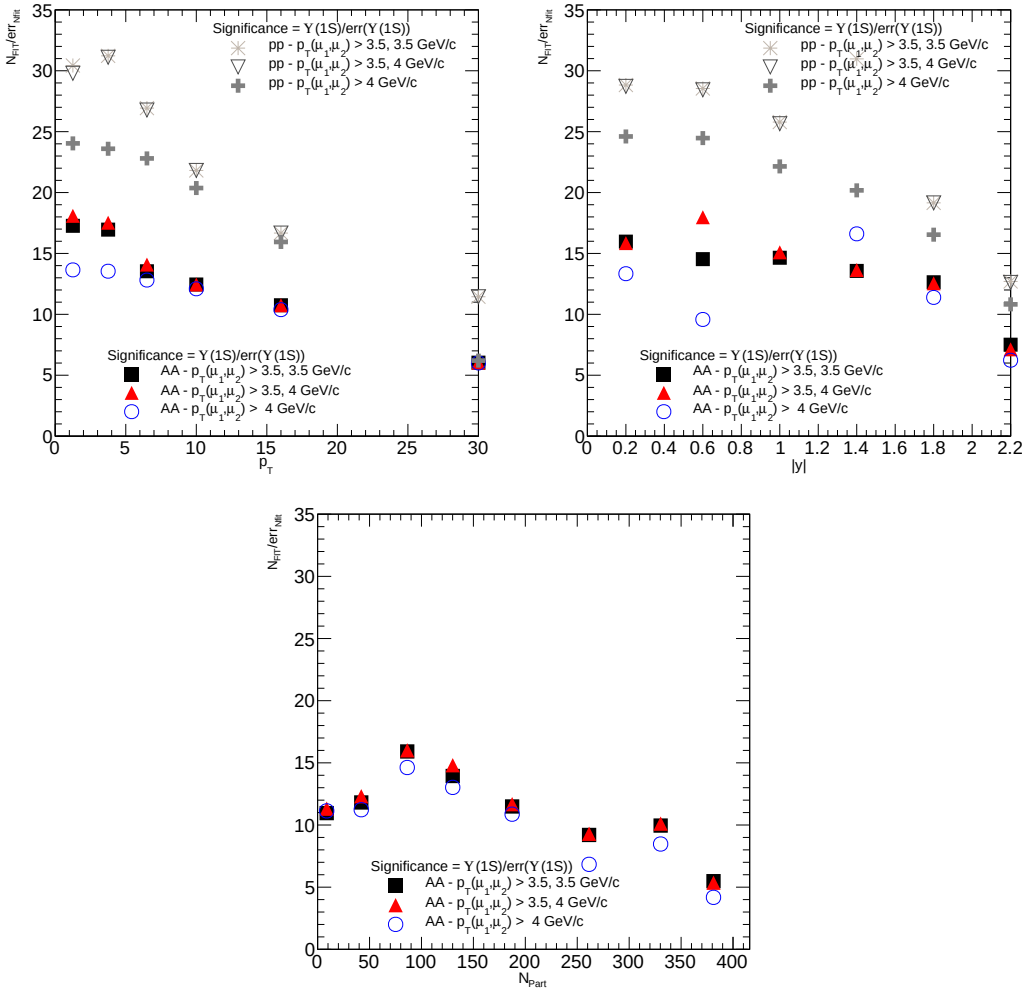

Figure 5.9: Signal over error ratios (i.e. fit significances) for each bin of the Υ(1S) analysis. First, transverse momentum binning; Second: rapidity binning; Third: N_{part} binning. Open triangles and filled triangles denote the most satisfactory cut ($p_{T1} >$ 3.5 GeV/c and $p_{T2} > 3.5$ GeV/c) in pp and PbPb data, respectively.

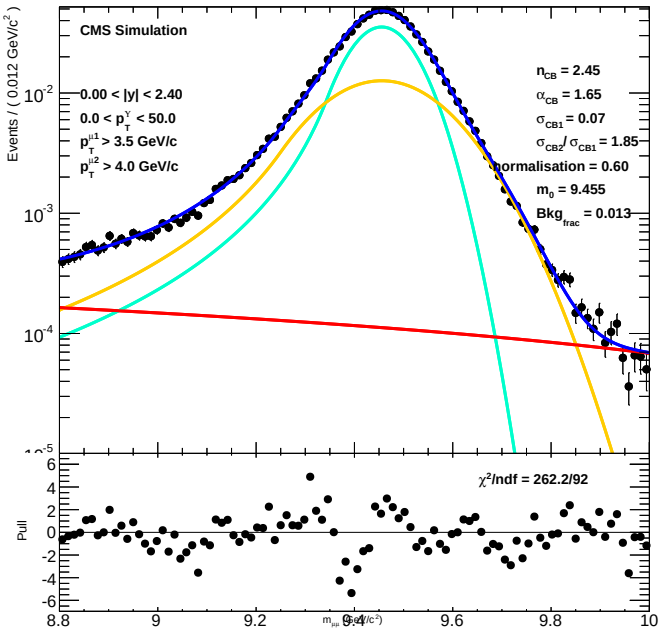

Figure 5.10: Minimum-bias fit of Υ(1S) mass from a simulated sample embedded in events generated with HYDJET. The total fit is displayed in blue. The yellow and green curves correspond to the two Crystal Ball functions added together. The red line takes a residual part of the simulation sample into account, coming from background simulation.

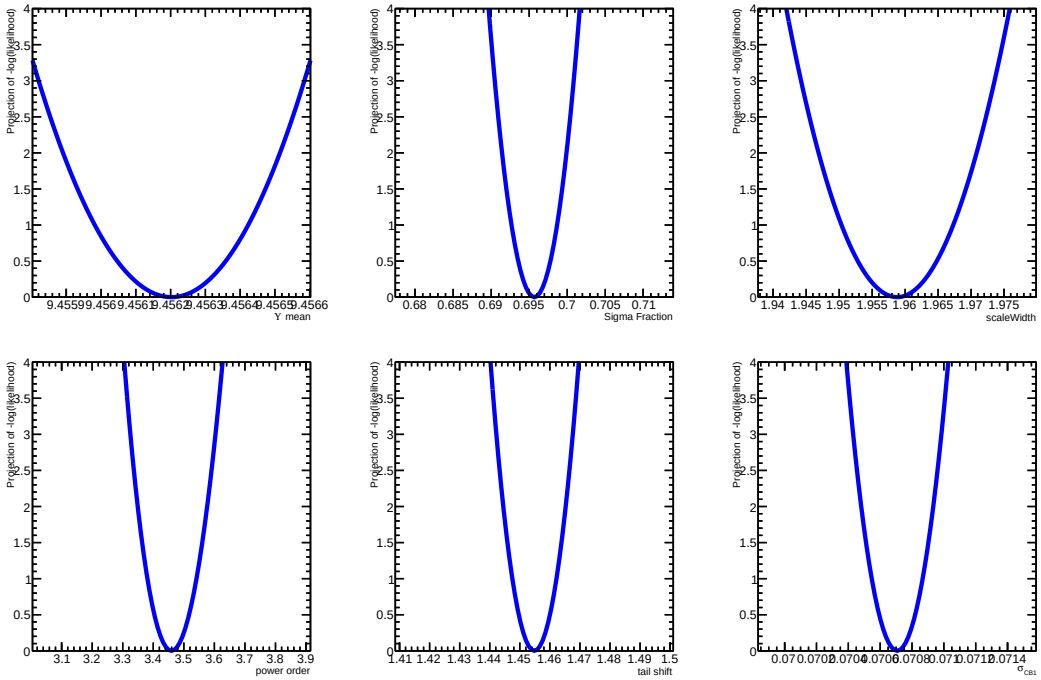

Figure 5.11: A good likelihood scan of the all integrated Υ(1S) sample.

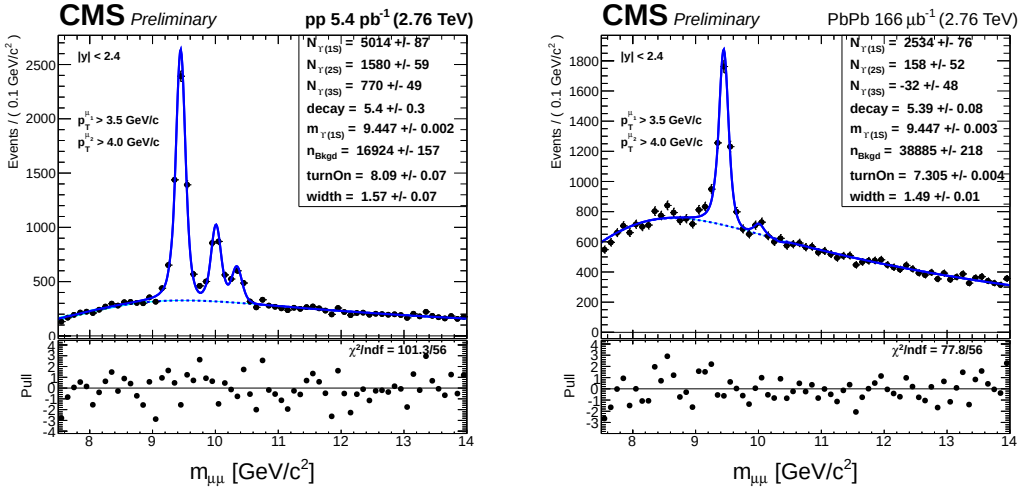

Figure 5.12: Invariant-mass fits to all pp data (left) and PbPb data (right). The solid blue line is the total fit function, the background being the underlying dashed curve. The light blue band around the background shape is the 1σ error band on background fitting.

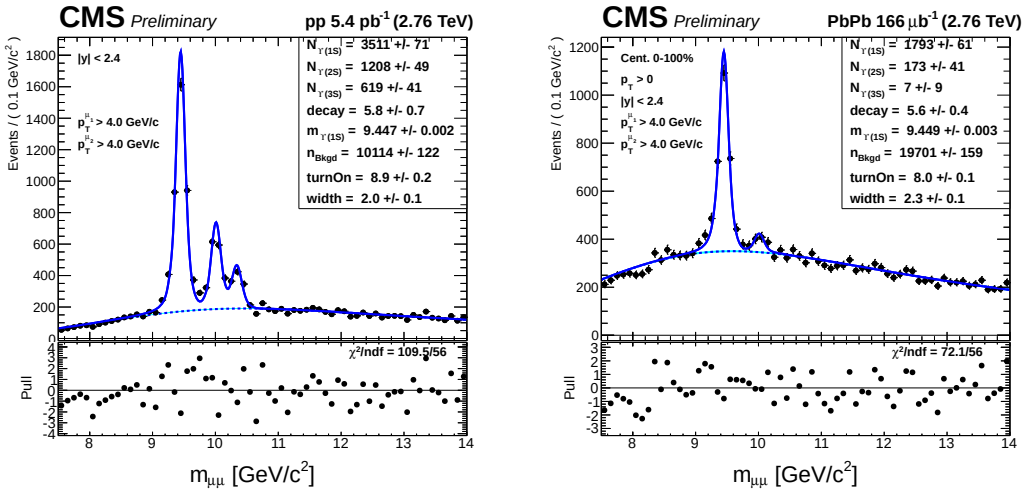

Figure 5.13: Same as Figure 5.12 using tight muon p_T cuts.

	Signal					Background		Total %
pp Υ(1S)	α	n_{CB}	σ_1	σ_2/σ_1	f	Pol(1)	Pol(2)	Tot. pp%
$p_T < 2.5$	4.41	3.71	-9.21	-9.33	-7.38	0.13	-2.51	8 %
$2.5 < p_T < 5$	4.55	3.86	-1.98	-1.05	-1.92	0.19	-4.07	5 %
$5 < p_T < 8$	-2.26	-7.44	-2.12	-2.17	-1.59	0.47	0.89	4 %
$8 < p_T < 12$	-1.84	0.25	-2.90	-2.71	-2.33	-0.02	-0.72	2 %
$12 < p_T < 20$	-0.07	-0.94	-1.04	-0.55	-1.01	0.00	0.00	1 %
$\|y\| < 0.4$	-5.02	-2.14	-1.79	-1.34	-0.01	1.08	1.38	3%
$0.4 < \|y\| < 0.8$	-1.54	-2.24	-2.61	-3.50	-2.70	0.78	-0.13	3%
$0.8 < \|y\| < 1.2$	-2.62	-4.35	-1.31	-0.50	-1.17	2.96	2.99	4%
$1.2 < \|y\| < 1.6$	-1.71	3.54	-3.99	-6.00	-2.66	1.93	-0.13	4%
$1.6 < \|y\| < 2$	3.07	1.99	-7.52	-7.71	-0.01	1.21	0.31	5%
$2 < \|y\| < 2.4$	1.35	-2.38	2.63	3.90	2.98	-7.73	-0.53	8%
PbPb Υ(1S)	α	n_{CB}	σ_1	σ_2/σ_1	f	Pol(1)	Pol(2)	Tot. PbPb%
$p_T < 2.5$	-15.18	-4.45	-5.95	-10.07	-4.66	0.03	0.69	9 %
$2.5 < p_T < 5$	-6.47	-0.84	-7.45	-6.24	-6.91	-0.00	-2.16	6 %
$5 < p_T < 8$	-17.25	-22.27	5.45	-9.37	3.27	-0.62	-2.38	12 %
$8 < p_T < 12$	5.28	1.60	-5.25	-1.84	-5.46	-0.35	-0.13	4 %
$12 < p_T < 20$	-0.73	0.72	0.05	-0.60	-0.47	-3.78	-2.00	4 %
$\|y\| < 0.4$	-11.11	-4.38	-0.63	0.37	-1.00	0.01	0.97	5%
$0.4 < \|y\| < 0.8$	-23.66	-4.96	-0.50	0.45	-0.73	1.74	-1.94	11%
$0.8 < \|y\| < 1.2$	-17.01	-4.45	-1.50	-8.49	-0.76	-5.66	-15.15	18%
$1.2 < \|y\| < 1.6$	5.05	4.37	-6.06	0.90	-8.69	-4.65	7.47	9%
$1.6 < \|y\| < 2$	-21.47	-10.51	-1.60	-0.82	-5.33	0.01	-18.56	22%
$2 < \|y\| < 2.4$	-43.54	-13.35	-14.46	-10.82	-12.77	-16.58	-15.77	28%
0-5	8.307	-18.687	13.935	12.136	12.161	-16.809	-0.002	14.4%
5-10	-1.265	3.440	-4.991	-1.337	-5.477	1.652	-3.915	12.0%
10-20	-24.197	-20.448	-8.347	-8.713	-6.883	4.301	-2.396	10.3%
20-30	-12.225	-19.523	-8.183	-7.417	-7.562	0.770	1.073	8.5%
30-40	1.041	1.333	0.893	1.038	0.655	-0.036	-8.471	12.0%
40-50	-5.149	-19.713	-3.219	-9.837	-1.663	0.332	-0.417	15.7%
50-70	-19.041	-16.327	-5.668	-2.435	-5.488	-1.896	2.248	5.4%
70-100	-25.068	-20.123	-0.930	-1.582	-1.285	0.152	0.209	21.5%

Table 5.4: Systematic deviations from the central result for Υ(1S) fitting in pp and PbPb, reported for each analysis bin. Last column: total systematic uncertainty from fitting.

	Signal					Background		Total %
pp Υ(2S)	α	n_{CB}	σ_1	σ_2/σ_1	f	Pol(1)	Pol(2)	Tot. Υ(2S)
$p_T < 2.5$	4.78	3.07	-3.00	0.49	-2.83	0.38	-10.60	11 %
$2.5 < p_T < 5$	5.33	4.37	-0.34	0.66	-1.15	0.02	-3.05	4 %
$5 < p_T < 8$	-5.32	-3.79	-3.71	-3.10	-2.97	1.47	-1.54	4 %
$8 < p_T < 12$	-3.84	-1.00	-3.92	-2.84	-3.49	-0.13	-0.45	3 %
$12 < p_T < 20$	0.53	0.81	-0.24	0.15	-0.15	0.37	0.87	1 %
$\|y\| < 0.4$	-1.74	2.54	-4.58	-5.21	-0.47	4.70	3.10	5%
$0.4 < \|y\| < 0.8$	-4.13	0.17	-4.95	-6.58	-4.35	-0.00	-2.36	5%
$0.8 < \|y\| < 1.2$	-4.22	-6.56	-3.63	-3.49	-3.41	9.57	-7.66	9%
$1.2 < \|y\| < 1.6$	0.85	3.80	-5.48	-6.60	-3.90	0.74	7.55	9%
$1.6 < \|y\| < 2$	-7.15	2.34	-8.97	-8.65	-1.81	-0.26	12.26	14%
$2 < \|y\| < 2.4$	3.59	-3.08	-0.13	0.03	0.08	0.02	1.85	3%
pp Υ(3S)	α	n_{CB}	σ_1	σ_2/σ_1	f	Pol(1)	Erf $\cdot$ exp + Pol(2)	Tot. 3S%
$p_T < 2.5$	7.10	4.28	-3.95	0.55	-3.77	0.49	-14.40	15 %
$2.5 < p_T < 5$	6.67	5.44	-0.35	0.52	-1.05	0.01	-3.09	5 %
$5 < p_T < 8$	-8.12	-5.05	-3.95	-2.01	-2.92	-0.28	-1.67	5 %
$8 < p_T < 12$	-6.56	-1.37	-3.50	-1.22	-3.36	-0.20	-0.93	4 %
$12 < p_T < 20$	1.11	1.13	-0.25	0.10	-0.15	0.78	1.75	2 %
$\|y\| < 0.4$	-2.40	3.45	-6.10	-6.78	-0.86	6.43	5.79	7%
$0.4 < \|y\| < 0.8$	-6.64	0.24	-8.26	-8.06	-6.87	-0.02	1.19	7%
$0.8 < \|y\| < 1.2$	-5.79	-8.00	-3.45	-2.64	-2.98	9.40	-10.04	0.11%
$1.2 < \|y\| < 1.6$	1.27	5.73	-5.01	-5.96	-3.72	-2.00	9.35	0.10%
$1.6 < \|y\| < 2$	-11.39	3.97	-2.92	-2.88	0.08	-0.85	1.38	6%
$2 < \|y\| < 2.4$	4.14	-3.17	-0.13	-0.13	-0.15	0.05	1.01	3%

Table 5.5: Systematic deviations from the central result for Υ(2S) and Υ(3S) fitting in pp, reported for each analysis bin. Last column: total systematic uncertainty from fitting.

	Signal					Background		Total %
PbPb Υ(2S)	α	n_{CB}	σ_1	σ_2/σ_1	f	Pol(1)	Pol(2)	Tot. Υ(2S)
$p_T < 5$	-12.70	-34.76	-9.03	-0.88	-8.64	11.6	0.16	17 %
$5 < p_T < 12$	-9.70	-15.42	-2.51	-6.93	-4.89	-1.3	-7.20	12 %
$12 < p_T < 40$	-1.39	-1.57	-0.17	-0.50	-0.29	-11.8	-9.72	12 %
$\|y\| < 1.2$	-13.42	-17.01	-3.21	-7.89	-2.38	6.56	27.51	29 %
$1.2 < \|y\| < 2.4$	-66.45	-13.63	-16.73	-0.20	-0.01	8.12	41.92	52 %
0-10	-54.2	-44.1	-19.0	-11.4	-18.8	21.8	28.0	45%
10-30	-21.8	-34.2	-19.3	-14.3	-15.5	28.2	-12.3	56%
30-50	-34.7	-55.3	-26.8	-24.4	-17.4	70.8	44.2	25%
50-100	-81.6	-46.7	-6.5	-11.6	-5.5	-12.4	-16.9	44%

Table 5.6: Systematic deviations from the central result for Υ(2S) fitting in PbPb, reported for each analysis bin. Last column: total systematic uncertainty from fitting.

Fit Results	pp			PbPb	
Loose cuts	$\mathcal{N}_{1S}$	$\mathcal{N}_{2S}$	$\mathcal{N}_{3S}$	$\mathcal{N}_{1S}$	$\mathcal{N}_{2S}$
$p_T < 2.5$	**1572 ± 53**	413 ± 34	190 ± 28	**761 ± 43**	39 ± 28
$2.5 < p_T < 5$	**1440 ± 46**	498 ± 33	266 ± 28	**679 ± 42**	61 ± 30
$5 < p_T < 8$	**992 ± 34**	330 ± 22	150 ± 17	**531 ± 34**	23 ± 24
$8 < p_T < 12$	**613 ± 28**	226 ± 19	108 ± 15	**362 ± 27**	33 ± 19
$12 < p_T < 20$	**338 ± 20**	129 ± 14	76 ± 11	**178 ± 16**	21 ± 9
$\|y\| < 0.4$	**1092 ± 38**	354 ± 25	165 ± 20	**502 ± 32**	26 ± 21
$0.4 < \|y\| < 0.8$	**1129 ± 40**	344 ± 26	171 ± 21	**505 ± 34**	48 ± 25
$0.8 < \|y\| < 1.2$	**996 ± 39**	314 ± 27	170 ± 23	**559 ± 38**	25 ± 27
$1.2 < \|y\| < 1.6$	**919 ± 38**	320 ± 28	123 ± 23	**533 ± 39**	-1 ± 28
$1.6 < \|y\| < 2$	**645 ± 34**	215 ± 24	86 ± 20	**365 ± 29**	34 ± 19
$2 < \|y\| < 2.4$	**251 ± 20**	49 ± 13	56 ± 12	**114 ± 17**	4 ± 11

Table 5.7: Fit results of signal parameters using the loose cuts (Υ(1S) analysis). The values actually used in the cross section computation are displayed with a bold font. Even if only the values fitted for the Υ(1S) peak will be used further, the fit results of Υ(2S) and Υ(3S) are also reported. The fit results follow the yields reported in Figures A.1, A.2, A.3 A.4 and A.5.

Fit Results	pp			PbPb	
Tight cuts	$\mathcal{N}_{1S}$	$\mathcal{N}_{2S}$	$\mathcal{N}_{3S}$	$\mathcal{N}_{1S}$	$\mathcal{N}_{2S}$
$p_T < 5$	1815 ± 53	**562 ± 37**	291 ± 33	846 ± 44	**54 ± 31**
$5 < p_T < 12$	1253 ± 40	**446 ± 27**	206 ± 22	660 ± 37	**45 ± 24**
$12 < p_T < 20$	307 ± 19	**119 ± 13**	69 ± 11	160 ± 15	**22 ± 9**
$\|y\| < 1.2$	2298 ± 55	**769 ± 37**	397 ± 31	1090 ± 46	**104 ± 31**
$1.2 < \|y\| < 2.4$	1213 ± 43	**451 ± 31**	222 ± 26	729 ± 40	**77 ± 27**
$p_T < 2.5$	967 ± 40	**299 ± 29**	**131 ± 24**	433 ± 34	49 ± 24
$2.5 < p_T < 5$	802 ± 35	**254 ± 24**	**166 ± 22**	385 ± 30	29 ± 21
$5 < p_T < 8$	722 ± 31	**246 ± 20**	**113 ± 16**	346 ± 27	8 ± 18
$8 < p_T < 12$	524 ± 26	**197 ± 18**	**90 ± 14**	300 ± 25	29 ± 18
$12 < p_T < 20$	307 ± 19	**119 ± 13**	**69 ± 11**	160 ± 15	22 ± 9
$\|y\| < 0.4$	782 ± 31	**265 ± 21**	**133 ± 17**	315 ± 24	15 ± 16
$0.4 < \|y\| < 0.8$	802 ± 33	**263 ± 21**	**130 ± 18**	355 ± 26	46 ± 18
$0.8 < \|y\| < 1.2$	700 ± 32	**240 ± 22**	**140 ± 19**	415 ± 29	43 ± 19
$1.2 < \|y\| < 1.6$	615 ± 30	**232 ± 22**	**103 ± 19**	390 ± 29	20 ± 19
$1.6 < \|y\| < 2$	437 ± 27	**180 ± 20**	**77 ± 16**	260 ± 24	49 ± 17
$2 < \|y\| < 2.4$	176 ± 16	**44 ± 11**	**46 ± 11**	83 ± 14	14 ± 10

Table 5.8: Fit results of signal parameters using the tight cuts (Υ(2S) analysis). The values actually used in the cross section computation are displayed with a bold font. Even if only the values fitted for the Υ(2S) and Υ(3S) peaks will be used further, the fit results of Υ(1S) are also reported. The fit results follow the yields reported in Figures A.18, A.19, A.20, A.21, A.22 and A.23.

Centrality percentiles	Yields		
Loose cuts	$\mathcal{N}_{1S}$	$\mathcal{N}_{2S}$	$\mathcal{N}_{3S}$
0-5	407 ± 36	60 ± 27	10 ± 25
5-10	410 ± 33	10 ± 23	9 ± 22
10-20	637 ± 40	23 ± 28	-46 ± 25
20-30	425 ± 31	-10 ± 20	-15 ± 20
30-40	283 ± 25	34 ± 16	-8 ± 14
40-50	170 ± 18	25 ± 12	23 ± 12
50-70	165 ± 17	12 ± 10	-8 ± 8
70-100	49 ± 9	4 ± 5	0 ± 4
0-100	2540 ± 79	158 ± 54	0 ± 35
pp	5014 ± 86	1580 ± 59	770 ± 49
Tight cuts	$\mathcal{N}_{1S}$	$\mathcal{N}_{2S}$	$\mathcal{N}_{3S}$
0-10	579 ± 37	44 ± 26	-3 ± 24
10-30	761 ± 39	55 ± 26	-12 ± 24
30-50	309 ± 24	60 ± 16	25 ± 15
50-100	148 ± 15	14 ± 10	-4 ± 8
0-100	1793 ± 61	173 ± 41	7 ± 38
pp (tight)	3511 ± 71	1208 ± 49	619 ± 41

Table 5.9: Fit results of signal yields in centrality bins (centrality integrated and pp data are inserted) for loose cuts (Υ(1S) analysis) and tight cuts (Υ(2S) analysis). The values for extractable for Υ(3S) are shown for completeness but are not used, except for the computation of the totally integrated cross section result.

Chapter 6

Corrections to the raw yield

Contents

I'll take a drive to Beverly Hills
Just before dawn
An' knock the little jockeys
Off the rich people's lawn
An' before they get up
I'll be gone, I'll be gone
Before they get up
I'll be knocking the jockeys off the lawn

Frank Zappa, in *Uncle Remus, Apostrophe (')*

6.1 Monte Carlo based corrections

6.1.1 Introduction

As described in Chapter 2, the Υ production rate is a rather abundant process at LHC energies, that is detected in CMS by the means of its dimuon decay, with the help of

the muon detectors. Although the production mechanisms at play are still to settle, we know that there are three separate resonances, the Υ(1S),Υ(2S) and Υ(3S) mesons, each of which decay into two muons in a somewhat standard QED annihilation process, easily identifiable in the dimuon invariant mass spectrum produced by e^+e^-, lepton-hadron, hadron-hadron and heavy-ion colliders. The width of such 'electromagnetic probes' is usually very small with respect to the current detector resolution, hence a distinct peak can be measured. Their production rate is estimated by repeating the collision enough times to record a statistically significant measurement.

Section 5 established such a rate, that I have called the *raw yields*, for our *pp* and PbPb samples. Measuring these raw yields was the first step towards estimating two important quantities:

- The Υ(nS) production rates in proton-proton collisions, called cross sections, $\sigma\left(pp \to \Upsilon(nS)X\right)$,

- The corrected invariant yields for Υ(nS) states in PbPb, $N\left(AA \to \Upsilon(nS)X\right)$.

These two quantities are to be properly normalised in order to obtain the nuclear modification factor from a direct comparison. This will be our third step, covered in Chapter 7.

The second step is covered here and consists of translating the raw yields into the actual number of events produced in the total number of collision events, whether they were detected or not. This is done by expressing our understanding of what can alter the Υ's decay in two muons up to the final step of offline reconstruction. Indeed, some candidate events are falling out of the detector sensitive material, and we should account for this, and some are simply not reconstructed.

Trying to cover the major sources of alteration in the signal, I have already mentioned the magnetic field, curving slow muons away from the outer muon chambers, and the p_T cuts applied to the individual muons. These two effects act in the same manner: the total accessible yield is constrained, reduced. The fraction of dimuon events that subsisted is defined as the *acceptance*, which I will detail in Section 6.1.2. The acceptance is computed in this case with a simple Monte Carlo simulation, and in principle does not require the use of detector level quantities, only generator level quantities, as we shall see.

Another source of alteration in the measurement is the reconstruction chain. It consists of three main sources, that can be taken as a common one for now. This includes the trigger performances, the global muon reconstruction, and the offline cleaning cuts applied. These effects are studied from detector based quantities, and for this reason I will treat them separately from the acceptance (although it is not unconceivable to see them as only one transfer function). Again, Monte Carlo simulations are used, this time to estimate the *efficiency* of triggering, reconstructing, and filtering offline. The efficiency will be covered in Section 6.1.3.

Finally, we will see that both definitions suffer from some assumptions regarding the simulated sample. The systematic uncertainties associated to the generated shapes and to the centrality determination will be treated in Section 6.1.4. In Section 6.2,

the accuracy of the detector simulation will be tested, and will open to second order corrections, obtained via a Tag and Probe method.

6.1.2 Acceptance

The raw Υ yields need to be corrected for the loss of events, caused by the kinematic cuts on the single muon η and p_T that are used in the analysis. Events are accepted if both muons are in the geometrical acceptance of the detector, i.e. within $|\eta^\mu| < 2.4$. The single muon p_T cuts for Υ(1S) are looser than for Υ(2S) and Υ(3S), as was presented in Section 5.3.1.

The acceptance is calculated as:

$$\alpha(p_T, y) = \frac{N^{\mu^+\mu^-}_{\text{detectable},M}(p_T, y)}{N^{\mu^+\mu^-}_{\text{GEN}\in|y|<2.4}(p_T, y)}, \tag{6.1}$$

where the numerator $N^{\mu^+\mu^-}_{\text{detectable},M}$ is the number of generated events passing the kinematical cuts, and $N^{\mu^+\mu^-}_{\text{GEN}\in|y|<2.4}(p_T, y)$ is the number of events generated, in the (p_T, y) analysis bin under consideration, within the coverage of the CMS muon stations.
The acceptance then depends on the single muon p_T^μ cuts applied to the analysis selection, which are recalled in Table 6.1.

Υ(1S)	"loose cut"	$\mathrm{p}_T^{\mu_1} > 3.5$ GeV/c	$\mathrm{p}_T^{\mu_2} > 4$ GeV/c
Υ(2S), Υ(3S)	"tight cut"	$\mathrm{p}_T^{\mu_1} > 4$ GeV/c	$\mathrm{p}_T^{\mu_2} > 4$ GeV/c

Table 6.1: Denominations and definitions of the cuts used in the Υ(1S) analysis and in the Υ(2S) and Υ(3S) analysis.

Since a non-zero quarkonium polarisation would impact the angular dimuon distributions, previous analyses [85, 86] used to study the effect of various polarisation configurations on the acceptance. Hence, Equation 6.1 should also exhibit a dependence on a polarisation anisotropy parameter λ_ϑ, itself depending on a choice of polarisation frame. We have seen in Chapter 2 the effect of various polarisation scenarii, in Figure 2.15 (the light blue band corresponding to various *spin alignment configurations*, as quoted in [85]). [86] reports that in the phase space of this analysis (low Υ p_T, and $|\eta| < 2.4$), anisotropies of $\pm 0.25, \pm 0.5$ and ± 1 would vary the obtained (pp) cross sections by about $\pm 5\%, \pm 10\%, \pm 20\%$, respectively.

However, it has been recently measured in [95] that the Υ polarisation in the phase space covered by CMS is small, up to a higher p_T range than what is covered in this analysis. For this reason, the acceptance is not accounting for other possibilities than the non-observed polarisations of Υ(1S), Υ(2S), Υ(3S).

If the polarisation were to change in heavy ion collisions, this would be an effect of the underlying physics in the medium in which the quarkonia are produced. Different

polarisations between *pp* and PbPb would mean different angular distributions for single muons in the laboratory frame. Having the same single muon cuts in *pp* and PbPb, a polarisation modification should hence reflect itself in the nuclear modification factor $R_{\rm AA}$, that we shall present in Chapter 7.

The acceptance being a quantity computed with generator-based number of events, we assume it is independent on the collision system[1]. Hence, there is only one acceptance computation for each state. Υ mesons are generated using official CMS configuration files for PYTHIA [136] particle generation. After making sure there is no kinematic filter in the generation, I have generated 1 million events for each state.

The acceptance is computed separately for each Υ state, and its value is by definition a number between 0 and 1, dependent on the considered portion of the ($p_T(\Upsilon)$, $|y(\Upsilon)|$) plane. In Figure 6.1, a smooth distribution of the generated Υ(1S) events is shown before and after applying the kinematic cuts of the analysis (left and right, respectively). I have removed the binning of the analysis in both panels, to get a better sense of how the events are distributed along p_T and rapidity. The z-axis is identical, to illustrate the loss in statistics after applying the acceptance cut.

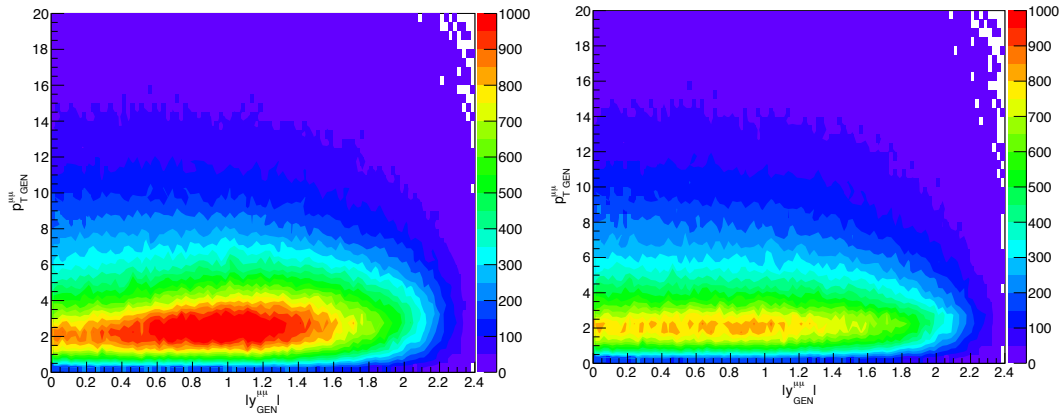

Figure 6.1: Phase space maps of the Υ(1S) generation sample: left, no cut applied; right, loose acceptance cut applied. A smooth contour drawing option is used.

The denominator of acceptance is represented by the left-hand-side plot, and the numerator appears to the right. The (p_T,$|y|$) binning presented in Section 5.3.3 is used to extract the acceptance corrections for the p_T- and y-differential analyses of each Υ state. The binned results for $\alpha(p_T,\mathrm{y})$ are presented for Υ(1S) in Table 6.2 with their statistical uncertainties (small since the MC samples used are very large).

The excited states, as we have seen in Table 6.1, are analysed with a tighter cut. Furthermore, the strong suppression seen in PbPb collisions for the excited states did not allow for such a fine binning as used for the *pp* yields. Coincidentally, Table 6.3 has the acceptance for Υ(2S) in two different sets of bins: the fine ones are used in the

[1]Unless the different collision systems are asymmetric, as in the case of p-A collisions. In such cases, the acceptance needs to be recomputed separately, the centre of mass of the collision not being at rest in the laboratory frame.

p_T [GeV/c]	α[1S](p_T)	$\|y\|$	α[1S](y)
0-2.5	0.456 ± 0.002	0-0.4	0.393 ± 0.002
2.5-5	0.298 ± 0.001	0.4-0.8	0.392 ± 0.002
5-8	0.277 ± 0.001	0.8-1.2	0.393 ± 0.002
8-12	0.374 ± 0.002	1.2-1.6	0.389 ± 0.002
12-20	0.513 ± 0.005	1.6-2	0.338 ± 0.002
0-100	**0.353 ± 0.001**	2-2.4	0.145 ± 0.001

Table 6.2: Acceptance correction factors as a function of p_T and y for Υ(1S). The left hand side contains the results for a p_T dependent binning. The right hand side contains the results for a rapidity-dependent binning. On the left hand side, the last entry at the bottom (boldfaced) corresponds to the integrated result.

p_T [GeV/c]	α[2S](p_T)	$\|y\|$	α[2S](y)
0-2.5	0.375 ± 0.002	0-0.4	0.310 ± 0.002
2.5-5	0.217 ± 0.001	0.4-0.8	0.310 ± 0.002
5-8	0.218 ± 0.002	0.8-1.2	0.307 ± 0.002
8-12	0.309 ± 0.003	1.2-1.6	0.308 ± 0.002
12-20	0.467 ± 0.007	1.6-2	0.271 ± 0.002
0-100	**0.279 ± 0.001**	2-2.4	0.117 ± 0.001
0-5	0.357 ± 0.001	0-1.2	0.309 ± 0.001
5-12	0.309 ± 0.001	1.2-2.4	0.241 ± 0.001
12-20	0.513 ± 0.005	-	-

Table 6.3: Acceptance correction factors as a function of p_T and y for Υ(2S). The left hand side contains the results for a p_T dependent binning. The right hand side contains the results for a rapidity-dependent binning. Bold font is used for the integrated result. The bottom panel has a coarser binning, corresponding to the PbPb analysis.

Υ(2S) pp cross section, while coarser ones are used for the PbPb invariant yields.

As we have seen in Chapter 5, the Υ(3S) yield is unobserved in PbPb. As a result, a confidence interval on the suppression of Υ(3S) will be presented later in Chapter 7, in which acceptance corrections would cancel in the ratio $\mathcal{N}_{3S}|_{\mathrm{PbPb}}/\mathcal{N}_{3S}|_{pp}$. For this reason, the Υ(3S) acceptance presented in Table 6.4 only applies to the pp Υ(3S) cross section.

Looking at the values obtained for α in all three states, we see that acceptances vary over the p_T and rapidity range studied. For example, let me compare the acceptance of Υ(1S) as a function of its transverse momentum, to the integrated value, $\alpha(\Upsilon(1S)) = 0.353 \pm 0.001$.

While it is approximately 30% higher in the lowest p_T bin ($\alpha(p_T \in [0., 2.5]\mathrm{GeV}/c) =$

p_T [GeV/c]	α[3S](p_T)	$\|y\|$	α[3S](y)
0-2.5	0.455 ± 0.001	0-0.4	0.367 ± 0.001
2.5-5	0.273 ± 0.001	0.4-0.8	0.366 ± 0.001
5-8	0.249 ± 0.001	0.8-1.2	0.366 ± 0.001
8-12	0.330 ± 0.001	1.2-1.6	0.361 ± 0.001
12-20	0.471 ± 0.002	1.6-2	0.312 ± 0.001
0-100	**0.329 ± 0.000**	2-2.4	0.136 ± 0.001

Table 6.4: Acceptance correction factors as a function of p_T and y for Υ(3S). The left hand side contains the results for a p_T dependent binning. The right hand side contains the results for a rapidity-dependent binning. Bold font is used for the integrated result. These factors are only used in the pp cross section calculation.

0.456 ± 0.002), $\alpha(\Upsilon(1S))$ decreases when $5 < p_T < 8$ GeV/c, to rise again at higher momenta. This can be understood when judging the kinematics of the $\Upsilon \to \mu\mu$ decay:

- When the resonance is produced almost at rest, the rest energy is of the order of the quarkonium's rest mass, $E \sim m_\Upsilon$. In this case, it will often occur that both muons will carry an energy of about $E_\mu \sim m_\Upsilon/2 \approx 5$ GeV/c^2, which is enough to reach the muon stations (i.e. 'fall in the acceptance of the detector');

- When the resonance rest frame is boosted with respect to the laboratory frame, the decay will appear asymmetric to the observer, with one muon carrying a larger fraction of the available decay momemtun than the other. Then, if the Υ is produced at a moderate p_T, say, between 3 and 8 GeV/c, it is likely that one of the muons will have a momentum p^μ_{LAB} such that $p^\mu_T < p_T$(cut). In this case the event does not pass the kinematic cut, and is lost;

- Finally reaching higher quarkonium momenta, both muons carry a large momentum and the acceptance increases again.

In this paragraph I have presented the acceptance, a computation of the number of Υ events passing the kinematical selection. This answered the question: "after producing X events of interest, what is α such that αX is the fraction of detectable events?". As we shall see in Section 6.1.4, the number X is not taken arbitrarily, as the kinematics of the production assumed by PYTHIA are varied to extract a systematic uncertainty on α.

6.1.3 Efficiency

The efficiency has been introduced above, saying that this correction accounts for all the other selection steps, namely: the trigger, the actual reconstruction chain that makes global dimuon pairs, and the offline quality and muon identification cuts. I have asserted that these sources can be treated in only one black box, with a single correction factor ε. Let me anticipate and say that although it is true at first order, a study has been done to assess the second order of this correction. This study has the advantage of being data-driven, so it also allows to gauge the level of understanding of our simulation of the detector. This so called *Tag and Probe* study is covered in Section 6.2.3.

The dimuon efficiency ε is defined as

$$\varepsilon(p_T, y, \text{cent.}) \quad = \quad \frac{N^{\mu^+\mu^-}_{\text{Reco.},M\in[R]}(p_T, y, \text{cent.})}{N^{\mu^+\mu^-}_{\text{detectable},M}(p_T, y)}. \tag{6.2}$$

Comparing with Equation 6.1, it is important to note that the denominator of ε, $N^{\mu^+\mu^-}_{\text{detectable},M}$, is the numerator of α, as defined above. This is the number of events that passed the kinematical cuts, i.e. falling in the acceptance of the detector.

The numerator of ε, $N^{\mu^+\mu^-}_{\text{Reco.},M\in[R]}$, is the number of dimuon events reconstructed in the (p_T, y, cent.)-bin under consideration. These events have passed all selection criteria of the analysis, namely:

- Two muons have fired the emulated version of the L1 trigger `L1DoubleMuOpen`, further filtered at HLT for `_HighQ`, which requests a confirmed signal from two combinations of RPC, CSC and DT subdetectors, as defined in Section 4.3;

- The muons have deposited enough hits in the muon stations to form *standalone muons*,

- These standalones could be matched to tracker tracks forming *global muon* refitted objects,

- Each global muon have passed the series of tracker and global quality cuts defined in Section 4.2.6,

- The combination of these global muons has resulted in a dimuon candidate falling in the Υ mass region $[R]$.

The dimuons are counted in the mass interval $[R_{1S}] \equiv [8.0, 10.5]$ GeV/c for Υ(1S), in $[R_{2S}] \equiv [8.5, 11]$ GeV/c for Υ(2S) and in $[R_{3S}] \equiv [8.8, 11.3]$ GeV/c for Υ(3S). Although the mass regions do overlap, there is no cross talk, since each state was simulated separately.

The numerator $N^{\mu^+\mu^-}_{\text{Reco.},M\in[R]}$ can also depend on the centrality of the heavy ion event. The HYDJET events are generated flat in centrality, and there is one PYTHIA Υ embedded in every event. I have thus removed the centrality dependence in the

p_T [GeV/c]	ε[1S]$_{pp}$	ε[1S]$_{\mathrm{PbPb}}$	$\lvert y \rvert$	ε[1S]$_{pp}$	ε[1S]$_{\mathrm{PbPb}}$
0-2.5	0.659 ± 0.002	0.589 ± 0.005	0-0.4	0.709 ± 0.003	0.611 ± 0.005
2.5-5	0.648 ± 0.002	0.588 ± 0.005	0.4-0.8	0.711 ± 0.003	0.639 ± 0.006
5-8	0.686 ± 0.003	0.651 ± 0.006	0.8-1.2	0.713 ± 0.003	0.674 ± 0.006
8-12	0.716 ± 0.004	0.712 ± 0.005	1.2-1.6	0.674 ± 0.003	0.656 ± 0.006
12-20	0.757 ± 0.005	0.753 ± 0.005	1.6-2	0.615 ± 0.003	0.611 ± 0.007
0-100	**0.679 ± 0.001**	**0.633 ± 0.003**	2-2.4	0.500 ± 0.004	0.521 ± 0.010

Table 6.5: Efficiency correction factors as a function of p_T and y for Υ(1S). From left to right, in order of appearance: p_T binning, pp efficiency *vs.* p_T, PbPb efficiency *vs.* p_T, rapidity binning, pp efficiency *vs.* y, PbPb efficiency *vs.* y. In bold font appears the integrated result for ε[1S]$_{pp}$ (left) and ε[1S]$_{\mathrm{PbPb}}$ (right).

Centrality	ε[1S](Cent.)$_{\mathrm{PbPb}}$
0%-5%	0.606 ± 0.007
5%-10%	0.626 ± 0.008
10%-20%	0.636 ± 0.006
20%-30%	0.646 ± 0.006
30%-40%	0.648 ± 0.006
40%-50%	0.651 ± 0.006
50%-70%	0.657 ± 0.004
70%-100%	0.656 ± 0.004

Table 6.6: Υ(1S) reconstruction efficiency as a function of centrality in PbPb. Increasing centrality percentiles correspond to lower multiplicities (e.g., the first line reads as the efficiency for the 5% most central events).

denominator of Equation 6.1, which is a generation level quantity, as well as in Equation 6.2. However, the heavy ion multiplicity environment may have an impact on the reconstruction or triggering performances, inducing a multiplicity dependence. As a result, the pp and PbPb efficiencies are not equal, and are computed separately for each collision setup.

The p_T- and y-dependent results for Υ(1S) are reported in Table 6.5. The heavy ion efficiencies $\varepsilon_{\mathrm{PbPb}}$ are slightly outperformed by the pp reconstruction efficiency ε_{pp}, especially at low p_T, where there is an approximately 10 % difference.

The centrality dependent efficiency $\varepsilon_{\mathrm{PbPb}}$ for Υ(1S) is presented in Table 6.6. There, one can notice that the efficiency does not vary with the event centrality by more than 8%, from the most peripheral to the most central events.

Table 6.7 sums up the efficiencies ε[2S]$_{pp}$ used in p_T- and rapidity dependent pp cross sections. As mentioned earlier, the PbPb analysis of Υ(2S) makes use of a different binning; For this reason, Table 6.8 contains PbPb efficiencies *vs.* p_T and y along with the corresponding pp efficiencies recomputed to reflect the proper binning.

p_T [GeV/c]	ε[2S]$(p_T)_{pp}$	$\|y\|$	ε[2S]$(y)_{pp}$
0-2.5	0.721 ± 0.002	0-0.4	0.791 ± 0.004
2.5-5	0.729 ± 0.003	0.4-0.8	0.795 ± 0.004
5-8	0.744 ± 0.004	0.8-1.2	0.781 ± 0.004
8-12	0.758 ± 0.005	1.2-1.6	0.726 ± 0.004
12-20	0.784 ± 0.007	1.6-2	0.643 ± 0.004
0-100	**0.743 ± 0.002**	2-2.4	0.519 ± 0.005

Table 6.7: Efficiency correction factors of Υ(2S) in pp, as a function of p_T and y. From left to right, in order of appearance: p_T binning, efficiency *vs.* p_T, rapidity binning, efficiency *vs.* y. The integrated result $\varepsilon[2S]_{pp}$ is in bold.

In Table 6.8, it can again be seen that the pp efficiencies are slightly higher than the PbPb ones. The centrality dependent efficiencies of the Υ(2S) PbPb analysis are shown in Table 6.9.

p_T [GeV/c]	ε[2S]$(p_T)_{pp}$	ε[2S]$(p_T)_{PbPb}$	$\|y\|$	ε[2S]$(y)_{pp}$	ε[2S]$(y)_{PbPb}$
0-5	0.726 ± 0.002	0.692 ± 0.005	0-1.2	0.789 ± 0.002	0.747 ± 0.004
5-12	0.750 ± 0.003	0.741 ± 0.005	1.2-2.4	0.666 ± 0.002	0.681 ± 0.005
12-20	0.784 ± 0.007	0.789 ± 0.004	**0-2.4**	**0.743 ± 0.002**	**0.722 ± 0.003**

Table 6.8: Efficiency correction factors of Υ(2S) in pp and PbPb, as a function of p_T and y for, in bins of the PbPb analysis. From left to right, in order of appearance: p_T binning, pp efficiency *vs.* p_T, PbPb efficiency *vs.* p_T, rapidity binning, pp efficiency *vs.* y, PbPb efficiency *vs.* y. In bold font appears the integrated results for $\varepsilon[2S]_{pp}$ (left) and $\varepsilon[2S]_{\mathrm{PbPb}}$ (right).

Centrality	ε[2S](Cent.)$_{\mathrm{PbPb}}$
0%-10%	0.698 ± 0.008
10%-30%	0.724 ± 0.005
30%-50%	0.734 ± 0.005
50%-100%	0.742 ± 0.004

Table 6.9: Reconstruction efficiency as a function of centrality for Υ(2S) in PbPb collisions.

Table 6.10 sums up the efficiencies $\varepsilon[3S]_{pp}$ used in p_T- and rapidity dependent pp cross sections. Given the fact that Υ(3S) was not observed in PbPb, we did not decide to generate a large sample to estimate the Υ(3S) reconstruction efficiency.

However, an estimation of what would be the efficiency for Υ(3S) in PbPb can be computed, assuming that the ratio of pp and PbPb efficiencies stays the same for Υ(3S)

p_T [GeV/c]	ε[3S]$(p_T)_{pp}$	$\|y\|$	ε[3S]$(y)_{pp}$
0-2.5	0.731 ± 0.003	0-0.4	0.804 ± 0.003
2.5-5	0.732 ± 0.002	0.4-0.8	0.804 ± 0.003
5-8	0.751 ± 0.003	0.8-1.2	0.787 ± 0.003
8-12	0.769 ± 0.003	1.2-1.6	0.734 ± 0.003
12-20	0.795 ± 0.004	1.6-2	0.649 ± 0.003
0-100	**0.752 ± 0.001**	2-2.4	0.522 ± 0.005

Table 6.10: Efficiency correction factors of Υ(3S) in pp, as a function of p_T and y. From left to right, in order of appearance: p_T binning, efficiency *vs.* p_T, rapidity binning, efficiency *vs.* y. In bold font appears the integrated results for $\varepsilon[3S]_{pp}$.

as it is for Υ(2S):

$$\frac{\varepsilon[3S]_{\mathrm{PbPb}}}{\varepsilon[3S]_{pp}} \approx \frac{\varepsilon[2S]_{\mathrm{PbPb}}}{\varepsilon[2S]_{pp}} = 0.972 \tag{6.3}$$

Using this scaling factor and the integrated efficiency in pp, $\varepsilon[3S]_{pp} = 0.752 \pm 0.001$, we get an efficiency $\varepsilon[3S]_{\mathrm{PbPb}} = 0.731$, that will be used in the computation of the upper limit on Υ(3S) suppression in PbPb.

The question answered at the end of the acceptance paragraph can be directly extended to acceptance times efficiency: "after producing X events of interest, out of which αX were detectable, what is ε such that $\alpha\varepsilon X$ is the fraction of detected events?". The importance of the assumed spectrum for X has been mentioned already, and impacts both α and ε. The next paragraph will test the various assumptions on generated shapes and thus will provide an estimate of the systematic uncertainty coming from these assumptions.

6.1.4 Systematic uncertainties

From the generated Υ spectrum

To validate the strategy used for acceptance and efficiency, I have compared the generated spectra of Υ states (in other words, the physical spectrum that PYTHIA assumes as 'true') to the final pp cross section results, obtained after signal extraction and applying all corrections, including the Tag and Probe presented in the next Section. The differences seen in Υ(1S),Υ(2S) and Υ(3S) p_T distributions between PYTHIA and pp data can be seen in the following Figure 6.2, alongside with their respective ratios (Data/PYTHIA). These ratios seem to increase linearly with p_T, so this trend was fitted to a straight line to obtain a re-weighting of the generated spectra. The same procedure was applied to rapidity-differential cross sections.

The reweighting functions w_1, w_2 and w_3, that are applied to Υ(1S), Υ(2S) and Υ(3S), are respectively defined in Equations 6.4 to 6.6

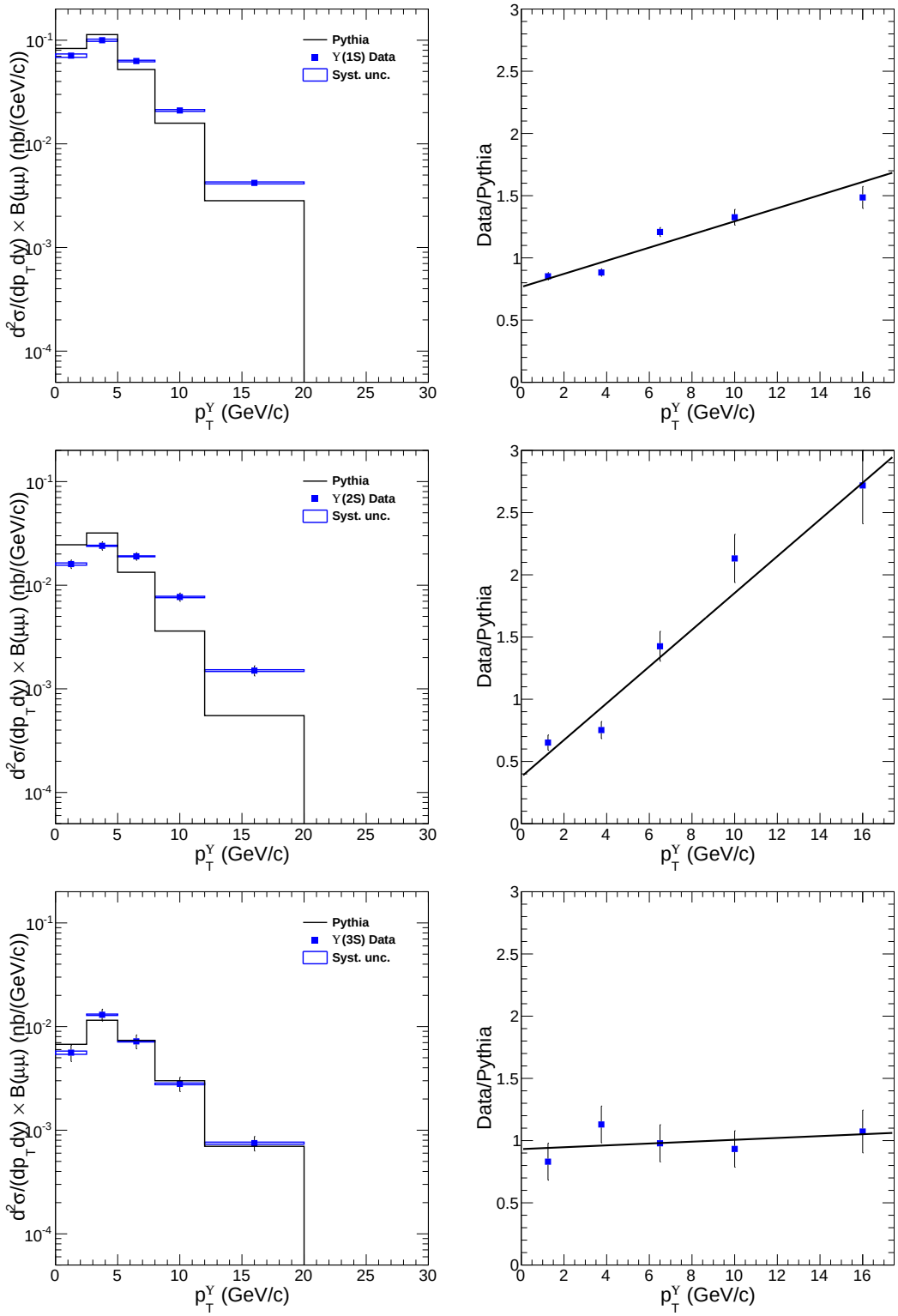

Figure 6.2: Left: p_T-spectrum of Υ(nS) production measured in pp data at $\sqrt{s}$= 2.76 TeV(blue squares), assumed by PYTHIA (histogram). Right: ratio of the two distributions Data/PYTHIA, fitted with a line to extract the weight functions $w_n(p_T)$. Top: Υ(1S); Middle: Υ(2S); Bottom: Υ(3S).

$$w_1(p_T) = 0.766 + 0.053 * p_T^{\rm GEN} \quad (6.4)$$
$$w_2(p_T) = 0.377 + 0.148 * p_T^{\rm GEN} \quad (6.5)$$
$$w_3(p_T) = 0.932 + 0.00745 * p_T^{\rm GEN} \quad (6.6)$$

After re-weighting the MC events used in acceptance and efficiency, nominal acceptance and efficiency corrections were obtained (which are the ones I have presented above in Sections 6.1.2, 6.1.3). For the purpose of estimating a systematic uncertainty accounting for the differences in observed spectra, variations are performed by changing the slope of w_1, w_2 and w_3 by $\pm 20\%$.

Changing the p_T slope of the weights by $\pm 20\%$ has an effect on the p_T- and y-dependence of $\alpha\varepsilon$, the product of acceptance and efficiency. To extract a systematic uncertainty on $\alpha\varepsilon$ from the slope variations, the maximum deviations *vs.* p_T and *vs.* y are used. In PbPb, an additional uncertainty source from the centrality distribution is considered, which is reviewed next.

For the case of Υ(1S), the nominal results for acceptance times efficiency *vs.* rapidity and p_T are presented in Table 6.11 for pp and Table 6.12 for PbPb. The statistical uncertainties displayed there are only related to the size of the simulation samples.

The systematic uncertainties $\alpha\varepsilon_{pp}$ presented in Table 6.11 for pp have a relative size of $2 \sim 3$ % for the Υ(1S) p_T-dependence, and $1 \sim 2$ % for the Υ(1S) rapidity dependence.

p_T [GeV/c]	$\alpha\varepsilon_{pp}$[1S](p_T)	$\lvert y\rvert$	$\alpha\varepsilon_{pp}$[1S](y)
0-2.5	0.301 ± 0.001 ±0.008	0-0.4	0.279 ± 0.002 ± 0.003
2.5-5	0.193 ± 0.001 ±0.004	0.4-0.8	0.278 ± 0.002 ± 0.003
5-8	0.190 ± 0.001 ±0.006	0.8-1.2	0.280 ± 0.002 ± 0.003
8-12	0.267 ± 0.002 ±0.008	1.2-1.6	0.262 ± 0.002 ± 0.003
12-20	0.388 ± 0.004 ±0.012	1.6-2	0.208 ± 0.001 ± 0.004
0-100	**0.239 ± 0.001 ±0.007**	2-2.4	0.073 ± 0.001 ± 0.002

Table 6.11: Acceptance × efficiency for Υ(1S) in the pp case. Listed uncertainties are first statistical from MC sample size, and systematic second. Integrated values are boldfaced.

From the generated centrality distribution

In PbPb, the centrality of the collision is used to characterise experimentally the impact parameter between the two Pb ions. Because of the high multiplicity in the final state, one must model correctly how the event reconstruction chain performs with increasing multiplicities, i.e. by measuring the efficiency as a function of the centrality of the event.

In order to do so, all Υ events simulated with PYTHIA are embedded in a HYDJET simulated event. HYDJET is a minimum bias event generator; as a result, the

distribution of generated events is uniform over all centrality percentiles (we often say it is 'flat' in centrality).

However, the natural production rate of quarkonia in heavy ions is *not* uniform with centrality. Since quarkonium production is a hard process, its rate scales (at first order) with the number of hard nucleon-nucleon collisions. Therefore, embedding one Υ event in each HYDJET event breaks the N_{coll}-dependence usually observed in hard processes. Measuring the efficiency of detecting Υ with a wrong centrality distribution would bias the result.

To mimick the true centrality distribution, the simulated Υ are reweighted to reflect to our best knowledge of the centrality dependence. Indeed, if Υ were not modified in heavy ions, we would see a perfect N_{coll} scaling, which is not the case.

The reweighting factor for each centrality bin is presented in Equation 6.7. It is the mean number of binary collisions for this bin, multiplied by the measured suppression factor $R_{\text{AA}}(\Upsilon(\text{nS}))$ (obtained with a simple N_{coll} weighting to the Υ simulated distributions):

$$w(c_0\%\text{–}c_1\%) = R_{\text{AA}}(c_0\%\text{–}c_1\%)\,\frac{1}{c_1 - c_0}\int_{c_0}^{c_1} N_{\text{coll}}\,\mathrm{d}c \equiv R_{\text{AA}}(\text{bin})\langle N_{\text{coll}}(\text{bin})\rangle, \quad (6.7)$$

where c_0, c_1 are the centrality percentiles of the bin considered (e.g. 5%–10%).

Figure 6.3 shows the centrality distributions for events in data and MC, after applying the centrality weighting.

We cannot get rid of the N_{coll} weighting to get a meaningful centrality distribution. Otherwise, the (red) MC distribution would look rather flat, and bias the efficiency.

Efficiencies are computed with the centrality reweighting, and compared to the efficiencies obtained with a simpler weighting of N_{coll}, that is, setting R_{AA} to 1 in Equation 6.7. The systematic uncertainty from this procedure is taken as the difference between the two efficiencies. The total Υ(1S) $\alpha \times \varepsilon$ systematic uncertainties are obtained by summing in quadrature this uncertainty and the two uncertainties from shifting the shapes *vs.* p_T and y.

The total Υ(1S) $\alpha \times \varepsilon$ with the systematic uncertainties are presented in Table 6.12 for PbPb efficiencies. Because the p_T and rapidity spectra came from PYTHIA, the effect of shifting the kinematics of the Υ is of the same order as what was seen in the previous paragraph for *pp*. However, the relative size of the uncertainties appear larger in PbPb, of the order of $7 - 10$ %, which is due to the centrality re-weighting procedure. In other words, the uncertainty on the assumed centrality distribution for Υ is dominating the systematic uncertainties on $\alpha\varepsilon$ in PbPb.

In this section, I have presented the first-order corrections applied to our extracted raw yields to evaluate the loss due to analysis cuts and detector inefficiencies. In the process, I have argued that $\alpha\varepsilon$ could be seen as the transfer function between the physical yield and the experimental measurement. This assumes that all sources of inefficiency (trigger, identification, etc.) are properly decscribed by Monte Carlo simulations. The next section details how this assumption is checked.

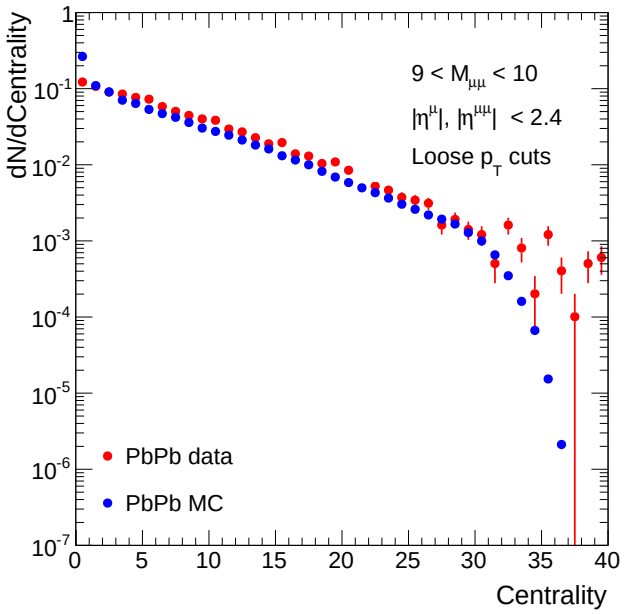

Figure 6.3: Centrality distribution of dimuon candidates in the mass range of the Υ measured in data (red), and Υ generated with HYDJET, after $N_{\rm coll}$ weighting (blue). The x axis corresponds to generated centrality bins: each bin is 2.5% of the centrality percentile table.

p_T [GeV/c]	$\alpha\varepsilon$[1S](p_T)	$\lvert y \rvert$	$\alpha\varepsilon$[1S](y)
0-2.5	0.269 ± 0.002 ± 0.022	0-0.4	0.240 ± 0.002 ± 0.012
2.5-5	0.175 ± 0.002 ± 0.013	0.4-0.8	0.250 ± 0.002 ± 0.012
5-8	0.181 ± 0.002 ± 0.012	0.8-1.2	0.265 ± 0.003 ± 0.014
8-12	0.266 ± 0.003 ± 0.016	1.2-1.6	0.255 ± 0.003 ± 0.019
12-20	0.387 ± 0.004 ± 0.020	1.6-2	0.206 ± 0.003 ± 0.025
0-100	**0.223 ± 0.001 ± 0.015**	2-2.4	0.076 ± 0.002 ± 0.011

Centrality	$\alpha\varepsilon$[1S](Cent.)$_{\rm PbPb}$
0%-5%	0.214 ± 0.002 ± 0.015
5%-10%	0.221 ± 0.003 ± 0.015
10%-20%	0.224 ± 0.002 ± 0.016
20%-30%	0.228 ± 0.002 ± 0.016
30%-40%	0.229 ± 0.002 ± 0.016
40%-50%	0.230 ± 0.002 ± 0.016
50%-70%	0.232 ± 0.002 ± 0.016
70%-100%	0.231 ± 0.002 ± 0.016

Table 6.12: Acceptance × efficiency for Υ(1S) in the PbPb case. Top: tables for p_T- and y-binned efficiencies. Bottom: Centrality-binned efficiencies. Listed uncertainties are statistical first and systematic second.

6.2 Data-driven corrections and comparison to simulation

6.2.1 Data-MC comparisons of muon kinematics

First, let us look at the kinematics of the muons produced in our collisions, and compare to what is obtained in the simulated samples.

Figure 6.4 has the distributions for single muons from the mass region of the Υ, for data and MC. One can see that within the statistical accuracy of the data, the distributions for ϕ and η are in a fairly good agreement.

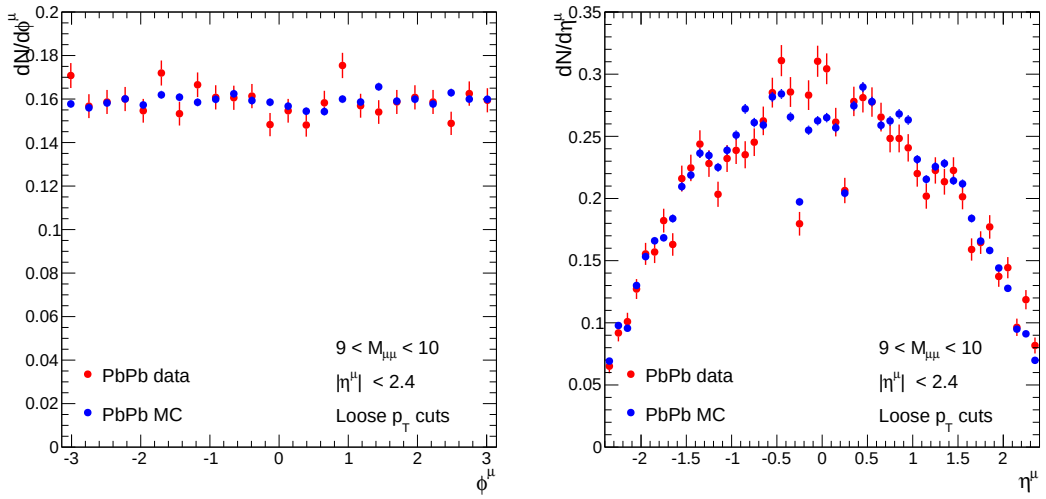

Figure 6.4: Left: azimuthal ϕ distribution of single muons from pairs in the mass region of the Υ. Right: pseudorapidity distribution of single muons from pairs in the mass region of the Υ. Generated Υ are in blue, and red is used for data.

The single muon p_T distributions are worth looking at as well. Since the collision data has signal and background, the p_T distribution for single muons is expected to be a mix of muons coming from Υ, and muons coming from the background. Consequently, the p_T distributions will not coincide automatically, and a proper comparison can only be done by looking at background subtracted data. Figure 6.5 (left) shows the single muon distributions in data and MC before background subtraction.

One can point out that the p_T distribution is harder in the Monte Carlo than in the data. In order to investigate the origin of this discrepancy, we first compare the distributions of same charge muons (hence, background only) and opposite charge muons (with signal and background contributions). We find that the p_T^μ distribution of same charge muons is softer than that of opposite charge muons, as can be seen in Figure 6.5 (right). This could indicate that the background yields softer p_T^μ distributions, thus possibly explaining the discrepancy observed on the opposite charge muon p_T^μ distributions in the data (hence, signal and background) and in the Monte Carlo (only signal generated).

For the sake of this comparison, we have therefore *corrected* the data by performing a background subtraction to the opposite-charge p_T^μ distributions to check whether the

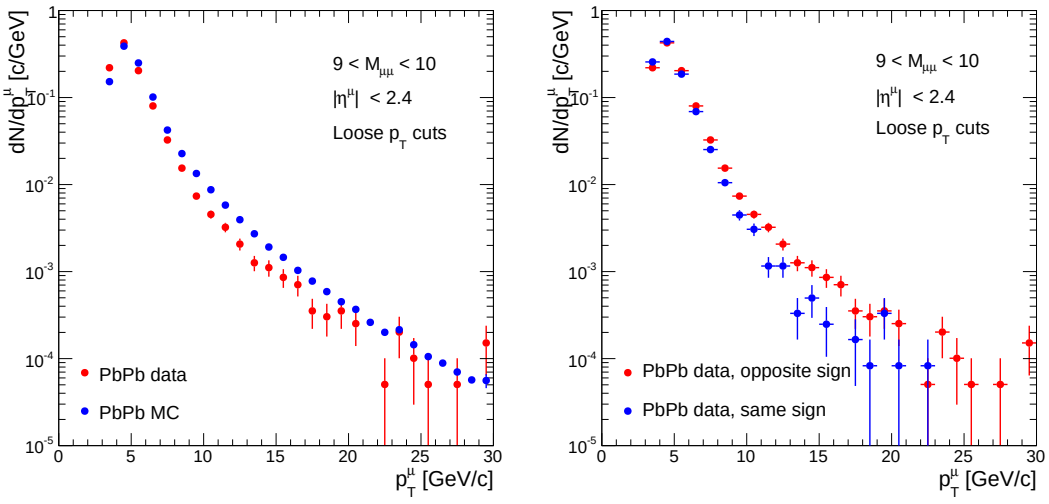

Figure 6.5: Single muon p_T distributions. Muons come from dimuon pairs in the mass region of the Υ, $9 < M < 10$ GeV/c^2. In both panels, red symbols represent the muon p_T distribution in PbPb collisions. On the left panel, muons from generated Υ are in blue. On the right, muons from same-charge pairs are in blue.

actual discrepancy between PbPb data and Monte Carlo is due to the background contribution and not from a genuine MC failure. Assuming that the p_T^μ distribution from the background has the same shape as that from the same-charge sample, the 'background-subtracted' data reads

$$\frac{dN^{\text{sub}}}{dp_T} = \frac{dN^{\text{opp. charge}}}{dp_T} - \frac{N^{\text{bkgd}}}{N^{\text{same charge}}} \frac{dN^{\text{same charge}}}{dp_T}, \tag{6.8}$$

where $N^{\text{same charge}}$ and N^{bkgd} are respectively the number of same-charge events and the number of background events in the mass range $9 < M < 10$ GeV/c^2. Assuming that the number of (full) background events over the number of same-charge events is identical in the mass ranges $[8;9]$ GeV/$c^2$and $[9;10]$ GeV/c^2, we estimate the number of background events in the signal mass range to be given by $N^{\text{bkgd}} = N^{\text{opp. charge}}(8 < M < 9)/N^{\text{same charge}}(8 < M < 9) * N^{\text{same charge}}$. This corrected distribution is compared to the Monte Carlo prediction in Figure 6.6 and now shows a very good agreement, giving confidence in the Monte Carlo used to compute acceptance and efficiency corrections.

6.2.2 Data-MC comparisons of muon quality

Understanding the effect of the muon identification cuts is especially important for the estimation of the dimuon reconstruction efficiency. As we have seen in Section 6.1.3, the reconstruction efficiency can be split in three main parts:

$$\varepsilon = \varepsilon(\text{trig}) \cdot \varepsilon(\text{ID}) \cdot \varepsilon(\text{trk}) \tag{6.9}$$

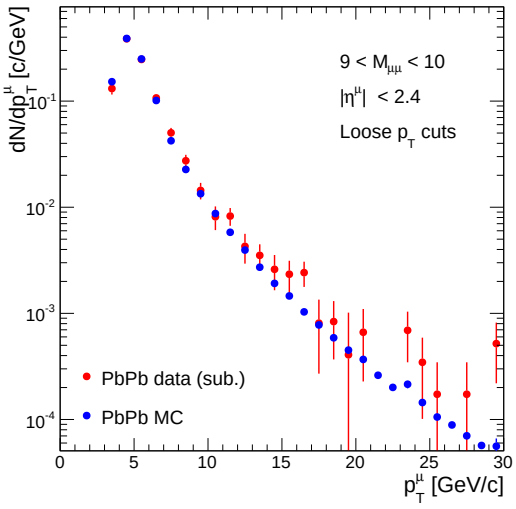

Figure 6.6: p_T distribution of single muons from pairs in the mass region of the Υ. Right: background subtracted data is in red, and muons from generated Υ are in blue.

where ε(trig) is the trigger efficiency, ε(ID) is the result of applying identification cuts, and ε(trk) is the silicon tracker's tracking efficiency. Note that I have not specified whether I speak about muons or Υ or any other particle. This point will be assessed later. The identification efficiency for muons, ε(MuonID), is defined to estimate the effect of the following cuts:

- each muon-track has been measured in at least one pixel layer,
- number of tracker hits of the muon-track > 10,
- reduced χ^2 of the muon-track < 4,
- reduced χ^2 of the global muon < 10,
- transverse impact parameter of each muon with respect to the primary vertex, $D_{xy} < 3$ cm,
- longitudinal impact parameter of each muon with respect to the primary vertex $D_z < 15$ cm,
- The track is arbitrated: coincides with an existing STA muon within 3 times the spread of the muon track in the x-y plane.
- isGlobalMuon() and isTrackerMuon() (cf. Section 4.2.6 for more information).

The plots in Figure 6.7 show a study of the Data and MC distributions for events in the J/ψ mass range (used for the much larger statistics than in the Υ case), passing the above cuts only. i.e. no p_T (μ) or trigger requirement was applied. The detail of each distribution is quite clear: there are a few discrepancies, and it is believed that these discrepancies may result in a mis-conceived MC dimuon efficiency.

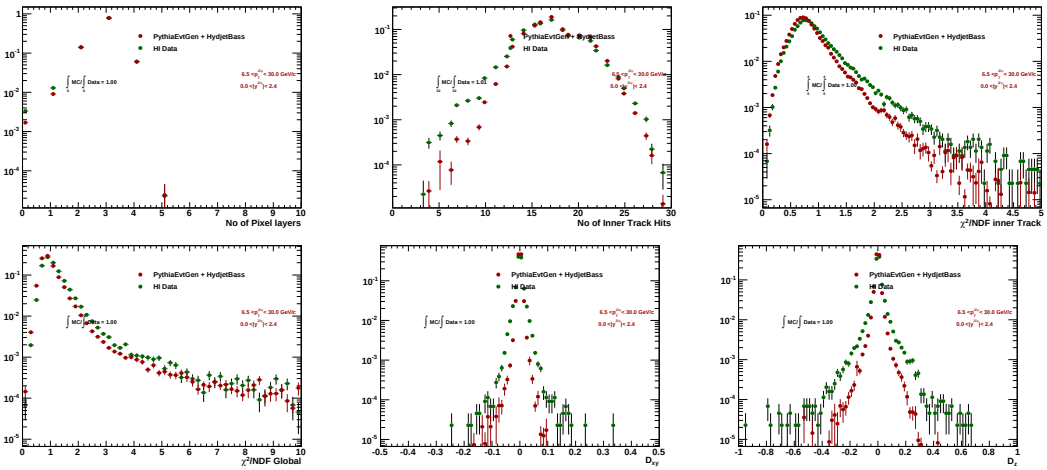

Figure 6.7: Tracker muon and global muon quality variables in MC and Data. Muons used are J/ψ decay muons.

6.2.3 The Tag and Probe method

In data analysis, one of the most important elements is to estimate the efficiency accurately and reliably. Monte Carlo (MC) simulation is generally used for the estimation of the efficiency but produces large systematic uncertainties due to the imperfections in modeling the detector response. Therefore, any measure of the particle efficiency from the data itself is of tremendous interest. One well established data-driven approach to measure efficiencies of particles is the 'Tag and Probe' technique [137].

The Tag and Probe method utilizes a known mass resonance (e.g. J/ψ, Υ, Z) to select decay particles, and probe the efficiency of a particular selection criterion on those particles. In general the "tag" is an object that passes a set of tight selection criteria designed to isolate the required particle type (usually an electron or muon, though in principle the method is not strictly limited to these). Tags are often referred to as "golden" electrons or muons, and the fake rate for passing tags selection criteria should be very small. A generic set of the desired particle type (i.e. with potentially very loose selection criteria) known as "probes" is selected by paring these objects with tags such that the invariant mass of the combination is consistent with the mass of the resonance. Combinatorial backgrounds may be eliminated through any of a variety of background subtraction methods such as fitting, or sideband subtraction. The definition of the probe object depends on the specifics of the selection criterion being examined.

Invariant mass plots are then made by requiring (or not) the probed criterion to be passed. The ratio of the number of resonances obtained with (or without) the probed criterion, measures its efficiency.

Since 2010, this method has been employed in CMS, in particular in the heavy ion group, for the validation of efficiencies measured with MC, as in [2, 3, 138, 139]. The data-driven Tag and Probe method will be employed to estimate single-muon trigger, identification, and tracking efficiencies. A comparison of the results obtained by apply-

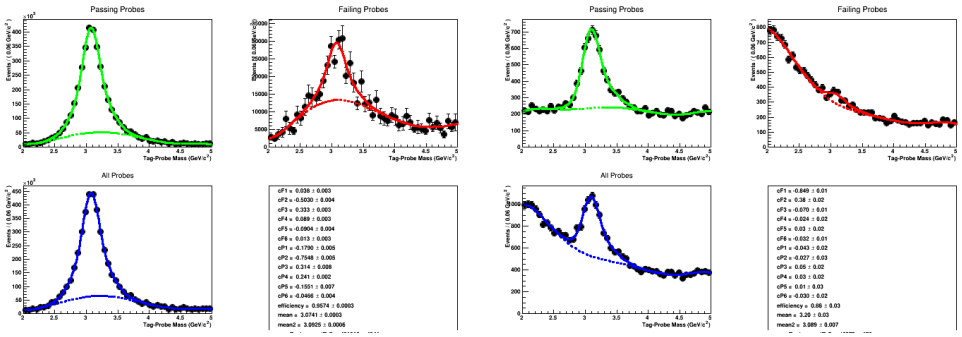

Figure 6.8: Examples of $pp \to J/\psi \to \mu\mu$ tag-probe invariant mass fits in data *(right)* MC *(left)*. Blue: tags paired to all probes, Red: tags paired to failing probes, Green: tags paired to passing probes. The ratio of (blue) and (green) integrated curves give the efficiency of the probed selection.

ing the technique to both data and MC simulation allows to estimate related systematic uncertainties. The J/ψ signal resonance is used for its large rate of production. Two tag-probe invariant mass distributions are formed, in the vicinity of the J/ψ nominal mass, according to whether the probe passes or fails the criteria for which the efficiency is being measured.

Depending on the (p_T, η) bin considered, the passing and failing probes peak can be more or less difficult to fit. In the following Figure 6.8, I have chosen an example where the pp tracking efficiency is taken from MC tag-probe pairs on the left and from real data on the right. In the following, I will detail more the various parts of the Tag and Probe workflow.

6.2.4 Single muon efficiencies

Here are defined the 'tag', 'probe' and 'passing probe' definitions used for the combined efficiency of muon identification and trigger requirements.

The tag muon selection/definition is the same in both cases: a high-quality muon passing all analysis cuts, as described in the item list above, that is matched to a single muon trigger.

Trigger+ID efficiency

- Muon reconstruction and identification efficiency (including the inner to outer track matching efficiency), and trigger efficiency within the single muon acceptance cut defined in Section 5.3.1:
  - probe: tracker muon in the acceptance, that pass inner tracker quality cuts
  - passing probe: probe that is also a global muon passing all analysis selection cuts, and is matched to the HLT_HIL1DoubleMu0_HighQ (for PbPb) and HLT_PAL1DoubleMu0_HighQ (for pp).

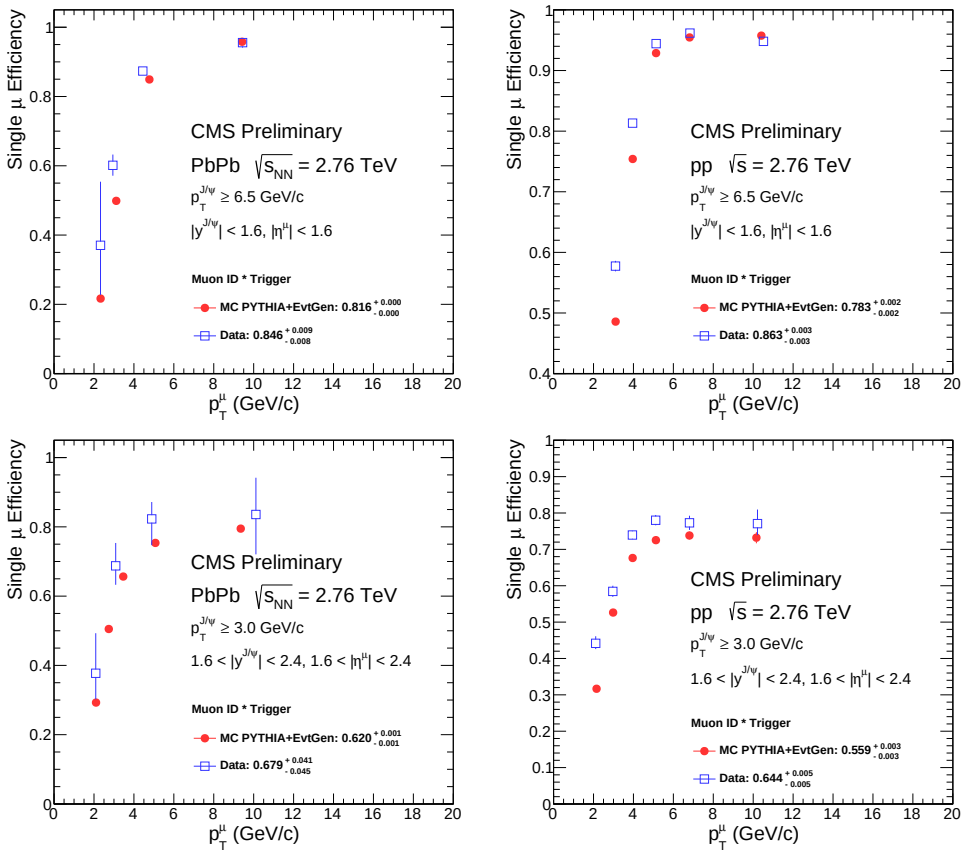

Figure 6.9: Trigger and ID single muon efficiencies computed with the tag and probe method. Comparison between data *(open blue squares)* and MC *(red full circles)*. Top, left: efficiencies in the barrel using PbPb data and MC. Top, right: efficiencies in the barrel using pp data and MC. Bottom, left: efficiencies in the endcaps using PbPb data and MC. Bottom, right: efficiencies in the endcaps using pp data and MC.

In the following Figure 6.9, the resulting single muon *pp* and PbPb efficiencies from the tag and probe method are presented in two phase space regions: First, the barrel (for p_T (J/ψ) above 6.5 GeV/c and muon $|\eta|$ <1.6) and second, the forward (for p_T (J/ψ) above 3 GeV/c and muon 1.6<$|\eta|$<2.4).

First of all, we see a clear difference in the overall efficiencies between endcaps and barrel pseudorapidities. This motivated the splitting of our data in the first place, to get a consistent correction for various detector areas. Second, there is an obvious difference in performance between the PbPb and pp cases. Still, it is worth noting that in both cases, our reconstruction, trigger and identification strategy is efficient down to the lowest p_T muons kept in our analysis (muon $p_T > 3.5$ GeV/c). Finally, and maybe most importantly, there are consistently some relatively small differences between data and MC, which justify the second-order corrections that we are trying to compute from single muons.

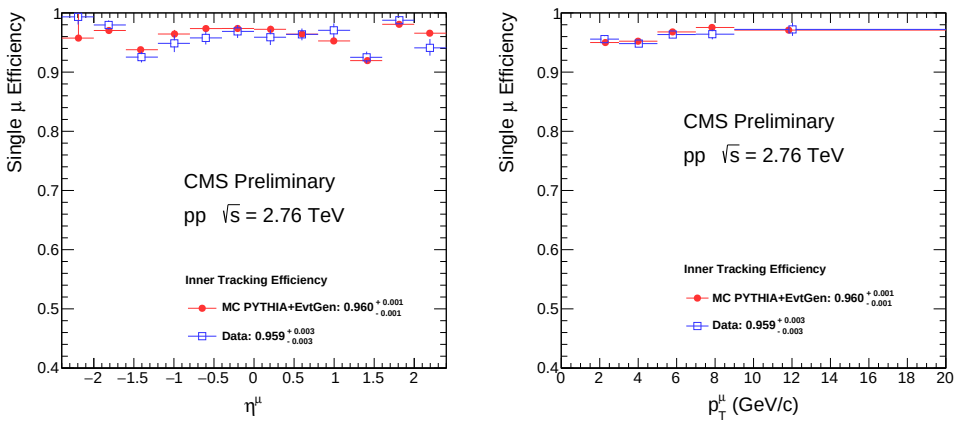

Figure 6.10: pp tracking and track matching efficiencies computed with tag and probe. Comparison between data *(open blue squares)* and MC *(red full circles)*. Left: efficiencies in pp data and MC *vs.* probe pseudo-rapdity. Right: efficiencies in pp data and MC *vs.* probe p_T.

Tracking efficiency in pp, PbPb collisions

- Inner track reconstruction efficiency (including the inner to outer track matching efficiency) and track (inner and global) quality selection within the single muon acceptance cut defined in Section 5.3.1:
  - probe: a standalone muon (the four-momentum information is taken from the standalone part exclusively)
  - passing probe: probe that is a global muon passing all track quality cuts.

In the following Figure 6.10, the resulting single muon tracking efficiencies from *pp* (data and MC) are presented. We can see that the tracking efficiencies in data and MC are consistent within uncertainties. As a result, it was decided not to correct for possible discrepancies in this part of the efficiency. The Muon Object Group (later called 'Muon POG') of CMS has suggested us for this preliminary result to use a conservative systematic uncertainty of 1.7% per track, which is applied to the final efficiency (twice, since there are two muons). For the final version of this analysis, a thorough study of the track reconstruction and inner to outer track matching sequences is being carried, and is not presented here.

Figure 6.11, shows the resulting single muon tracking efficiencies from PbPb are presented. Generally speaking, the integrated data and MC efficiencies seem to disagree. Large uncertainties appear in the η-binned plot, for the data efficiencies, and the lowest-p_T bin does not enter our analysis. Nonetheless, it is good to see that tracking efficiencies do not depend on the multiplicity in the event, confirming that the tracking works well up to the most central PbPb collisions.

Upon various consultations with the Muon POG of CMS, it was decided to opt for a conservative 5% systematic uncertainty per track instead of assigning a correction,

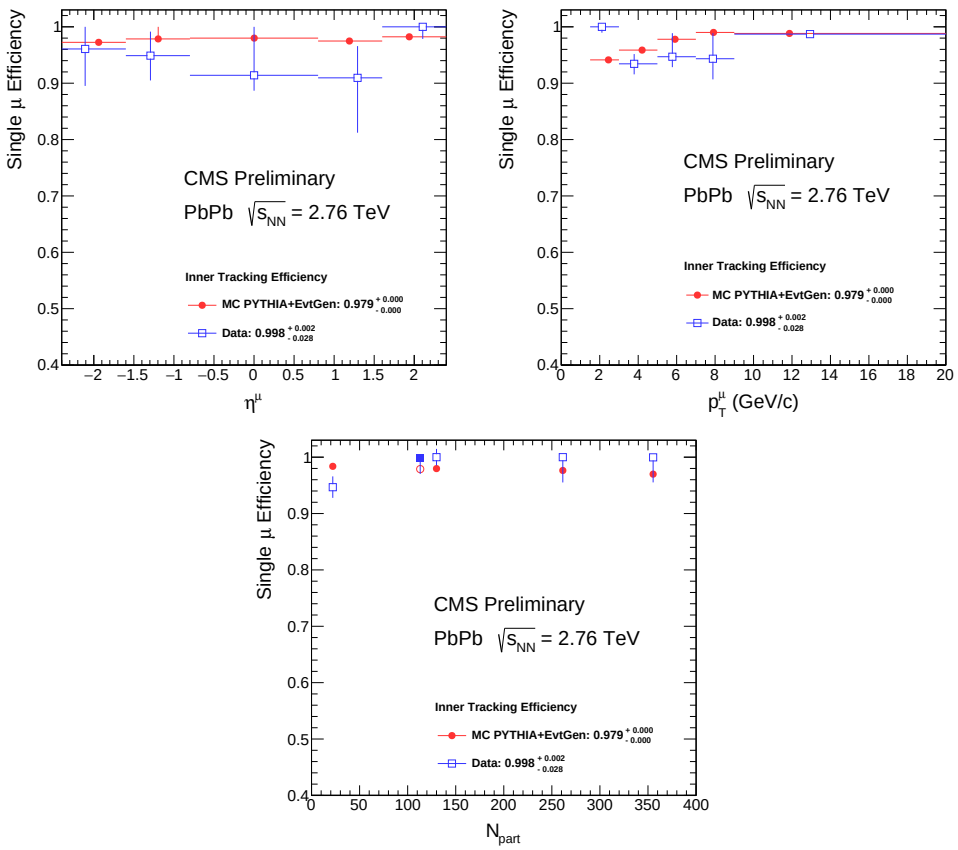

Figure 6.11: PbPb Tracking and track matching efficiencies computed with tag and probe. Comparison between data *(open blue squares)* and MC *(red full circles)*. Left: efficiencies in PbPb data and MC *vs.* probe pseudo-rapdity. Right: efficiencies in PbPb data and MC *vs.* probe p_T. Bottom: efficiencies in PbPb data and MC *vs.* probe p_T.

for this preliminary result, while we investigate more on the nature of this underperformance.

6.2.5 Correction to the dimuon efficiency

In the previous paragraphs, I have presented the differences between single muon efficiencies in MC and data, using the Tag and Probe method on muons coming from J/ψ. Now, let us try to go from the discrepancies at single muon level to their effect on the dimuon efficiency. Since the efficiencies are p_T-dependent, one can take the ratio $\varepsilon^{data}/\varepsilon^{MC}$ as a function of the probe p_T

$$C^{\mathrm{TNP}} = \frac{\varepsilon_{\mu}^{\mathrm{data}}(\mathrm{trig}|\mathrm{ID})}{\varepsilon_{\mu}^{\mathrm{MC}}(\mathrm{trig}|\mathrm{ID})}, \tag{6.10}$$

where $\mathrm{C}^{\mathrm{TNP}}$ is a single-muon data-MC correction function. This correction is only limited by the statistical accuracy of the data sample, hence the main uncertainty will

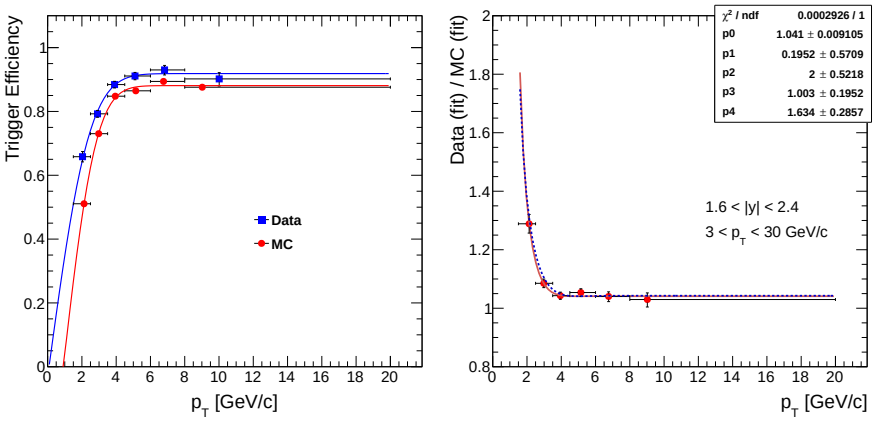

Figure 6.12: Left: single muon efficiencies in PbPb forward data and MC *vs.* p_T. Both efficiencies are fitted to an error function. Right: single muon correction factor $\mathrm{C}^{\mathrm{TNP}}$ in PbPb forward data, as a function of probe-p_T. Reminder: muons below $p_T = 3.5$ GeV/c are not included in this analysis.

come from varying the ε^{data} part. Figure 6.12 (left) shows the single muon efficiencies when probing the trigger+ID part, for the PbPb forward sample (which is the part where corrections are the largest). Both ε^{data} and ε^{MC} are fitted using an error function, and the ratio $\mathrm{C}^{\mathrm{TNP}}$ is presented (right), with a fit to the ratio of two error functions (red line), compared to the ratio of the error functions fitted on the left (dashed line).

By virtue of Equation 6.10, $\mathrm{C}^{\mathrm{TNP}}$ is a continuous function of p_T, differential (2 bins) in muon η. Figure 6.13 shows the $\mathrm{C}^{\mathrm{TNP}}$ functions for pp, barrel and forward, and for PbPb, barrel and endcap regions .

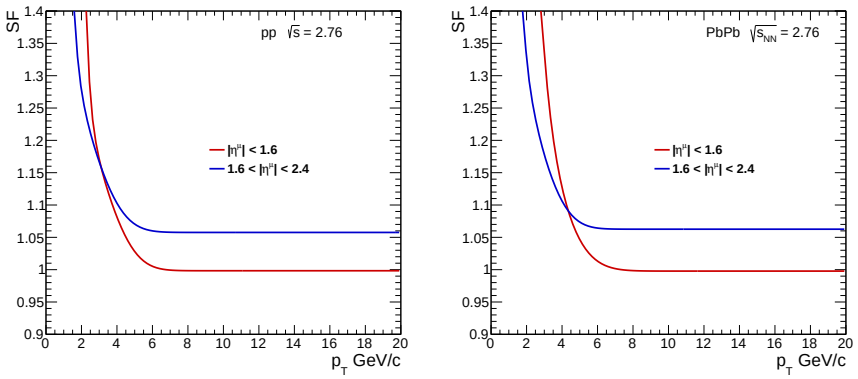

Figure 6.13: Left: $\mathrm{C}^{\mathrm{TNP}}$ correction functions *vs.* probe muon p_T, in pp collisions. Right: $\mathrm{C}^{\mathrm{TNP}}$ correction functions *vs.* probe muon p_T, in PbPb collisions.

To correct our dimuon efficiencies, each dimuon entry in the numerator of ε in Equation 6.2 is weighted by $\mathrm{C}^{\mathrm{TNP}}{}_1 \times \mathrm{C}^{\mathrm{TNP}}{}_2$, i.e. the product of $\mathrm{C}^{\mathrm{TNP}}$ computed at p_T-η of the first muon and $\mathrm{C}^{\mathrm{TNP}}$ computed at p_T-η of the second muon. This has

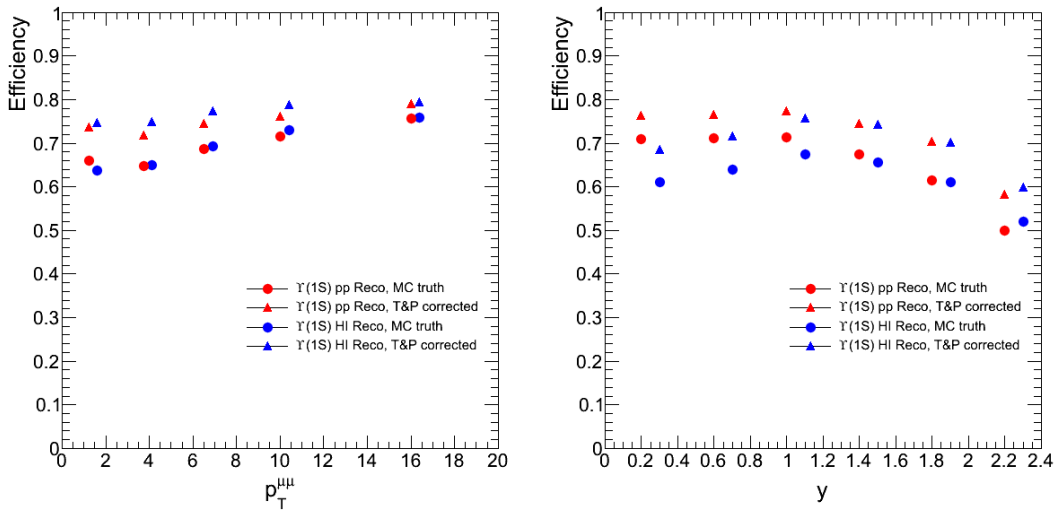

Figure 6.14: Dimuon efficiencies applied to *pp* (red) and PbPb data (blue), in analysis bins of p_T (left) and y (right). In both panels, triangles represent the efficiency correction obtained from simulation ('MC truth') and circles represent the same efficiency after applying the tag and probe corrective factors C^{TNP}.

the effect of shifting the dimuon efficiencies up, as can be seen in fig 6.14. It can be noted that the efficiencies preserve the same trend after being weighted with the C^{TNP} corrections.

6.2.6 Systematic uncertainties

Since the Tag and Probe method is based on simulations and data, the reliability of the result is largely dependent on the statistics available in data. In our case study, the PbPb collisions yield a limited statistical precision on forward pseudorapidity muons.

Another source of uncertainty comes from the Tag and Probe settings. Let me take a concrete example: in the efficiency of track reconstruction, the tag (global muon with a good quality track) is matched to a standalone muon (the probe). This probe passes the selection if it is also a global muon, i.e. if it is matched to a good quality track. In this case, it is difficult to assess the probability that another track very close in pseudorapidity passed the matching to the standalone in place of the actual muon track. This is especially important in a high multiplicity environment such as heavy ion collisions, and can yield a wrong, larger tracking efficiency.

To evaluate a systematic accounting for this, the ε^{data} is recomputed for tag-probe pairs where the probe p_T requirement is tighter (probe $p_T > 5$ GeV/c). To get an idea of the statistical uncertainty on the C^{TNP} weighting procedure, the $\varepsilon^{data}_{p_T>5}$ and $\varepsilon^{data}_{p_T>3.5}$ are taken as seeds for 100 random generations following asymmetric Gaussian distributions, for each probe p_T setting. The varied efficiencies are refitted with an error function, which leads to 200 variations on the C^{TNP}. The resulting variations on C^{TNP} are presented for the pp efficiencies in Figure 6.15, and for the PbPb efficiencies

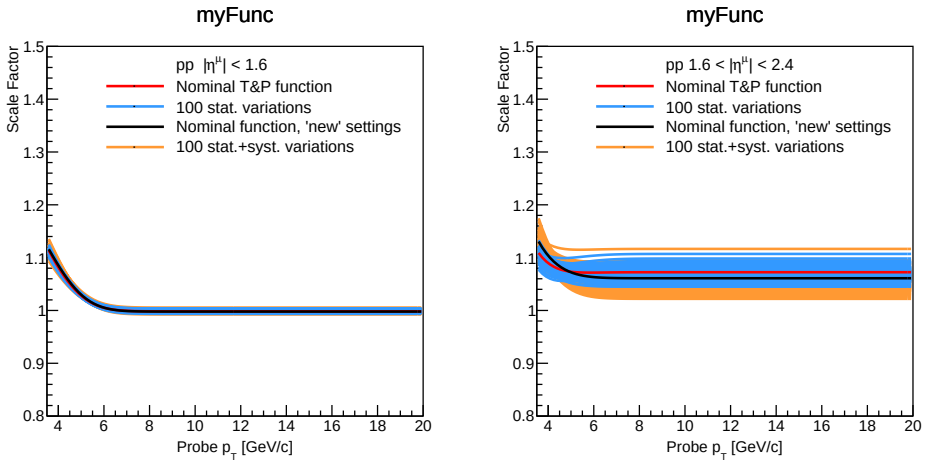

Figure 6.15: 100 variations of the ε^{data} part of C^{TNP}(pp collisions), using alternate tag-probe settings (orange) and using standard settings (blue). The blue curves make up for a statistical uncertainty of the procedure, while orange curves take also a systematic uncertainty into account.

in Figure 6.16.

We can see that modifying the probe p_T requirements does not change the nominal C^{TNP} function, as can be seen in red and black curves of Figures 6.15 and 6.16. It was also checked that the ε^{MC} part of C^{TNP} remains unchanged after requesting (probe p_T > 5 GeV/c). However, the blue curves, which are the 100 variations without changing the probe requirement, yield a reduced uncertainty compared to the orange curves, which represent a combination of the statistical and systematic uncertainty of the Tag and Probe method.

We can also see that pp efficiencies, being defined with more statistics than in the PbPb case, yield smaller uncertainties. In both cases, the muons measured in the forward region of the detector need larger corrections, as expected.

The resulting 100 C^{TNP} variations are used to reweight the dimuon efficiencies. In the end, the uncertainty related to this procedure is taken, for each dimuon efficiency bin, as the RMS of the distribution of the 100 reweighted efficiencies.

For the preliminary result presented in this thesis, the uncertainties regarding the tag and probe procedure have been taken relatively conservative. At the time of finalising the document, additional studies aiming at a better assessment of the systematic uncertainties and the efficiencies are underway. The largest part of the work to be completed regards the systematic uncertainties in the tracking efficiency, and a closure test related the procedure. These improvements are to be included in the final publication.

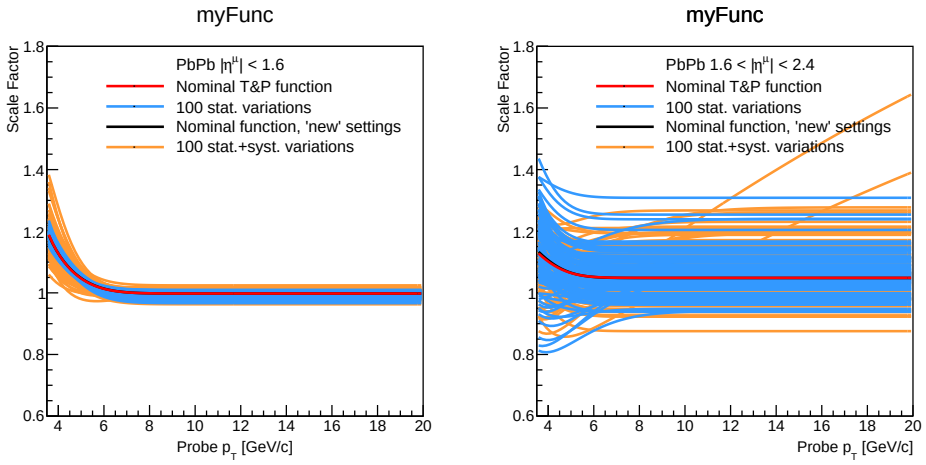

Figure 6.16: 100 variations of the ε^{data} part of $\mathrm{C}^{\mathrm{TNP}}$(PbPb collisions), using alternate tag-probe settings (orange) and using standard settings (blue). The blue curves make up for a statistical uncertainty of the procedure, while orange curves take also a systematic uncertainty into account.

In this section, I have laid out the basics of the Tag and Probe method, a standard method to attribute data-driven values to the efficiencies, of wide-spread use to dilepton analyses, in CMS and other experiments. We have seen that there is a difference between our estimation of the efficiencies using the MC simulations and the data. This contributes to the $\alpha\varepsilon$ factor. The following section will sum up the findings on $\alpha\varepsilon$ and weightings applied, to extract the net correction applied to the raw yields.

6.3 Summary

6.3.1 Summary of Υ(nS) corrections

In the previous section, the following corrections and systematic uncertainties were presented:

- For each Υ state in pp and PbPb data:
  - $\alpha\varepsilon(\mu\mu)$, the dimuon acceptance and efficiency, differential in p_T, y (or N_{part}) of the Υ state,
  - $\mathrm{C}^{\mathrm{TNP}}{}_1 \times \mathrm{C}^{\mathrm{TNP}}{}_2$, acting as an event-by-event weight to candidates entering in the numerator of $\alpha\varepsilon$, changing $\alpha\varepsilon(\mu\mu)$ in $\alpha\varepsilon(\mu\mu)_w$,
  - systematic uncertainties on assumed spectra (and centrality determination in PbPb), computed for each p_T, y (N_{part}) bin of $\alpha\varepsilon$,
  - systematic and statistical uncertainties on the Tag and Probe method, acting directly as an uncertainty on the $\alpha\varepsilon(\mu\mu)_w$ correction.

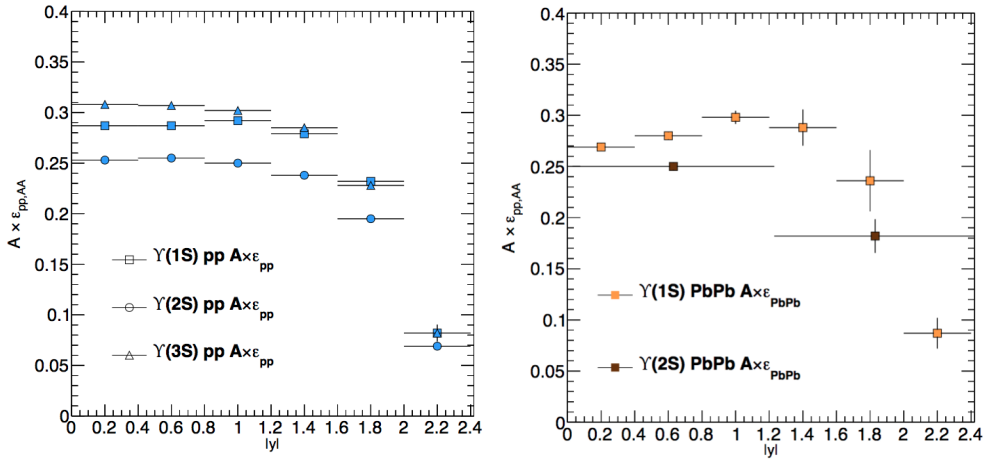

Figure 6.17: Total correction factor $\alpha\varepsilon_w$ applied to Υ states, with uncertainties. Left: correction for pp yields. Right: correction for PbPb yields.

This is summarised in Figure 6.17.

- Common to all states, the tracking efficiency, taken as a global systematic uncertainty:
  - 1.7% for each muon track in pp,
  - 5% for each muon track in PbPb.

  This will appear as a global uncertainty band in R_{AA}, in Section 7.2.2.

Figure 6.17 shows the total $\alpha\varepsilon_{\mathrm{weighted}}$ dimuon correction for all Υ states, *vs.* the dimuon rapidity. Both plots show that Υ(1S) is reconstructed more efficiently than Υ(2S): this is due to the kinematic cuts applied to the Υ(1S), increasing the acceptance fraction for the Υ(1S).

One can also note the increasing uncertainty at large rapidities. This is due to both Tag and Probe and the shape uncertainties, having more effect in PbPb at high rapidities as shown in Table 6.12.

6.3.2 Tabulated results

The tabulated version of $\alpha\varepsilon_w$ corrections is presented in Table 6.13 for Υ states in *pp* collisions, and in Table 6.14 for Υ states in PbPb collisions. Since the statistical uncertainty in α and ε is very small and only due to the size of our simulations (not dependent of the measurement, but on the number of generated events), I add it in quadrature all the sources of systematic uncertainties, at the exception of the tracking uncertainties which are global and do not appear here. As a consequence, the results are shown in the format $\alpha\varepsilon_w \pm \sigma$, where σ is the quadratic sum of all statistical and systematic uncertainties covered in Sections 6.1.4 and 6.2.6.

p_T [GeV/c]	$\alpha\varepsilon_w$[1S](p_T)	$\|y\|$	$\alpha\varepsilon_w$[1S](y)
0-2.5	0.339 ± 0.008	0-0.4	0.300 ± 0.003
2.5-5	0.214 ± 0.004	0.4-0.8	0.299 ± 0.003
5-8	0.207 ± 0.006	0.8-1.2	0.303 ± 0.002
8-12	0.284 ± 0.008	1.2-1.6	0.289 ± 0.003
12-20	0.404 ± 0.011	1.6-2	0.238 ± 0.003
0-100	**0.262 ± 0.002**	2-2.4	0.085 ± 0.002
p_T [GeV/c]	$\alpha\varepsilon_w$[2S](p_T)	$\|y\|$	$\alpha\varepsilon_w$[2S](y)
0-2.5	0.293 ± 0.007	0-0.4	0.253 ± 0.004
2.5-5	0.171 ± 0.004	0.4-0.8	0.255 ± 0.004
5-8	0.172 ± 0.005	0.8-1.2	0.250 ± 0.003
8-12	0.246 ± 0.008	1.2-1.6	0.238 ± 0.004
12-20	0.379 ± 0.011	1.6-2	0.195 ± 0.003
0-100	**0.218 ± 0.001**	2-2.4	0.069 ± 0.002
p_T [GeV/c]	$\alpha\varepsilon_w$[3S](p_T)	$\|y\|$	$\alpha\varepsilon_w$[3S](y)
0-2.5	0.361 ± 0.009	0-0.4	0.308 ± 0.003
2.5-5	0.214 ± 0.005	0.4-0.8	0.307 ± 0.003
5-8	0.199 ± 0.005	0.8-1.2	0.302 ± 0.003
8-12	0.267 ± 0.008	1.2-1.6	0.285 ± 0.003
12-20	0.389 ± 0.011	1.6-2	0.228 ± 0.003
0-100	**0.263 ± 0.001**	2-2.4	0.082 ± 0.002

Table 6.13: Final $\alpha\varepsilon_w$ for all Υ states in the pp case. All uncertainties have been summed in quadrature, except tracking (not shown here). Integrated results displayed in bold font.

p_T [GeV/c]	$\alpha\varepsilon_w$[1S](p_T)	$\|y\|$	$\alpha\varepsilon_w$[1S](y)
0-2.5	0.315 ± 0.022	0-0.4	0.269 ± 0.012
2.5-5	0.202 ± 0.013	0.4-0.8	0.280 ± 0.012
5-8	0.202 ± 0.012	0.8-1.2	0.298 ± 0.014
8-12	0.288 ± 0.016	1.2-1.6	0.289 ± 0.019
12-20	0.406 ± 0.020	1.6-2	0.237 ± 0.024
0-100	**0.252 ± 0.014**	2-2.4	0.087 ± 0.011

Centrality	$\alpha\varepsilon_w$[1S](Cent.)$_{\mathrm{PbPb}}$
0%-5%	0.241 ± 0.010
5%-10%	0.249 ± 0.012
10%-20%	0.253 ± 0.011
20%-30%	0.257 ± 0.011
30%-40%	0.258 ± 0.011
40%-50%	0.259 ± 0.011
50%-70%	0.262 ± 0.011
70%-100%	0.261 ± 0.011

p_T [GeV/c]	$\alpha\varepsilon_w$[2S](p_T)	$\|y\|$	$\alpha\varepsilon_w$[2S](y)
0-5	0.203 ± 0.009	0-1.2	0.250 ± 0.005
5-12	0.202 ± 0.010	1.2-2.4	0.182 ± 0.016
12-20	0.402 ± 0.021	-	-
0-100	**0.221 ± 0.009**	-	-

Centrality	$\alpha\varepsilon_w$[2S](Cent.)$_{\mathrm{PbPb}}$
0%-10%	0.213 ± 0.010
10%-30%	0.220 ± 0.010
30%-50%	0.224 ± 0.010
50%-100%	0.226 ± 0.010

Table 6.14: Final $\alpha\varepsilon_w$ for Υ(1S),Υ(2S) states in the PbPb case. All uncertainties have been summed in quadrature, except tracking (not shown here). Integrated results displayed in bold font.

52

Chapter 7

Results on Υ production and suppression

Contents

Life as a shorty shouldn't be so rough.

Inspectah Deck, in *C.R.E.A.M.*,
Wu-Tang Clan

In this Chapter, the information from Chapters 5 and 6 is collected to produce the results of the analysis of Υ data in PbPb and *pp* collisions. In the two cases, full corrections $\alpha\varepsilon_w$ are applied to the raw yields. These corrected yields are further normalised by the luminosity recorded in *pp* in 2013 and by the number of minimum bias events in PbPb to get production rates.

The cross section for Υ(1S), Υ(2S) and Υ(3S) production in *pp* collisions is presented in Section 7.1. Having the *pp* spectra available for each state at this centre-of-mass energy is a new and important addition to the already collected quarkonium data. This, combined with the same measurement at other centre-of-mass energies, can help towards a better understanding of quarkonium production.

The PbPb spectra are presented in Section 7.2, and represent a considerable improvement with respect to [2]. The Υ(2S) spectrum is measured differentially for the first time in heavy ion collisions. It was discovered with the first heavy ion run of the LHC in 2010 that Υ states are suppressed in heavy ions, with excited states being more

suppressed than the Υ(1S), as reported in [2] and [3]. In the updated reference [4], the centrality dependent result exhibits an ordering pattern, in agreement with the sequential melting picture. The present study confirms this statement and allows to investigate its kinematical dependencies, thanks to the twenty times larger statistics of the *pp* reference. For example, it becomes possible to check if the few surviving Υ(2S) would not be produced at high p_T and escaping the plasma early on. In the present Chapter, updated measurements of the nuclear modification factor $R_{\rm AA}$ are presented, differential in centrality, p_T and rapidity.

When a particle is not measurable with a good precision, it can be more informative or more accurate to compute an upper limit on the observed rate. This is what is done for the Υ(3S), using a fully frequentist statistical treatment of Υ(3S) yields from fits to PbPb and *pp* data, as presented in Section 7.2.4.

The results for Υ suppression are compared to other experiments and to theoretical models in Section 7.3.

7.1 Measurement of the *pp* cross section

7.1.1 Corrected yields

First, let us collect the raw yields from Tables 5.7 and 5.8, and divide them by their relative total corrections, $\alpha\varepsilon_w$ from Table 6.13. This gives an indication of the total number of events that have produced an Υ in the rapidity range $|y| < 2.4$. The variations on signal extraction performed in Section 5.3.4 and reported in Tables 5.4 and 5.5 are used to quote a systematic uncertainty on the total number of Υ. The corrected yields, statistical and systematic uncertainties included, for Υ(1S), Υ(2S) and Υ(3S), are presented in Tables 7.1, 7.2 and 7.3, respectively. Each table contains the results of the p_T-differential analysis, the rapidity differential analysis, and the integrated result highlighted in bold font.

p_T [GeV/c]	Total N[Υ(1S)](p_T)	$\|y\|$	Total N[Υ(1S)](y)
0-2.5	4638 ± 157 ± 371	0-0.4	3642 ± 126 ± 109
2.5-5	6729 ± 217 ± 336	0.4-0.8	3774 ± 133 ± 113
5-8	4794 ± 162 ± 192	0.8-1.2	3286 ± 128 ± 131
8-12	2158 ± 99 ± 43	1.2-1.6	3180 ± 133 ± 127
12-20	838 ± 50 ± 8	1.6-2.0	2711 ± 141 ± 135
0-20	**19137 ± 328 ± 628**	2.0-2.4	2957 ± 234 ± 236

Table 7.1: Corrected yields of Υ(1S) as a function of p_T and y in *pp* collisions at $\sqrt{s} = 2.76$ TeV. The left-hand side contains the results for the p_T-dependent binning. The right-hand side contains the results for the rapidity-dependent binning. On the left-hand side, the last entry at the bottom (bold font) corresponds to the integrated result.

It is to be noted that the systematic uncertainty from fitting decreases significantly

with p_T, which is due to the background level dropping, making the remaining signal easier to fit.

p_T [GeV/c]	Total N[Υ(2S)](p_T)	$\|y\|$	Total N[Υ(2S)](y)
0-2.5	1022 ± 99 ± 112	0-0.4	1046 ± 82 ± 52
2.5-5	1483 ± 140 ± 59	0.4-0.8	1031 ± 84 ± 52
5-8	1431 ± 118 ± 57	0.8-1.2	962 ± 87 ± 87
8-12	801 ± 72 ± 24	1.2-1.6	974 ± 94 ± 88
12-20	313 ± 34 ± 3	1.6-2.0	924 ± 102 ± 129
0-20	**5541 ± 225 ± 116**	2.0-2.4	634 ± 166 ± 19

Table 7.2: Corrected yields of Υ(2S) as a function of p_T and y in pp collisions at $\sqrt{s}$ = 2.76 TeV. Same conventions as Table 7.1.

p_T [GeV/c]	Total N[Υ(3S)](p_T)	$\|y\|$	Total N[Υ(3S)](y)
0-2.5	362 ± 67 ± 54	0-0.4	431 ± 54 ± 30
2.5-5	775 ± 102 ± 39	0.4-0.8	422 ± 57 ± 30
5-8	570 ± 82 ± 28	0.8-1.2	465 ± 62 ± 51
8-12	338 ± 51 ± 13	1.2-1.6	360 ± 66 ± 36
12-20	178 ± 27 ± 3	1.6-2.0	340 ± 71 ± 20
0-20	**2353 ± 156 ± 71**	2-2.4	559 ± 137 ± 17

Table 7.3: Corrected yields of Υ(3S) as a function of p_T and y in pp collisions at $\sqrt{s}$ = 2.76 TeV. Same conventions as Table 7.1.

7.1.2 Differential cross sections

The differential cross sections for Υ(nS) production in pp are defined as the fraction of Υ(nS) events measured in a given bin, corrected for acceptance and efficiency (including the tag and probe efficiency corrections), normalised with $\mathcal{L}_{pp}$, the luminosity of the pp sample, and divided by the width of the bin considered. Since the analysis is single differential in p_T and rapidity, one can define a p_T-differential and a rapidity-differential cross section, namely:

$$\frac{1}{\Delta y}\,\frac{\mathrm{d}\sigma\left(pp\to\Upsilon(nS)X\right)}{\mathrm{d}p_T}\cdot B_{\mu\mu} = \frac{1}{\Delta y\Delta p_T}\cdot\frac{1}{\mathcal{L}_{pp}}\cdot\frac{\mathcal{N}_{\mathrm{nS}}}{\alpha\;\varepsilon_{pp,w}} \tag{7.1}$$

$$\frac{\mathrm{d}\sigma\left(pp\to\Upsilon(nS)X\right)}{\mathrm{d}y}\cdot B_{\mu\mu} = \frac{1}{\Delta y}\cdot\frac{1}{\mathcal{L}_{pp}}\cdot\frac{\mathcal{N}_{\mathrm{nS}}}{\alpha\;\varepsilon_{pp,w}} \tag{7.2}$$

where:

- $\mathcal{N}_{\mathrm{nS}}$ is the number of measured Υ(nS) decaying to two muons, extracted from the fit to data in Section 5.3,

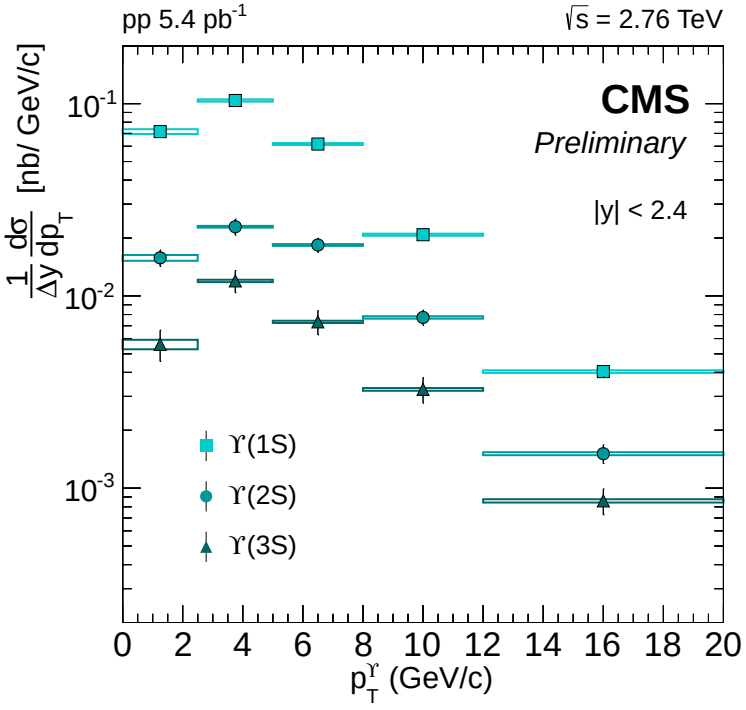

Figure 7.1: Cross sections for $pp \to \Upsilon(nS) \to \mu\mu$ in $|y| < 2.4$, as a function of the Υ transverse momentum. A global systematic uncertainty (luminosity, tracking efficiency) of 5% is not displayed.

- α is the geometric acceptance, computed in Section 6.1.2,
- $\varepsilon_{pp,w}$ is the dimuon detection efficiency, weighted with its own tag and probe corrections,
- $\mathcal{L}_{pp} = (5.4 \pm 0.2)$ pb^{-1} is the integrated luminosity of the pp sample,
- Δp_T and Δy are the bin widths in p_T and y, as described in Section 5.3.3. In Equation 7.1 as well as in Tables 7.1, 7.3 and 7.3, the p_T-binned cross sections are divided by $\Delta y = 4.8$ to ease the comparison with other experiments,
- $B_{\mu\mu}$ is the branching fraction of each Υ state into its dimuon decay. It is implicit in the result, and is not used in the present calculation.

The pp cross sections are shown as a function of p_T in Figure 7.1 and as a function of y in Figure 7.2. Tabulated results for Υ(1S), Υ(2S) and Υ(3S) are reported in Tables 7.4, 7.5 and 7.6, respectively.

The pp cross sections are presented with systematic uncertainties, which are computed as the quadratic sum of the following contributions:

- The fitting uncertainty from Section 5.3.4: This source of uncertainty decreases continuously with the amount of background under the peak, when increasing

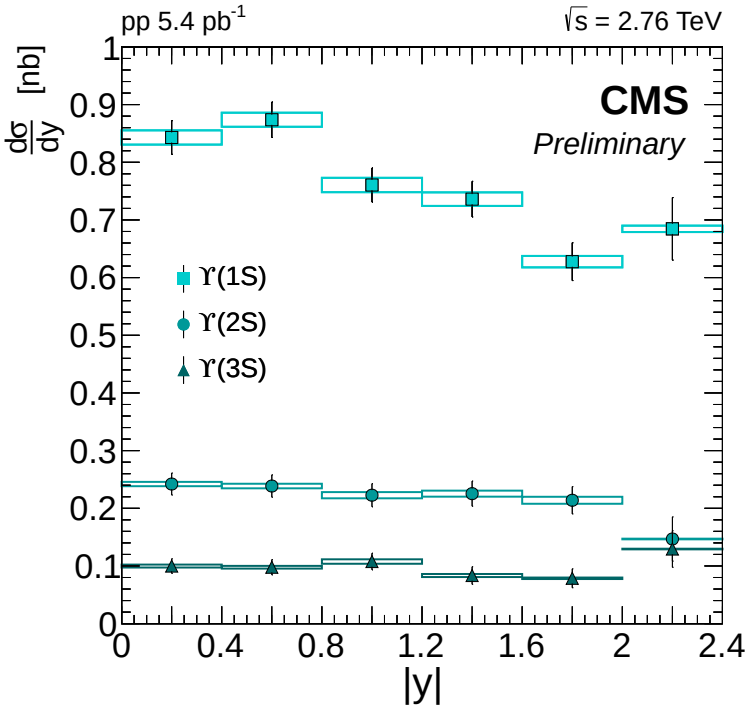

Figure 7.2: Cross sections for $pp \to \Upsilon(nS) \to \mu\mu$ in $|y| < 2.4$, as a function of the Υ rapidity. A global luminosity uncertainty (luminosity, tracking efficiency) of 5% is not displayed.

p_T [GeV/c]	$\frac{1}{\Delta y}\frac{d\sigma(\Upsilon(1S))}{dp_T}\cdot B_{\mu\mu}$ [nb · c/GeV]	$\lvert y\rvert$	$\frac{d\sigma(\Upsilon(1S))}{dy}\cdot B_{\mu\mu}$ [nb]
0-2.5	0.073 ± 0.0025 ± 0.0020	0-0.4	0.881 ± 0.031 ± 0.012
2.5-5	0.105 ± 0.0034 ± 0.0014	0.4-0.8	0.910 ± 0.032 ± 0.012
5-8	0.062 ± 0.0021 ± 0.0006	0.8-1.2	0.789 ± 0.031 ± 0.012
8-12	0.021 ± 0.0009 ± 0.0002	1.2-1.6	0.762 ± 0.032 ± 0.012
12-20	0.0041 ± 0.0002 ± $6\cdot10^{-5}$	1.6-2.0	0.644 ± 0.034 ± 0.010
0-20	**3.544 ± 0.067 ± 0.109**	2.0-2.4	0.710 ± 0.056 ± 0.006

Table 7.4: Υ(1S) differential cross sections in pp collisions as a function of p_T and y. Same conventions as Table 7.1, with the exception that the integrated cross section, lower left line, is note divided by Δy.

p_T [GeV/c]	$\frac{1}{\Delta y}\frac{d\sigma(\Upsilon(2S))}{dp_T}\cdot B_{\mu\mu}$ [nb · c/GeV]	$\lvert y\rvert$	$\frac{d\sigma(\Upsilon(2S))}{dy}\cdot B_{\mu\mu}$ [nb]
0-2.5	0.0158 ± 0.0015 ± 0.0006	0-0.4	0.242 ± 0.019 ± 0.004
2.5-5	0.0229 ± 0.0021 ± 0.0002	0.4-0.8	0.239 ± 0.019 ± 0.004
5-8	0.0184 ± 0.0015 ± 0.0002	0.8-1.2	0.223 ± 0.020 ± 0.005
8-12	0.0077 ± 0.0007 ± 0.0001	1.2-1.6	0.225 ± 0.022 ± 0.005
12-20	0.0015 ± 0.0002 ± $2\cdot10^{-5}$	1.6-2.0	0.214 ± 0.024 ± 0.006
0-20	**1.026 ± 0.042 ± 0.037**	2.0-2.4	0.147 ± 0.038 ± 0.001

Table 7.5: Υ(2S) differential cross sections in pp collisions as a function of p_T and y. Same conventions as Table 7.4.

the p_T range considered. The first p_T bin, $p_T < 2.5$ GeV/c has systematic uncertainties of 8%, 11%, 15% for Υ(1S), Υ(2S) and Υ(3S), respectively,

- The generated spectrum assumed by PYTHIA, as seen in Section 6.1.4 ranging around 2-3%.

- The tag and probe single muon efficiencies, computed in Section 6.2.3, whose effect on the dimuon efficiency has been assigned a systematic uncertainty in Section 6.2.6. The size of the uncertainty (2-15%) depends on the collision setup (pp, PbPb) and the region of phase space (p_T, η) studied.

Additionally, global uncertainties (affecting all points together) are computed to be 5% in pp, and are not shown in the Figures 7.1 and 7.2. The luminosity $\mathcal{L}_{pp}$ is known to the 3.7% accuracy. The tracking efficiency in pp adds another source of systematic uncertainty of 1.7% per muon.

p_T [GeV/c]	$\frac{1}{\Delta y}\frac{d\sigma(\Upsilon(3S))}{dp_T}\cdot B_{\mu\mu}$ [nb · c/GeV]	$\lvert y\rvert$	$\frac{d\sigma(\Upsilon(3S))}{dy}\cdot B_{\mu\mu}$ [nb]
0-2.5	$0.0056 \pm 0.0010 \pm 0.0003$	0-0.4	$0.100 \pm 0.013 \pm 0.003$
2.5-5	$0.0120 \pm 0.0016 \pm 0.0001$	0.4-0.8	$0.098 \pm 0.013 \pm 0.002$
5-8	$0.0073 \pm 0.0010 \pm 0.0001$	0.8-1.2	$0.108 \pm 0.014 \pm 0.004$
8-12	$0.0033 \pm 0.0005 \pm 5\cdot10^{-5}$	1.2-1.6	$0.083 \pm 0.015 \pm 0.003$
12-20	$0.0008 \pm 0.0001 \pm 1\cdot10^{-5}$	1.6-2.0	$0.079 \pm 0.016 \pm 0.001$
0-20	$\mathbf{0.436 \pm 0.029 \pm 0.008}$	2.0-2.4	$0.129 \pm 0.032 \pm 0.001$

Table 7.6: Υ(3S) differential cross sections in pp collisions as a function of p_T and y. Same conventions as Table 7.4.

In this section, we have seen that the LHC has provided almost twenty thousand $\Upsilon(1S)$, more than five thousand $\Upsilon(2S)$, and two thousand $\Upsilon(3S)$ decaying in two muons in the CMS detector during its running time in 2013, with pp collisions at the centre-of-mass energy of $\sqrt{s}$ = 2.76 TeV. These were produced when accumulating a luminosity of $\mathcal{L}_{pp}$ = (5.4 ± 0.2) pb^{-1}. The integrated cross sections $\sigma(pp \to \Upsilon(nS)X)\cdot B_{\mu\mu}$ measured in $|y| < 2.4$, are:

$$\begin{aligned}
\sigma\left(pp \to \Upsilon(1S)X\right)\cdot B_{\mu\mu} &= 3.544 \pm 0.067 \pm 0.109 \text{ nb} \\
\sigma\left(pp \to \Upsilon(2S)X\right)\cdot B_{\mu\mu} &= 1.026 \pm 0.042 \pm 0.037 \text{ nb} \\
\sigma\left(pp \to \Upsilon(3S)X\right)\cdot B_{\mu\mu} &= 0.436 \pm 0.029 \pm 0.008 \text{ nb}.
\end{aligned}$$

In the following section, we will see how this compares to the observed Υ yields in PbPb collisions.

7.2 Υ suppression in heavy ion collisions

7.2.1 Normalised cross sections

The differential Υ yield is corrected for acceptance and tag and probe weighted efficiencies, and further normalised by the product of N_{MB} and T_{AA}, the normalisation factors for heavy ion experiments already encountered in Chapter 4.

Equation 7.3 shows the T_{AA}-scaled corrected Υ(nS) yields as a function of p_T, and Equation 7.4 as a function of rapidity:

$$\frac{1}{T_{\mathrm{AA}}} \cdot \frac{1}{\Delta y} \cdot \frac{\mathrm{d}N\left(AA \to \Upsilon(nS)\right)}{\mathrm{d}p_T} \cdot B_{\mu\mu} = \frac{1}{T_{\mathrm{AA}}} \cdot \frac{1}{N_{\mathrm{MB}}} \cdot \frac{\mathcal{N}_{\mathrm{nS}}^{\mathrm{PbPb}}}{\alpha\ \varepsilon_{\mathrm{PbPb}}\ \Delta p_T \Delta y}, \quad (7.3)$$

$$\frac{1}{T_{\mathrm{AA}}} \cdot \frac{\mathrm{d}N\left(AA \to \Upsilon(nS)\right)}{\mathrm{d}y} \cdot B_{\mu\mu} = \frac{1}{T_{\mathrm{AA}}} \cdot \frac{1}{N_{\mathrm{MB}}} \cdot \frac{\mathcal{N}_{\mathrm{nS}}^{\mathrm{PbPb}}}{\alpha\ \varepsilon_{\mathrm{PbPb}}\ \Delta y}, \quad (7.4)$$

where

- $\mathcal{N}_{\mathrm{nS}}^{\mathrm{PbPb}}$ is the number of measured Υ(nS) decaying to two muons, from the fit to data in Section 5.3.1;
- α is the geometric acceptance, as computed in Section 6.1.2;
- $\varepsilon_{\mathrm{PbPb}}$ is the dimuon trigger and reconstruction efficiency computed from the embedded sample and corrected for tag and probe;
- N_{MB}= 1.161×10^9 is the number of minimum bias PbPb events, after correction for a minimum bias selection efficiency of 97%;
- Δy and Δp_T are the bin widths in rapidity and p_T, respectively.

In order to compare the PbPb yields to the *pp* cross section, the invariant corrected yields in PbPb collisions are divided by the nuclear thickness function T_{AA}, which is usually obtained from a Glauber model calculation and is the same for all analyses using the same nuclei and collision energy. The corrected yields for Υ(1S) and Υ(2S) are presented in Figure 7.3 and Figure 7.4 as a function of their transverse momentum and rapidity, respectively.

These results represent a first differential measurement of the Υ(2S) spectrum in tranvserse momentum and rapidity, as well as a significantly improved measurement of the Υ(1S) up to p_T = 20 GeV/c.

From the computation of T_{AA}-scaled yields, the comparison with *pp* results becomes automatic. At first sight, the spectra look qualitatively similar, with a different normalisation. Additionally, the Υ(2S) looks much less significant than its *pp* counterpart: this is the sign of the known strong suppression of excited states, first measured in [3]. To get a quantitative account of the suppression observed in this measurement, I will now turn to the nuclear modification factor, R_{AA}, and present the results for all three Υ states.

Tabulated versions of the invariant yields will be reported in the next Section 7.2.2, side by side with the tabulated R_{AA} results.

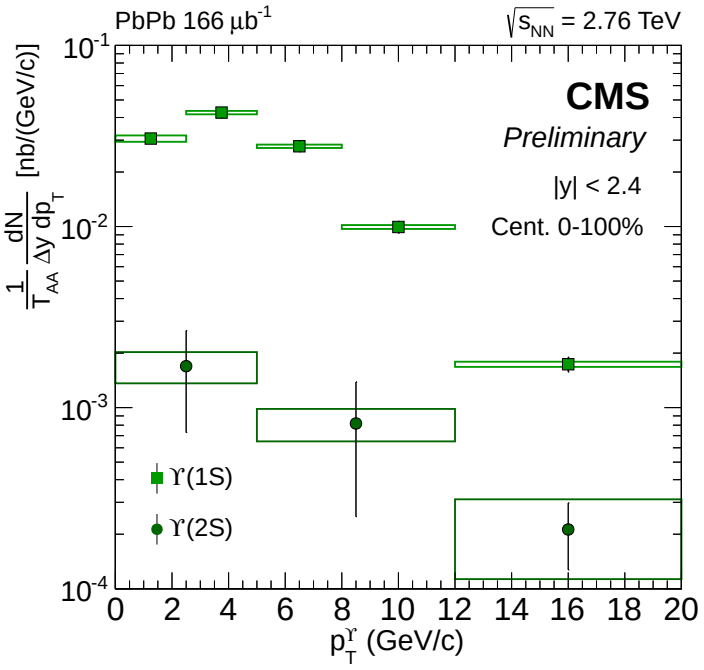

Figure 7.3: Normalised cross sections for PbPb $\rightarrow \Upsilon(nS) \rightarrow \mu\mu$ in $|y| < 2.4$, as a function of the Υ transverse momentum. A global luminosity uncertainty (luminosity, tracking efficiency) of 10% is not displayed.

7.2.2 Nuclear modification factor

To compare the production rate of a given particle (hard or soft probe) in pp to its heavy ion counterpart, one usually invokes the nuclear modification factor, defined as:

$$R_{\mathrm{AA}} = \frac{\mathcal{L}_{pp}}{T_{\mathrm{AA}} N_{\mathrm{MB}}} \cdot \frac{\mathrm{N}(\Upsilon(nS))_{\mathrm{PbPb}}}{\mathrm{N}(\Upsilon(nS))_{pp}} \cdot \frac{\varepsilon_{pp,w}}{\varepsilon_{\mathrm{PbPb},w}} \tag{7.5}$$

With this definition, R_{AA} is dependent on:

- the bin in which the raw yields and efficiency corrections are considered,
- N_{MB}, the total number of minimum bias hadronic events recorded in the experiment,
- $\mathcal{L}_{pp}$, the integrated luminosity recorded in pp,
- T_{AA}, the nuclear overlap function in a given centrality bin, that has the same dimension as the luminosity, and accounts for the amount of nucleon-nucleon interactions during the time of the nucleus-nucleus interaction.

Both pp and PbPb quantities have to be recorded at the same nucleon-nucleon centre-of-mass energy. The centrality dependent results are usually plotted as a function of N_{part}, the number of participating (or wounded) nucleons in the collision. The

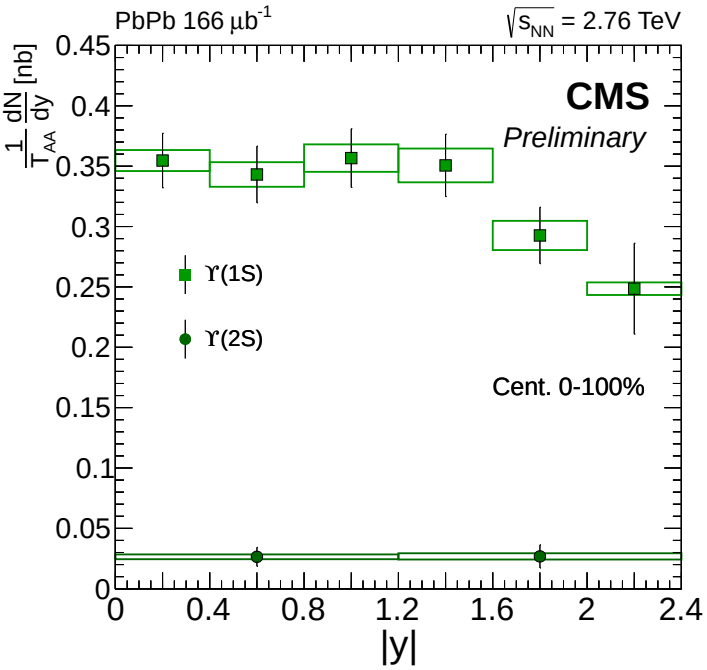

Figure 7.4: Normalised cross sections for PbPb $\rightarrow \Upsilon(nS) \rightarrow \mu\mu$ in $|y| < 2.4$, as a function of the Υ rapidity. A global luminosity uncertainty (luminosity, tracking efficiency) of 10% is not displayed.

nuclear modification factor of Υ(1S), Υ(2S), is measured in bins of p_T, y, and $N_{\rm part}$ in Figures 7.6, 7.7, 7.5 respectively.

The PbPb corrected yields and $R_{\rm AA}$ for Υ(1S) and Υ(2S) are tabulated as a function of p_T and y in Tables 7.8 and 7.9, respectively.

The centrality dependence of the suppression has been computed in various $N_{\rm part}$ bins for Υ(1S) and Υ(2S). Some additional features should be noted with respect to the previous analysis from CMS, using a lower pp reference [4]:

- the Υ(1S) analysis is now performed with the yield extraction method using the 'loose' single muon p_T cuts, cf. Section 5.3.1,

- an additional peripheral bin in the 1S result is measured: The peripheral 50−100% bin is now splitted into 50−70% and 70−100%. This is possible thanks to the extended reference as well as the improved heavy ion reconstruction,

- to get a clearer impression of the Υ(2S) suppression with increasing centrality, a coarser binning than in [4] was used: instead of seven bins, one can now find four centrality bins, each of them merging two of the bins used in the present Υ(1S) analysis.

The choice of having less bins for the Υ(2S) is motivated by the low significance of this signal overall, yielding only $\sim$ 200 Υ(2S) events in PbPb. Furthermore, the

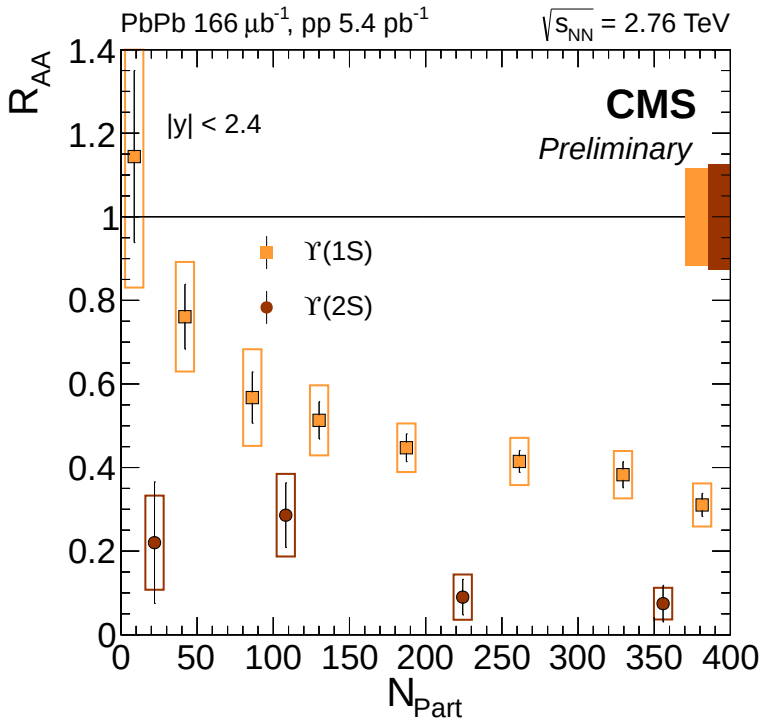

Figure 7.5: PbPb nuclear modification factor R_{AA} in PbPb collisions at $\sqrt{s_{NN}} = 2.76$ TeV, as a function of the number of participants.

previous analysis of ϒ(2S) used as many bins in ϒ(2S) and ϒ(1S) mostly because of the yield extraction technique used at the time, taking the yield ratio ϒ(1S)/ϒ(2S) as the parameter of interest. Now that the yields are analysed separately for each state, the analysis does not rely on this ratio parameter anymore.

7.2.3 Systematic uncertainties on R_{AA}

A break-down of the systematic uncertainties is given in the following Table 7.10 for the p_T- and y-dependent analyses of ϒ(1S). The listed uncertainties from left to right are:

- statistical uncertainty from the nominal fit to the *pp* yield,
- systematic uncertainty from fit variations on *pp* data,
- systematic uncertainty from fit variations on PbPb data,
- generator level shape variation uncertainties on *pp* and PbPb corrections $\alpha\varepsilon_w$,
- Tag and Probe uncertainty for efficiency corrections in *pp* data,
- Tag and Probe uncertainty for efficiency corrections in PbPb data,

Centrality percentiles	$\mathcal{Y}_{\mathrm{PbPb}}[\Upsilon(1S)]/T_{\mathrm{AA}}$ [nb]	$R_{\mathrm{AA}}[\Upsilon(1S)]$
0-5	1.12 ± 0.099 ± 0.043	0.310 ± 0.027 ± 0.050
5-10	1.38 ± 0.112 ± 0.048	0.383 ± 0.031 ± 0.055
10-20	1.50 ± 0.094 ± 0.048	0.415 ± 0.026 ± 0.055
20-30	1.62 ± 0.120 ± 0.050	0.447 ± 0.033 ± 0.057
30-40	1.85 ± 0.161 ± 0.075	0.513 ± 0.044 ± 0.082
40-50	2.05 ± 0.222 ± 0.106	0.567 ± 0.061 ± 0.115
50-70	2.76 ± 0.281 ± 0.120	0.764 ± 0.077 ± 0.130
70-100	4.15 ± 0.746 ± 0.292	1.150 ± 0.207 ± 0.314
0-100	**1.537 ± 0.081 ± 0.028**	**0.425 ± 0.029± 0.070**
pp	3.544 ± 0.067 ± 0.109	—
	$\mathcal{Y}_{\mathrm{PbPb}}[\Upsilon(2S)]/T_{\mathrm{AA}}$ [nb]	$R_{\mathrm{AA}}[\Upsilon(2S)]$
0-10	0.076 ± 0.045 ±0.039	0.074 ± 0.044 ± 0.038
10-30	0.092 ± 0.044 ±0.056	0.090 ± 0.042 ± 0.054
30-50	0.293 ± 0.079 ±0.103	0.286 ± 0.077 ± 0.100
50-100	0.226 ± 0.149 ±0.116	0.220 ± 0.145 ± 0.113
0-100	**0.119 ± 0.029 ± 0.002**	**0.116 ± 0.028 ± 0.022**
pp	1.026 ± 0.042 ± 0.037	—

Table 7.7: T_{AA}-scaled cross sections and nuclear modification factors R_{AA} for different centrality bins (and for centrality-integrated value, bold font) for Υ(1S) and Υ(2S)in PbPb collisions at $\sqrt{s_{NN}} = 2.76$ TeV.

$\lvert y\rvert$ <2.4	$\mathcal{Y}_{\mathrm{PbPb}}[\Upsilon(1S)]/T_{\mathrm{AA}}$ [nb]	$R_{\mathrm{AA}}[\Upsilon(1S)]$
p_T [GeV/c] < 2.5	0.0306 ± 0.0017 ± 0.0011	0.428 ± 0.029 ± 0.067
2.5 < p_T [GeV/c] < 5	0.0426 ± 0.0026 ± 0.0008	0.410 ± 0.029 ± 0.051
5 < p_T [GeV/c] < 8	0.0277 ± 0.0018 ± 0.0007	0.450 ± 0.034 ± 0.053
8 < p_T [GeV/c] < 12	0.00994 ± 0.00074 ± 0.0002	0.478 ± 0.042 ± 0.044
12 < p_T [GeV/c] < 20	0.00174 ± 0.00016 ± $5.4 \cdot 10^{-5}$	0.430 ± 0.048 ± 0.035
$\lvert y\rvert$ <2.4	$\frac{1}{T_{\mathrm{AA}}} \cdot \frac{1}{\Delta y} \cdot \frac{\mathrm{d}N\,(AA \to \Upsilon(nS)X)}{\mathrm{d}p_T} \cdot B_{\mu\mu}$ [nb]	$R_{\mathrm{AA}}[\Upsilon(2S)]$
p_T [GeV/c] < 5	0.00169 ± 0.00096 ±0.00033	0.082± 0.047 ± 0.018
5 < p_T [GeV/c] < 12	0.00082 ± 0.00056 ±0.00016	0.066± 0.046 ± 0.011
12 < p_T [GeV/c] < 20	0.00021 ± $8.5 \cdot 10^{-5}$ ± $9.9 \cdot 10^{-5}$	0.141± 0.058 ± 0.025

Table 7.8: Normalized yields $\mathcal{Y}_{\mathrm{PbPb}}/T_{\mathrm{AA}}$ and R_{AA} as a function of p_T for Υ(1S) (top) and Υ(2S) (bottom) states, in PbPb collisions at $\sqrt{s_{NN}} = 2.76$ TeV. Listed uncertainties are statistical (first) and systematic (second).

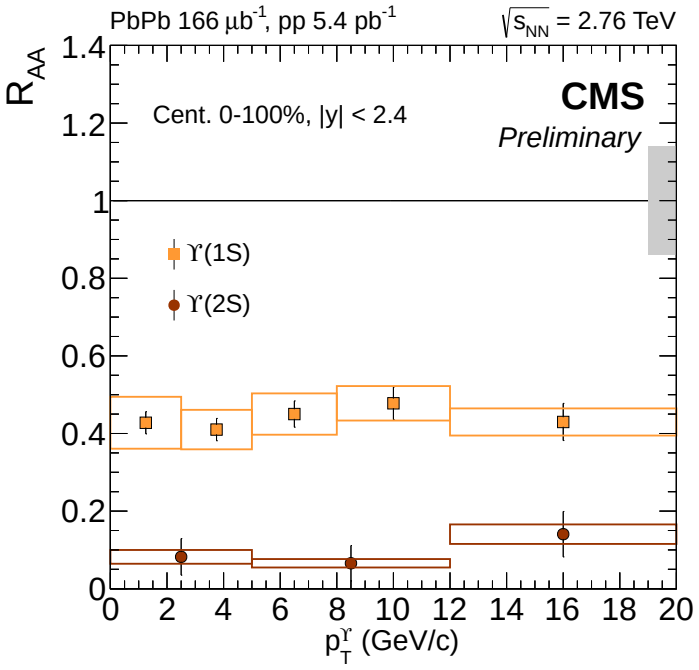

Figure 7.6: PbPb nuclear modification factor of Υ(1S) and Υ(2S) in PbPb collisions at $\sqrt{s_{NN}} = 2.76$ TeV, as a function of the Υ transverse momentum. The gray error bar at unity is the global systematic uncertainty due to *pp* tracking efficiency and luminosity.

- **correlated sub-total**: total of *correlated* systematic uncertainties, computed as the quadratic sum of the previous items,

- **total**: quadratic sum of correlated and 'global' uncertainties (common to all points, i.e. luminosities and tracking efficiencies).

Table 7.11 sums up the systematic uncertainties used in the centrality dependence result.

- systematic uncertainty from fit variations on PbPb data,

- efficiency correction, from tag-and-probe in *pp* data,

- uncertainty on the value of the nuclear thickness function,

- global *pp* uncertainty: summing up $\mathcal{L}_{pp}$, integrated for *pp* efficiency, statistical and systematic uncertainty from fitting,

- total of 'correlated' point-to-point systematic uncertainties, computed as the quadratic sum of the four previous columns,

- total of 'correlated' and global uncertainty.

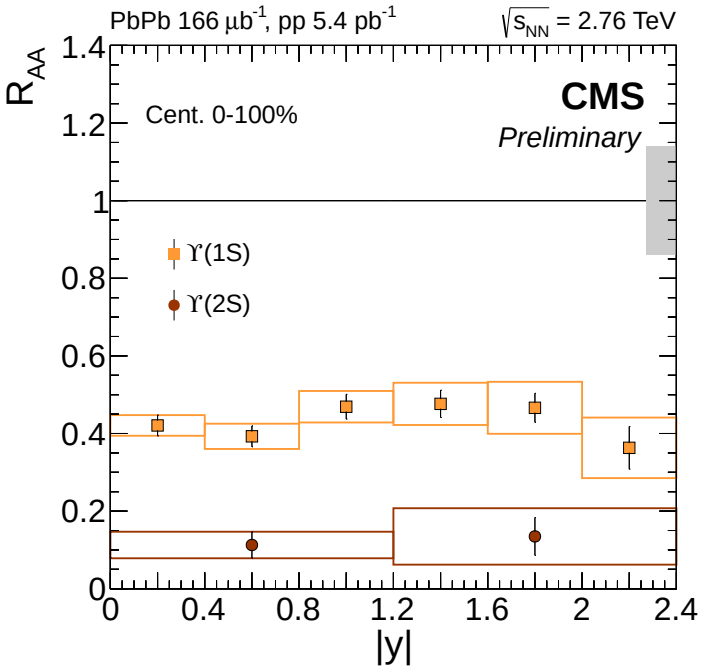

Figure 7.7: PbPb nuclear modification factor of ϒ(1S) and ϒ(2S) in PbPb collisions at $\sqrt{s_{NN}} = 2.76$ TeV, as a function of the ϒ rapidity. The gray error bar at unity is the global systematic uncertainty due to *pp* tracking efficiency and luminosity.

7.2.4 Upper limits on ϒ(3S) production in PbPb collisions

Once the signal is extracted from the maximum likelihood fit, we employ the Feldman-Cousins (FC) method to set a limit at the 95% confidence level [140]. While the expected limit on the nuclear modification factor is close to a non-physical (negative) limit, the FC prescription guarantees a physically meaningful result and tells us how to smoothly transition from a one-sided limit to a two-sided interval. In other words, this method will return a two-sided interval in the case of a significant result, and an upper limit in the case of a non-significant result, the transition between the two cases being smooth and well-defined from a statistical point of view (i.e. with a proper coverage).

The Feldman Cousins method is applied via its implementations in RooStats [141]. In practice the class `HypoTestInverter` is used, with two possible settings: frequentist (using pseudo-experiments) or asymptotic (using asymptotic formulae). The latter is less reliable and can only be used as a fast cross-check. The test statistic used is a profile likelihood ratio.

In the lack of MC simulation for the ϒ(3S), we assume the ratio of PbPb to *pp* efficiencies to be the same for the ϒ(2S) and ϒ(3S), and take the value (0.95) from the ϒ(2S) simulation.

Systematic uncertainties are included as nuisance parameters in the fit, with a log-normal distribution. The following systematic uncertainties are included for now:

- T_{AA} (6.2%),

	$\mathcal{Y}_{\mathrm{PbPb}}[\Upsilon(1S)]/T_{\mathrm{AA}}$ [nb]	$R_{\mathrm{AA}}[\Upsilon(1S)]$
$\lvert y\rvert < 0.4$	0.355± 0.022± 0.007	0.421±0.027± 0.027
$0.4 < \lvert y\rvert < 0.8$	0.343± 0.023± 0.012	0.393±0.027± 0.033
$0.8 < \lvert y\rvert < 1.2$	0.357± 0.024± 0.019	0.469±0.032± 0.041
$1.2 < \lvert y\rvert < 1.6$	0.352± 0.025± 0.013	0.476±0.035± 0.054
$1.6 < \lvert y\rvert < 2$	0.300± 0.025± 0.019	0.466±0.037± 0.067
$2 < \lvert y\rvert < 2.4$	0.249± 0.037± 0.007	0.363±0.055± 0.078
	$\mathcal{Y}_{\mathrm{PbPb}}[\Upsilon(2S)]/T_{\mathrm{AA}}$ [nb]	$R_{\mathrm{AA}}[\Upsilon(2S)]$
$\lvert y\rvert < 1.2$	0.0264 ±0.0077 ± 0.0019	0.113 ± 0.034 ± 0.034
$1.2 < \lvert y\rvert < 2.4$	0.0268 ±0.0095± 0.0025	0.135 ± 0.049 ± 0.073

Table 7.9: Normalized yields $\mathcal{Y}_{\mathrm{PbPb}}/T_{\mathrm{AA}}$ and R_{AA} as a function of y for Υ(1S)(top) and Υ(2S) (bottom) states in PbPb collisions at $\sqrt{s_{NN}} = 2.76$ TeV. Listed uncertainties are statistical (first) and systematic (second).

- *pp* luminosity (3.7%),
- ratio of efficiencies between *pp* and PbPb data (including the systematic uncertainty on tag and probe) (5.3%),
- number of background events in *pp* data (from the fit variations) (4%),
- number of background events in PbPb data (from the fit variations) (2%),
- number of signal events in *pp* data (from the fit variations) (8%),
- number of signal events in PbPb data (from the fit variations) (20%).

A reliable systematic uncertainty on the Υ(3S) in PbPb data could not be determined from fit variations, given its non significant yield. For this reason, this systematic uncertainty was deduced in the following way: $\mathrm{syst}(\Upsilon(1S), \mathrm{PbPb}) \times \mathrm{syst}(\Upsilon(3S), \mathrm{pp})/\mathrm{syst}(\Upsilon(1S), \mathrm{pp})$, which gives $0.11 \times 0.08/0.045 = 0.20$.

Using the asymptotic calculation, we obtain an upper limit $R_{\mathrm{AA}}(\Upsilon(3S)) < 0.13$ at 95% C.L. Using the full frequentist calculation (using pseudo-experiments), we obtain

$$\begin{aligned} R_{\mathrm{AA}}(\Upsilon(3S)) &< 0.14 \text{ at } 95\% \text{ C.L.} \\ R_{\mathrm{AA}}(\Upsilon(3S)) &< 0.08 \text{ at } 68\% \text{ C.L.} \end{aligned}$$

The result of the scan is shown on Fig. 7.8, on the left for the asymptotic calculation and on the right for the frequentist calculation. Visually, the upper limit is obtained from the place where the observed CL_s (red dots) crosses the horizontal threshold (red line, at $0.05 = 1 - 0.95$ for 95% C.L.). Fig. 7.9 shows the scan for the frequentist calculation, zoomed in on smaller values of $R_{\mathrm{AA}}(\Upsilon(3S))$ for the determination of the 68% C.L. upper limit.

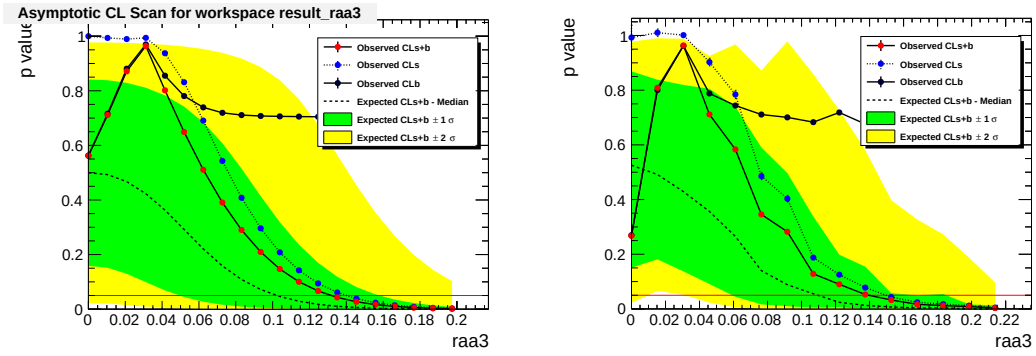

Figure 7.8: Asymptotic scan (left) and frequentist scan (right) of the ratio of raw 3S yields in *pp* and PbPb collisions, based on the Feldman and Cousins approach, giving the 95% C.L. upper limit on $R_{\mathrm{AA}}(\Upsilon(3S))$.

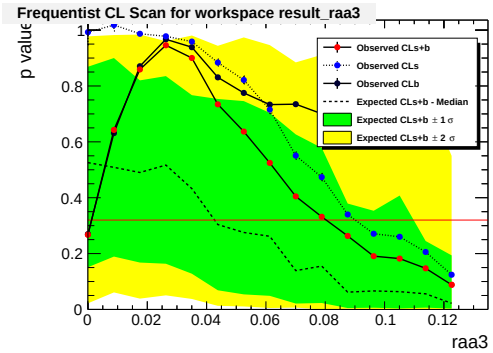

Figure 7.9: Frequentist scan of the ratio of raw 3S yields in *pp* and PbPb collisions, based on the Feldman and Cousins approach, giving the 68% C.L. upper limit on $R_{\mathrm{AA}}(\Upsilon(3S))$.

The $\Upsilon(1S)$, $\Upsilon(2S)$ and $\Upsilon(3S)$ mesons have been searched for in PbPb collisions, and compared to their yields in *pp* collisions at the same centre-of-mass energy of 2.76 TeV per nucleon pair. The $\Upsilon(1S)$ and $\Upsilon(2S)$ are suppressed by a factor of ≈ 2 and 9, respectively, while the unobserved $\Upsilon(3S)$ corresponds to a suppression by a factor of more than 7, at the 95% confidence level. Though a strong centrality dependence of the suppression is observed for the $\Upsilon(1S)$ and $\Upsilon(2S)$ as a function of centrality, no noticeable dependence is observed, neither as a function of transverse momentum, nor as a function of rapidity. The $\Upsilon(3S)$ being not observed, an upper limit on its R_{AA} is derived, using the Feldman-Cousins prescription. The centrality integrated results for the nuclear modification factors of $\Upsilon(1S)$, $\Upsilon(2S)$ and $\Upsilon(3S)$ are:

$$\begin{aligned} R_{\mathrm{AA}}(\Upsilon(1S)) &= 0.425 \pm 0.029\ (\mathrm{stat.}) \pm 0.070\ (\mathrm{syst.}), \\ R_{\mathrm{AA}}(\Upsilon(2S)) &= 0.116 \pm 0.028\ (\mathrm{stat.}) \pm 0.022\ (\mathrm{syst.}), \\ R_{\mathrm{AA}}(\Upsilon(3S)) &< 0.14 \text{ at } 95\% \text{ CL}. \end{aligned}$$

7.3 Discussions

7.3.1 Experimental comparisons

The ALICE collaboration has published in 2013 in [5] a measurement of $\Upsilon(1S)$ suppression in PbPb, extending the available R_{AA} results to the rapidity range $2.5 < y < 4$. This publication shows a centrality integrated R_{AA} for $\Upsilon(1S)$ at the value of $R_{AA}(\Upsilon(1S)) = 0.30 \pm 0.05$ (stat.) $\pm$ 0.04 (syst.). This result came before the present study was made public, and in terms of CMS data, could only be compared to the previous measurement [4]. The integrated result for $R_{AA}(\Upsilon(1S))$ of CMS [4] is compared to rapidity-dependent ALICE results of [5] in Figure 7.10, taken form the ALICE paper [5].

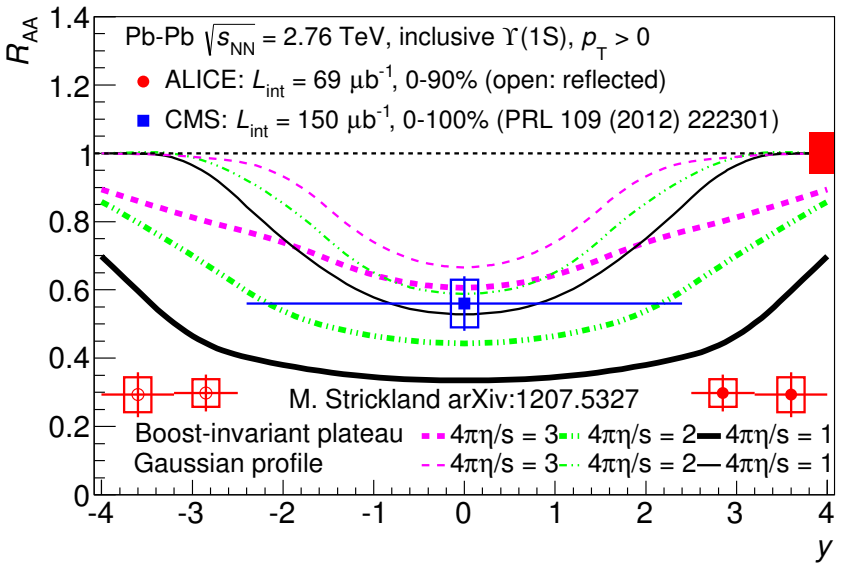

Figure 7.10: PbPb nuclear modification factor R_{AA} in PbPb collisions at $\sqrt{s_{NN}} = 2.76$ TeV, as a function of Υ rapidity, taken from [5]. Data from CMS publication using 2010 *pp* data [4] and ALICE [5]. The data is plotted against a potential model for quarkonium suppression described in [142].

Visually, the plot suggest a stronger suppression at forward rapidities, i.e. in the acceptance of the ALICE spectrometer. The centrality integrated R_{AA} obtained by CMS (with the smaller *pp* dataset taken in 2010) was $R_{AA}(\Upsilon(1S)) = 0.56 \pm 0.08$ (stat.) $\pm$ 0.07 syst.. Since the ALICE and CMS make independent measurements of the $\Upsilon(1S)$ suppression, one can write a weighted sum of squared errors:

$$\chi^2 = \frac{(0.56 - 0.30)^2}{0.08^2 + 0.07^2 + 0.05^2 + 0.04^2} = 4.60\,. \tag{7.6}$$

For this χ^2 there is a 3.20% probability that another measurement yields an observed χ^2 at least as large [143]. This holds even if the hypothesis of no additional suppression in ALICE data was correct (in which case, one of the experiments just got unlucky).

Assuming all the uncertainties are normally distributed, this translates into a deviation of only 2.1 sigmas between the two measurements. Hence, the claim in [5] that the data observed in ALICE and CMS showed a rapidity dependent ϒ(1S) suppression is not statistically significant. However, the larger statistics of the measurement presented here could allow a more stringent test for this hypothesis.

The latest $R_{\mathrm{AA}}(\Upsilon(1S))$ of CMS and ALICE data are displayed as a function of rapidity in Figure 7.11. There is no strong R_{AA} dependence on the rapidity range considered. Indeed, using the new integrated result $R_{\mathrm{AA}}(\Upsilon(1S)) = 0.425 \pm 0.029$ (stat.) $\pm$ 0.070 syst. and applying the same chi-square test as in Equation 7.6, one obtains a 1.3-sigma deviation between the two integrated results. Given that the CMS result is still at the preliminary stage and final systematic uncertainties may be reduced, one should be cautious as with the significance computed here, as it may change again. As a quick example of an extreme case, assuming infinite precision in the final CMS result (with the same central value, i.e. turning the CMS uncertainties to zero in Equation 7.6) would yield a 2 sigma deviation from the 'flat suppression' hypothesis.

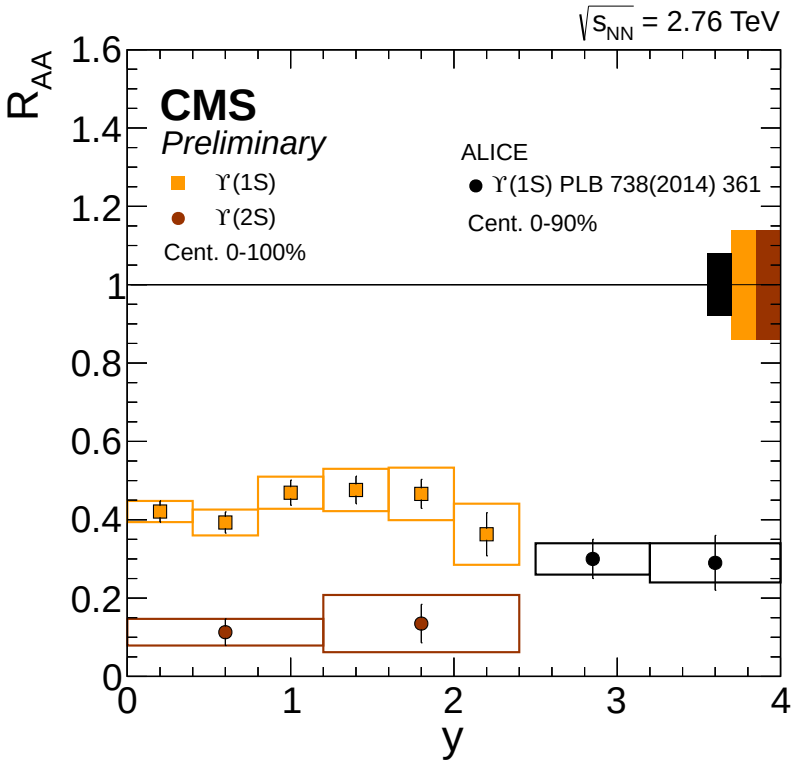

Figure 7.11: PbPb nuclear modification factor R_{AA} in PbPb collisions at $\sqrt{s_{NN}} = 2.76$ TeV, as a function of ϒ rapidity. Data from CMS and ALICE [5].

RHIC uses gold nuclei (A = 197) while LHC uses lead nuclei (A = 208). Comparing RHIC energies with LHC energies results in a factor 14 increase in $\sqrt{s_{NN}}$. However, an increase of a factor 14 in $\sqrt{s_{NN}}$ does not change dramatically the QGP properties (i.e. the energy density). Indeed, the charged particle multiplicity per colliding nucleon pair

measured by ALICE [144] and CMS [47] in PbPb collisions at $\sqrt{s_{NN}} = 2.76$ TeV for the most central collisions is about three times that measured at PHENIX [145] and PHOBOS [146] at RHIC in AuAu collisions at $\sqrt{s_{NN}} = 200$ GeV. In that sense, one does expect a sizeably different Υ suppression at LHC and RHIC, however not as large as the increase in center of mass energy.

The CMS Υ data of the present analysis can be compared to RHIC data in a similar rapidity range: the STAR Collaboration has published in [132] a AuAu measurement of Υ suppression at $\sqrt{s_{NN}} = 200$ GeV, exhibiting a lesser suppression at equivalent N_{part}. It is exciting to see that recently, this AuAu data has been supplemented by reports of a slightly more pronounced Υ suppression in UU data at the same energy, involving a larger number of participants than in AuAu [147]. The suppression seen in AuAu and UU by the STAR experiment is compared as a function of N_{part} in Figure 7.12.

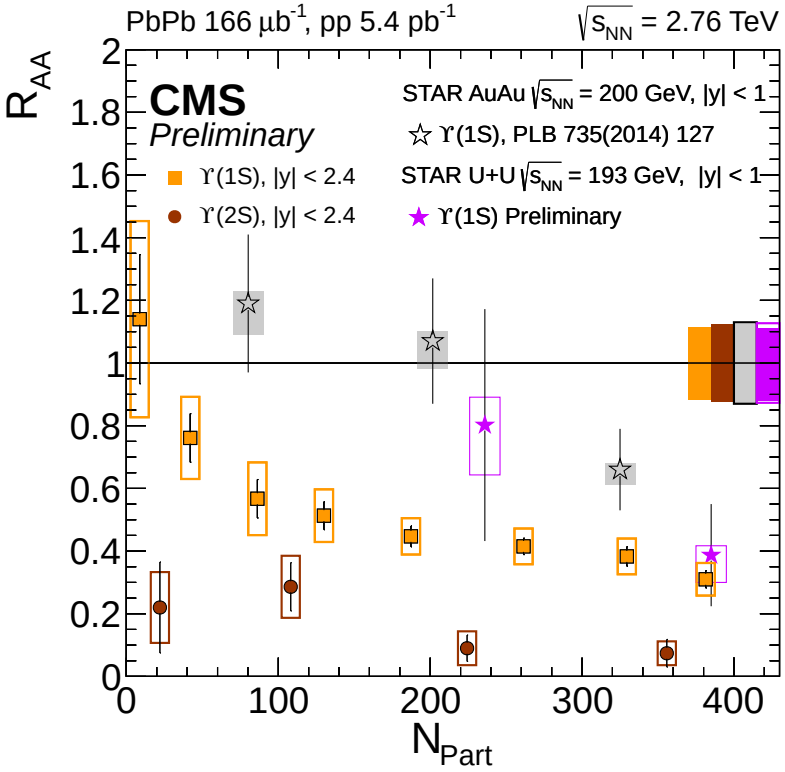

Figure 7.12: PbPb nuclear modification factor R_{AA} as a function of the number of participating nucleons. Data from CMS and STAR [132, 147] in AuAu and UU at $\sqrt{s_{NN}} = 200$ GeV and 193 GeV, respectively. ALICE data is gathered in centrality bins [0-20%], [20-90%].

Within large uncertainties, the suppression seen by the STAR collaboration in the most central point (the 10% most central UU events) finds close compatibility with several high-N_{part} CMS points, from $N_{\text{part}} = 200$ and above. Additionally, the suppression seen in STAR at $N_{\text{part}} \sim 200$ is about the same as what is reported by CMS in the most peripheral bin. These two observations are giving interesting insight on the

evolution of the QGP-induced suppression with higher energy densities, and should be investigated further: for example, additional dAu data at RHIC would help to clarify the effect of cold nuclear matter on ϒ production at RHIC energies. Indeed, this is at the moment subject to large uncertainties [132]. Additionally, one can wonder what is the status of excited state suppression at RHIC. Since the onset of ϒ(1S) suppression is visible in RHIC data in more central events than in LHC data (because the energy density is smaller at RHIC than at LHC for a given N_{part}), the suppression of ϒ(2S), ϒ(3S) should also be 'shifted' to higher energy densities.

So far, we are still lacking a comparison with another experiment for our new $R_{\mathrm{AA}}(\Upsilon)$ result as a function of p_T. Keeping in mind that the bottomonium and charmonium families have quite different masses, hence different Q^2, one could compare the p_T-dependence of the suppression seen in inclusive J/ψ events recorded with ALICE [78] with the flat suppression seen in our ϒ measurement. This comparison is shown in 7.13, and can be extended to higher charmonium p_T using the CMS results of [81].

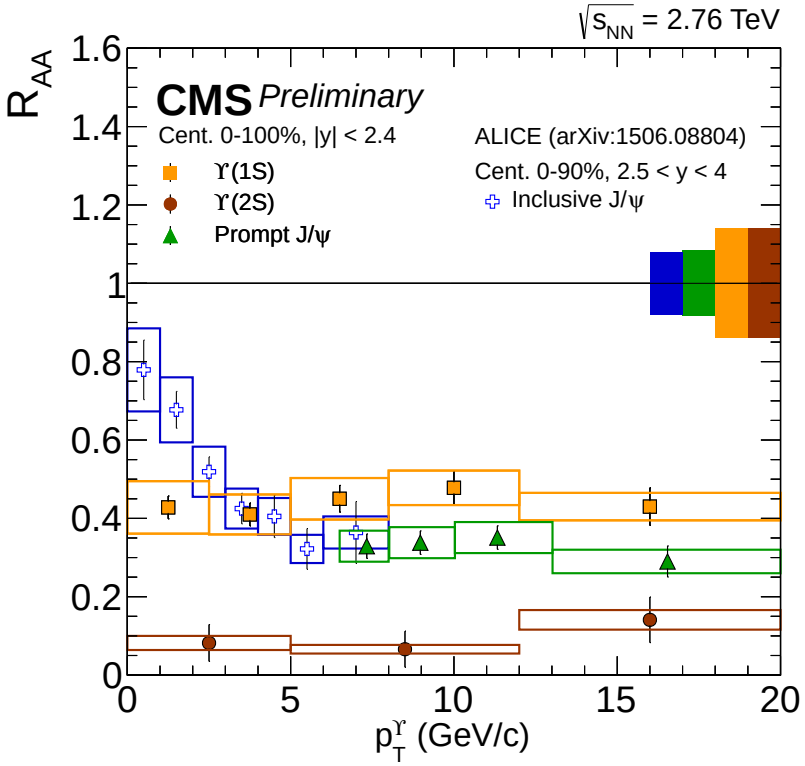

Figure 7.13: Comparison of the ϒ(1S), ϒ(2S) and J/ψ nuclear modification factors in the CMS measurement [81] and with ALICE inclusive J/ψ data from [78], as a function of transverse momentum.

It is interesting to see that J/ψ and ϒ seem to behave very differently at low momenta at the LHC. At high-p_T the suppression is independent of p_T for both species. When reducing the p_T of the quarkonium pair, the suppression remains about

the same for the Υ family, as we have seen. However, the suppression for J/ψ starts to diminish at $p_T(J/\psi) \sim m_{J/\psi}$. This observation could be considered as an indirect confirmation of a sizeable regeneration mechansism in the charmonium spectrum at low-p_T, setting off as the momentum increases.

Before moving to comparisons with theoretical models for Υ suppression, I should discuss the impact of nuclear absorption or other cold nuclear matter effects in all of the figures above. Obviously, the beginning of a data-based distinction between cold and hot effects is very difficult at this stage: the data is still quite insufficient in peripheral events, where hot effects are not expected to dominate. Additionally, one would need a R_{pA} for individual Υ at the same center of mass energy and in the same rapidity range as the CMS measurement, to get a grasp of the cold nuclear effects due to one heavy nucleus. The ATLAS collaboration has recently put forth a measurement of the pPb nuclear modification factor, based on an extrapolated pp cross section at $\sqrt{s} = 5.02$ TeV from other energies [148]. This interesting first attempt at estimating the Υ(1S) cold nuclear effects in the central rapidity region shows that they are small.

For what concerns the excited states Υ(2S) and Υ(3S), it has been demonstrated first in [149] that these suffer slight additional modification in pPb at $\sqrt{s_{NN}} = 5.02$ TeV, with respect to the ground state. This modification is smaller than what is observed in PbPb collisions at LHC energies. Additional studies of the peripheral AA collisions, as well as pA collisions of increasing centralities, are needed to better understand what are the various processes at play in this regime.

7.3.2 Comparisons with suppression models in PbPb

Figure 7.14 shows a comparison of centrality binned data from CMS with the transport model of Rapp *et al.* using a rate equation approach detailed in [150], and applied in the strong binding scenario [151]. In this model, primordial and regenerated contributions are taken into account. However, it is worth pointing out that regeneration necessitates a large initial number of quark pairs produced. In other words, the regeneration component is expected to depend on the total $q\bar{q}$ production cross section. In the case of $b\bar{b}$ it is unclear how many pairs are produced in central PbPb collisions, however the exact number should be of the order of 5$\sim$10, preventing Υ a sizeable regeneration effect to occur at present LHC energies.

I have plotted the regeneration and primordial contributions on Figure 7.14 for completeness. The model manages to reproduce the data. It should be pointed out from [151] that the primordial component is constantly suppressed over the p_T range scanned in [151] (computed there for J/ψ, not Υ). This would suggest that a constant suppression over p_T could also be expected when this model is applied to Υ. I am not aware of the actual calcultation leading to the amount of nuclear absorption shown in this figure; at large $N_{\rm part}$, a good fraction of the agreement between model and data could be accounted to this contribution, which cannot be confirmed.

Figure 7.15 shows a comparison of centrality-binned data from CMS with a hydrodynamic model from Strickland *et al.* [152]. This result is an update of a computation using a complex-valued binding potential for the quark pair, described in [142]. The

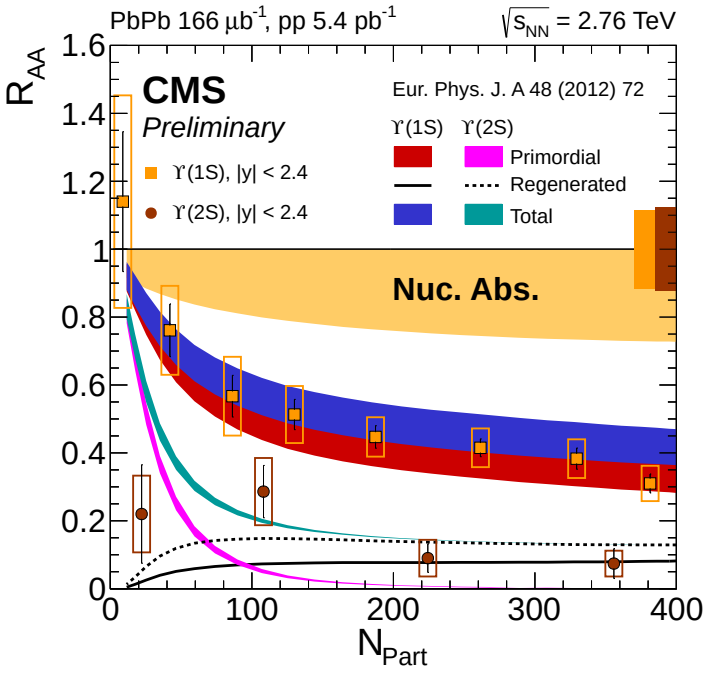

Figure 7.14: PbPb nuclear modification factor R_{AA} in PbPb collisions at $\sqrt{s_{NN}} = 2.76$ TeV, as a function of the number of participants.

value of the real part of the potential informs on the binding of the state: if the real part is positive (negative), the quarkonium is bound (unbound). The imaginary part of the potential gives a description of the dissociation rate of a given state as a function of the medium temperature. From $T \sim 250$ MeV and above, the imaginary part of the potential is related to a Landau-damping process of the gluon fields, which gives a decay width to the quarkonium state, as reported in [153]. The thermodynamic evolution considered here was initially described in [154], and accounts for large momentum-space anisotropies in the plasma. In the version shown in [152] and in Figure 7.15, the anisotropic hydrodynamical model accounts for transverse expansion (3+1D dynamics) which is an improvement compared to [142].

The hydrodynamical treatment can be tuned to different values of the shear viscosity to entropy ratio, η/s. The data seem to favor a scenario where η/s is close to $1/4\pi \sim/4\pi$. A clear overview of the importance of the value of η/s in strongly coupled theories is available in [155].

The same model is tested against data as a function p_T and y, in Figures 7.16 left and right. On the left hand side, the R_{AA} as a function of p_T is presented. The model suggest a slow reduction of the suppression factor with increasing momentum. From this figure it is difficult to tell whether the data would follow this slowly rising trend at higher momentum values. More data in the forthcoming heavy ion physics runs of CMS and other LHC experiments may shed more light on the high-p_T regime. On the right hand side, the rapidity dependence of the model is tested against CMS and ALICE ϒ(1S) data from [5].

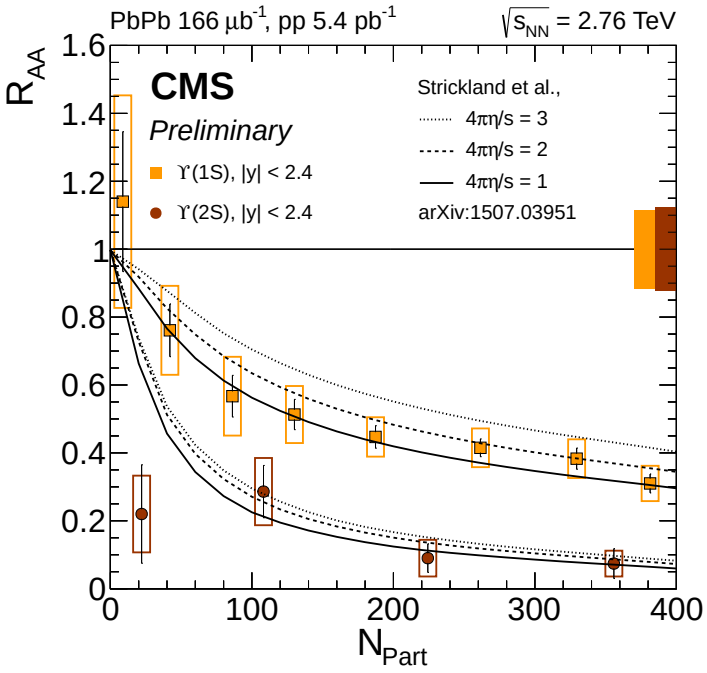

Figure 7.15: PbPb nuclear modification factor R_{AA} in PbPb collisions at $\sqrt{s_{NN}} = 2.76$ TeV, as a function of the number of participants. Comparison with updated calculations from Strickland [152].

Some tension appears at high rapidity, where the ALICE data appears below the expected suppression for this model. It should be noted that this discrepancy was already visible at the beginning of this section, in Figure 7.10, where the modeled $\Upsilon(1S)$ suppression wore off faster at larger rapidities. The version presented in Figures 7.16 and 7.15 includes an update for how the Υ are distributed over the centrality variable. In other words, the model benefitted of a N_{coll}-reweighting to mimick the proper centrality distribution for hard probes (previously assuming a flat distribution). This fix visibly reduced the discrepancy between the model and the forward rapidity data from ALICE.

p_T bin	Stat. (pp)	Stat. (AA)	Syst(PDF)$_{pp}$	Syst(PDF)$_{AA}$	TNP$_{pp}$	TNP$_{AA}$	Correlated	total
p_T [GeV/c] < 2.5	0.034	0.057	0.076	0.091	0.007	0.040	0.133	0.151
$2.5 < p_T$ [GeV/c] < 5	0.032	0.061	0.050	0.065	0.006	0.040	0.103	0.126
$5 < p_T$ [GeV/c] < 8	0.034	0.066	0.039	0.125	0.006	0.038	0.146	0.163
$8 < p_T$ [GeV/c] < 12	0.046	0.074	0.023	0.043	0.006	0.035	0.081	0.108
$12 < p_T$ [GeV/c] < 20	0.060	0.093	0.008	0.038	0.007	0.034	0.071	0.101
$\|y\| < 0.4$	0.035	0.064	0.030	0.055	0.004	0.010	0.063	0.005
$0.4 < \|y\| < 0.8$	0.035	0.068	0.026	0.110	0.004	0.011	0.114	0.009
$0.8 < \|y\| < 1.2$	0.039	0.068	0.038	0.175	0.004	0.018	0.180	0.019
$1.2 < \|y\| < 1.6$	0.042	0.074	0.039	0.093	0.007	0.053	0.114	0.010
$1.6 < \|y\| < 2$	0.052	0.085	0.051	0.216	0.012	0.108	0.247	0.038
$2 < \|y\| < 2.4$	0.079	0.151	0.082	0.281	0.015	0.150	0.329	0.066

Table 7.10: Systematic uncertainties recap for Υ(1S), in (p_T,y)-differential $R_{\rm AA}$ analyses.

1S Centrality	Syst(PDF)$_{AA}$	TNP$_{AA}$	T$_{AA}$	Global *pp*	Correlated	total
0-5	0.144	0.036	0.041	0.035	0.160	0.164
5-10	0.120	0.038	0.046	0.035	0.141	0.146
10-20	0.103	0.037	0.052	0.035	0.129	0.134
20-30	0.085	0.038	0.066	0.035	0.122	0.127
30-40	0.120	0.038	0.084	0.035	0.157	0.161
40-50	0.157	0.038	0.109	0.035	0.199	0.202
50-70	0.054	0.039	0.147	0.035	0.167	0.171
70-100	0.215	0.039	0.154	0.035	0.271	0.273
2S Centrality	Syst(PDF)$_{AA}$	TNP$_{AA}$	T$_{AA}$	Global *pp*	Correlated	total
0-10	0.458	0.035	0.043	0.056	0.510	0.513
10-30	0.560	0.036	0.058	0.056	0.603	0.605
30-50	0.255	0.036	0.093	0.056	0.346	0.350
50-100	0.440	0.036	0.150	0.056	0.512	0.515

Table 7.11: Systematic uncertainties recap for Υ(1S) and Υ(2S), in bins of centrality.

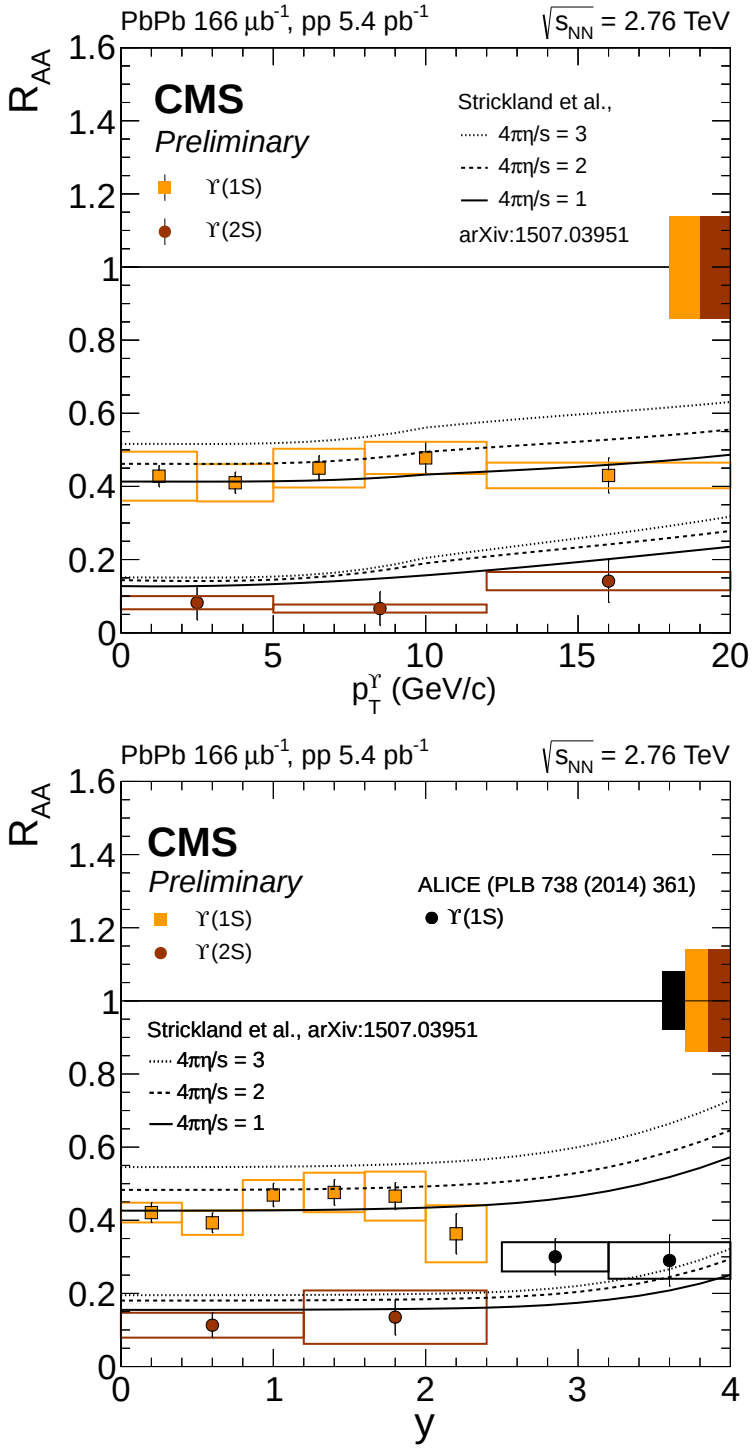

Figure 7.16: PbPb nuclear modification factor R_{AA} in PbPb collisions at $\sqrt{s_{NN}} = 2.76$ TeV, as a function of the ϒ p_T and y. Theoretical curves obtained from anisotropic hydrodynamics from [152].

Appendix A

Additional figures

A.1 Fits to dimuon invariant mass spectra

A.1.1 p_T dependent analysis of pp and PbPb yields

The following Figures A.1 to A.5 present the yields used in the computation of the Υ(1S) cross section and R_{AA} in fine bins of p_T.

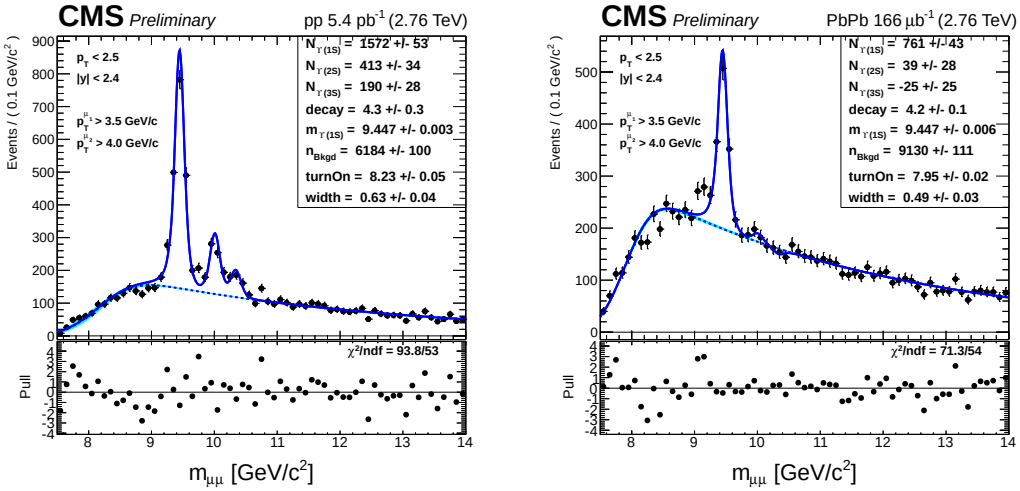

Figure A.1: Fits to pp (left) and PbPb (right) datasets with loose muon cuts (Υ(1S) analysis) in the bin p_T [GeV/c] $\in [0 - 2.5]$.

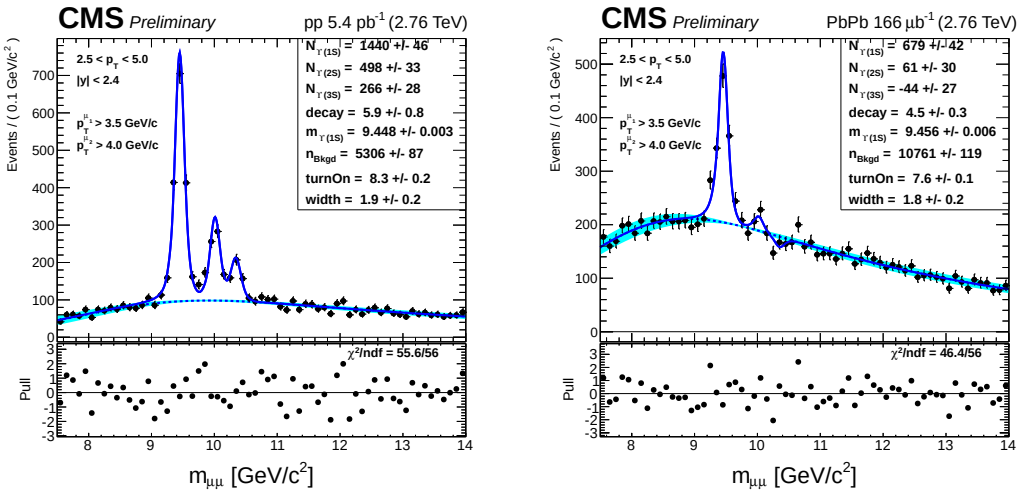

Figure A.2: Same as Figure A.1 in the bin p_T [GeV/c] $\in [2.5 - 5]$.

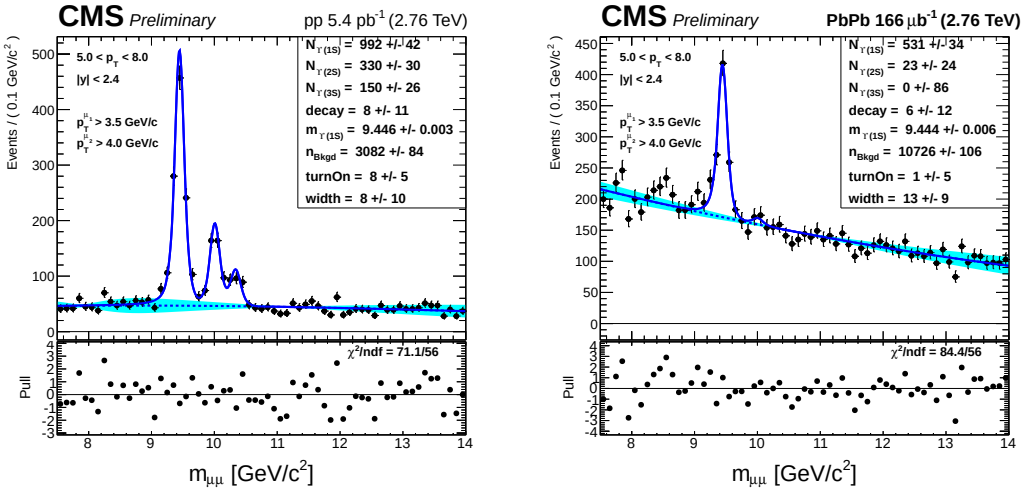

Figure A.3: Same as Figure A.1 in the bin p_T [GeV/c] $\in [5-8]$.

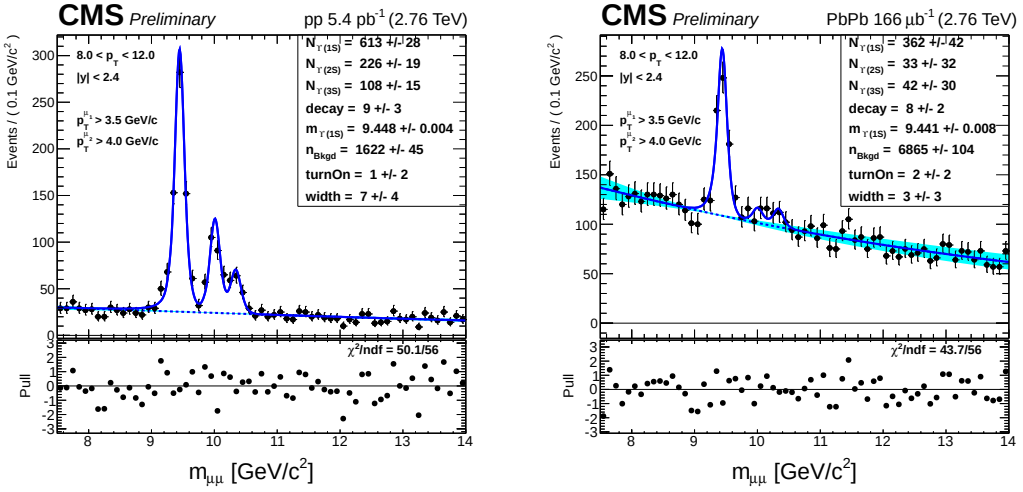

Figure A.4: Same as Figure A.1 in the bin p_T [GeV/c] $\in [8-12]$.

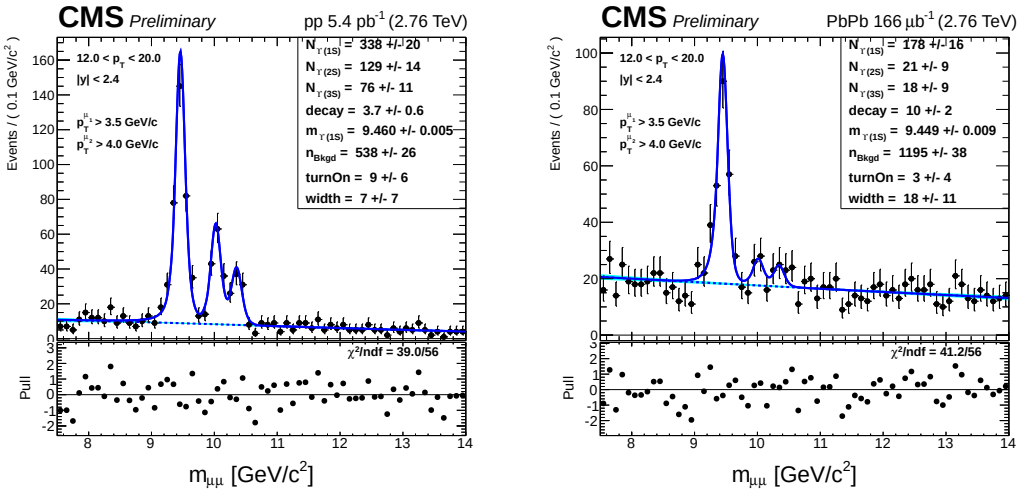

Figure A.5: Same as Figure A.1 in the bin p_T [GeV/c] $\in [12 - 20]$.

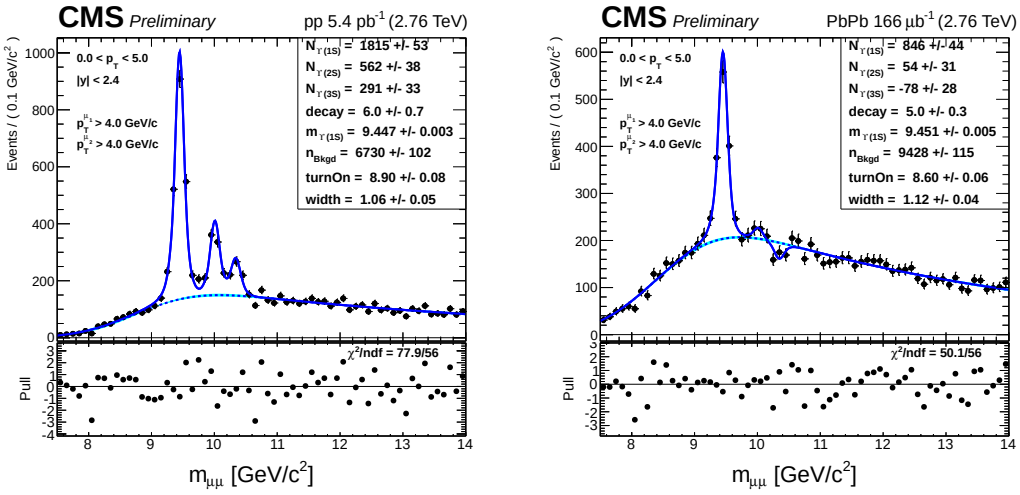

Figure A.6: Fits to pp (left) and PbPb (right) datasets with tight muon cuts (Υ(2S) analysis) in the bin p_T [GeV/c] $\in [0-5]$.

Figures from A.6 to A.8 present the three p_T bins of the Υ(2S) analysis in PbPb collisions.

Figure A.9: Bin $20 < p_T < 50$ GeV/c, not included in analysis so far.

A.1.2 Rapidity dependent analysis of *pp* and PbPb yields

The following Figures A.10 to A.15 are used in the computation of the rapidity dependent cross section for Υ(1S) and its corresponding $R_{\rm AA}$.

Figure A.16 and A.17 present the two rapidity bins of the Υ(2S) analysis, used in the computation of the $R_{\rm AA}(\Upsilon(2S))$ in wide bins of rapidity.

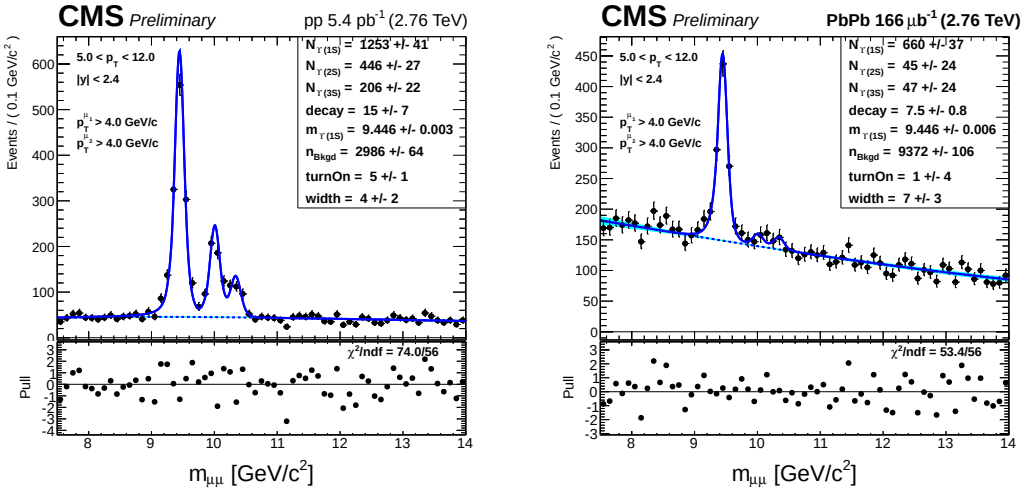

Figure A.7: Same as Figure A.6 in the bin p_T [GeV/c] $\in [5-12]$.

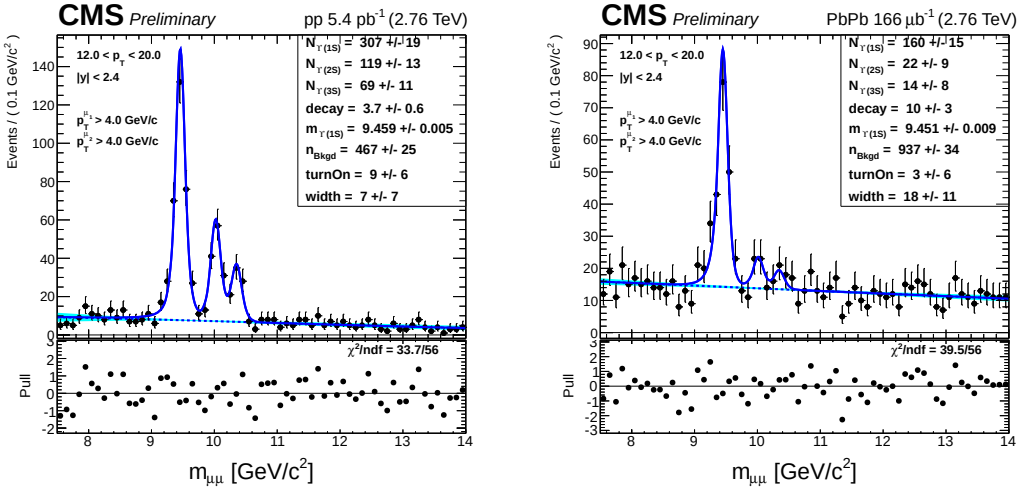

Figure A.8: Same as Figure A.6 in the bin p_T [GeV/c] $\in [12-20]$.

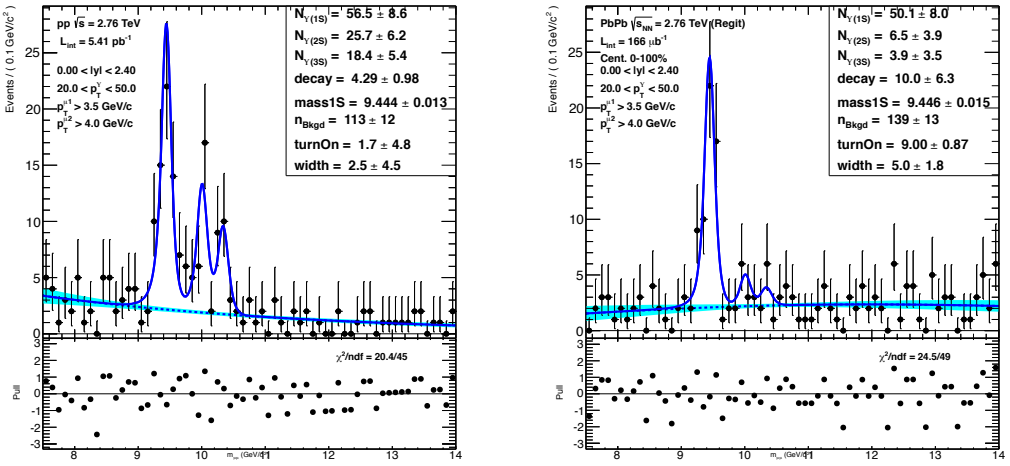

Figure A.9: Υ raw yields in the $20 < p_T < 50\text{GeV}/c$ bin. Left: pp, right: PbPb. These events are not included in the present analysis.

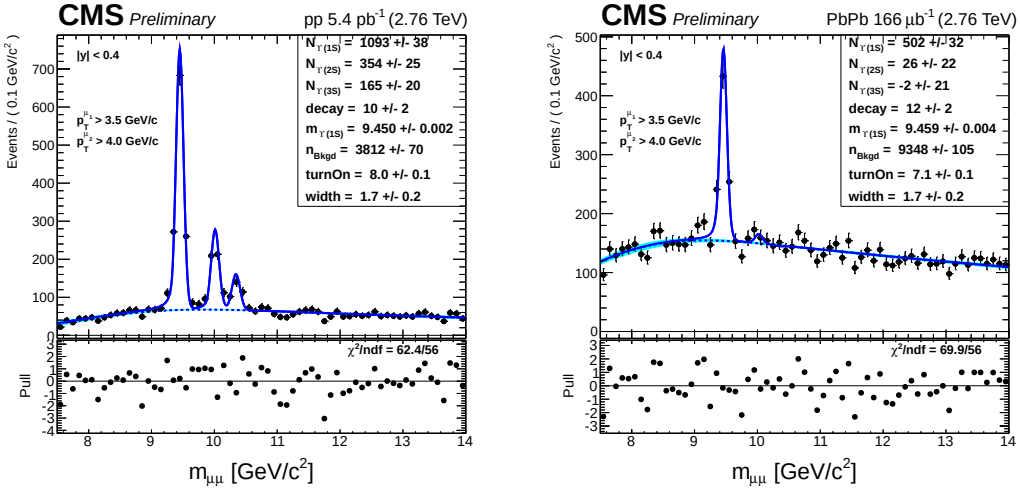

Figure A.10: Fits to pp (left) and PbPb (right) datasets with loose muon cuts (Υ(1S) analysis) in the bin $y \in [0 - 0.4]$.

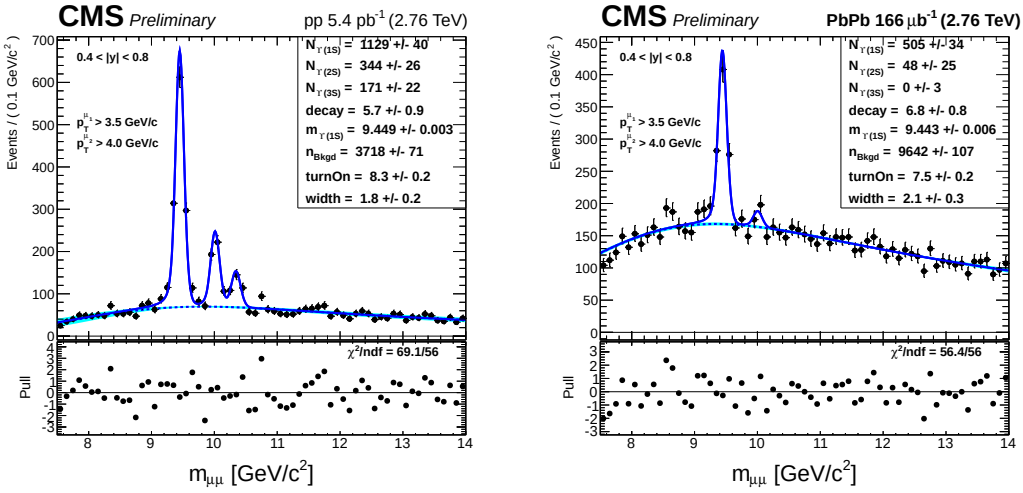

Figure A.11: Same as Figure A.10 in the bin $y \in [0.4 - 0.8]$.

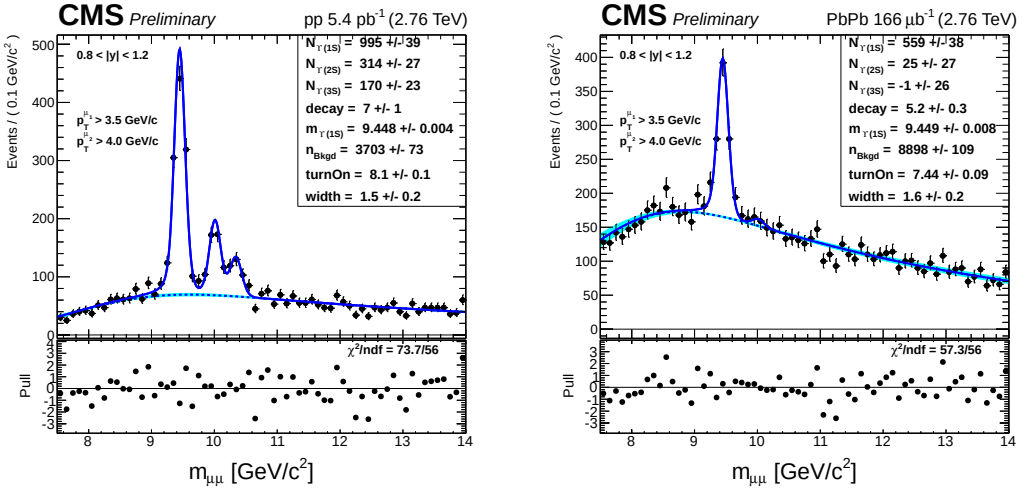

Figure A.12: Same as Figure A.10 in the bin $y \in [0.8 - 1.2]$.

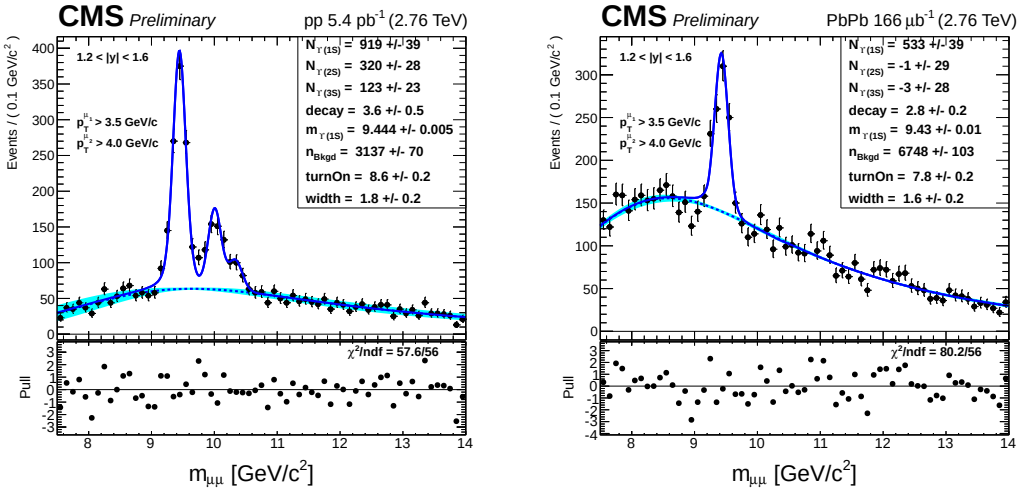

Figure A.13: Same as Figure A.10 in the bin $y \in [1.2 - 1.6]$.

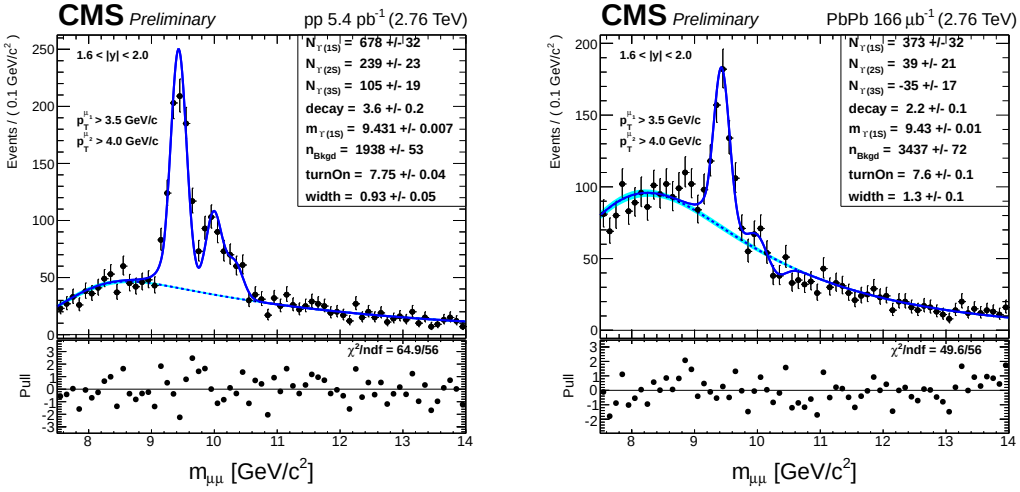

Figure A.14: Same as Figure A.10 in the bin $y \in [1.6 - 2]$.

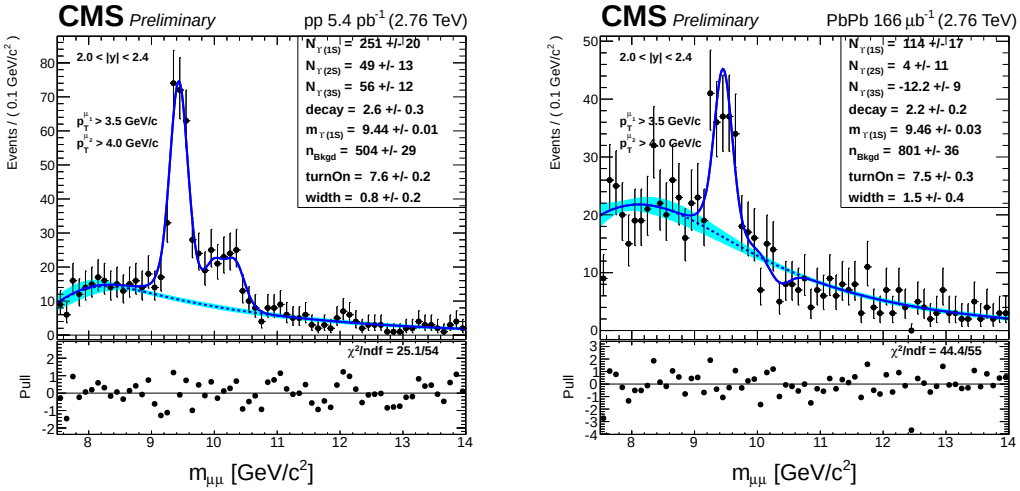

Figure A.15: Same as Figure A.10 in the bin $y \in [2 - 2.4]$.

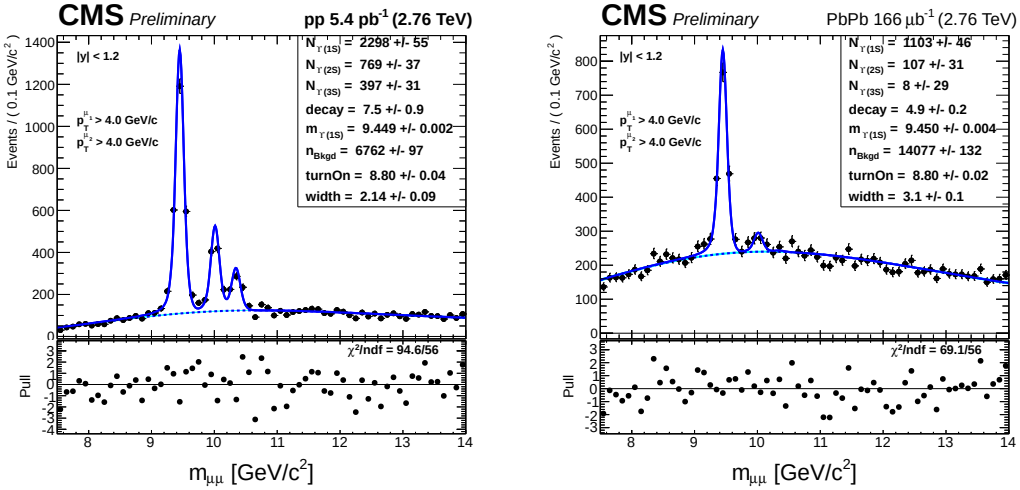

Figure A.16: Fits to pp (left) and PbPb (right) datasets with tight muon cuts (Υ(2S) analysis) in the bin $y \in [0 - 1.2]$.

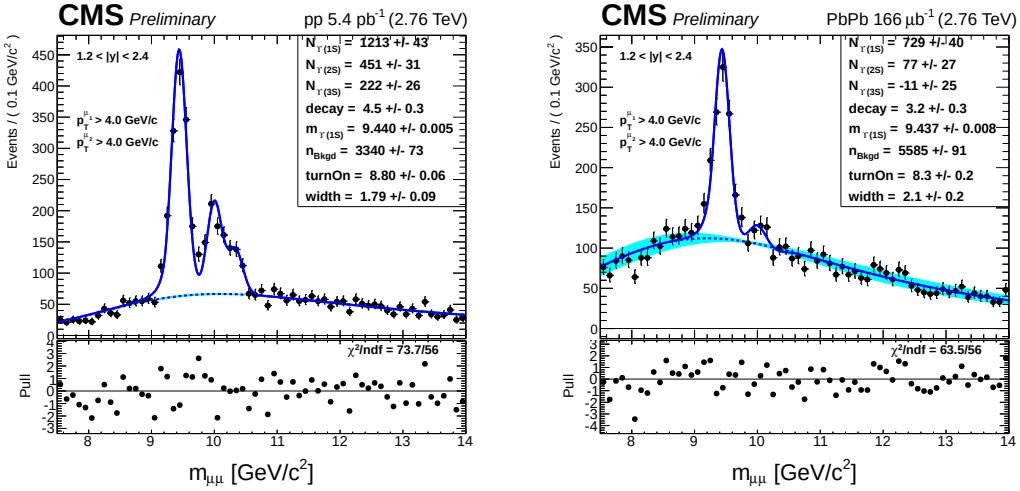

Figure A.17: Same as Figure A.16 in the bin $y \in [1.2 - 2.4]$.

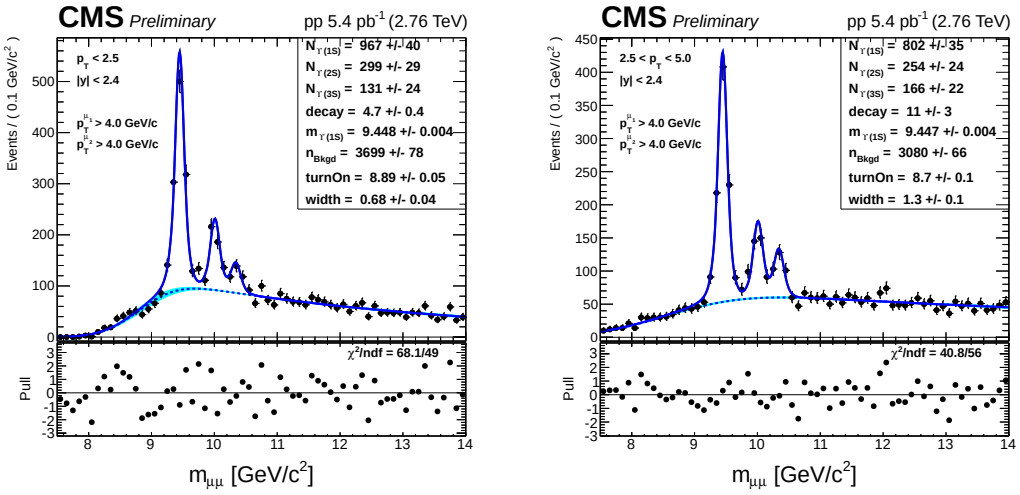

Figure A.18: Fits to the pp dataset with the tight muon p_T cut applied, for the extraction of the pp Υ(2S) and Υ(3S) cross sections in fine bins of p_T. Left:p_T [GeV/c] $\in$ [0 − 2.5]. Right:p_T [GeV/c] $\in$ [2.5 − 5].

A.1.3 pp cross section measurements for excited states

Figures from A.18 to **??** present the p_T and rapidity bins of the Υ(2S) and Υ(3S) cross section in pp collisions.

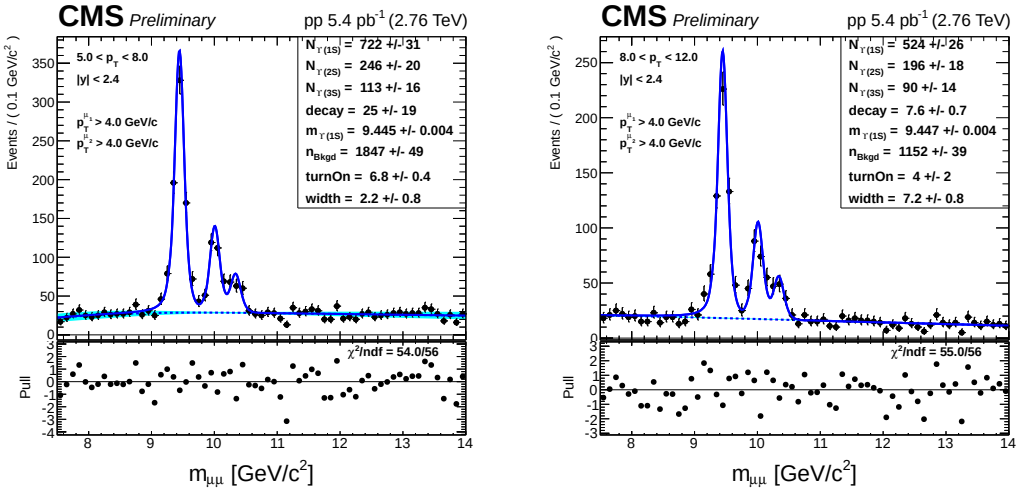

Figure A.19: Fits to the pp dataset with the tight muon p_T cut applied, for the extraction of the pp Υ(2S) and Υ(3S) cross sections in fine bins of p_T. Left:p_T [GeV/c] $\in$ [5 – 8]. Right:p_T [GeV/c] $\in$ [8 – 12].

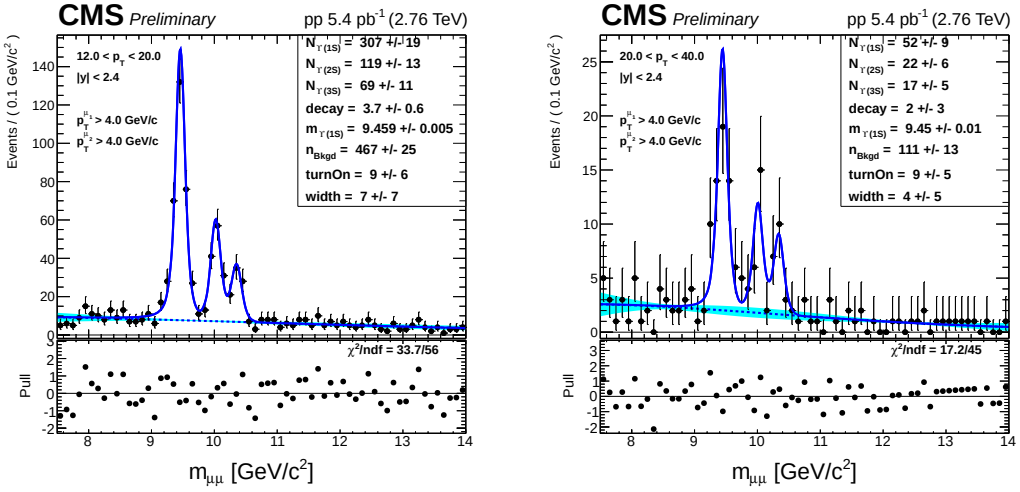

Figure A.20: Fits to the pp dataset with the tight muon p_T cut applied, for the extraction of the pp Υ(2S) and Υ(3S) cross sections in fine bins of p_T. Left:p_T [GeV/c] $\in$ [12 – 20]. Right:p_T [GeV/c] $\in$ [20 – 40].

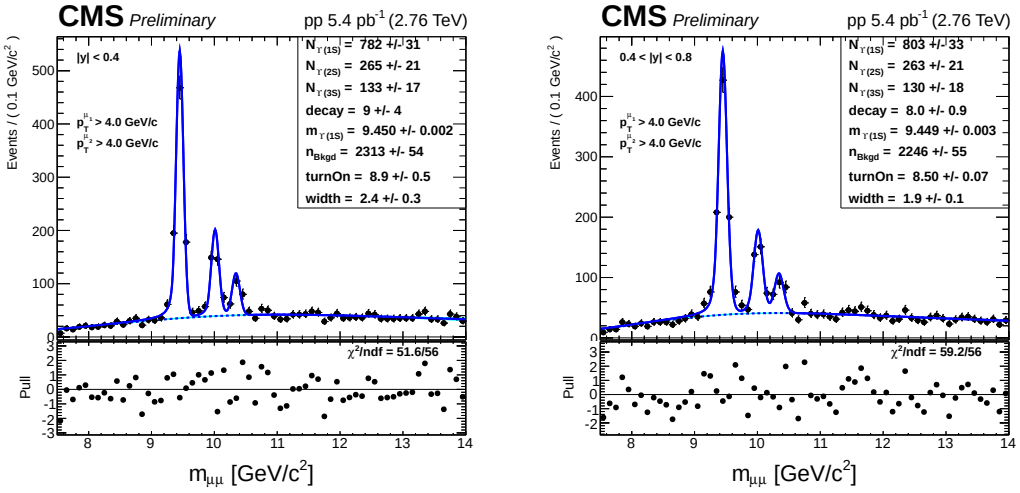

Figure A.21: Fits to the pp dataset with the tight muon p_T cut applied, for the extraction of the pp $\Upsilon(2S)$ and $\Upsilon(3S)$ cross sections in fine bins of rapidity. Left:$y \in [0. - 0.4]$. Right:$y \in [0.4 - 0.8]$.

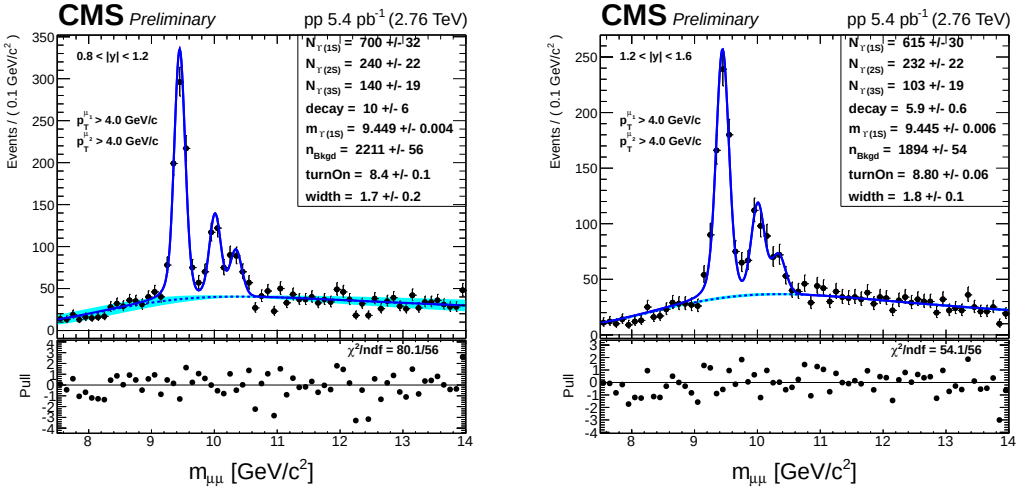

Figure A.22: Fits to the pp dataset with the tight muon p_T cut applied, for the extraction of the pp $\Upsilon(2S)$ and $\Upsilon(3S)$ cross sections in fine bins of rapidity. Left:$y \in [0.8 - 1.2]$. Right:$y \in [1.2 - 1.6]$.

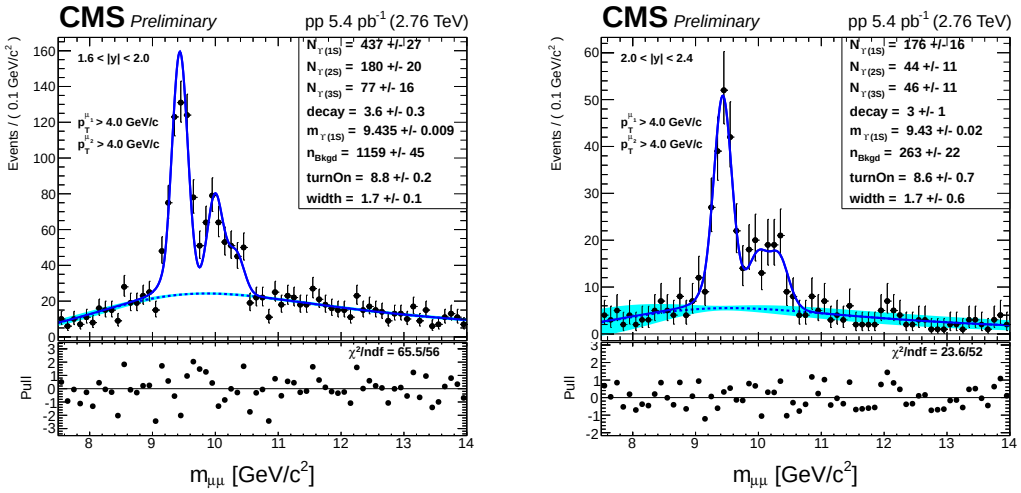

Figure A.23: Fits to the pp dataset with the tight muon p_T cut applied, for the extraction of the pp $\Upsilon(2S)$ and $\Upsilon(3S)$ cross sections in fine bins of rapidity. Left:$y \in [1.6-2.0]$. Right:$y \in [2.0-2.4]$.

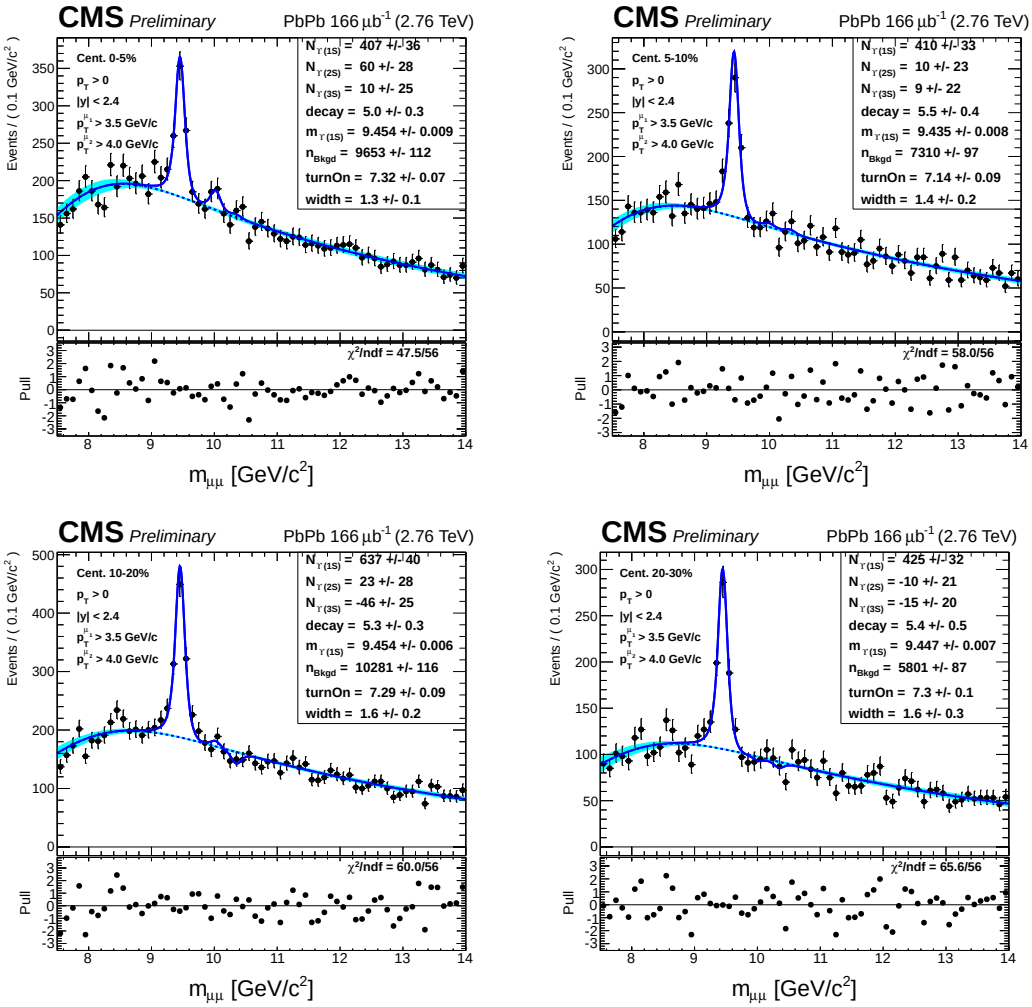

Figure A.24: Centrality-dependent fits to PbPb data (bins 0-5% to 20-30%)using loose muon pt cuts (Υ(1S) analysis).

A.1.4 Centrality dependent analysis of PbPb yields

Figure A.24, A.25 report the centrality dependent fit results for the Υ(1S) analysis, and A.26 report the centrality dependent fit results of the Υ(2S)analysis.

A.1.5 Systematic uncertainty on fitting

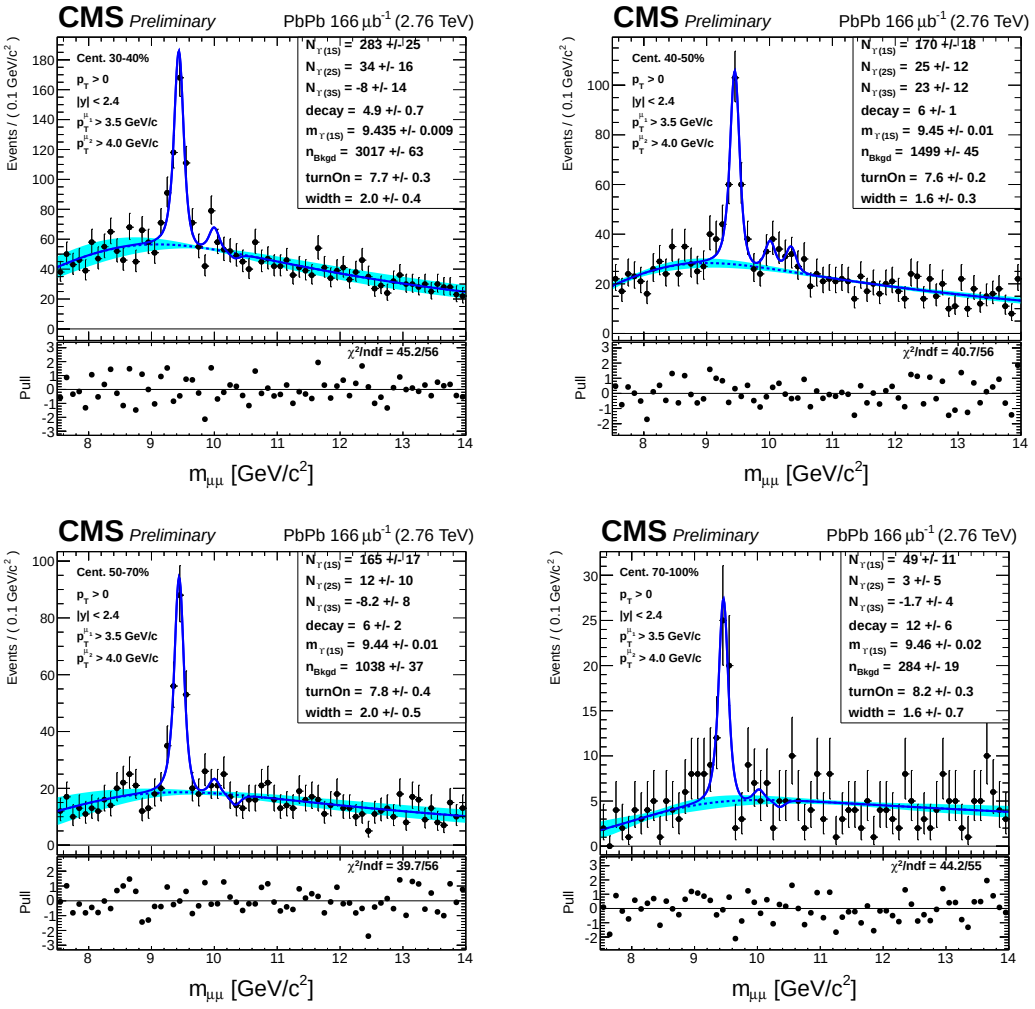

Figure A.25: Centrality-dependent fits to PbPb data (Continued: from 20-30 to 70-100% Centrality) using loose muon cuts (Υ(1S) analysis).

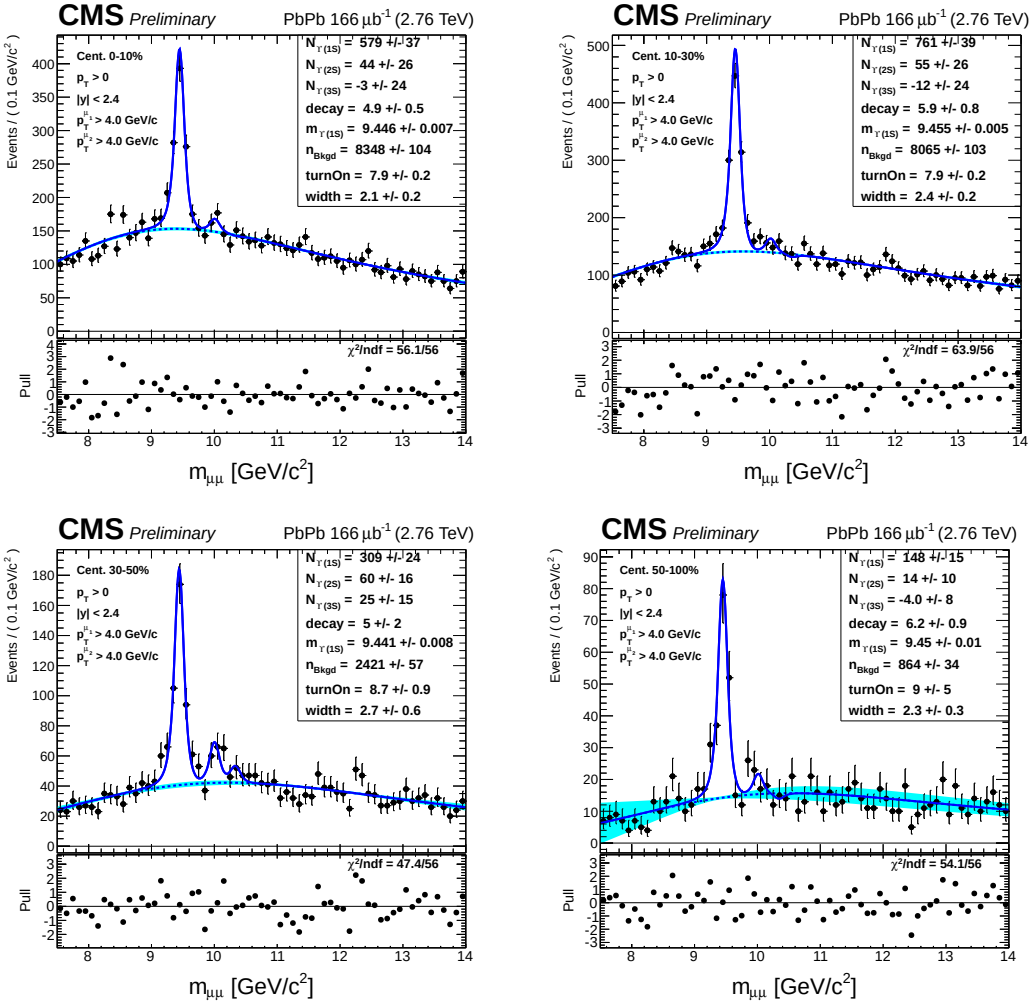

Figure A.26: Centrality-dependent fits to PbPb data (bins 0-10%, 10-30, 30-50, 50-100%)using tight muon pt cuts (Υ(2S) analysis).

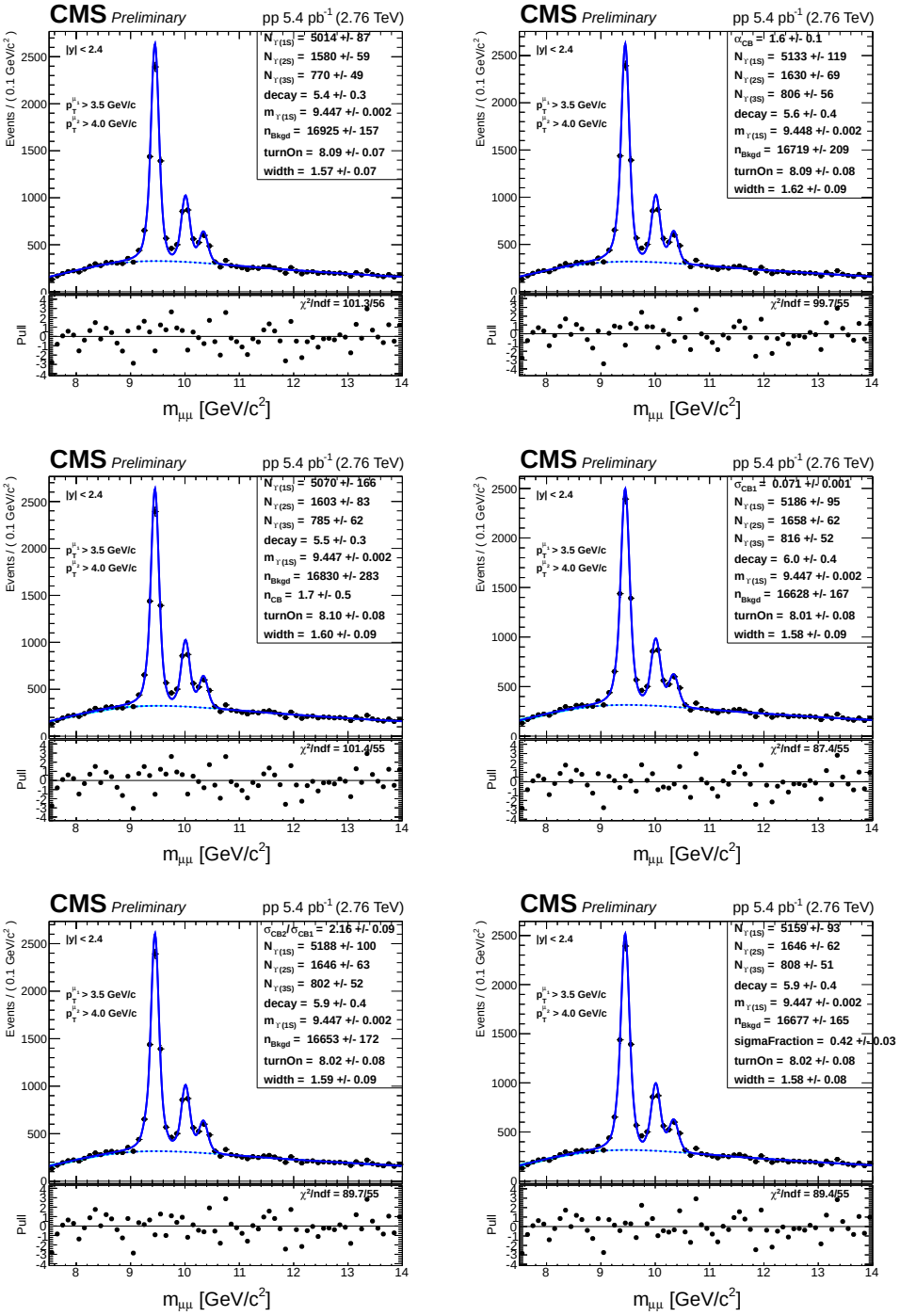

Figure A.27: Fit Variations of the all-integrated pp data, cases where the signal shape was varied.

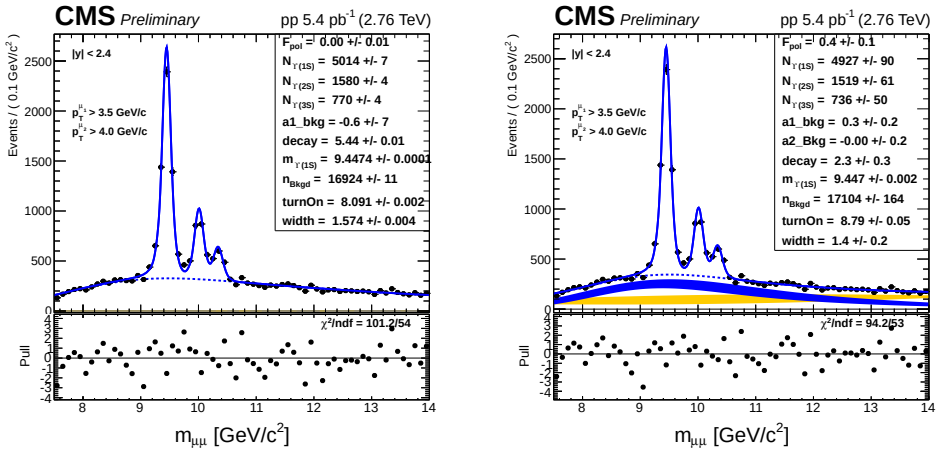

Figure A.28: Fit Variations of the all-integrated pp data, continued. Cases where additional background components were tried.

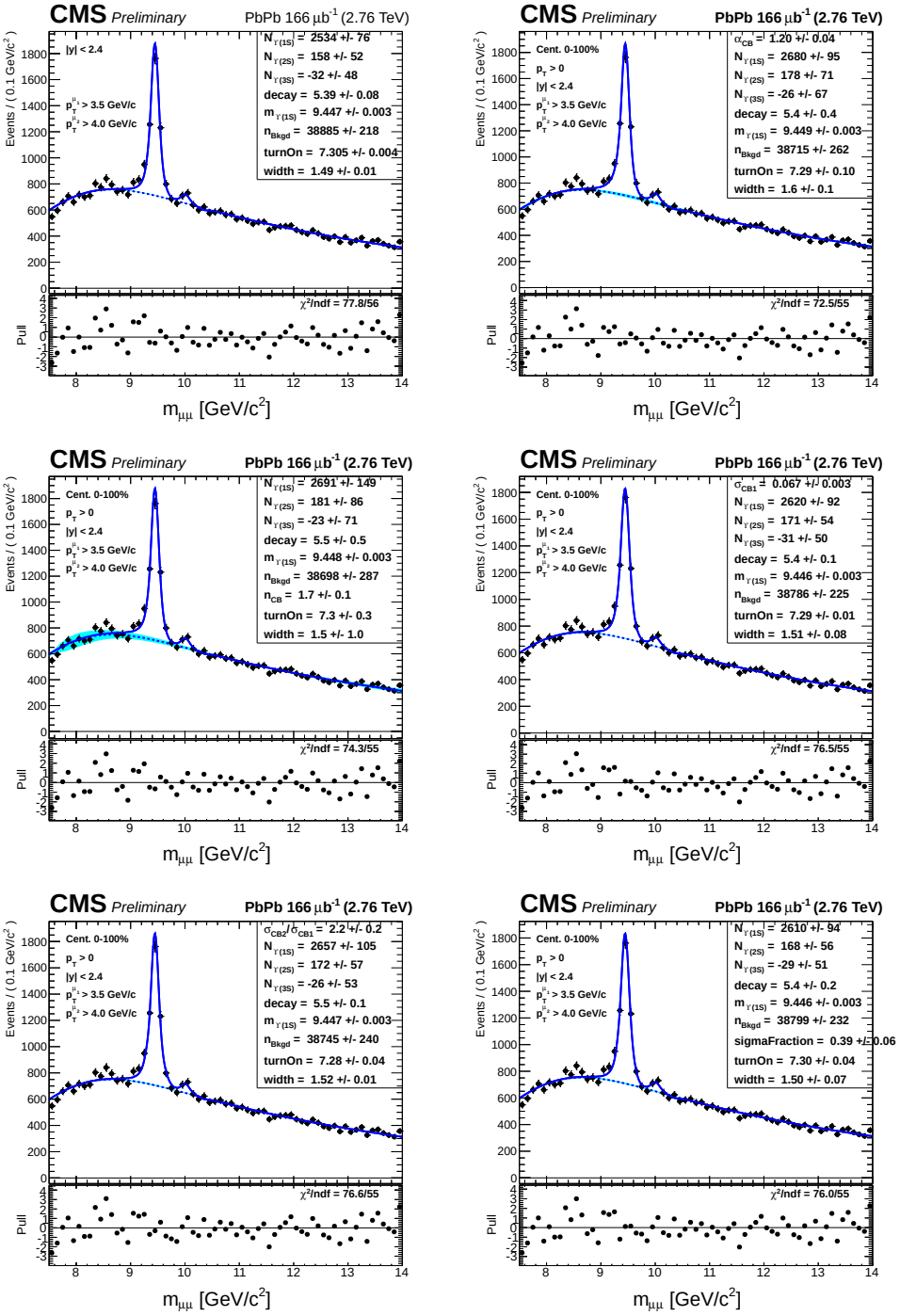

Figure A.29: Fit Variations of the all-integrated PbPb data, cases where the signal shape was varied.

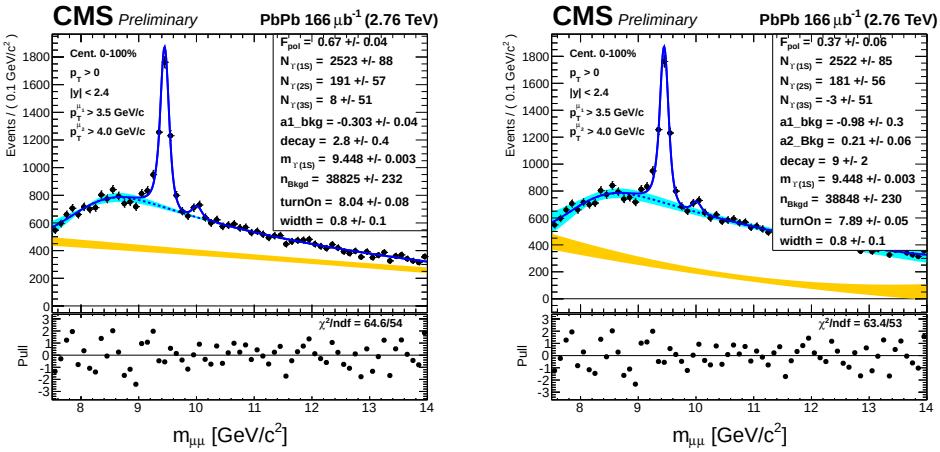

Figure A.30: Fit Variations of the all-integrated PbPb data, continued. Casses where additional background components were tried.

Σ parameters	power-law		the rest		
Bin	n_{CB}	α_{CB}	σ_1(MeV)	x (scale)	f (norm)
pt<2.5	11.86	1.322	0.0651	1.766	0.552
2.5<pt<5	17.39	1.312	0.0654	1.798	0.562
5<pt<8	28.63	1.197	0.0691	1.747	0.655
8<pt<12	21.34	1.418	0.0675	1.664	0.541
12<pt<20	40.28	1.165	0.0679	1.824	0.661
0< |y| <0.4	7.433	1.339	0.0445	1.472	0.448
0.4< |y| <0.8	1.449	1.895	0.0694	2.160	0.964
0.8< |y| <1.2	3.048	1.631	0.0769	1.410	0.559
1.2< |y| <1.6	8.799	1.725	0.0871	1.496	0.512
1.6< |y| <2.0	2.512	1.930	0.1272	2.033	0.991
2.0< |y| <2.4	36.89	1.408	0.1448	1.223	0.698
pt<5	28.30	1.280	0.0662	1.83	0.619
5<pt<12	25.03	1.257	0.0664	1.86	0.637
12<pt<20	3.092	1.605	0.0706	1.58	0.575
0< |y| <1.2	13.44	1.323	0.0556	1.662	0.577
1.2< |y| <2.4	11.87	1.667	0.1020	1.515	0.647
Min.Bias(loose pt)	2.452	1.650	0.0670	1.85	0.603
Min.Bias(tight pt)	4.651	1.559	0.0655	1.83	0.582

Table A.1: Fit results of signal shape parameters.

A.2 More figures from the MC lineshape study

Following Figures A.33, Figures A.34 and A.31, A.32 present p_T binned and rapidity binned fits of the MC Υ(1S) simulation, used to estimate the lineshape parameters to be used in the nominal signal extraction on data.

Figure A.35 shows the likelihood scan of fit variables in the range $2.4 < |y| < 2.4$.

A.3 Tabulated results of the lineshape study

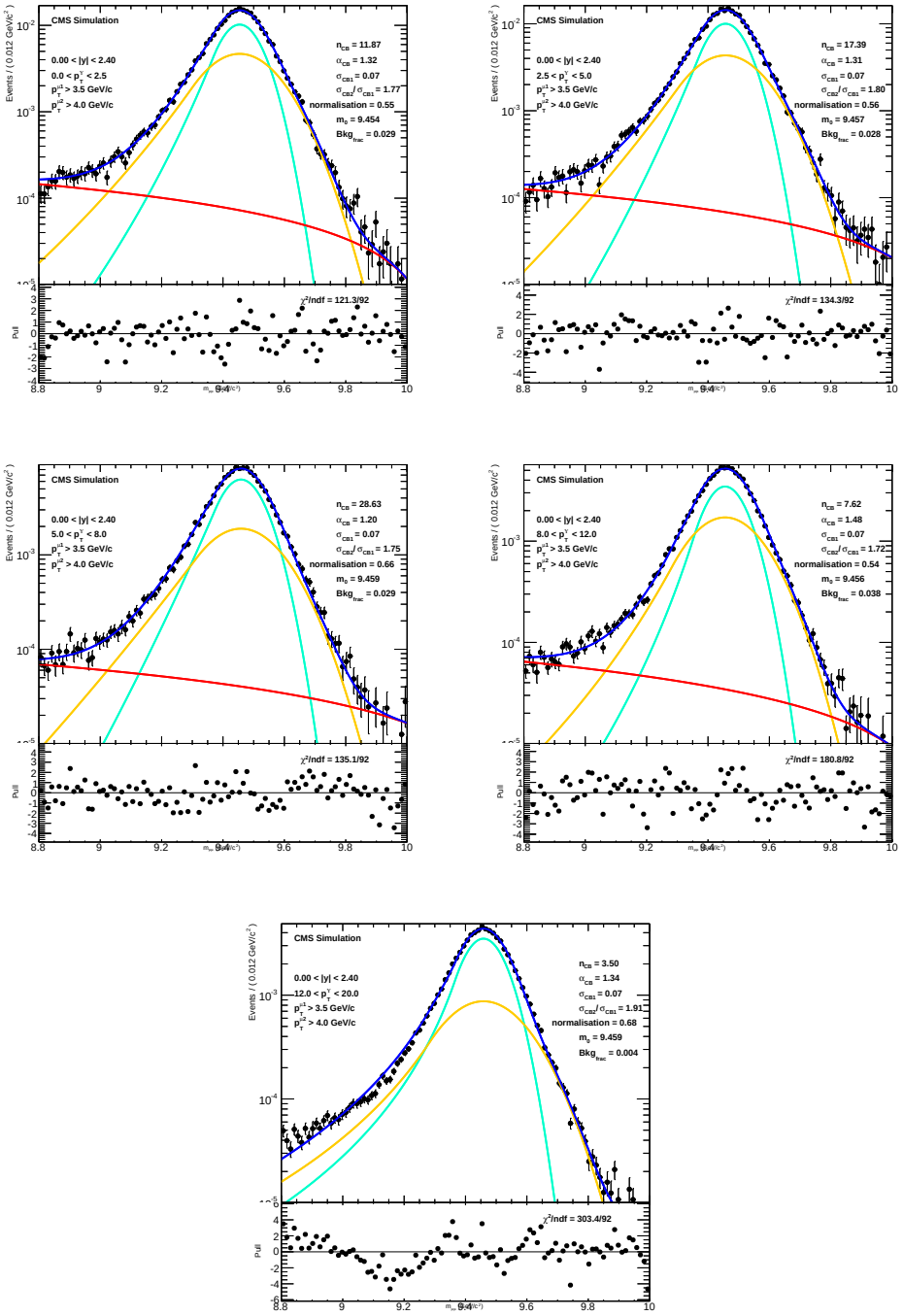

Figure A.31: p_T-binned fits of Υ(1S) mass from a simulated sample embedded in events generated with HYDJET(Bass) for 1S bins.

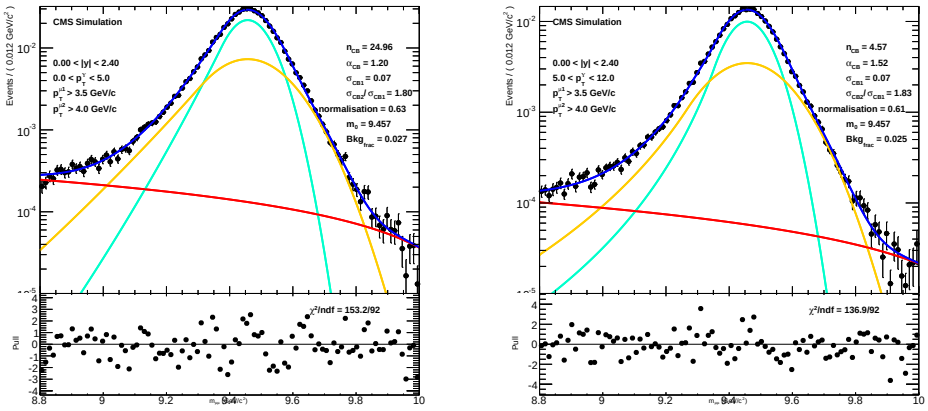

Figure A.32: p_T-binned fits of Υ(1S) mass from a simulated sample embedded in events generated with HYDJET(Bass) for 2S bins.

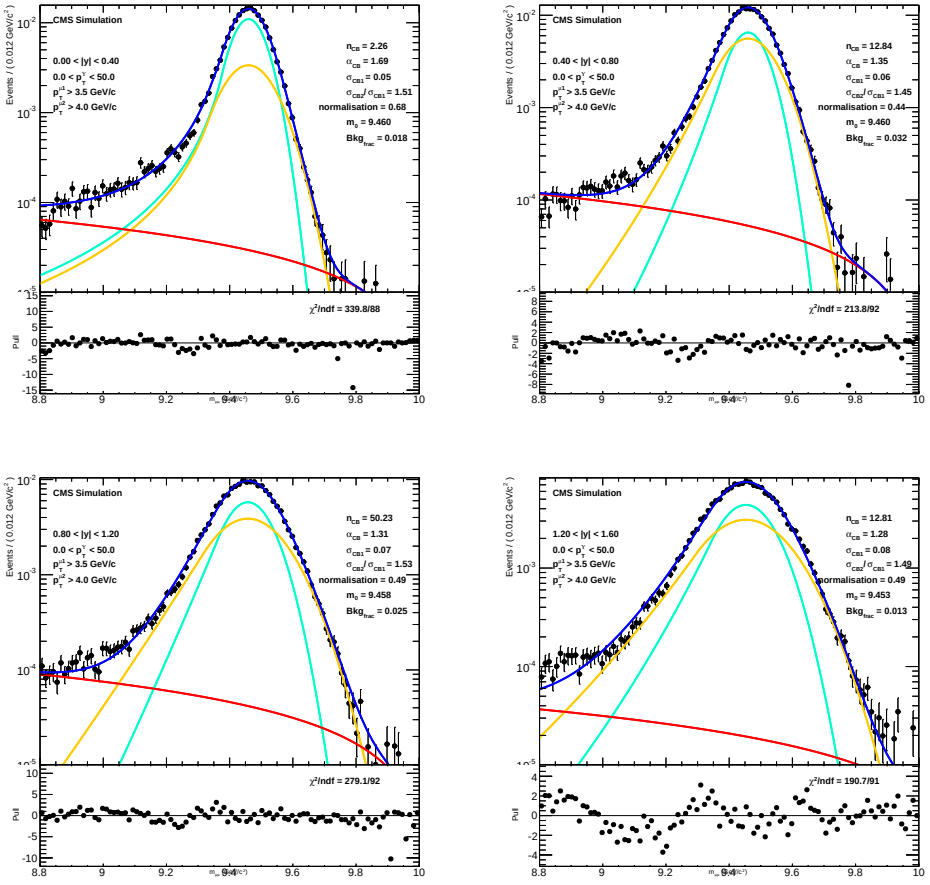

Figure A.33: Rapidity-binned fits of Υ(1S) mass from a simulated sample embedded in events generated with HYDJET(Bass) (Entries 1 to 6 for 1S bins, entries 7 and 8 for 2S bins).

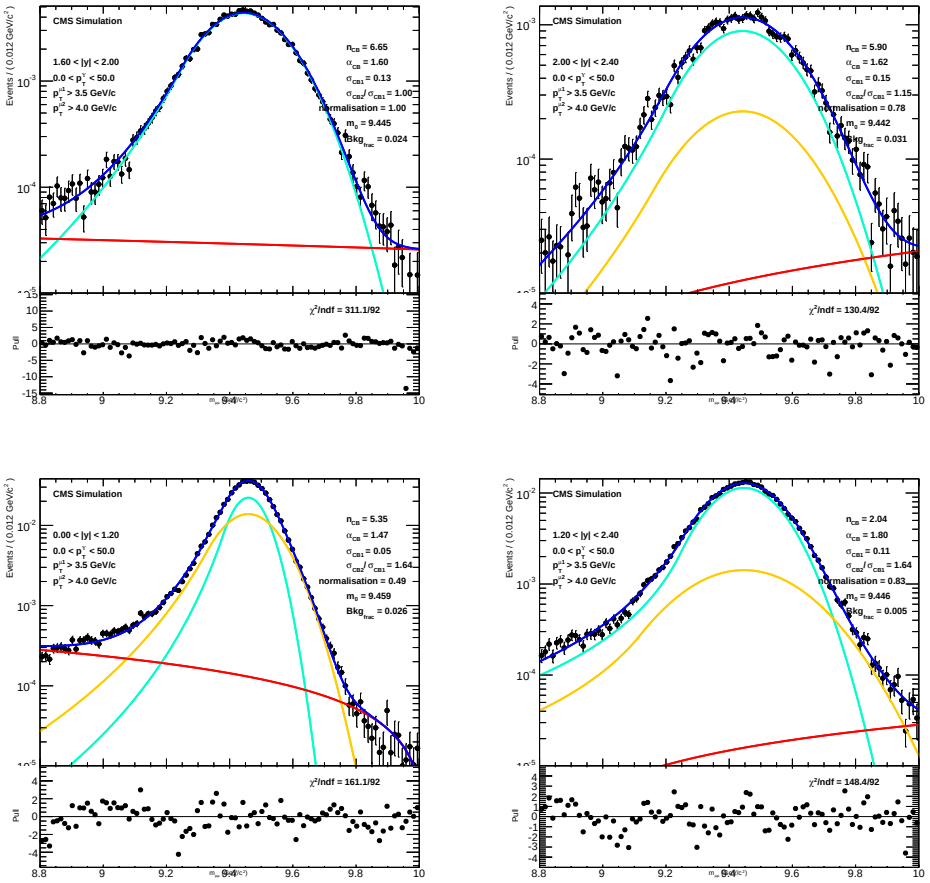

Figure A.34: Same as Figure A.33, continued Rapidity-binned fits for high rapidity 1S bins, and for wide 2S bins.

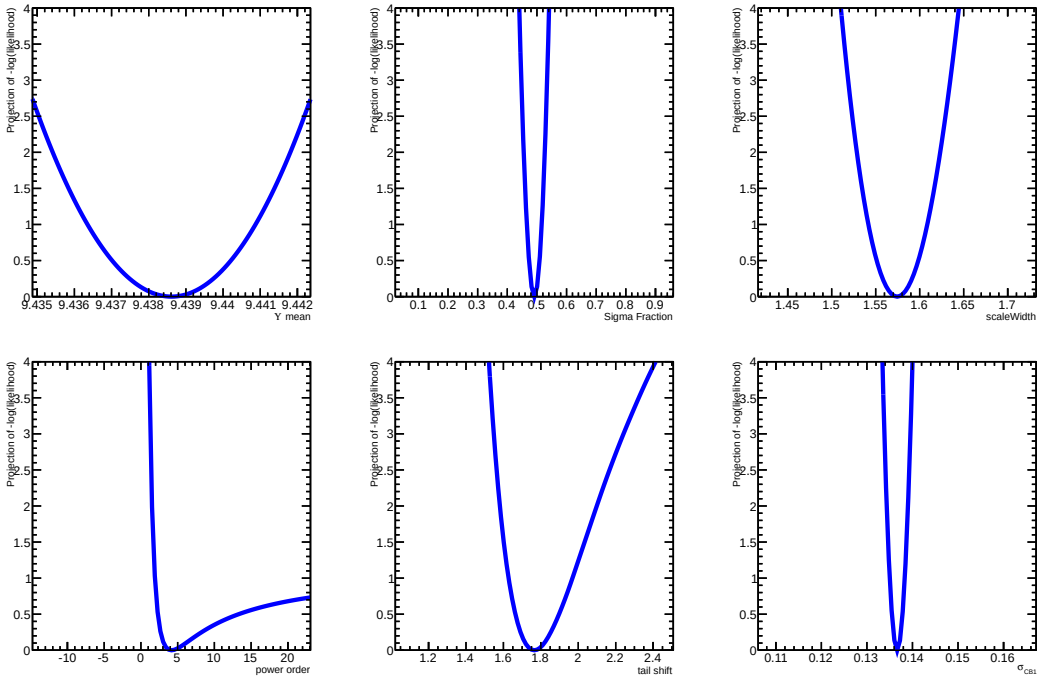

Figure A.35: A not so good likelihood scan of the 2< |y| < 2.4 Υ(1S) subsample.

Appendix B

Centrality table

Table 74: N_{coll}, N_{part} and impact parameter b values

Bin	NpartMean	NpartSigma	NcollMean	NcollSigma	bMean	bSigma
0	393.633	12.3245	1747.49	128.036	1.87663	0.784673
1	368.819	17.187	1566.92	153.374	3.02075	0.746574
2	343.073	17.7878	1393.97	148.214	3.88968	0.623658
3	317.625	17.9506	1237.02	143.028	4.60791	0.586918
4	292.932	19.2584	1095.03	143.623	5.24572	0.586829
5	271.917	19.9822	979.836	140.132	5.76362	0.571731
6	249.851	18.8188	863.228	127.639	6.29562	0.532749
7	230.72	16.7584	765.968	113.475	6.75185	0.48751
8	212.465	15.6287	677.894	103.99	7.18228	0.466444
9	194.752	15.4522	594.481	97.7168	7.60734	0.468356
10	178.571	13.68	522.453	86.541	7.99763	0.442211
11	163.23	13.5873	456.049	81.577	8.37317	0.450792
12	149.187	12.5759	399.178	73.2004	8.72411	0.446035
13	136.011	11.1909	347.174	64.3388	9.061	0.431178
14	123.414	10.8185	299.925	58.7095	9.39947	0.436542
15	111.7	9.59171	258.411	51.3798	9.71608	0.427932
16	100.831	9.50304	221.374	46.995	10.024	0.442836
17	90.7831	8.7603	188.676	41.4122	10.3287	0.443385
18	80.9823	8.17986	158.896	36.6026	10.6321	0.455668
19	72.6236	7.54442	135.117	31.969	10.9012	0.459105
20	64.1508	7.3129	112.481	28.2834	11.1962	0.479811
21	56.6284	6.58096	93.5697	23.7557	11.4625	0.48193
22	49.9984	6.29835	77.9192	20.7327	11.7259	0.500502
23	43.3034	5.84386	63.2538	17.6459	12.0007	0.514535
24	37.8437	5.18182	52.0938	14.501	12.2434	0.523403
25	32.6659	5.03181	42.3553	12.5434	12.5018	0.542598
26	27.83	4.45605	33.7461	10.0383	12.7655	0.563615
27	23.7892	4.10721	27.3213	8.48271	13.005	0.591446
28	20.1745	3.75359	21.8348	7.01648	13.2398	0.6175
29	16.8453	3.51951	17.1722	5.82912	13.503	0.65892
30	14.0322	3.25086	13.5661	4.80855	13.7387	0.707501
31	11.602	2.91458	10.6604	3.98013	13.9905	0.742967
32	9.52528	2.65321	8.31383	3.26375	14.2377	0.797312
33	7.6984	2.38598	6.37662	2.69301	14.5011	0.868373
34	6.446	2.08793	5.12347	2.22318	14.6931	0.901613
35	4.96683	1.75962	3.73576	1.74411	14.9996	0.976476
36	4.23649	1.66135	3.07268	1.59476	15.1928	1.03734
37	3.50147	1.21143	2.41358	1.13331	15.385	1.05542
38	3.16107	1.0419	2.10707	0.978846	15.4879	1.06168
39	2.7877	0.644417	1.76851	0.601808	15.5952	1.06894

Figure B.1: Centrality distribution of events passing minimum bias triggers compared to dimuon triggered events, in bins of 2.5% [2].

Bibliography

[1] Université Paris-Saclay Monsieur Pierre-Jacques Henri. Procédure de soutenance de doctorat.

[2] S. Chatrchyan et al. *Suppression of non-prompt J/ψ, prompt J/ψ, and Υ(1S) in PbPb collisions at $\sqrt{s_{NN}} = 2.76$ TeV.* JHEP 05 (2012) 063, arXiv:1201.5069.

[3] S. Chatrchyan et al. *Indications of suppression of excited Υ states in PbPb collisions at $\sqrt{s_{NN}} = 2.76$ TeV.* Phys. Rev. Lett. 107 (2011) 052302, arXiv:1105.4894.

[4] S. Chatrchyan et al. *Observation of sequential Upsilon suppression in PbPb collisions.* Phys. Rev. Lett. 109 (2012) 222301, arXiv:1208.2826.

[5] B. Abelev et al. *Suppression of $\Upsilon(1S)$ at forward rapidity in Pb-Pb collisions at $\sqrt{s_{\rm NN}} = 2.76$ TeV.* Phys. Lett. B738 (2014) 361-372, arXiv:1405.4493.

[6] S. Dawson. Introduction to electroweak symmetry breaking. In *High energy physics and cosmology. Proceedings, Summer School, Trieste, Italy, June 29-July 17, 1998*, (1998)1-83.

[7] Gerard 't Hooft and M. J. G. Veltman. *Regularization and Renormalization of Gauge Fields.* Nucl. Phys. B44 (1972) 189-213.

[8] H. Fujii and D. Kharzeev. *Long range forces of QCD.* Phys. Rev. D60 (1999) 114039, hep-ph/9903495.

[9] H. Yukawa. *On the Interaction of Elementary Particles. I.* Proceedings of the Physico-Mathematical Society of Japan. 3rd Series 17 (1935) 48-57.

[10] W. Heisenberg. Zeits. f. Phys. 11 (1932) 1.

[11] M. Gell-Mann. *The Eightfold Way: A Theory of Strong Interaction Symmetry.* California Institute of Technology Report.

[12] Y. Ne'eman. *Derivation of Strong Interactions from a Gauge Invariance.* Nucl. Phys. 26 (1961) 222–229.

[13] A. Pevsner, R. Kraemer, M. Nussbaum, C. Richardson, P. Schlein, R. Strand, T. Toohig, M. Block, A. Engler, R. Gessaroli, and C. Meltzer. *Evidence for a Three-Pion Resonance Near 550 MeV.* Phys. Rev. Lett. 7 (1961) 421–423.

[14] M. Gell-Mann and H. Fritzsch. *Selected Papers*, volume ISBN:978-981-283-685-4.

[15] V. E. Barnes et al. *Observation of a Hyperon with Strangeness Minus Three.* Phys. Rev. Lett. 12 (1964) 204–206.

[16] M. Gell-Mann. *Symmetries of Baryons and Mesons.* Phys. Rev. 125 (1962) 1067–1084.

[17] S. Okubo. *Note on Unitary Symmetry in Strong Interactions.* Prog. Theor. Phys. (Kyoto) 27 (1962) 949–966.

[18] G. Dissertori, I. G. Knowles, and M. Schmelling. *Quantum Chromodynamics - High Energy Experiments and Theory (2nd edition).* Oxford University Press,

[19] B. R. Webber. QCD phenomenology at high energy. Chapter 3. page Slides from streaming video, Geneva, Feb 2008. CERN, CERN.

[20] B. R. Webber. QCD phenomenology at high energy. Chapter 1. page Slides from streaming video, Geneva, Feb 2008. CERN, CERN.

[21] K. A. Olive et al. *Review of Particle Physics.* Chin. Phys. C38 (2014) 090001.

[22] C. H. Lai. *Selected Papers on Gauge Theory of Weak and Electromagnetic Interactions.* World Scientific Publishing, Singapore.

[23] A brief discussion on Gauge Theories. `http://www.damtp.cam.ac.uk/user/ch558/pdf/Gauge_theories.pdf`. Accessed: 2015-08-30.

[24] S. L. Glashow, J. Iliopoulos, and L. Maiani. *Weak Interactions with Lepton-Hadron Symmetry.* Phys. Rev. D2 (1970) 1285-1292.

[25] J. J. Aubert, U. Becker, P. J. Biggs, J. Burger, M. Chen, G. Everhart, P. Goldhagen, J. Leong, T. McCorriston, T. G. Rhoades, M. Rohde, Samuel C. C. Ting, Sau Lan Wu, and Y. Y. Lee. *Experimental Observation of a Heavy Particle J.* Phys. Rev. Lett. 33 (1974) 1404–1406.

[26] B. Richter. *Total Hadron Cross Section, New Particles, and Muon Electron Events in e^+e^- Annihilation at SPEAR.* SLAC-PUB-1706.

[27] S. W. Herb, D. C. Hom, L. M. Lederman, J. C. Sens, H. D. Snyder, J. K. Yoh, J. A. Appel, B. C. Brown, C. N. Brown, W. R. Innes, K. Ueno, T. Yamanouchi, A. S. Ito, H. Jöstlein, D. M. Kaplan, and R. D. Kephart. *Observation of a Dimuon Resonance at 9.5 GeV in 400-GeV Proton-Nucleus Collisions.* Phys. Rev. Lett. 39 (1977) 252–255.

[28] J. Ellis. *The Discovery of the Gluon.* arXiv:1409.4232.

[29] J. R. Ellis, M. K. Gaillard, and G. G. Ross. *Search for gluons in e^+e^- annihilation.* Nucl. Phys. B 111 (1976) 253-71.

[30] B. H. Wiik. *First Results from PETRA.* Conf. Proc. C7906181 (1979) 113-154.

[31] R. Brandelik et al. *Evidence for Planar Events in e^+e^- Annihilation at High-Energies.* Phys. Lett. B86 (1979) 243.

[32] B. Adeva et al. *A Test of QCD based on four jet events from Z^0 decays.* Phys. Lett. B248 (1990) 227-234.

[33] M. Bengtsson and P. M. Zerwas. *Four Jet Events in e^+e^- Annihilation: Testing the Three Gluon Vertex.* Phys. Lett. B208 (1988) 306.

[34] B. R. Webber. QCD phenomenology at high energy. Chapter 2. page Streaming video, Geneva, Feb 2008. CERN, CERN. CERN, Geneva, 18 - 22 Feb 2008.

[35] S. Bethke. *Eleven years of QCD at LEP.* Eur. Phys. J.direct C4 (2002) 1, hep-ex/0112032.

[36] R. Kogler. *Precision jet measurements at HERA and determination of α_s.* Nucl. Phys. Proc. Suppl. 222-224 (2012) 81-93, arXiv:1112.5117.

[37] A. Cooper-Sarkar. *Determination of Charm Quark Mass and $\alpha_s(M_Z)$ from HERA data.* Mod. Phys. Lett. A28 (2013) 1360017, arXiv:1307.7875.

[38] Yuri L. Dokshitzer, Valery A. Khoze, Alfred H. Mueller, and S. I. Troian.

[39] E. Paul. Inclusive-jet photoproduction at HERA and determination of α_s. In *Proceedings, 20th International Workshop on Deep-Inelastic Scattering and Related Subjects (DIS 2012)*, (2012)729-732.

[40] H. Abramowicz et al. *Combination of Measurements of Inclusive Deep Inelastic $e^{\pm}p$ Scattering Cross Sections and QCD Analysis of HERA Data.* arXiv:1506.06042.

[41] R. Hagedorn. *Statistical thermodynamics of strong interactions at high-energies.* Nuovo Cim. Suppl. 3 (1965) 147-186.

[42] N. Cabibbo and G. Parisi. *Exponential hadronic spectrum and the quark liberation.* Phys. Lett. B 59 (1975) 67.

[43] J. Engels, F. Karsch, H. Satz, and I. Montvay. *High Temperature SU(2) Gluon Matter on the Lattice.* Phys. Lett. B101 (1981) 89.

[44] F. Karsch. *Lattice QCD at high temperature and density.* Lect. Notes Phys. 583 (2002) 209.

[45] M. Strickland. *Anisotropic Hydrodynamics: Three lectures.* Acta Phys. Polon. B45 (2014) 2355-2394, arXiv:1410.5786.

[46] C. Adler et al. *Disappearance of back-to-back high p_T hadron correlations in central Au+Au collisions at $\sqrt{s_{NN}}$ = 200-GeV.* Phys. Rev. Lett. 90 (2003) 082302, nucl-ex/0210033.

[47] S. Chatrchyan et al. *Dependence on pseudorapidity and centrality of charged hadron production in PbPb collisions at a nucleon-nucleon centre-of-mass energy of 2.76 TeV.* JHEP 08 (2011) 141, arXiv:1107.4800.

[48] R. J. Glauber and G. Matthiae. *High-energy scattering of protons by nuclei.* Nucl. Phys. B21 (1970) 135-157.

[49] T. Matsui and H. Satz. *J/ψ Suppression by Quark-Gluon Plasma Formation.* Phys. Lett. B178 (1986) 416.

[50] T. A. DeGrand and C. E. DeTar. *Static Screening Lengths in the Gluon Plasma.* Phys. Rev. D34 (1986) 2469.

[51] N. Brambilla et al. *Heavy quarkonium: progress, puzzles, and opportunities.* Eur. Phys. J. C71 (2011) 1534, arXiv:1010.5827.

[52] S. Okubo. *Phi meson and unitary symmetry model.* Phys. Lett. 5 (1963) 165-168.

[53] Jugoro Iizuka. *Systematics and phenomenology of meson family.* Prog. Theor. Phys. Suppl. 37 (1966) 21-34.

[54] G Zweig. *An SU_3 model for strong interaction symmetry and its breaking; Version 2.*

[55] R. Barbieri, R. Gatto, and E. Remiddi. *Singular Binding Dependence in the Hadronic Widths of 1++ and 1+- Heavy Quark anti-Quark Bound States.* Phys. Lett. B61 (1976) 465.

[56] R. Baier and R. Ruckl. *Hadronic Collisions: A Quarkonium Factory.* Z. Phys. C19 (1983) 251.

[57] Eric Braaten and Sean Fleming. *Color octet fragmentation and the psi-prime surplus at the Tevatron.* Phys. Rev. Lett. 74 (1995) 3327-3330, hep-ph/9411365.

[58] G. T. Bodwin, E. Braaten, and G. P. Lepage. *Rigorous QCD analysis of inclusive annihilation and production of heavy quarkonium.* Phys. Rev. D 51 (1994) 1125. 126 p. Comments: Revised to clarify the velocity-scaling rules for spin-flip transitions, to correct error estimates, and to emphasize probabilities of Fock states, rather than amplitudes, 117 pages in REVTEX plus 11 Postscript figures. Erratum to Phys. Rev. D article included as a separate file, 4 pages in REVTEX.

[59] J. F. Amundson, Oscar J. P. Eboli, E. M. Gregores, and F. Halzen. *Quantitative tests of color evaporation: Charmonium production.* Phys. Lett. B390 (1997) 323-328, hep-ph/9605295.

[60] F. Abe et al. *J/ψ and $\psi(2S)$ production in $p\bar{p}$ collisions at $\sqrt{s} = 1.8$ TeV.* Phys. Rev. Lett. 79 (1997) 572-577.

[61] J/ψ, $\Upsilon \to \mu^+\mu^-$ and $B \to J/\psi$, ψ' cross-sections.

[62] J.-M. Richard. *An introduction to the quark model.* arXiv:1205.4326.

[63] G. Aad et al. *Observation of a new χ_b state in radiative transitions to $\Upsilon(1S)$ and $\Upsilon(2S)$ at ATLAS.* Phys. Rev. Lett. 108 (2012) 152001, arXiv:1112.5154.

[64] Roel Aaij et al. *Measurement of the $\chi_b(3P)$ mass and of the relative rate of $\chi_{b1}(1P)$ and $\chi_{b2}(1P)$ production.* JHEP 10 (2014) 88, arXiv:1409.1408.

[65] Hermine Woehri. Critical review of quarkonium production results at hadron colliders. `https://indico.cern.ch/event/278195/contribution/104`. Accessed: 2015-10-02.

[66] C. Baglin et al. *The Production of J/ψ in 200-GeV/nucleon Oxygen Uranium Interactions.* Phys. Lett. B220 (1989) 471-478.

[67] M. C. Abreu et al. *Anomalous J / psi suppression in Pb - Pb interactions at 158 GeV/c per nucleon.* Phys. Lett. B410 (1997) 337-343.

[68] M. C. Abreu et al. *Transverse momentum distributions of J / psi, psi-prime, Drell-Yan and continuum dimuons produced in Pb Pb interactions at the SPS.* Phys. Lett. B499 (2001) 85-96.

[69] M. C. Abreu et al. *Evidence for deconfinement of quarks and gluons from the J / psi suppression pattern measured in Pb + Pb collisions at the CERN SPS.* Phys. Lett. B477 (2000) 28-36.

[70] B. Alessandro et al. *A New measurement of J/psi suppression in Pb-Pb collisions at 158-GeV per nucleon.* Eur. Phys. J. C39 (2005) 335-345, hep-ex/0412036.

[71] R. Arnaldi et al. *J/ψ Production in Indium-Indium Collisions at* 158 GeV/*Nucleon.* Phys. Rev. Lett. 99 (2007) 132302.

[72] O. Linnyk, E. L. Bratkovskaya, and W. Cassing. *Open and hidden charm in proton-nucleus and heavy-ion collisions.* Int. J. Mod. Phys. E17 (2008) 1367-1439, arXiv:0808.1504.

[73] Centrality Categorization and its Application to Physics Effects in High-Energy d+A Collisions. `https://www.phenix.bnl.gov/phenix/WWW/talk/archive/2014/ndww14/t2235.pdf`. Accessed: 2015-09-15.

[74] A. Adare et al. *J/ψ Production versus Centrality, Transverse Momentum, andRapidity in* Au + Au *Collisions at* $\sqrt{s_{NN}}$ = 200 GeV. Phys. Rev. Lett. 98 (2007) 232301.

[75] A. Adare et al. *Nuclear Modification of $\psi(2S)$, χ_c, and J/ψ Production in d+Au Collisions at* $\sqrt{s_{NN}}$ = 200 *GeV.* Phys. Rev. Lett. 111 (2013) 202301, arXiv:1305.5516.

[76] S. S. Adler et al. *J/ψ Production and Nuclear Effects for* d + Au *and* $p + p$ *Collisions at* $\sqrt{s_{NN}} = 200$ GeV. Phys. Rev. Lett. 96 (2006) 012304.

[77] A. Adare et al. *Transverse-Momentum Dependence of the J/ψ Nuclear Modification in d+Au Collisions at* $\sqrt{s_{NN}} = 200$ *GeV.* Phys. Rev. C87 (2013) 034904, arXiv:1204.0777.

[78] B. Abelev et al. *Centrality, rapidity and transverse momentum dependence of J/ψ suppression in Pb-Pb collisions at $\sqrt{s_{\rm NN}}$=2.76 TeV.* Phys. Lett. B734 (2014) 314-327, arXiv:1311.0214.

[79] P. Braun-Munzinger and J. Stachel. *(Non)thermal aspects of charmonium production and a new look at J/ψ suppression.* Phys. Lett. B490 (2000) 196-202, nucl-th/0007059.

[80] L. Grandchamp and R. Rapp. *Charmonium suppression and regeneration from SPS to RHIC.* Nucl. Phys. A709 (2002) 415-439, hep-ph/0205305.

[81] CMS Collaboration. *J/psi results from CMS in PbPb collisions, with 150 μb^{-1} data.* CMS-PAS-HIN-12-014.

[82] CMS Collaboration. *J/ψ production in pPb collisions.* CMS-PAS-HIN-14-009.

[83] B. Abelev et al. *J/ψ production and nuclear effects in p-Pb collisions at $\sqrt{S_{NN}}$ = 5.02 TeV.* JHEP 02 (2014) 073, arXiv:1308.6726.

[84] Vardan Khachatryan et al. *Measurement of Prompt $\psi(2S) \to J/\psi$ Yield Ratios in Pb-Pb and pp collisions at nucleon-nucleon center-of-mass energy = 2.76 TeV.* Phys. Rev. Lett. 113 (2014) 262301, 1410.1804.

[85] G. Aad et al. *Measurement of upsilon production in 7 TeV pp collisions at ATLAS.* Phys. Rev. D 87 (2013) 052004.

[86] S. Chatrchyan et al. *Measurement of the $\Upsilon(1S), \Upsilon(2S)$, and $\Upsilon(3S)$ cross sections in pp collisions at $\sqrt{s}$ = 7 TeV.* Phys. Lett. B727 (2013) 101-125, arXiv:1303.5900.

[87] V. Khachatryan et al. *Measurements of the Υ(1S), Υ(2S), and Υ(3S) differential cross sections in pp collisions at $\sqrt{s}$ = 7 TeV.* Phys. Lett. B749 (2015) 14-34, arXiv:1501.07750.

[88] R Aaij et al. *Measurement of Upsilon production in pp collisions at $\sqrt{s}$ = 7 TeV.* Eur. Phys. J. C72 (2012) 2025, arXiv:1202.6579.

[89] B. Abelev et al. *Measurement of quarkonium production at forward rapidity in pp collisions at $\sqrt{s} = 7$ TeV.* Eur. Phys. J. C74 (2014) 2974, arXiv:1403.3648.

[90] Georges Aad et al. *Measurement of the muon reconstruction performance of the ATLAS detector using 2011 and 2012 LHC proton–proton collision data.* Eur. Phys. J. C74 (2014) 3130, 1407.3935.

[91] *Measurement of Momentum Scale and Resolution of the CMS Detector using Low-mass Resonances and Cosmic Ray Muons.*

[92] R. Aaij et al. Forward production of Υ mesons in *pp* collisions at $\sqrt{s} = 7$ and 8 TeV. Technical Report arXiv:1509.02372. LHCB-PAPER-2015-045. CERN-PH-EP-2015-232, CERN, Geneva, Sep 2015. Comments: 36 pages, 7 figures, 16 tables.

[93] K. Wang, Y.-Q. Ma, and K.-T. Chao. $\Upsilon(1S)$ *prompt production at the Tevatron and LHC in nonrelativistic QCD.* Phys. Rev. D85 (2012) 114003, arXiv:1202.6012.

[94] J. P. Lansberg. J/ψ *production at* $\sqrt{s}$*=1.96 and 7 TeV: Color-Singlet Model, NNLO* and polarisation.* J. Phys. G38 (2011) 124110, arXiv:1107.0292.

[95] S. Chatrchyan et al. *Measurement of the* Υ*(1S),* Υ*(2S) and* Υ*(3S) polarizations in pp collisions at* $\sqrt{s} = 7$ *TeV.* Phys. Rev. Lett. 110 (2013) 081802, arXiv:1209.2922.

[96] David G. d'Enterria et al. *CMS physics technical design report: Addendum on high density QCD with heavy ions.* J. Phys. G34 (2007) 2307-2455.

[97] Lyndon Evans and Philip Bryant. *LHC Machine.* JINST 3 (2008) S08001.

[98] Karlheinz Schindl. *The Injector Chain for the LHC; rev. version.*

[99] L. Arnaudon, M. Disdier, P. Maesen, and M. Prax. Control of the LHC 400 MHz RF System (ACS).

[100] A. Beuret et al. The LHC Lead Ion Injector Chain.

[101] LHC Experiment Accelerator Data Exchange Working Group Jowett, J. Lead Ions in the LHC. `https://lhc-data-exchange.web.cern.ch/lhc-data-exchange/jowett_feb04.pdf`. Accessed: 2015-10-23.

[102] CMSPublic TWiki page. CMS Luminosity - Public results. `https://twiki.cern.ch/twiki/bin/view/CMSPublic/LumiPublicResults`. Accessed: 2015-10-29.

[103] G. Aad et al. *The ATLAS Experiment at the CERN Large Hadron Collider.* JINST 3 (2008) S08003.

[104] ATLASPublic TWiki page. ATLAS Experiment - Public results (Heavy Ions WG). `https://twiki.cern.ch/twiki/bin/view/AtlasPublic/HeavyIonsPublicResults`. Accessed: 2015-10-29.

[105] K. Aamodt et al. *The ALICE experiment at the CERN LHC.* JINST 3 (2008) S08002.

[106] ALICEPublic TWiki page. ALICE Public Results. `https://twiki.cern.ch/twiki/bin/view/ALICEpublic/ALICEPublicResults`. Accessed: 2015-10-29.

[107] S. Chatrchyan et al. *The CMS experiment at the CERN LHC.* JINST 3 (2008) S08004.

[108] CMSPublic TWiki page. CMS Heavy-Ion Public Physics Results. `https://twiki.cern.ch/twiki/bin/view/CMSPublic/PhysicsResultsHIN`. Accessed: 2015-10-29.

[109] A. Augusto Alves, Jr. et al. *The LHCb Detector at the LHC.* JINST 3 (2008) S08005.

[110] Fanfan Jing, Yuanning Gao, Zhenwei Yang, and Burkhard Schmidt. *Study of Cold Nuclear Matter Effects on Heavy Quarkonia in Proton-Lead Collisions at LHCb.* PhD thesis, Tsinghua U., Beijing, Jun 2014. Presented 11 Jun 2014.

[111] Lucas Taylor. Using Russian navy shells. `http://cms.web.cern.ch/news/using-russian-navy-shells`. Accessed: 2015-10-28.

[112] Serguei Chatrchyan et al. *The performance of the CMS muon detector in proton-proton collisions at $\sqrt{s}$ = 7 TeV at the LHC.* JINST 8 (2013) P11002, 1306.6905.

[113] Lucas Taylor. Resistive Plate Chambers. `http://cms.web.cern.ch/news/resistive-plate-chambers`. Accessed: 2015-10-29.

[114] Georges Aad et al. *Combined Measurement of the Higgs Boson Mass in pp Collisions at $\sqrt{s} = 7$ and 8 TeV with the ATLAS and CMS Experiments.* Phys. Rev. Lett. 114 (2015) 191803, arXiv:1503.07589.

[115] S. Dasu et al. *CMS. The TriDAS project. Technical design report, vol. 1: The trigger systems.*

[116] LHC schedule beyond LS1. `http://lhc-commissioning.web.cern.ch/lhc-commissioning/schedule/LHC%20schedule%202015-2034%20FkBordry%202-december-2013.pdf`. Accessed: 2015-09-30.

[117] Daniele Trocino. *The CMS High Level Trigger.* J. Phys. Conf. Ser. 513 (2014) 012036.

[118] Alan.J. Bell. Beam and Radiation Monitoring for CMS. In *Nuclear Science Symposium Conference Record, 2008. NSS '08. IEEE*, pages 2322–2325, Oct 2008.

[119] Serguei Chatrchyan et al. *Performance of CMS muon reconstruction in pp collision events at $\sqrt{s} = 7$ TeV.* JINST 7 (2012) P10002, 1206.4071.

[120] G. L. Bayatian et al. *CMS physics: Technical design report.*

[121] R. Fruehwirth. *Application of Kalman filtering to track and vertex fitting.* Nuclear Instruments and Methods in Physics Research Section A: Accelerators, Spectrometers, Detectors and Associated Equipment 262 (1987) 444 - 450.

[122] S Chatrchyan et al. *Performance of CMS Muon Reconstruction in Cosmic-Ray Events.* JINST 5 (2010) T03022, 0911.4994.

[123] The CMS Muon Physics Object Group (Muon POG). Muons in minimum-bias events at 7 TeV in CMS: data-MC comparisons for a few basic kinematic distributions.

[124] The CMS Muon Physics Object Group (Muon POG). CMS Muon Results.

[125] Performance of muon identification in pp collisions at $\sqrt{s}$ = 7 TeV. Technical Report CMS-PAS-MUO-10-002, CERN,

[126] Marco Rovere. CMS reconstruction improvements for tracking in large pile-up events. `https://indico.cern.ch/event/304944/session/2/contribution/276/attachments/578474/796604/CHEP2015_MR_Tracking.pdf`. Accessed: 2015-10-20.

[127] C. Liu et al. *Reconstruction of cosmic and beam-halo muons with the CMS detector.* The European Physical Journal C 56 (2008) 449-460.

[128] V. Khachatryan et al. *Transverse-momentum and pseudorapidity distributions of charged hadrons in pp collisions at* $\sqrt{s}$ = 7 *TeV.* Phys. Rev. Lett. 105 (2010) 022002, arXiv:1005.3299.

[129] Serguei Chatrchyan et al. *Observation and studies of jet quenching in PbPb collisions at nucleon-nucleon center-of-mass energy = 2.76 TeV.* Phys. Rev. C84 (2011) 024906, 1102.1957.

[130] Michael L. Miller, Klaus Reygers, Stephen J. Sanders, and Peter Steinberg. *Glauber modeling in high energy nuclear collisions.* Ann. Rev. Nucl. Part. Sci. 57 (2007) 205-243, nucl-ex/0701025.

[131] De Jager, CW and De Vries, H and De Vries, C. *Nuclear charge-and magnetization-density-distribution parameters from elastic electron scattering.* Atomic data and nuclear data tables 14 (1974) 479–508.

[132] L. Adamczyk et al. *Suppression of* Υ *production in d+Au and Au+Au collisions at* $\sqrt{s_{NN}}$*=200 GeV.* Phys. Lett. B735 (2014) 127, arXiv:1312.3675. [Erratum: Phys. Lett.B743,537(2015)].

[133] Wouter Verkerke and David P. Kirkby. *The RooFit toolkit for data modeling.* eConf C0303241 (2003) MOLT007, physics/0306116. [,186(2003)].

[134] CMS Collaboration. Υ*(1S),* Υ*(2S) and* Υ*(3S) cross section measurements in pp collisions at* $\sqrt{s}$ = 7 *TeV.* CMS-PAS-BPH-12-006.

[135] The ROOT data analysis framework. class ROOT::Minuit2::MnMinos. `https://root.cern.ch/root/html/ROOT__Minuit2__MnMinos.html`.

[136] T. Sjostrand, S. Mrenna, and P. Z. Skands. *PYTHIA 6.4 Physics and Manual.* JHEP 05 (2006) 026, hep-ph/0603175.

[137] The CMS collaboration. *Performance of CMS muon reconstruction in pp collision events at* $\sqrt{s}$ = 7 *TeV.* Journal of Instrumentation 7 (2012) P10002.

[138] S. Chatrchyan et al. *Study of Z boson production in PbPb collisions at* $\sqrt{s_{NN}}$ = 2.76 *TeV.* Phys. Rev. Lett. 106 (2011) 212301, arXiv:1102.5435.

[139] S. Chatrchyan et al. *Measurement of prompt ψ(2S) to J/ψ yield ratios in PbPb and p-p collisions at $\sqrt{s_{NN}}$ = 2.76 TeV.* Physical Review Letters 113 (2014) 262301.

[140] G. J. Feldman and R D. Cousins. *Unified approach to the classical statistical analysis of small signals.* Phys. Rev. D 57 (1998) 3873–3889, arXiv:9711021.

[141] Lorenzo Moneta, Kevin Belasco, Kyle S. Cranmer, S. Kreiss, Alfio Lazzaro, Danilo Piparo, Gregory Schott, Wouter Verkerke, and Matthias Wolf. *The RooStats Project.* PoS ACAT2010 (2010) 057, 1009.1003.

[142] Michael Strickland. *Thermal Bottomonium Suppression.* AIP Conf. Proc. 1520 (2013) 179-184, 1207.5327.

[143] The ROOT data analysis framework. ROOT method TMath::Prob. `https://root.cern.ch/root/html524/TMath.html#TMath:Prob`.

[144] Kenneth Aamodt et al. *Centrality dependence of the charged-particle multiplicity density at mid-rapidity in Pb-Pb collisions at $\sqrt{s_{NN}}$ = 2.76 TeV.* Phys. Rev. Lett. 106 (2011) 032301, 1012.1657.

[145] S. S. Adler et al. *Systematic studies of the centrality and s(NN)**(1/2) dependence of the d E(T) / d eta and d (N(ch) / d eta in heavy ion collisions at mid-rapidity.* Phys. Rev. C71 (2005) 034908, nucl-ex/0409015. [Erratum: Phys. Rev.C71,049901(2005)].

[146] B. Alver et al. *Phobos results on charged particle multiplicity and pseudorapidity distributions in Au+Au, Cu+Cu, d+Au, and p+p collisions at ultra-relativistic energies.* Phys. Rev. C83 (2011) 024913, 1011.1940.

[147] Bottomonium in heavy ion collisions at STAR. `https://indico.triumf.ca/getFile.py/access?contribId=86&sessionId=38&resId=0&materialId=slides&confId=1922`. Accessed: 2015-09-28.

[148] Measurement of Υ(nS) production with p+Pb collisions at $\sqrt{s_{\mathrm{NN}}}$ = 5.02 TeV and pp collisions at $\sqrt{s}$ = 2.76 TeV. Technical Report ATLAS-CONF-2015-050, CERN, Geneva, Sep 2015.

[149] Serguei Chatrchyan et al. *Event activity dependence of Y(nS) production in $\sqrt{s_{NN}}$=5.02 TeV pPb and $\sqrt{s}$=2.76 TeV pp collisions.* JHEP 04 (2014) 103, 1312.6300.

[150] A. Emerick, X. Zhao, and R. Rapp. *Bottomonia in the Quark-Gluon Plasma and their Production at RHIC and LHC.* Eur. Phys. J. A48 (2012) 72, 1111.6537.

[151] Xingbo Zhao and Ralf Rapp. *Medium Modifications and Production of Charmonia at LHC.* Nucl. Phys. A859 (2011) 114-125, 1102.2194.

[152] Brandon Krouppa, Radoslaw Ryblewski, and Michael Strickland. *Bottomonia suppression in 2.76 TeV Pb-Pb collisions.* arXiv:1507.03951.

[153] M. Laine, O. Philipsen, P. Romatschke, and M. Tassler. *Real-time static potential in hot QCD.* JHEP 03 (2007) 054, hep-ph/0611300.

[154] Michael Strickland and Dennis Bazow. *Thermal Bottomonium Suppression at RHIC and LHC.* Nucl. Phys. A879 (2012) 25-58, 1112.2761.

[155] Edward Shuryak. *Why does the quark gluon plasma at RHIC behave as a nearly ideal fluid?* Prog. Part. Nucl. Phys. 53 (2004) 273-303, hep-ph/0312227.

This work is funded by the ERC, n° contrat 259612 «QuarkGluonPlasmaCMS»

European Research Council

Measurements of Υ meson suppression in heavy ion collisions with the CMS experiment at the LHC

Summary Measurements of Υ suppression in ultrarelativistic heavy ion collisions are key to understanding the hot and deconfined phase of matter called Quark-Gluon Plasma (QGP). The cross section of Upsilon states Υ(nS) are measured in proton-proton collisions and in lead-lead collisions at the centre-of-mass energy of 2.76 TeV per nucleon pair. Individual states are measured through their dimuon decay channel using the Compact Muon Solenoid (CMS) at CERN. The cross sections measured in *pp* and PbPb are compared by computing the nuclear modification factor, R_{AA}. This observable is extracted for Υ(1S) and Υ(2S) in several bins of transverse momentum, rapidity and centrality of the collision. An upper limit on the suppression factor of Υ(3S) is constructed. These measurements exhibit a clear and ordered suppression pattern, consistent with the hypothesis of sequential melting of quarkonia in the QGP. The measured Υ(1S) and Υ(2S) suppressions are observed to be independent of transverse momentum and rapidity. Comparisons with available phenomenological models are presented, however fail to reproduce the full set of observations. This novel measurement thus provides new constraints on the modeling of the screening of strong interactions in a deconfined medium.

Keyowrds: LHC ; Quark-gluon Plasma ; Υ ; muons ; sequential suppression ; nuclear matter absorption.

Résumé en français La suppression des Υ en collisions d'ions lourds ultrarelativistes est une mesure clé pour la compréhension de l'état de la matière chaude et déconfinée appelé plasma de quarks et de gluons (PQG). Les sections efficaces des états Upsilon Υ(nS) sont mesurées en collisions proton-proton et plomb-plomb à une énergie dans le centre de masse de 2.76 TeV par paires de nucléons. Les états individuels sont mesurés via leur canal de désintégration en deux muons, en utilisant le détecteur CMS au CERN. Les sections efficaces mesurées en pp et PbPb sont comparées grâce au facteur de modification nucléaire, R_{AA}. Cette observable est calculée pour Υ(1S) et Υ(2S) dans plusieurs intervalles d'impulsion transverse, de rapidité et de centralité de la collision. Une limite supérieure sur la production de Υ(3S) est estimée. Ces mesures montrent une suppression claire et ordonnée, en accord avec l'hypothèse de fonte séquentielle des quarkonia dans le PQG. La suppression mesurée pour Υ(1S) et Υ(2S) apparaît indépendante de l'impulsion transverse et de la rapidité. Des comparaisons avec les modèles phénoménologiques disponibles sont présentées, ne reproduisant pas totalement toutes les observations. Cette mesure apporte ainsi de nouvelles contraintes sur la modélisation du déconfinement des quarks lourds.

Mots Clés : LHC ; Plasma quark-gluon ; Υ ; muons ; fonte séquentielle ; absorption nucléaire.